Moments of parton distribution functions for the pion and rho meson from $N_f = 2 + 1$ lattice QCD

Dissertation

zur Erlangung des Doktorgrades
der Naturwissenschaften (Dr. rer. nat.)
der Fakultät für Physik
der Universität Regensburg

vorgelegt von

Marius Löffler

aus Kulmbach

im Jahr 2022

Promotionsgesuch eingereicht am: 22. Oktober 2021
Die Arbeit wurde angeleitet von: Prof. Dr. Andreas Schäfer

Prüfungsausschuss:
PD Dr. Jonathan Eroms
Prof. Dr. Andreas Schäfer
Prof. Dr. Christoph Lehner
Prof. Dr. Juan Diego Urbina

Datum Promotionskolloquium: 06.05.2022

Moments of parton distribution functions for the pion and rho meson from $\mathbf{N_f = 2 + 1}$ lattice QCD

Abstract

We compute the second Mellin moments of parton distribution functions for the pion and rho meson from $N_f = 2+1$ lattice QCD using improved Wilson fermions. Our results are presented in terms of singlet and non-singlet flavor combinations and, for the first time, take disconnected contributions fully into account. Besides condensing the common knowledge about spin-1 structure functions and parton distribution functions, we provide a detailed description of the software stack implemented by our group, in order to compute quark-line connected three-point functions using stochastic estimators. The main application is based on the factorization of the entire correlation function into two parts which are evaluated with open spin- (and to some extent flavor-) indices. This allows us to estimate the two contributions of the factorization simultaneously for many different initial and final states and momenta, with little computational overhead.

Our numerical analysis yields moments of the structure function F_1 (pion and rho) and of the structure function b_1, providing additional contributions in the case of spin-1 particles. To this end we use 26 gauge ensembles, mainly generated by the CLS effort, with pion masses ranging from 214 MeV up to 420 MeV and with five different lattice spacings in the range of 0.05 fm to 0.1 fm in our numerical analysis. This choice of gauge configurations enables us to resolve the quark mass dependencies reliably, as well as to extrapolate to the continuum limit. However, due to the resonance character of the rho meson, our final results are possibly contaminated by additional two-pion states, which we also discuss. We present

our results in the $\overline{\text{MS}}$ scheme at $\mu = 2\,\text{GeV}$. We find

$$
\begin{aligned}
v_2^{(u+d+s)} &= 0.220(207)\,, & v_2^{(u+d-2s)} &= 0.344(28)\,,\\
a_2^{(u+d+s)} &= 0.285(295)\,, & a_2^{(u+d-2s)} &= 0.384(52)\,,\\
d_2^{(u+d+s)} &= 0.226(124)\,, & d_2^{(u+d-2s)} &= 0.163(39)\,,
\end{aligned}
$$

for the second moment v_2 of the pion structure function F_1, the second moment a_2 of the rho structure function F_1, and the second moment d_2 of the rho structure function b_1 respectively. Based on these values we finally conclude, that the valence quarks in the pion carry about 35% of the total momentum, in the rho the valence quarks carry about 40% of the total momentum, and the non-vanishing values for d_2 suggest that the quarks in the rho meson carry a substantial amount of orbital angular momentum.

Moments of parton distribution functions for the pion and rho meson from $N_f = 2 + 1$ lattice QCD

Zusammenfassung

Wir berechnen die zweiten Mellin Momente von Parton-Verteilungsfunktionen für das Pion und das Rho Meson mittels Gitter QCD Simulationen, unter Zuhilfenahme von Clover Fermionen. Unsere Ergebnisse werden als Singlet- und Non-Singlet Farbkombinationen angegeben und wir berücksichtigen erstmals die Beiträge von nicht zusammenhängenden Dreipunktfunktionen. Neben einer Einführung in Spin-1 Strukturfunktionen und Parton-Verteilungsfunktionen gehen wir insbesondere auf die während dieser Arbeit erstellten Computerprogramme ein, die benötigt werden, um zusammenhängende Dreipunktfunktionen mit Hilfe stochastischer Verfahren zu approximieren. Das Hauptaugenmerk richten wir dabei auf den Kern unserer Simulationssoftware, in dem wir die Korrelationsfunktion in zwei unabhängige Teile faktorisieren, um Teilergebnisse mit offenen Spin- und teilweise offenen Farb-Indizes zu produzieren. Dieses Vorgehen erlaubt es uns die beiden Beiträge der Faktorisierung gleichzeitig für viele verschiedene Anfangs- und Endzustände sowie Impulse zu simulieren, ohne die Gesamtrechenzeit merklich zu erhöhen.

Mit Hilfe unserer numerischen Analyse können wir Momente der Strukturfunktion F_1 (Pion und Rho) und der Strukturfunktion b_1 berechnen. Letztere liefert zustätzliche Beiträge für Spin-1 Teilchen. Zu diesem Zweck nutzen wir 26 verschiedene Ensembles an Eichfeldern, die großteils im Rahmen der CLS Initivative erzeugt wurden. Die Konfigurationen decken Pionmassen von 214 MeV bis 420 MeV und fünf verschiedene Gitterabstände zwischen 0.05 fm und 0.1 fm ab. Durch die Benutzung dieser Ensembles können wir Quarkmassen-Abhängigkeiten vollständig auflösen und außerdem eine Kontinuums-Extrapolationen durchführen. Insbesondere im Fall des Rho Mesons könnte jedoch dessen Resonanzcharakter und damit einhergehende Zwei-Pion-Zustände, zu einer Verfälschung der Ergeb-

nisse führen. Dies wird in der Arbeit ausführlich diskutiert. Unsere Ergebnisse werden im $\overline{\text{MS}}$ Schema für $\mu = 2\,\text{GeV}$ angegeben. Wir erhalten

$$
\begin{aligned}
v_2^{(u+d+s)} &= 0.220(207)\,, & v_2^{(u+d-2s)} &= 0.344(28)\,,\\
a_2^{(u+d+s)} &= 0.285(295)\,, & a_2^{(u+d-2s)} &= 0.384(52)\,,\\
d_2^{(u+d+s)} &= 0.226(124)\,, & d_2^{(u+d-2s)} &= 0.163(39)\,,
\end{aligned}
$$

für das zweite Moment v_2 der Pion Strukturfunktion F_1, das zweite Moment a_2 der Rho Strukturfunktion F_1 und das zweite Moment d_2 der Rho Strukturfunktion b_1. Aufgrund dieser Werte schließen wir, dass die Valenzquarks im Pion ungefähr 35% und im Rho Meson ungefähr 40% des Gesamtimpuls tragen. Der nicht verschwindende Wert für d_2 legt nahe, dass die Quarks im Rho Meson zusätzlich einen nicht vernachlässigbaren Drehimpulsanteil aufweisen.

Contents

Acknowledgments

I would like to express my gratitude to the people who made this work possible.

First of all, I am much obliged to Andreas Schäfer, who made it possible for me to do this work and, thus, allowed me to dive even deeper into the world of particle physics. His theoretical guidance and physical insight was always a great help navigating through the almost endless spaces in the field of QCD.

Further, I am grateful to the examining board, Jonathan Eroms, Christoph Lehner, and Juan Diego Urbina, for the time they have taken.

I would also like to thank Philipp Wein. Through the constant work over the past years we were able to realize projects that would have been unthinkable before. Along with his tireless efforts and the many hours spent together in online calls and meetings as well as with his always open-minded way of discussing any topic he became one of the most important people for me during this work. Furthermore, I am also indebted to Rudolf Rödl, who accompanied me in almost all projects since the beginning of my master thesis and has become a good friend in the meantime. I will definitively keep in mind the countless hours of debugging and writing code together with Rudi in everyday work and during all of the weekends we spent together in front of our computers.

I am also indebted to Gunnar Bali, Lorenzo Barca, Simon Bürger, Sara Collins, Peter Georg, Benjamin Gläßle, Meinulf Göckeler, Peter Plößl, Andreas Rabenstein, Daniel Richtmann, Maximilian Schlemmer, Jakob Simeth, and Lisa Walter. Thank you for the various fruitful discussions and the mutual assistance during the last years. A special thanks goes to Simon Weishäupl, who has accompanied me through all the ups and downs since the first semester of our studies. I also spent many hours with him in discussions and in front of the screen to debug weird codes and solve physical problems. Even though it was often exhausting, it was always fun. In addition, I am deeply grateful to Thomas Wurm and Daniel Jenkins for the joint work and various discussions during the last years.

I am deeply grateful to Andreas Rabenstein, Philipp Wein, Thomas Wurm, Rudi Rödl, and Jakob Simeth for their invaluable and tireless proofreading.

Besides my colleagues, I would like to thank two other people without whom this

work would not have been possible. On the one hand, my former physics teacher Markus Englhart, who continuously encouraged me to study physics – the world needs more teachers like him! And on the other hand, to PD Dr. Bernd Semsch, who always stood by my side as a mentor and also accompanied me, even through the toughest phases of this work.

Last but not least, I want to thank my parents and my brother as well as my beloved girlfriend Stephanie for their unconditional and immeasurable support in all imaginable situations.

List of Publications

M. Löffler, P. Wein, T. Wurm, S. Weishäupl, D. Jenkins, R. Rödl, A. Schäfer, and L. Walter (RQCD Collaboration), *Mellin moments of spin dependent and independent PDFs of the pion and rho meson*, Phys. Rev. D **105**, 014505 (2022), arXiv:2108.07544 [hep-lat] .

S. Bürger, T. Wurm, M. Löffler, M. Göckeler, G. Bali, S. Collins, A. Schäfer, and A. Sternbeck (RQCD), *Lattice results for the longitudinal spin structure and color forces on quarks in a nucleon*, Phys. Rev. D **105**, 054504 (2022), arXiv:2111.08306 [hep-lat] .

G. S. Bali, L. Barca, S. Collins, M. Gruber, M. Löffler, A. Schäfer, W. Söldner, P. Wein, S. Weishäupl, and T. Wurm (RQCD), *Nucleon axial structure from lattice QCD*, JHEP **05**, 126 (2020), arXiv:1911.13150 [hep-lat] .

G. S. Bali, S. Collins, B. Glässle, S. Heybrock, P. Korcyl, M. Löffler, R. Rödl, and A. Schäfer, *Baryonic and mesonic 3-point functions with open spin indices*, EPJ Web Conf. **175**, 06014 (2018), arXiv:1711.02384 [hep-lat] .

This work is dedicated to my former teacher Markus Englhart.

1 Introduction

At the beginning of the twentieth century, a new generation of physicists turned the world upside down by starting to focus their interest on the smallest known objects in the universe. They were chasing the idea of understanding the world in its smallest, innermost components, but at that time no one could have guessed that this would develop into a completely new view on physics that would change the entire world. In the beginning, it was scientists like Thomson, Rutherford, Planck, and Bohr who developed a fundamental understanding of the structure of atoms and tiny particles [1–8]. Their groundbreaking research eventually led to a theory that initially seemed so outlandish to some of its developers that it took several more years for it to become widely accepted. We know it today as quantum mechanics [9]. It was masterminds like Heisenberg, Born, de Broglie, and Schrödinger who paved the way for a completely new way of thinking with their revolutionary ideas on wave-particle duality or the uncertainty principle [9–18]. How important these ideas are for our present understanding of matter and the resulting structure of the universe is made clear by the numerous Nobel Prizes that the above-mentioned scientists and numerous other colleagues, whom we cannot name all in this context, have received. Although there were groundbreaking developments in many areas of physics at that time, we want to focus our attention on the development of quantum field theory (QFT). The starting point of this development was the quantization of the electro-magnetic field and the electron field in the late 1920s by Paul Dirac [19]. In the following decades, his approach

proved to be extremely promising and some years later Tomonaga, Feynman, Schwinger, and Dyson succeeded in formulating quantum electrodynamics (QED) as the corresponding QFT, mainly by adapting renormalization to eliminate the occurring infinities [20–23]. This theory allowed, e.g., to describe processes in which the number of particles in the initial and final state differs, as for the emission of a photon, when the energy state of an atom changes by dropping an electron into a quantum state of lower energy. To date, QED represents one of the most accurately experimentally verified physical theories [24–27] and is the most prominent example of a QFT. Based on the underlying U(1) symmetry group, it describes the interaction for systems consisting of electromagnetic fields with the associated massless gauge boson (photon). For this work, Feynman, Schwinger, and Tomonaga were awarded the Nobel Prize in Physics in 1965.

Looking back again to the beginning of the twentieth / end of the nineteenth-century one finds the discovery of a further theory, namely the theory of weak interactions. At that time Wilhelm Roentgen discovered X-rays [28] and three years later Marie and Pierre Curie investigated the ionizing radiation of 'pechblende' [29, 30]. From these kinds of observations, which turned out to be radioactive decays, Enrico Fermi derived the first theory of the weak interaction in the 1930s. Therefore he assumed that the radioactive beta decay can be described by a simple four-fermion interaction [31]. In the 1960s Glashow, Salam, and Weinberg finally succeeded in combining the weak interaction with the electromagnetic force using the SU(2) $\times$ U(1) symmetry group to form the theory of electroweak interactions [32–34]. The associated gauge bosons are nowadays known as $W^{\pm}$ and Z and were experimentally detected in the early 1980s [35–39]. For their efforts, Glashow, Salam, and Weinberg jointly received the Nobel Prize in Physics in 1979 and Rubbia and van der Meer in 1984 for the experimental measurement.

In addition to these achievements, the first experiments with cloud chambers in the 1950s led to the discovery of more and more different particles, whose behavior could be explained only inadequately with the help of available theories. It took well over one decade until in 1973 the concept of color charge could be incorporated into a non-Abelian Yang-Mills gauge theory in such a way that all previously unexplained phenomena of the so-called strong interaction could be described with the help of a QFT. At this point, Fritzsch, Leutwyler, and Gell-Mann had developed a theory which is known today as quantum chromodynamics (QCD) [40]. Essentially, with the help of the SU(3) symmetry group, the concept of color charge was introduced, analogous to the electric charge of QED. The underlying fundamental particles are now known as quarks [41, 42] and the corresponding gauge bosons as gluons. With the help of this theory, and the concept of asymptotic freedom [43, 44], already some years later various high energy experiments could

be described very precisely in the context of a perturbative expansion of QCD. In the course of the years, the performed experiments became more and more precise, so that the validity of QCD can be verified in the meantime in the single-digit percentage range [45]. Nevertheless, there are numerous open questions, such as the behavior of QCD in the non-perturbative limit. A famous example is the observation that the attraction between two particles with color charge does not decrease with their distance (confinement). Corresponding evidence can be confirmed in the framework of lattice QCD (LQCD) [46] calculations, but is not yet mathematically proven. The search for a corresponding proof is listed as one of the seven millennium problems by the Clay Mathematics Institute [47].

At the beginning of the 1960s, Peter Higgs postulated another particle, which should finally lead to the fact that all elementary particles could be provided with corresponding masses [48, 49]. When the Higgs boson, now named after him, was experimentally confirmed about 50 years later, Peter Higgs and François Englert were awarded the Nobel Prize in Physics in 2013.

Finally, in 1975 the electroweak- and the strong interaction were combined to form the standard model (SM) of particle physics [32–34] which is – neglecting gravitational effects – a state-of-the-art QFT model in modern physics, relying on a $\mathrm{SU}(3) \times \mathrm{SU}(2) \times \mathrm{U}(1)$ gauge theory. Driven by the search for a unifying theory, both experimental and theoretical physicists have developed a model that has been verified by numerous experiments so far, e.g., measurements of the fine structure constant α [50]. Nevertheless, numerous open questions remain, such as the combination of gravity and the SM. However, the SM represents an indispensable cornerstone in the search for new models, e.g., supersymmetry.

In summary, since the 1970s, most physicists agree that the matter around us is composed of fermions that interact with each other through the exchange of gauge bosons. The elementary fermions can be divided into two groups: Six leptons like the electron and the associated neutrino and six quarks which form colorless bound states, commonly known as hadrons. The corresponding charge carriers are the four gauge bosons, e.g., the gluon for the strong interactions. As the last particle of the Standard Model, for the time being, the Higgs particle shall be listed here, which results directly from the second quantization of the Higgs field. These elementary particles are described by the SM, cf. the overview given in Fig. 1.0.1.

Essentially, the quantum field theories presented above form the basic framework for the considerations in this thesis. LQCD is of special importance in the following deliberations. Its formalism allows us to map the continuous Minkowski spacetime onto a four-dimensional Euclidean lattice. The method developed by K. Wilson [46] allows the computation of quantities that are not accessible by the

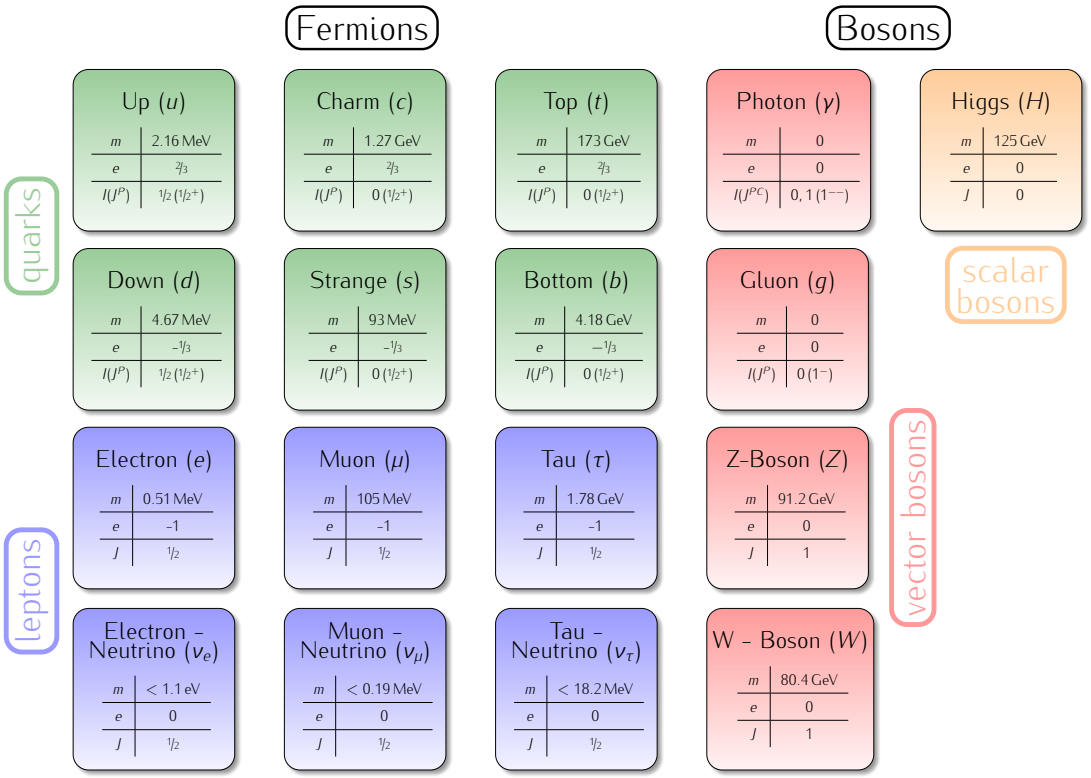

Figure 1.0.1: Particles of the SM. The first three columns show the three generations/families of fermions, the fourth column the four gauge bosons, and the last column the scalar Higgs boson. In addition we list the mass of the particles, their electrical charge in multiples of the unit charge e, and the isospin I, spin J, charge conjugation C, and parity P quantum numbers, depending on the corresponding particles. All values are taken from [51].

perturbative QCD expansion.

In this context also the parton model developed by Bjorken and Feynman plays an equally important role. It started with Bjorken's proposal in 1969, that the structure functions for inelastic electron scattering off a fixed target obey a certain scaling property - nowadays known as Bjorken scaling [52]. This was quickly confirmed by experiments [53] and only a few months later Feynman and Bjorken/Paschos independently worked out the so-called parton model [54, 55]. Therefore Feynman interpreted the Bjorken scaling due to the point-like nature of fundamental particles in the scattering target when they were scattered by the electron – he named them partons. Since QCD was not yet fully developed at that time, it was still unclear whether the partons were the quarks postulated by Gell-Mann, and also gluons did not play a role at this point.

However, we are interested in the structure functions inherent in the theory, which will give us information about the momentum distribution of the individual quarks within a hadron. This work aims mainly at computing Mellin moments of parton distribution functions (PDFs) for spin-0 and spin-1 mesons. Based on

the concept of LQCD, a new type of analysis software to analyze gauge fields, has been developed in the course of this thesis [56]. The goal of this work is to determine the structure functions F_1, F_2 (spin-0 and spin-1), and b_1 (spin-1 only) as accurately as possible using a maximum subset of the current lattice data available to our group. With the contributions considered, it is possible to present new (or rather improved) results that may play a significant role in planned EIC experiments [57, 58] and the new AMBER experiment planned for M2 beamline at the CERN super proton synchrotron [59, 60].

This thesis is structured as follows: We set the stage with a general introduction to QCD, the parton model, and the LQCD formalism together with numerical parameters, which are used to compute all the observables presented in this work. In Chapter 3 we discuss structure functions and PDFs and their relation to deep inelastic scattering (DIS) processes including various techniques like the operator product expansion (OPE). This finally yields the quantities computed in this thesis, called reduced matrix elements v_2, a_2, and d_2. Chapter 4 is finally devoted to the numerical simulations used to extract moments of PDFs of the pion and rho meson. We put special emphasis on the calculation of connected three-point functions using stochastic estimators since the development of the corresponding software was one of the main tasks for this thesis. At the end of Chapter 4 we present results for the quark mass dependence and continuum extrapolation of our quantities, where we, for the first time, also included quark-line disconnected contributions. A brief conclusion is given in Chapter 5.

2

Basic concepts

This chapter summarizes the textbook knowledge on the theoretical foundations of this thesis. In the first place, a short introduction to the theory of the strong interaction is given and the development of the parton model mentioned in Chapter 1 is discussed in more detail. Afterward, LQCD, which represents the basic framework of this thesis, will be discussed in greater detail. In particular, it shall be elaborated how the QCD path integral on a Minkowski space-time can be evaluated using statistical Monte Carlo methods on a four-dimensional Euclidean lattice in order to draw conclusions about the structure of the particles we want to analyze by appropriate simulations.

2.1 Quantum chromodynamics

QCD describes the interaction of the quarks and gluons of the SM. In Chapter 1 we stated that the quarks involved in the strong interaction occur in $N_f = 6$ different flavors, reflecting the current evidence provided by accelerator experiments. However, it cannot be ruled out that additional fermion generations exist in nature. In the following we will point out that quarks and gluons further occur in $N_c = 3$ different variants, denoted as color c, and how the interactions between the consequent $N_c \times N_f = 3 \times 6$ quarks and $N_c^2 - 1 = 8$ gluons, cf. Fig. 1.0.1, are

described by QCD as a non-Abelian SU(3) gauge theory[1].

Measurements in different experiments suggest that quarks and gluons are never observed as isolated particles (confinement) but always appear in bound states and are ordered to groups with very similar internal quark-gluon wave functions. Neglecting the mass differences of the individual quarks, these multi quark states can be described in the framework of a global SU(N_f) symmetry group. However, this SU(N_f) is completely independent of the local SU(3) gauge group of QCD. Historically, the approximation of this flavor symmetry allowed for successful predictions of numerous, until then unknown, particles which, despite its weaknesses, plays an important role in numerous QCD calculations. An example for such an experimentally determined composite state of quarks are the nucleons (protons, neutrons) known from atomic physics, which were measured to be spin-$\frac{1}{2}$ particles. From the total spin of the nucleons, and all other baryons, it follows directly that all quarks themselves have to be Dirac particles with spin-$\frac{1}{2}$ so that the correct wave function can be constructed. The quality for predictions that use the SU(N_f) flavor symmetry just described depends of course on the accuracy of the approximation. Altogether the symmetry imposes that all physics is invariant under the exchange of the N_f quark types. If one compares the masses of the individual quarks from Fig. 1.0.1 with each other, and also with the typical energy scales of $\mathcal{O}(100\,\mathrm{MeV})$ in hadron physics, it becomes clear that the symmetry assumptions will not necessarily lead to good predictions. m_u and m_d are approximately equal and thus SU(2) is a very good symmetry assumption. Although m_s is already significantly larger, good results in the range of 20% - 30% accuracy can still be obtained for SU(3). However, the symmetry is not exact but broken explicitly to $\mathrm{SU}(2)_I \times \mathrm{U}(1)_Y$ where I denotes the isospin and Y corresponds to the hypercharge[2]. The small mass differences within the SU(3) multiplet are described by the Gell-Mann-Okubo formula [62–64]. For the heavier quark flavors, however, one no longer assumes symmetry. As an introductory example we want to pick out the construction of wave functions in $\mathrm{SU}(3)_{\mathrm{flavor}} \times \mathrm{SU}(2)_{\mathrm{spin}}$. From the lowest lying states of the baryon decuplet we use the simplest state, called Δ^{++} resonance,

$$\left|\Delta^{++}, j_z = \frac{3}{2}\right\rangle = \left|u \Uparrow, u \Uparrow, u \Uparrow\right\rangle , \tag{2.1}$$

[1]There are various valuable introductions to QCD in nearly every QFT textbook. However, the introduction given here relies mainly on [61] and the lecture notes of the QCD courses of A. Schäfer and T. Wettig and the group theory course of T. Wettig, all attended at the University of Regensburg. Whenever necessary additional references are provided.

[2]In the fundamental representation $I_3 = t_3$ and $Y = 2t_8/\sqrt{3}$, cf. Appendix A.2.

a very exotic and short-lived particle with $J = \frac{3}{2}$ and z-component $j_z = +\frac{3}{2}$, with completely symmetric spin-flavor structure. Furthermore, we assume a S-wave state with corresponding orbital angular momentum $L = 0$ and hence see that the Pauli principle seems to be violated. To make the wave function antisymmetric an additional degree of freedom was introduced, the color charge. Using this additional information we generalize the model wave function u from the Δ^{++} to $q_a^{f,s}(x)$ with color index $a = 1, 2, 3$, flavor $f \in [u, d, s, c, b, t]$ and spin $s = \Uparrow / \Downarrow$. If the wave function is odd in color the spin-statistics problem of the combined wave function is solved. Therefore we re-write (2.1) as

$$\left|\Delta^{++}, j_z = \frac{3}{2}\right\rangle = \frac{1}{\sqrt{6}}\,\varepsilon_{abc}\left|q_a^{u,\Uparrow}(x)\right\rangle\left|q_b^{u,\Uparrow}(x)\right\rangle\left|q_c^{u,\Uparrow}(x)\right\rangle\,, \tag{2.2}$$

using the completely antisymmetric tensor ε_{abc} defined in Appendix A.1. However, by performing the completely antisymmetric coupling one finds that the corresponding states always appear as color singlets, as predicted by experiments. The theory that describes all experiments is that with three colors. One of the best known experiments for the validation of $N_c = 3$ is the so-called R-ratio. The following equation gives the ratio of hadronic decays related to a leptonic decay channel in first order perturbation theory

$$R = \frac{\sigma\left(e^+ + e^- \to \text{hadrons}\right)}{\sigma\left(e^+ + e^- \to \mu^+ + \mu^-\right)} = N_c \sum_f e_f^2\,, \tag{2.3}$$

where we sum over all quark flavors f, and e_f is the electrical quark charge in units of the elementary charge. Considering quarks with mass much smaller than half of the energy in electron-positron annihilations, this ratio gives the number of quarks and their electric charges. E.g., for $3\,\text{GeV} < E < 10\,\text{GeV}$, i.e., $f \in [u, d, s, c]$ one gets $R = \frac{10}{3}$ if we assume $N_c = 3$. Comparing this result to the world data on R, shown in Figure 52.2 of [51], one finds that the assumption of three different colors is reflected very precisely in the experimental data.

The simplest color singlet states can be realized as 3-quark states (baryons)[3] or quark-antiquark states (mesons). As mentioned above, the QCD Lagrangian $\mathcal{L}_{\text{QCD}}$ – see below – is invariant only for flavor SU(3), i.e., for $m_u = m_d = m_s$. Using this behavior, one obtains for the approximation of exact SU(3) flavor symmetry the

[3]In 2015 the LHCb collaboration also presented first experimental evidence for so-called pentaquarks and tetraquarks dicussed in [65–67]. For a recent review see also [68].

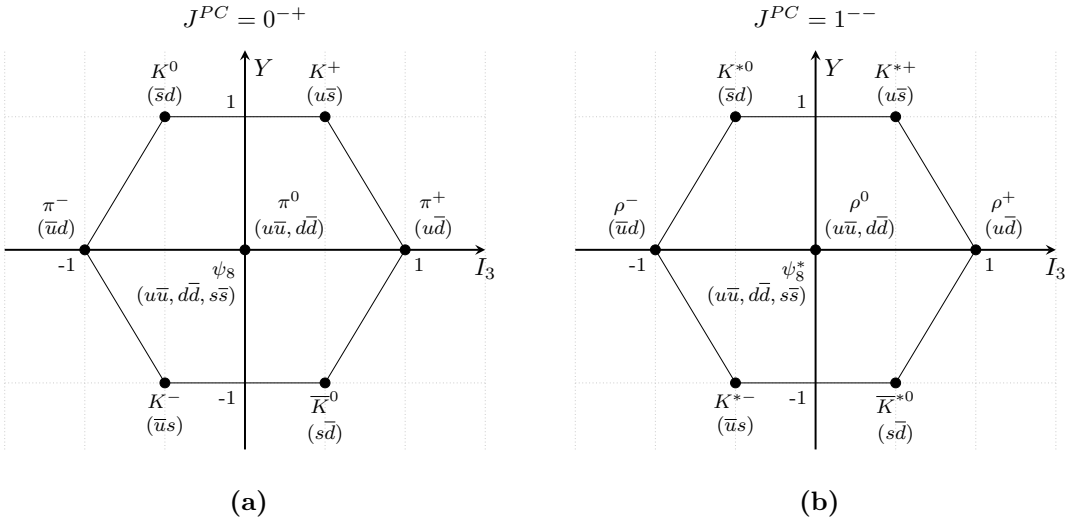

(a) **(b)**

Figure 2.1.1: Meson octet for **(a)** $J^{PC} = 0^{-+}$ and **(b)** $J^{PC} = 1^{--}$. A detailed overview of all quantum numbers and physical states up to SU(4) is given in [51]. Note that the quantum number C is only defined for states built by a quark and its antiquark, e.g., $u\overline{u}$.

fundamental representation of the quarks as vectors

$$\boldsymbol{q}(x) = \begin{pmatrix} q_a^{u,s_1}(x) \\ q_b^{d,s_2}(x) \\ q_c^{s,s_3}(x) \end{pmatrix} , \tag{2.4}$$

where s_i labels the spin of the quark. The corresponding antiquarks for the meson states are obtained by applying the charge conjugation operator $\mathrm{C} = -i\gamma_2\mathrm{K}$ to the quark fields q as $\overline{q}_a^{f,s}(x) = \mathrm{C}\, q_a^{f,s}(x)$ where K is the complex conjugation operator. Resulting antiquarks transform as elements of the anti-multiplet $\overline{3}$. To obtain all meson states we finally compute all product states of the form $3 \otimes \overline{3}$ and decompose them into their irreducible components

$$3 \otimes \overline{3} = 8 \oplus 1 \,, \tag{2.5}$$

resulting in a multiplet with 8 roughly degenerated particles and a second multiplet with only one particle. Experimental observations show that the lightest (ground-state) mesons indeed form an octet and a singlet with quantum numbers $J = 0$ (spin), $P = -1$ (parity), and $C = +1$ (charge conjugation) abbreviated as $J^{PC} = 0^{-+}$. A detailed overview of the ground-state meson octet is shown in Fig. 2.1.1a, the corresponding singlet state is denoted by ψ_1. Assuming exact SU(3) flavor symmetry this picture suggests that the isospin singlet state $\psi_8 = 1/\sqrt{6}(u\overline{u} + d\overline{d} - 2s\overline{s})$ of the SU(3) octet and the isospin singlet state $\psi_1 = 1/\sqrt{3}(u\overline{u} + d\overline{d} + s\overline{s})$ of the SU(3) singlet would be physical states, i.e., particles, since they transform in

different irreducible representations of SU(3), sharing the same quantum numbers. However, SU(3) is broken explicitly so that the ψ_1 and ψ_8 transform in different irreps, but with the same quantum numbers. The corresponding physical states η and η' can be parametrized as

$$\begin{pmatrix} \cos\Theta & -\sin\Theta \\ \sin\Theta & \cos\Theta \end{pmatrix} \begin{pmatrix} \psi_8 \\ \psi_1 \end{pmatrix} = \begin{pmatrix} \eta \\ \eta' \end{pmatrix} , \tag{2.6}$$

where Θ is the nonet mixing angle [51]. The weight diagrams for the lightest SU(3) vector meson octet is depicted in Fig. 2.1.1b and the corresponding isospin singlet state is ψ_1^*.

An analogous approach can be used to determine all baryon states composed of three quarks. Again assuming exact SU(3) flavor symmetry the product states are decomposed into their irreducible components

$$3 \otimes 3 \otimes 3 = 10_S \oplus 8_{M_S} \oplus 8_{M_A} \oplus 1_A \, , \tag{2.7}$$

and one finds multiplets of 10, 8, and 1 particles. The indices S and A denote tensors totally symmetric or antisymmetric under S_3, i.e., permutations of quarks, while M_S and M_A are tensors of mixed symmetry, symmetric or antisymmetric under the exchange of the first two quarks respectively. In ground-state baryons the singlet contribution is forbidden by Fermi statistics while the octet appears as a linear combination of 8_{M_S} and 8_{M_A}. Experiments show that the lightest baryons indeed form a decuplet and an octet with $J^P = \frac{3}{2}^+$ and $J^P = \frac{1}{2}^+$. However, a second octet and also the singlet contributions are possible in excited state baryons. A complete list of quantum numbers and the corresponding SU(4) multiplets are given in [51].

Up to this point, we have shown that the quarks can be represented as vectors in the fundamental representation, furnished with three colors. To complete the theory just the corresponding gauge bosons are missing.

Gluons are the charge carriers of the strong interaction, which finally lead to the formation of hadronic states. Generally speaking, each gluon carries a color charge and an anti-color charge, which leads to a total of nine possible combinations for three colors, represented by a color singlet and a color octet. However, a more detailed analysis of all possible gluon states leads to the fact that the (theoretically possible) color singlet state (or color-invariant) could occur as a free particle and thus would not be bound by confinement. I.e., a coupling with a very long range would occur which is in clear contradiction to the short-range behavior of the strong interaction. So in the observed universe only eight different gluons appear, which reflects the SU(3) gauge group of QCD. The corresponding generators are

the Gell-Mann matrices, cf. Appendix A.2. While the quarks correspond to the fundamental representation, the gluons are described by linear combinations of elements in the adjoint representation

$$(t_j)_{kl} = -i f_{jkl} \ , \tag{2.8}$$

which could be represented by the structure constants as $(N^2-1) \times (N^2-1)$ matrices. Analogous to the photons in QED, the gluons correspond to massless spin-1 particles.

Taking into account the considerations made so far, it is now possible to state the QCD Lagrangian density by

$$\mathcal{L}_{\mathrm{QCD}} = \sum_{\alpha\beta} \sum_{f} \sum_{ij} \overline{q}_{\alpha}^{f,i} \left(i \not{D}_{\alpha\beta}^{ij} - m_f \delta^{ij} \delta_{\alpha\beta} \right) q_{\beta}^{f,j} - \frac{1}{2} \operatorname{tr}_c \left[F_{\mu\nu} F^{\mu\nu} \right] , \tag{2.9}$$

with $\overline{q} = q^{\dagger}\gamma^0$ and the Feynman slash notation $\not{a} \equiv a_\mu \gamma^\mu$ using the Dirac gamma matrices defined in Appendix A.3. In contrast to the definitions at the beginning of this section, the structure of q is now made explicit using additional Dirac indices (Greek letters) which reflect the spin structure of the quarks. In (2.9) the gluon fields are hidden in the covariant derivative defined as

$$D_\mu = \partial_\mu + i g A_\mu \ , \tag{2.10}$$

and in the field strength tensor

$$F_{\mu\nu} = \partial_\mu A_\nu - \partial_\nu A_\mu + i g \left[A_\mu, A_\nu \right] = \frac{-i}{g} \left[D_\mu, D_\nu \right] \ , \tag{2.11}$$

where g is the strong coupling constant and $A_\alpha = \sum_j A_\alpha^j t^j$ are the gluon fields using the SU(3) generators t^j defined in Appendix A.2. By substituting (2.11) into (2.9) one immediately sees that we encounter terms cubic and quadratic in terms of the gauge fields, already at tree level. This gives rise to the self-interaction of QCD and is thus responsible for confinement, one of the most prominent features of QCD.

Using the QCD Lagrangian we require that the corresponding action is invariant under gauge transformations, i.e.,

$$S\left[q, \overline{q}, A\right] = \int \mathrm{d}^4 x \, \mathcal{L}_{\mathrm{QCD}} = S\left[q', \overline{q}', A'\right] \ , \tag{2.12}$$

using the local gauge transformations

$$\begin{aligned} q(x) &\to q'(x) = \Omega(x) q(x)\,, \\ A_\mu(x) &\to A'_\mu(x) = \Omega(x) A_\mu(x) \Omega^\dagger(x) + i\,[\partial_\mu\,\Omega(x)]\,\Omega^\dagger(x)\,, \end{aligned} \tag{2.13}$$

with $\Omega(x) \equiv \exp\left(i \sum_j \Theta_j(x) t_j\right)$ and $\Omega^\dagger(x) = \Omega^{-1}(x)$. However, if one uses the Lagrangian density just presented, one finds that especially in the calculation of the gauge field propagators (with the help of the path integral formalism) two unphysical light-like polarization states of the gluons occur in loop diagrams. To compensate these unwanted states, Faddeev and Popov introduced so-called ghost fields by fixing the gauge condition via adding a gauge fixing and a gauge compensating term to the Lagrangian [69]. Note that the ghost fields appear only in non-Abelian theories while they decouple completely otherwise, e.g., in QED. The extension of (2.9) comes along with a new symmetry of the gauge fixed Lagrangian, taking into account how the compensation of the ghost-fields affects the complete interacting theory. It is called Becchi, Rouet, Stora, and Tyutin (BRST) invariance [70, 71]. Since all of the following discussions are not affected by gauge fixing – this thesis is dedicated to the computation of gauge-invariant quantities using LQCD – we stop the discussion here and will not discuss BRST invariance and gauge fixing any further.

Based on the QCD action (2.12) the behavior and interactions of elementary particles – and also the ghost fields introduced above – can be described by the well known Feynman diagrams[4]. In this text, we will skip an introduction to Feynman diagrams and refer the reader to the satisfactory literature. However, we do not want to hide one of the main problems in Feynman diagram calculus: The occurrence of ultra violet (UV) divergences in loop diagrams, describing quantum corrections to the field theory. It is shown in, e.g., [75], that the masses, couplings, and fields in (2.9) do not reflect the exact quantities of a single, physical particle. Rather, they describe what is called the bare parameters of the system. To overcome this issue we exploit that QCD is a renormalizable field theory and define the renormalized Lagrangian density by [76]

$$\mathcal{L}_{\mathrm{QCD}}(q_0, m_0, A_0, g_0, \dots) = \mathcal{L}_{\mathrm{QCD}}(q, m, A, \mu g, \dots) + \delta\mathcal{L}_{\mathrm{QCD}}(q, m, A, \mu g, \dots)\,, \tag{2.14}$$

where q_0, etc. denotes the bare parameters. The connection between the renormalized and bare parameters finally defines the counterterms $\delta\mathcal{L}_{\mathrm{QCD}}$ and the UV

[4]Frank Wilczek remarks in the column [72] that the very first Feynman diagram was published in [73]. However, the construction of Feynman diagrams and the corresponding calculus is part of nearly every textbook about elementary particle physics, e.g., [61, 74].

divergences are absorbed into the renormalized parameters of the Lagrangian. However, in the discussion of (2.14) we disregarded that the loop integrals presume that the divergences are regularized, i.e., the divergences are isolated in well-defined expressions. A state-of-the-art regularization method for perturbative calculations is dimensional regularization [77]. In the LQCD computations of this work, we implicitly introduce another regularization scheme through the lattice spacing a which provides a natural cutoff $\Lambda \sim 1/a$ to regularize the theory, since it acts as a momentum cut-off, cf. Section 2.3. Final results are obtained in the limit $a \to 0$ or $\Lambda \to \infty$ respectively using proper renormalization methods. On the one hand, this cut-off regularization has the clear advantages to be well-defined and to be understandable already at a very intuitive level. On the other hand, calculations can become disproportionately cumbersome. Choosing a particular regularization combined with the freedom to rescale the fields and parameters by the renormalization procedure described above finally cancels all divergences of the theory. At this point, the discussion is actually completed but nevertheless, we have to make one additional remark. The counterterms defined in (2.14) provide the opportunity to introduce arbitrary, but finite, constant terms. Specific types of these terms are grouped in so-called subtraction schemes where the modified minimal subtraction ($\overline{\text{MS}}$) scheme [78] is, without doubt, the most popular choice in perturbative QCD. Through the regularization we secretly introduced the energy scale μ in (2.14) to well define the counterterms via a specific regularization scheme. Since μ does not show up in the original theory our final results have to be independent of the energy scale, which yields a set of differential equations referred to as renormalization group (RG) equations. The RG equations describe the dependence of the renormalization factors on the energy scale μ. While the final results have to be independent of μ all intermediate steps now may depend on the energy scale, which entails a scale dependence for the parameters of the theory. Using the $\overline{\text{MS}}$ scheme we ensure that bare parameters depend only implicitly on the renormalization scale via the renormalized parameters. A prominent example for the scale dependence of such a parameter is the running coupling of QCD.

Perturbative QCD expectations for observables are given in terms of the renormalized strong coupling $\alpha_s(\mu) = g^2(\mu)/(4\pi)$ as a function of the renormalization scale μ and, following [51], satisfies the RG equation

$$\mu^2 \frac{\mathrm{d}\alpha_s}{\mathrm{d}\mu^2} = \beta(\alpha_s) = -\left(\beta_0 \alpha_s^2 + \beta_1 \alpha_s^3 + \beta_2 \alpha_s^4 + \dots\right). \tag{2.15}$$

The values β_i are referred to as the $(i+1)$-loop β-function coefficients. Note that the coefficients depend on the subtraction scheme for $i > 1$ and the factor -1 in

front of the expansion indicates asymptotic freedom for $\beta_0 > 0$, i.e., the coupling becomes weak for hard processes while it is strong for energies around and below the typical hadronic scale of 1 GeV. Assuming a theory with a constant number of N_f light quarks ($m_q \ll \mu$) an exact solution for the 1-loop ($i = 0$) strong coupling is given by

$$\alpha_s(\mu^2) = \frac{4\pi}{\left(\frac{11}{3}N_c - \frac{2}{3}N_f\right)\ln\left(\frac{\mu^2}{\Lambda^2}\right)} \,, \tag{2.16}$$

where N_c defines the gauge group, i.e., $N_c = 3$ for QCD, and Λ corresponds to the scale where the perturbatively calculated strong coupling would diverge and non-perturbative dynamics become dominant. A possible choice for μ^2 is the invariant momentum transfer Q^2 of a given process, e.g., a DIS reaction introduced in the next section. If one chooses $\mu^2 \simeq Q^2$ higher order corrections become minimal.

2.2 Parton model

Based on the introductory remarks about the theory of strong interactions in the last section, we can make predictions and interpret the results of experiments using QCD. However, even before the introduction of non-Abelian gauge theories, there existed already other theories to describe the behavior of elementary particles. One famous example is the parton model, introduced by Feynman and Bjorken/Paschos [54, 55]. In this section, we will point out that this seminal model, incomplete as it is, implicates a series of prescriptions that are still used in high energy physics and also in the computation done in this thesis.

A first, naive starting point for the invention of the parton model are hadron-hadron scattering experiments. At high energies ($E_{\mathrm{cm}} \gtrsim 10\,\mathrm{GeV}$), collisions of hadrons produce a high number of pions with momenta almost collinear with the collision axis [61]. In other words: Instead of filling the whole phase space, as one would assume for interacting particles, the final particles are furnished with a very limited amount of transverse momentum and thus it seems natural to describe the initial hadrons by a bundle of almost free particles, called partons. Later it turned out that the partons correspond to the particles predicted by QCD. A first crucial test of this picture was performed by the SLAC-MIT experiments in the late 1960s [79] using electron-nucleon DIS experiments as shown in Fig. 2.2.1. Using a 20 GeV electron beam scattered off hydrogen atoms these experiments saw a substantial rate of hard scattering events, comparable to the scattering of a fundamental, point-like particle according to simplest expectations from QED. So it was assumed that partons are fundamental particles, incapable of exchanging large momenta Q^2 through strong interactions, but the partons interact with electrons

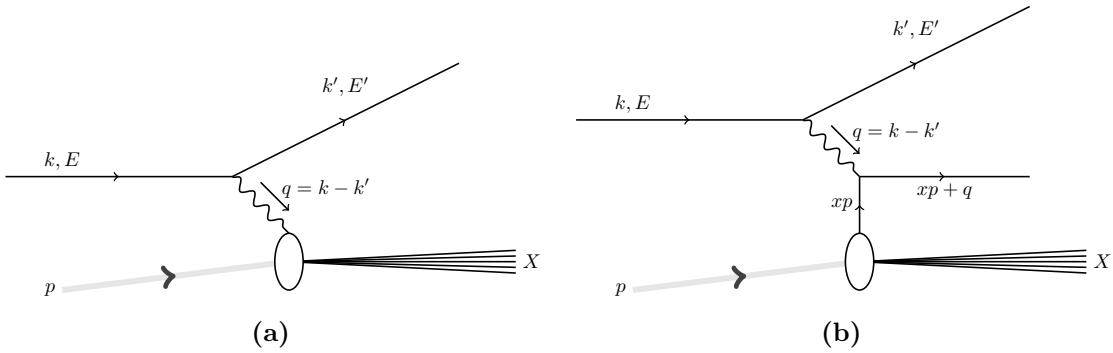

Figure 2.2.1: (a) Basic diagram for a inclusive DIS reaction. The black line depicts the initial (final) lepton with momentum k and energy E (k', E'). The virtual photon momentum is denoted by q and p corresponds to the target momentum. The unknown final states are denoted by X. **(b)** Kinematic of the DIS reaction in the parton model. The longitudinal parton momentum fraction is denoted by xp.

(leptons) via electromagnetic interactions. This imposes a strong constraint on the DIS cross-section, as we will see in the subsequent calculations.

Starting from an unpolarized inclusive DIS process as shown in Fig. 2.2.1a one can factorize the matrix element of the DIS cross-section into a leptonic and a hadronic tensor, cf. Chapter 3 for details. In the unpolarized case, the decomposition of the hadronic tensor $W^{\mu\nu}$ defines two structure functions via

$$W^{\mu\nu} = \left(g^{\mu\nu} - \frac{q^\mu q^\nu}{q^2}\right) W_1(x, Q^2) + \left(p^\mu - \frac{q^\mu (p\cdot q)}{q^2}\right)\left(p^\nu - \frac{q^\nu (p\cdot q)}{q^2}\right) W_2(x, Q^2)\,, \tag{2.17}$$

using $Q^2 = -q^2$ and $x = Q^2/(2p\cdot q)$. The structure functions $W_{1/2}$ were measured by the SLAC-MIT experiment [79] and surprisingly it was found that they are approximately independent of Q^2, for large invariant momentum transfers Q^2.

Following the basic operations, e.g., shown in [76], naive parton model calculations are performed using the sub-process shown in Fig. 2.2.1b. By decomposing the DIS process into a hard scattering kernel, containing the interaction of the photon and the struck parton, and a soft contribution, containing the information about the hadron structure, the computation can be split into two independent parts. While the first part can be calculated in perturbation theory the second part requires the PDFs to be computed using non-perturbative methods, in our case LQCD. More formally, this can be written as

$$W^{\mu\nu} = \int \mathrm{d}x\, f_q(x)\, C^{\mu\nu}_{q,\text{partonic}}\,, \tag{2.18}$$

where $f_q(x)$ is the weight-function to find a quark of flavor q with momentum fraction x inside the target hadron and $C^{\mu\nu}_q$ is the corresponding coefficient for

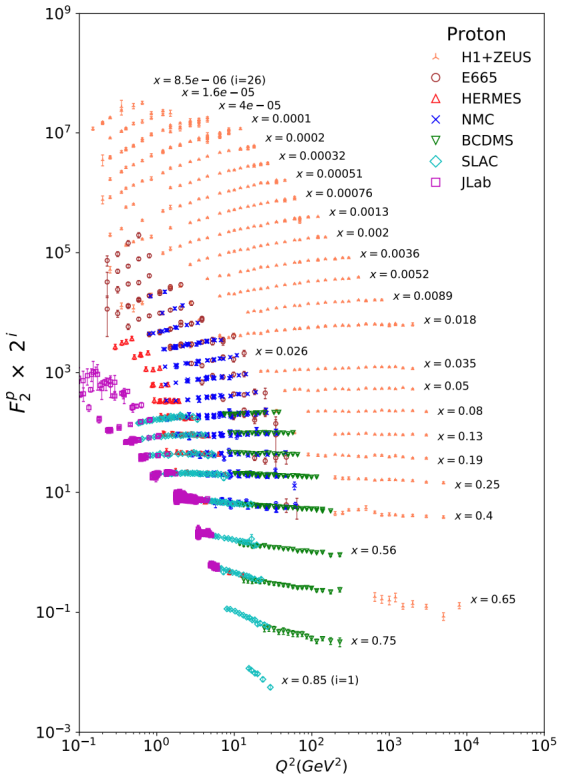

Figure 2.2.2: World-data for the structure function $F_2(x, Q^2)$ of the proton. Note that the data sets for the different values of x would sit on top of each other and are therefore shifted by an additional factor 2^i where i denotes the number of the data set. Figure taken from [51] under the Creative Commons CC-BY license.

flavor q. Comparing this to the expansion of the hadronic tensor in terms of structure functions one finally finds

$$F_2(x,Q^2) = \sum_q e_q^2\, x\, f_q(x), \qquad F_1(x,Q^2) = \frac{1}{2x} F_2(x,Q^2),$$
$$\text{with} \quad F_1(x,Q^2) = -W_1(x,Q^2), \qquad F_2(x,Q^2) = (p\cdot q) W_2(x,Q^2). \tag{2.19}$$

The sum in the first term of (2.19) runs over all flavors $1 \leq q \leq N_f$ and the charge of the individual quarks is given in units of the elementary charge, cf. Fig. 1.0.1. According to the naive parton model the structure functions are independent of Q^2 which is known as Bjorken scaling [52]. The Bjorken variable x corresponds to the momentum fraction of the hit quark in the target hadron. Furthermore, the second equation in (2.19) is the Callan-Gross relation [80], stating that in lowest order the structure functions F_1 and F_2 are not independent and thus the process is described by a single structure function. The world-data on the structure function F_2 of the proton is given, e.g., in [51], and one finds that the predictions made by the parton model are quite accurate for medium values of x. However, in the limiting cases $x \to 0$ and $x \to 1$, correction terms have to be taken into account. An overview is shown in Fig. 2.2.2.

In the following, we introduce an explicit expression for the PDFs $f_q(x)$ and complete the discussion with the introduction of leading order correction terms. Within the parton model the PDFs can be expressed in terms of matrix elements

of bilocal twist-2 operators [81, 82]

$$f_q(x) = \int_{-\infty}^{\infty} \frac{\mathrm{d}z^-}{4\pi}\, e^{ixp^+z^-} \left\langle \boldsymbol{p},\lambda \middle| \overline{q}\left(-\frac{z}{2}\right) \Gamma\, q\left(+\frac{z}{2}\right) \middle| \boldsymbol{p},\lambda \right\rangle \Big|_{z^+=0,\boldsymbol{z}=0} , \tag{2.20}$$

where the right-hand side quark flavor is set implicitly via the quark spinor definition, e.g., $q(x) = u(x)$ for up quarks, and the light-cone coordinates p^+ and z^- are defined according to Appendix A.8. Gluon PDFs are defined in close analogy to (2.20). In explicit calculations we set $\Gamma = \gamma^+$ for unpolarized PDFs, $\Gamma = \gamma^+\gamma_5$ for helicity PDFs, or $\Gamma = i\sigma^{+i}$ with $i = 1, 2$ for transversity PDFs, see also [83]. The definition in (2.20) is, however, only correct neglecting additional collinear gluons connecting the hard scattering kernel and the soft contributions given by the PDFs. These additional gauge links are introduced by Wilson lines[5] between the fields at positions $\frac{-z}{2}$ and $\frac{z}{2}$ defined as

$$W[a,b] = P\, e^{ig\int_b^a \mathrm{d}x^- A^+(x^- n_-)} , \tag{2.21}$$

where P denotes path ordering from a to b [82]. What remains is the incorporation of the Wilson lines into the definition (2.20) to obtain

$$f_q^B(x) = \int \mathrm{d}k^-\, \mathrm{d}^2\boldsymbol{k} \int_{-\infty}^{\infty} \frac{\mathrm{d}z^-}{4\pi}\, e^{ik\cdot z} \left\langle \boldsymbol{p},\lambda \middle| \overline{q}\left(\frac{-z}{2}\right) W\left[-\frac{z^-}{2},\frac{z^-}{2}\right] \Gamma\, q\left(\frac{z}{2}\right) \middle| \boldsymbol{p},\lambda \right\rangle , \tag{2.22}$$

as the definition of the bare quark PDF. We fix the UV divergences by an appropriate regularization and renormalization procedure

$$f_q(x,\mu) = \int_x^1 \frac{\mathrm{d}z}{z} Z_{qr}\left(\frac{x}{z},\mu\right) f_r^B(z) , \tag{2.23}$$

where Z_{qr} is the renormalization factor, and thus introduce a scale dependence into the definition of the PDFs. The scale μ separates high and low momentum physics, however, final results have to be scale-independent. Predictions for scale variations in the computations of PDFs are governed by the Dokshitzer, Gribov, Lipatov, Altarelli, and Parisi (DGLAP) evolution equations [84–86] which have the form

$$\frac{\mathrm{d}}{\mathrm{d}\log\mu^2} f_q(x,\mu) = \int_x^1 \frac{\mathrm{d}z}{z} P_{qr}\left(\frac{x}{z},\mu\right) f_r(z,x) , \tag{2.24}$$

[5] One can just as well argue with the introduction of a general gauge instead of the light-cone gauge $A^+ = 0$, cf. [82].

where the splitting kernels P are defined as

$$\frac{\mathrm{d}}{\mathrm{d}\log\mu^2} Z_{qr}\left(\frac{x}{z},\mu\right) = \int_x^1 \frac{\mathrm{d}z}{z} P_{qk}\left(\frac{x}{z},\mu\right) Z_{kr}\left(z,\mu\right) \,. \tag{2.25}$$

Finally, we can rewrite the naive factorization of the hadronic tensor (2.18) using the approximation

$$W^{\mu\nu}(p,q) \approx \int_x^1 \frac{\mathrm{d}z}{z} f_q(z,\mu)\, H_q^{\mu\nu}\Big(z,q,\mu,\alpha_s(\mu)\Big)\,, \tag{2.26}$$

neglecting higher-order terms. $H_q^{\mu\nu}$ is the hard scattering kernel, computed in perturbation theory for sufficiently large values of q. With this statement, we conclude the discussion about the collinear factorization of the hadronic tensor and the introduction of quark PDFs and DIS structure functions. The parton model quantities derived in this section allow for the extraction of PDFs from experimental data, e.g., HERA [87, 88] and JLab Hall A [89], and by the use of (l)QCD input we are able to predict cross-sections of upcoming experiments[6], e.g., EIC [57] and AMBER at CERN [60]. A physical interpretation of the PDFs in the infinite momentum frame is given by a rather simple, probabilistic picture: The function $f_q(x,\mu)$ corresponds to the number of quarks q carrying the fraction x of the total longitudinal target momentum. If one increases the scale μ the DGLAP equations predict that the number of partons will also increase, i.e., we increase the resolution of the process [76]. However, it has to be mentioned that collinear PDFs do not represent the complete non-perturbative structure of hadrons. Further contributions are given by, e.g., generalized parton distributions [81, 82] or transverse momentum distributions [90–92]. In Chapter 3 we will present the connection between the PDFs defined in (2.23) and matrix elements of specific operators computed using LQCD techniques introduced in the next section. This will finally enable us to draw conclusions about the polarized and unpolarized structure functions of the pion and rho mesons.

2.3 Lattice QCD

This section is devoted to the formulation of QCD on the lattice, which is a way to perform non-perturbative, first principle calculations in quantum field theories. The crucial reasons for this are the non-perturbative regularization of the theory and the ability to directly compute path integrals by the projection onto a four-dimensional lattice, which allows performing calculations at low energies. In

[6] There is a vast number of experiments planned by different accelerator facilities around the world. However, we restrict ourselves to the citation of a few experiments that are relevant for this thesis.

this way, one can extract, e.g., hadron masses or information about the hadron structure from the underlying computations.

The first formulation of LQCD was given by Wilson in 1974 [46] and meanwhile there exist various excellent textbooks treating lattice field theories, e.g., [93–95], in a didactically valuable way without omitting necessary details. In the following, we will collect the knowledge about LQCD that we need for the computations done in this work from the references mentioned above[7]. Whenever necessary, additional references to the primary literature are provided.

With all the technical details explained in this section, it is easy to lose track of the big picture. Therefore, we would like to conclude this introduction with the words of R. Hamming, which we should always keep in mind: "The purpose of computing is insight, not numbers." [96].

2.3.1 The lattice action

Starting from (2.12) in Minkowski space-time we get the Euclidean action $S_E\left[q, \overline{q}, A\right]$ by rotating to imaginary times $t = i\tau$ and replacing the Dirac (Minkowski) gamma matrices by their Euclidean counterparts, cf. Appendix A.4. Now the QCD action reads

$$S_E\left[q, \overline{q}, A\right] = \int \mathrm{d}^4x \sum_f \overline{q}^f \left(\gamma_\mu D_\mu + m^f\right) q^f + \frac{1}{2}\,\mathrm{tr}_c\Big[F_{\alpha\beta}F^{\alpha\beta}\Big]\,, \tag{2.27}$$

where we omitted the explicit sums over Dirac- and color indices. Unless explicitly stated, from now on we use $S\left[q, \overline{q}, A\right] = S_E\left[q, \overline{q}, A\right]$, i.e., we drop the subscript E for better readability. Furthermore, we rescale the gauge fields (and also the covariant derivative) by

$$A_\mu \to \frac{1}{g} A_\mu \qquad\qquad \Rightarrow \quad D_\mu = \partial_\mu + i\,A_\mu, \tag{2.28}$$

so that the gauge coupling g appears as an overall constant in the gauge part of the action. In the next step we discretize the four-dimensional space-time as a $N_T \times N^3$ lattice Λ with

$$\Lambda = \Big\{n = (\boldsymbol{n}, n_4)\,|\,n_{1,2,3} = 0, 1, 2, \ldots, N; n_4 = 0, 1, 2, \ldots, N_T\Big\}, \tag{2.29}$$

[7] In addition to these references, the lecture contents and personal notes of both, the courses Lattice QCD 1 and 2 by S. Collins, and the course about Monte-Carlo Methods by J. Bloch, attended at the University of Regensburg, provided information that is included in this section.

where the spinor fields $q(x)$ live on the lattice sites, denoted as

$$q(x) = q(an) \equiv q(n), \qquad \text{with } n \in \Lambda. \tag{2.30}$$

From now on a denotes the distance between individual lattice sites in spatial and temporal directions using physical units. The corresponding partial derivative is discretized using the central difference

$$\partial_\mu q(x) \to \frac{q(x + a\hat{\mu}) - q(x - a\hat{\mu})}{2a} + \mathcal{O}\big(a^2\big)\,. \tag{2.31}$$

This approach looks promising and we already have discretized the fermionic part of the action. However, the introduction of the discretized derivative violates the gauge invariance of the action. A possible solution is the introduction of link variables $U_\mu(n)$ and $U_{-\mu}(n)$ as elements of the SU(3) gauge group. Defining the gauge transformations of the new fields by

$$U_\mu(n) \to U'_\mu(n) = \Omega(n)\, U_\mu(n)\, \Omega^\dagger(n + \hat{\mu})\,, \tag{2.32a}$$

$$U_{-\mu}(n) \to U'_{-\mu}(n) = \Omega(n)\, U_{-\mu}(n)\, \Omega^\dagger(n - \hat{\mu})\,, \tag{2.32b}$$

restores gauge invariance for the discretized derivative. Note that the fields $U_\mu(n)$ and $U_{-\mu}(n)$, and thus also their transformations, are introduced as elements of the gauge group SU(3) and not as elements of the Lie algebra, cf. Section 2.1. At this point, we can write down a first version of the fermionic part of the discretized lattice gauge action

$$\begin{aligned} &S_F[q, \overline{q}, U] = \\ &\quad a^4 \sum_f^{N_f} \sum_{n \in \Lambda} \Big(\overline{q}^f(n) \sum_{\mu=1}^{4} \gamma_\mu \frac{U_\mu(n) q^f(n + \hat{\mu}) - U_{-\mu}(n) q^f(n - \hat{\mu})}{2a} + m^f \overline{q}^f(n) q^f(n) \Big). \end{aligned} \tag{2.33}$$

To connect the link variables U and the algebra valued gauge fields A of the continuum action we make use of the parallel transporter

$$G(y, x) = P e^{\,i \int_{\mathcal{C}_{y,x}} A_\mu \cdot \mathrm{d}s_\mu}\,, \tag{2.34}$$

where P refers to the path ordered product [61] and the integration contour $\mathcal{C}_{y,x}$ is a valid path between y and x. By construction, the parallel transporter has exactly the same transformation properties as the link variables and therefore it can be used as a continuum equivalent to the link variables arising from the lattice discretization. And of course, to compare vectors using the local gauge

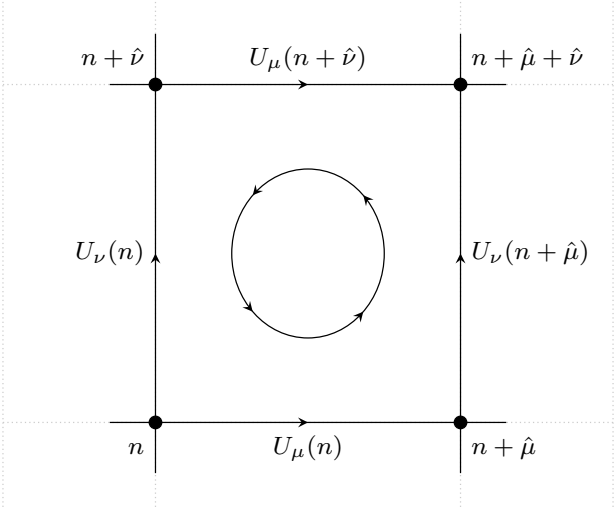

Figure 2.3.1: The plaquette (2.36) is built by four link variables depicted by the square. The order that the links are run through is indicated by the circle in the middle.

transformations, occurring on each lattice site, one has to translate the vectors from, e.g., x to y, using the parallel transporter. By introducing algebra valued gauge fields $A_\mu(n)$ we rewrite

$$U_\mu(n) = e^{iaA_\mu(n)} + \mathcal{O}\Big(a^2\Big) \,, \tag{2.35}$$

to approximate the integral in (2.34) by $aA_\mu(n)$. Using this approximation in (2.33) restores the fermionic part of the continuum action (2.27) in the limit $a \to 0$.

For the gluonic part of the action, we use Wilson's approach [46] to build a gauge-invariant combination of link variables using the plaquette, defined by the product of four link variables

$$U_{\mu\nu}(n) = U_\mu(n)\, U_\nu(n+\hat{\mu})\, U_{-\mu}(n+\hat{\mu}+\hat{\nu})\, U_{-\nu}(n+\hat{\nu}) \,, \tag{2.36}$$

depicted in Fig. 2.3.1. Looking at

$$P[U] = \mathrm{tr}\left[\prod_{(n,\mu)\in\mathcal{P}} U_\mu(n)\right] = \mathrm{tr}\left[\Omega(n_0) \prod_{(n,\mu)\in\mathcal{P}} U_\mu(n)\Omega^\dagger(n_0)\right] = P[U'] \,, \tag{2.37}$$

it is easy to see that the gauge transformation of the trace over a closed path of link variables is indeed a gauge-invariant object and, thus, the trace over (2.36) is also gauge-invariant. In his seminal work Wilson used this approach to write down the pure gauge action $S_G[U]$ as a sum over all plaquettes counted with only

one orientation

$$S_G[U] = \frac{2}{g^2} \sum_{n\in\Lambda} \sum_{\mu<\nu} \mathrm{Re}\,\mathrm{tr}[\mathbb{I} - U_{\mu\nu}(n)]\,. \tag{2.38}$$

In the limit $a \to 0$ it is straightforward to show that (2.38) approximates the continuum part of the gauge action (2.27) up to $\mathcal{O}(a^2)$.

Collecting all the facts derived so far we can write down the first version of a discretized LQCD action as

$$S[q, \overline{q}, U] = S_F[q, \overline{q}, U] + S_G[q, \overline{q}, U]\,, \tag{2.39}$$

and start to compute physical observables. However, at least for the fermionic part we first have to replace the spinors q by Grassmann numbers, to fulfill Fermi statistics and the Pauli principle, and also for the gluonic part one has to consider some subtleties in the computation of observables. The necessary details are explained in Section 2.3.2.

Incorporating all the relevant details, and considering that S_F is bilinear in q and $\overline{q}$, allows us to rewrite (2.33) for a single flavor f as

$$S_F^f[q, \overline{q}, U] = a^4 \sum_{n,m\in\Lambda} \overline{q}_{\alpha,a}(n) D^f_{\alpha\beta,ab}(n|m) q_{\beta,b}(m)\,, \tag{2.40}$$

and define the naive lattice Dirac operator by

$$D^f_{\alpha\beta,ab}(n|m) = \sum_{\mu=1}^{4} (\gamma_\mu)_{\alpha\beta} \frac{U_{\mu,ab}(n)\delta_{n+\hat{\mu},m} - U_{-\mu,ab}(n)\delta_{n-\hat{\mu},m}}{2a} + m_f\, \delta_{n,m}\delta_{\alpha\beta}\delta_{ab}\,. \tag{2.41}$$

Using trivial link variables $U_\mu(n) = \mathbb{I}$, and the Fourier transformation presented in Appendix A.6, one can write down the Dirac operator in momentum space as

$$\widetilde{D}(p) = m\mathbb{I} + \frac{i}{a} \sum_\mu \gamma_\mu \sin(a p_\mu)\,, \tag{2.42}$$

and the inverse Dirac operator as

$$\widetilde{D}^{-1}(p) = \frac{m - \frac{i}{a}\sum_\mu \gamma_\mu \sin(a p_\mu)}{m^2 + \frac{1}{a^2}\sum_\mu \sin^2(a p_\mu)} \quad \xrightarrow[m=0]{a\to 0} \quad \frac{-i\gamma_\mu p_\mu}{p^2}\,, \tag{2.43}$$

with the correct naive continuum limit for fixed values of p. However, looking at the momentum space $\widetilde{\Lambda}$ in Appendix A.6, one finds that the inverse Dirac operator on the lattice contains 15 additional unphysical poles for $p_\mu = \pi/a$, so-called doublers. To overcome this issue we take advantage of the freedom to add arbitrary

irrelevant operators to the lattice action as long as these additional operators do not change the continuum behavior of the theory, cf. [97] and references specified therein. Following this idea Wilson added a discretized version of $a\, r\, \overline{q}\, \partial_\mu \partial_\mu\, q$ to the action, which leads to a modified version of the Dirac operator

$$D(p) = m + \frac{i}{a} \sum_\mu \gamma_\mu \sin(a p_\mu) + \frac{r}{a} \sum_\mu \left[1 - \cos(a p_\mu)\right]. \tag{2.44}$$

Introducing this additional term the fifteen extra species p_μ, for which one has an extra contribution $\pi/a - p_\mu$, get a mass of $m + r/a$ while the sixteenth has mass m. Thus in the continuum limit $a \to 0$ the doublers decouple from the theory. Incorporating this extra term into (2.40) allows us to replace the naive Dirac operator (2.41) by

$$\begin{aligned} D^W_{\alpha\beta,ab}(n|m) &= \delta_{n,m}\delta_{\alpha\beta}\delta_{ab} \\ &+ \frac{\kappa}{a} \sum_\mu \left(\gamma_\mu - r\right)_{\alpha\beta} U_{\mu,ab}(n)\delta_{n+\hat{\mu},m} \\ &- \frac{\kappa}{a} \sum_\mu \left(\gamma_\mu + r\right)_{\alpha\beta} U_{-\mu,ab}(n)\delta_{n-\hat{\mu},m}\,, \end{aligned} \tag{2.45}$$

using the rescaled field definition

$$q^L(n) = \sqrt{ma + 4r}\; q(n) = \frac{q(n)}{\sqrt{2\kappa}}, \qquad \text{with } \kappa = \frac{1}{2ma + 8r}. \tag{2.46}$$

The local term of the action ties the fermion to the lattice site, while the non-local term is responsible for the fermion hopping to nearest neighbor sites, with strength κ. Therefore κ is known as the hopping parameter and is used to tune the mass

$$am = \frac{1}{2\kappa} - \frac{1}{2\kappa_c(a)}\,, \tag{2.47}$$

where $\kappa_c(a)$ is the critical value of the hopping parameter, corresponding to the chiral limit $m = 0$. The hop from one lattice site to another comes along with a twist of the fermion in spin space $(\gamma_\mu - r)$ and in color by U_μ. Choosing $r = 1$ is a common choice, since $(1 \pm \gamma_\mu)$ is a projection operator of rank 2.

Now the doublers have been removed from the theory, but on the way we introduced some other issues. One prominent example is the explicit breaking of chiral symmetry [98] caused by the introduction of the Wilson term in (2.44). Furthermore, the leading order discretization errors are now $\mathcal{O}(a)$. However, using Symanzik's improvement [99–101] for the Wilson fermion action, e.g., Sheikoleslami and Wohlert added a second five-dimensional operator to the Wilson action and

tuned it to cancel the $\mathcal{O}(a)$ term, obtaining an $\mathcal{O}(a)$ improved action for on-shell quantities [102]. We further want to stress that the Wilson fermion and gauge actions have the same discrete symmetry as the naive action (2.27), i.e., it is invariant under parity, charge conjugation, and time reversal. The Wilson Dirac operator and its inverse are in addition γ_5-hermitian, i.e., $(D^W)^\dagger = \gamma_5 D^W \gamma_5$.

Up to this point, our remarks have been merely theoretical. A concrete example of the action used to compute the observables of this thesis is given in Section 2.3.6.

2.3.2 Path-integral formalism

In particle physics, the path-integral formulation is often used as an alternative approach to quantize fields, which is, especially for non-Abelian gauge theories, easier to apply than, e.g., canonical methods. While in quantum mechanics the path-integral literally describes the integral over all possible trajectories of a particle between two fixed endpoints, a path-integral in field theory actually corresponds to an integral over all possible field configurations. Detailed explanations of the path-integral formalism can be found in most textbooks about particle physics, e.g., [61, 103]. However, in this section, we will focus on the computation of correlation functions in LQCD without going too much into formal details about the method itself.

In the first place, this work aims at determining observables with the help of two- and three-point functions. The former shall serve as an example for the computation of lattice correlators, in this chapter. Introducing general operators O_1 and O_2, built from field operators $q^f_{\mu,a}$, to create physical states from the vacuum, the Euclidean correlator can be written as

$$\left\langle O_2(t) O_1(0) \right\rangle = \frac{1}{Z} \int \mathcal{D}\left[q, \overline{q}\right] \mathcal{D}[U]\, e^{-S_F[q,\overline{q},U] - S_G[U]}\, O_2\left[q, \overline{q}, U\right] O_1\left[q, \overline{q}, U\right] , \quad (2.48)$$

using the partition function

$$Z = \int \mathcal{D}\left[q, \overline{q}\right] \mathcal{D}[U]\, e^{-S_F[q,\overline{q},U] - S_G[U]} . \quad (2.49)$$

The corresponding measures of the path-integral are defined as

$$\mathcal{D}\left[q, \overline{q}\right] = \prod_{n\in\Lambda} \prod_{f,\mu,a} \mathrm{d}q^f_{\mu,a}(n)\, \mathrm{d}\,\overline{q}^f_{\mu,a}(n), \qquad \text{and} \quad \mathcal{D}\left[U\right] = \prod_{n\in\Lambda} \prod_{\mu=1}^{4} \mathrm{d}U_\mu(n) . \quad (2.50)$$

A priori it is not clear that one can reconstruct n-point functions (respectively two-point functions) with Minkowski metric from Euclidean correlators (2.48). One possible approach for the Wilson formulation of LQCD is shown in [104], using the Osterwalder-Schrader reconstruction. An alternative approach, based on the

transfer matrix, is given in [105].

As mentioned above the operators $O_{1,2}$ are built by field operators $q^f_{\mu,a}$ so one could rewrite the l.h.s. of (2.48) for a more general n-point function as a product of the form

$$\left\langle q^{f_1}_{\mu_1,a_1} q^{f_2}_{\mu_2,a_2} \cdots q^{f_n}_{\mu_1,a_1} \overline{q}^{f_1}_{\mu_1,a_1} \overline{q}^{f_2}_{\mu_2,a_2} \cdots \overline{q}^{f_n}_{\mu_n,a_n} \right\rangle , \tag{2.51}$$

ignoring the link variables. As stated in Section 2.3.1 the field operators have to obey Fermi statistics to achieve physically meaningful results. So, the vacuum expectation value (2.51) must be antisymmetric under the interchange of quantum numbers of any two fermions. A common way to achieve this is to describe the corresponding field operators $q^f_{\mu,a}$ by Grassmann numbers, see Appendix A.5 for a short introduction. In the next step, we show how to compute the fermionic expectation value (2.51).

Starting from (A.25) the generating functional for fermions is given by

$$W\left[\Theta, \overline{\Theta}\right] = \int \mathrm{d}\eta \mathrm{d}\overline{\eta}\, \mathrm{e}^{\overline{\eta}_\mathrm{i} \mathrm{M}_\mathrm{ij} \eta_\mathrm{j} + \overline{\Theta}\eta + \overline{\eta}\Theta} = (\det \mathrm{M})\ \mathrm{e}^{-\overline{\Theta}_\mathrm{i} \mathrm{M}^{-1}_\mathrm{ij} \Theta_\mathrm{j}} , \tag{2.52}$$

where the generators Θ and $\overline{\Theta}$ serve as source terms and $\det M$ can be interpreted as the fermion determinant. Note that (2.52) can be generalized by a $4N$-dimensional Grassmann algebra using $\overline{\eta}_i, \eta_i, \overline{\Theta}_i, \Theta_i$ with $i = 1, 2, 3, \ldots, N$, to finally return to Green functions of the form (2.51). These functions can be obtained from the generating functional via functional derivatives with respect to the source fields Θ and $\overline{\Theta}$. Using the form given in (2.52) generalized to N fields one obtains Wick's theorem

$$\left\langle q_{i_1} q_{j_n} \cdots \overline{q}_{i_1} \overline{q}_{i_n} \right\rangle = (-1)^n \sum_{P(1,2,\ldots,n)} \mathrm{sign}(P)\, M^{-1}_{i_1 j_{P_1}} M^{-1}_{i_2 j_{P_2}} \cdots M^{-1}_{i_n j_{P_n}} , \tag{2.53}$$

where we use the compact notation $q^{f_1}_{\mu_1,a_1} = q_{i_1}$. The sum runs over all possible permutations P of the numbers $1, \ldots, n$ and $\mathrm{sign}(P) = \pm 1$ is the sign of the permutation, defined as $+1$ for even permutations and -1 for odd permutations of the indices. The expectation values in Wick's theorem are called n-point functions. For the simple case of $n = 2$ this corresponds to the quark propagator. Note that the structure of (2.41) reflects exactly Wick's theorem (2.53), if one replaces the general $N \times N$ matrix M with $M = a^{-4} D$.

In contrast to the fermionic expectation values the gauge part of (2.48) is computed implicitly for most applications, e.g., Metropolis and microcanonical Monte Carlo algorithms sample the group space in such a way that the corresponding measure (2.50) is generated automatically, see Section 2.3.4. Therefore we will

omit the explicit computation at this point. However, cases where dU has to be known explicitly, e.g., the strong coupling expansion, are covered in, e.g., [46, 104].

2.3.3 Hopping parameter expansion

In the last section we have shown how to compute n-point functions using Wick's theorem. These computations will capture a prominent position for the special cases of $n = 2$ and $n = 3$ in the analysis of this thesis, cf. Chapter 4, and we will finally discover that the expectation value of a two-point function of fermions corresponds to the inverse of the Dirac operator, i.e., the quark propagator, introduced in Section 2.3.1. The corresponding equation can be written down as

$$\left\langle q(n)^f_{\alpha_1 a_1} \overline{q}(m)^f_{\alpha_2 a_2} \right\rangle = a^{-4}\ D^{-1}(n|m)^f_{\alpha_1\alpha_2, a_1 a_2}\,. \tag{2.54}$$

Technical details of the calculation will be discussed in Chapter 4. However, for the moment let us concentrate on the analysis of the Dirac operator for large quark masses, which will play an important role in the estimation of three-point functions by stochastic methods shown in Section 4.2.5.

The limit of large quark masses allows us to expand the propagator in terms of the hopping parameter κ introduced in (2.46), using the hopping parameter expansion (HPE).

Rewriting the Wilson Dirac operator (2.45) in matrix-vector notation for the special case $r = 1$ yields

$$\begin{aligned} & D(n|m) = \mathbb{I} - \kappa\, H(n|m), \\ \text{with} \quad & H(n|m)_{\alpha_1\alpha_2, a_1 a_2} = a^{-1} \sum_{\mu=\pm 1}^{\pm 4} \left(\mathbb{I} - \gamma_\mu\right)_{\alpha_1\alpha_2} U_\mu(n)_{a_1 a_2}\, \delta_{n+\hat{\mu}, m}\,, \end{aligned} \tag{2.55}$$

where we use the abbreviated sum notation $\mu = \pm 1$ to incorporate backward hops in the sum. Rewriting (2.55) as geometric series gives

$$D^{-1}(n|m) = \left[\mathbb{I} - \kappa\, H(n|m)\right]^{-1} = \sum_{i=0}^{\infty} \kappa^i H^i(n|m)\,, \tag{2.56}$$

which converges for $\kappa\,||H|| < 1$. Using (2.46) it follows that $||H|| \leq 8$ and thus $\kappa < 1/8$. What remains is the computation of a general expression for $H^i(n|m)$, given by

$$\begin{aligned} H^i(n|m)_{\alpha_1\alpha_2, a_1 a_2} = & \sum_{\mu_j=\pm 1}^{\pm 4} \left[\prod_{j=1}^{i} \left(\mathbb{I} - \gamma_{\mu_j}\right)\right]_{\alpha_1\alpha_2} \times \\ & \left[U_{\mu_1}(n) U_{\mu_2}(n+\hat{\mu}_1) \cdots U_{\mu_i}(n+\hat{\mu}_1+\hat{\mu}_2+\cdots+\hat{\mu}_{i-1})\right]_{a_1 a_2} \delta_{n+\hat{\mu}_1+\hat{\mu}_2+\cdots+\hat{\mu}_i, m}\,, \end{aligned} \tag{2.57}$$

containing a product of i link variables. For the special case of $i = 0$ we find the trivial expression

$$H^0(n|m) = \delta_{\alpha_1\alpha_2}\,\delta_{a_1a_2}\,\delta_{n,m}\,, \tag{2.58}$$

which cancels all diagonal contributions in (2.55) and infinitely heavy quarks do not hop. However, in the general case, the propagator from n to m is a sum over link variables connecting the two points on the lattice. Depending on the length of the path it is furnished with additional factors κ and is only non-vanishing for lattice points n and m connected via

$$m = n + \hat{\mu}_1 + \hat{\mu}_2 + \cdots + \hat{\mu}_i, \quad \text{for } \mu_j \in \{\pm1, \pm2, \pm3, \pm4\}, \text{ with } 1 \leq j \leq i\,. \tag{2.59}$$

In Dirac space it is interesting to notice that so-called back-tracking paths are forbidden due to $(\mathbb{I} - \gamma_\mu)(\mathbb{I} + \gamma_\mu) = 0$, i.e., we are on a one-way road.

With this result we close the discussion of the HPE. In summary, we have justified the expansion of the propagator into a sum of non-back-tracking paths with length i coming along with factors of κ^i. To leading order this yields the shortest path only, while for higher orders additional terms arise.

2.3.4 Monte Carlo methods

In (2.48) we stated that the Euclidean correlator is a typical example for the computation of expectation values in LQCD. As introduced in Section 2.3.2, the path integral formalism is used to perform these kinds of simulations and for very small lattices this can indeed be done analytically. However, for analyzing the lattice volumes used in this work it is necessary to perform the corresponding simulations on computers. Thus, it is mandatory to solve the problems given in Section 2.3.2 using numerical methods. A prominent example for such a simulation procedure of physical systems are Monte Carlo methods: a statistical framework based on averaging the results for a large number of random settings.

One of the key tasks is the computation of expectation values of observables, distributed according to a probability distribution. The expectation value of a function $y(x)$ is defined by

$$y \equiv \langle y \rangle = \int \mathrm{d}x \rho(x) y(x)\,, \tag{2.60}$$

using the probability distribution $\rho(x)$ of the states x. The corresponding variance

is given by

$$\sigma_y^2 = \langle (y-\mu)^2 \rangle = \langle y^2 \rangle - \langle y \rangle^2 \,, \tag{2.61}$$

where μ is defined as the average of y. In principle, it would be beneficial to directly compute (2.60) and (2.61), however, in the numerical simulations elaborated in this work we will estimate these expectation values by the sample mean since a direct computation is not possible. Using a sample $S = \{x_i \,|\, 1 < i < N\}$ of N configurations drawn according to $\rho(x)$ the sample mean is given by

$$\overline{y} = \frac{1}{N} \sum_{i=1}^{N} y(x_i) \,. \tag{2.62}$$

The corresponding standard error is defined as the standard deviation of the sample means $\overline{y}$, measured over all possible samples S of size N, drawn independently from the population x. It is given by

$$\sigma_{\overline{y}} = \frac{\sigma_y}{\sqrt{N}} \,, \tag{2.63}$$

so a measured estimate can be written down as

$$\langle y \rangle = \overline{y} \pm \frac{\sigma_y}{\sqrt{N}}, \qquad \text{with} \;\; \sigma_y \approx \sqrt{\frac{1}{N-1} \sum_{i_1}^{N} \left(y_i - \overline{y}\right)^2} \,. \tag{2.64}$$

Following the central limit theorem we know that for $N \to \infty$ the sample mean $\overline{y}$ is normally distributed, with mean μ and standard deviation $\sigma_y/\sqrt{N}$ approximated by the sample variance. This holds for independent and identically distributed original distributions. For large N the standard error $\sigma_{\overline{y}}$ can be related to the probability that the estimate $\overline{y}$ lies within a distance $\sigma_{\overline{y}}$ (68.3%), $2\sigma_{\overline{y}}$ (95.4%), $3\sigma_{\overline{y}}$ (99.7%), ..., away from the true mean μ. Since one of our main objectives is the computation of physically meaningful results it would be beneficial to draw random numbers from a given probability distribution and thus reduce the standard errors of our results by suppressing contributions with low-impact. An effective way to reduce the variance is the idea of importance sampling. By introducing a second probability distribution $\widetilde{\rho}(x)$ in (2.60) one gets

$$\langle y \rangle_p = \int \mathrm{d}x \, \widetilde{\rho}(x) \frac{\rho(x) y(x)}{\widetilde{\rho}(x)} = \left\langle \frac{\rho y}{\widetilde{\rho}} \right\rangle \,, \tag{2.65}$$

i.e., on the one hand, the states x can be sampled according to $\rho(x)$ or $\widetilde{\rho}(x)$ to estimate y. On the other hand, the distribution $\widetilde{\rho}(x)$ can be chosen such that the variance of $(\rho y)/\widetilde{\rho}$ is small because states with a high probability are sampled

more often.

Exploiting the results of the discussion about expectation values, error estimates, and importance sampling allows us to illustrate the computation of LQCD observables using the pedagogical example of a simple multi-dimensional integral. Starting from

$$I_d = \int_V \mathrm{d}^d x \rho(x) \left[\frac{f(x)}{\rho(x)}\right] = \left\langle \frac{f}{\rho} \right\rangle , \qquad \text{where} \quad x \in V \subseteq \mathbb{R}^d , \tag{2.66}$$

with a positive and properly normalized probability distribution $\rho(x)$ over V, we find that I_d is an expectation value of f/ρ. Thus the integral can be estimated numerically using a Monte Carlo integration and sampling the points according to $\rho(x)$ as

$$I_d \approx \frac{1}{N} \sum_{i=1}^{N} \frac{f(x_i)}{\rho(x_i)}, \qquad \text{with} \quad \sigma_{I_d} = \frac{\sigma_{f/\rho}}{\sqrt{N}}. \tag{2.67}$$

The standard deviation σ_{I_d} decreases as $1/\sqrt{N}$, independent of the dimension d. Compared to standard quadrature methods, e.g., the Gaussian quadrature [106][8], which scale as $1/N^{\frac{k}{d}}$, where k is the order of the quadrature, this yields a key advantage especially for higher-dimensional integrals. The points x_i used in the Monte Carlo integration are randomly sampled according to $\rho(x)$ using a random number generator. Common examples, suitable for Monte Carlo simulations, are the Mersenne twister [108], or the RANLUX [109] algorithms. This is, however, not a random choice. The random number generators used in Monte Carlo simulations have to furnish uniformly distributed numbers with (very) long periods and small correlations. Additionally, the used algorithms should be optimized and as fast as possible to minimize the runtime of the integration procedure.

Depending on the problems we want to solve numerically one often needs random number generators producing values of x in a finite range from a non-uniform probability distribution $\rho(x)$. A widely used algorithm to produce these kinds of random numbers is the acceptance-rejection method introduced in [110]. It relies on the approximation of $\rho(x)$ by a function $g(x)$ satisfying

$$g(x) \geq \rho(x) \qquad \forall\ x \in [a, b) . \tag{2.68}$$

Using this approximation one can generate a random number x from the proba-

[8]Here we refer to textbook literature about numerical integration, where the Gauss quadrature is represented in a well comprehensible way. However, the method was invented by Gauss already at the beginning of the 19th century, the representation used today was formulated by Jacobi in 1826 [107].

bility distribution

$$\frac{g(x)}{\int_a^b \mathrm{d}x g(x)}\ , \tag{2.69}$$

and accept x with probability $q = \rho(x)/g(x) \leq 1$. This accept-reject step is achieved by the generation of a second uniformly distributed random number $\widetilde{x} \in [0, 1)$ and x is accepted only if $\widetilde{x} \leq q$.

After this general discussion, we now want to adapt the framework of Monte Carlo simulations to the computation of path integrals and observables as shown in Section 2.3.2. Focusing on the gauge part of (2.48) and simplifying to the case of a single operator the expectation value of $\mathcal{O}$ can be approximated as

$$\langle \mathcal{O} \rangle \approx \frac{1}{N} \sum_{i=1}^{N} \mathcal{O}[U_i]\,, \tag{2.70}$$

where now the gauge fields U_i are random variables, sampled according to the measure

$$\mathrm{d}P(U) = \frac{e^{-S_G[U]}\,\mathcal{D}[U]}{\int \mathcal{D}[U]\, e^{-S_G[U]}} \prod_f \det D_f\,[U] \tag{2.71}$$

where D_f is the fermion determinant, c.f. (2.52). Note that even for lattices of moderate size the Dirac operator D is a huge matrix and has to be computed for every gauge configuration. Thus the computational cost of calculating $\det M$ becomes prohibitively high. In Section 2.3.6 we provide further references how this problem is solved for the gauge configurations used in this work.

One could also sample the random gauge field configurations U_i uniformly, i.e., use every configuration of the configuration-space weighted with the same probability. This would, however, yield a non-manageable number of configurations to achieve reasonable errors already for very small volumes Λ, and in addition, one would sample mainly samples of irrelevant states that contribute only negligibly to the result. To overcome this issue we replace the set of all configurations by a much smaller subset $U_N = \{U_i \,|\, 1 \leq i \leq N\}$ of configurations, as mentioned above, where i is called the Monte Carlo time. In addition the configurations are chosen according to (2.71), to get a valid approximation from the subset U_N. Taking into account these considerations the main task is to generate configurations according to (2.71), using a Markov chain. It describes a stochastic process to generate a configuration U_i, generated from the configuration U_{i-1}, characterized

by transition probabilities $P(U_{i-1} \to U_i)$ with the requirements

$$0 \leq P(U_{i-1} \to U_i) \leq 1, \qquad \text{and} \quad \sum_{U_i \in \Omega} P(U_{i-1} \to U_i) = 1\,, \tag{2.72}$$

where Ω is the configuration space. I.e., every state U_i can be reached from U_{i-1} with the possibility that $U_i = U_{i-1}$ and that not all states U_i can be reached in a single step. But note that any configuration can be reached in a finite number of Markov steps (ergodicity). Furthermore, P depends only on U_{i-1} and U_i and P is independent of the Markov time i. Once the system has reached equilibrium, according to the desired probability distribution, each state U_i is created and annihilated with the same probability and the equilibrium equation reads

$$\sum_{U_{i-1} \in \Omega} P(U_{i-1}) P(U_{i-1} \to U_i) = P(U_i)\,, \tag{2.73}$$

where $P(U_i)$ is the probability to find a configuration U_i. Configurations generated after the equilibrium is reached reproduce the canonical ensemble and can be used to compute observables. At this point the system is called thermalized. In practice, almost every algorithm in use satisfies the detailed balance condition

$$P(U_{i-1}) P(U_{i-1} \to U_i) = P(U_i) P(U_i \to U_{i-1})\,, \tag{2.74}$$

which is even more restrictive than (2.73) but not strictly necessary to converge to the correct probability distribution. However, the transition probabilities $P(U_{i-1} \to U_i)$ are not uniquely determined and one has some freedom of choice in

$$\frac{P(U_{i-1} \to U_i)}{P(U_i \to U_{i-1})} = \frac{P(U_i)}{P(U_{i-1})}\,, \tag{2.75}$$

used in the different implementations of various Monte Carlo algorithms. Common examples are the Metropolis [111] and the heat bath [112] algorithms. The gauge ensembles in this thesis are generated using hybrid Monte Carlo algorithms [113] which are better suitable to treat fermions. In most cases the underlying principle relies on the division of the transition probability $P(U_{i-1} \to U_i)$ into a proposal probability $g(U_{i-1} \to U_i)$ and an acceptance probability $A(U_{i-1} \to U_i)$. The detailed balance equation (2.75) yields

$$\frac{P(U_{i-1} \to U_i)}{P(U_i \to U_{i-1})} = \frac{g(U_{i-1} \to U_i) A(U_{i-1} \to U_i)}{g(U_i \to U_{i-1}) A(U_i \to U_{i-1})}\,, \tag{2.76}$$

which allows us to generate states with a simple g and tune A such that detailed balance is satisfied. If the configuration U_i is accepted it is appended to the

Markov chain otherwise a new proposal configuration is created and we restart the accept-reject procedure[9]. Using this method we finally achieve adequate statistical accuracy with less computational effort.

However, in contradiction to the assumption entering in (2.63) configurations provided by the Markov chain are correlated, while the computation of the standard error (2.63) only holds for N independent measurements. While we still get a correct estimate for the expectation value (measured on an ensemble of Markov chains) the naive standard error underestimates the true statistical error of the observable according to

$$\sigma_{\overline{y}}^2 = \frac{\sigma_y^2}{N} 2\tau_{\mathrm{int},y} \ , \tag{2.77}$$

with integrated autocorrelation time

$$\tau_{\mathrm{int},y} = \frac{1}{2} + \frac{1}{\sigma_y^2} \sum_{t=1}^{N} \left(1 - \frac{t}{N}\right) \Big(\langle y_i y_{i+t} \rangle - \langle y_i \rangle \langle y_{i+t} \rangle \Big) \ , \tag{2.78}$$

where $t = j - i$ with $j > i$ is defined as the difference in Monte Carlo time between two points of the chain. We further define the autocorrelation function

$$R_y(t) \equiv \frac{C_y(t)}{C_y(0)} \, , \qquad \text{with} \quad C_y(t) = \langle y_i y_{i+t} \rangle - \langle y_i \rangle \langle y_{i+t} \rangle \ , \tag{2.79}$$

which depends on the time difference t, the update process, and the observable y. Due to the high computational cost of the ensemble generation for LQCD simulations, we are not able to compute the ensemble average of Markov chains to get $\overline{y}$. Instead, we estimate the ensemble average and the autocovariance function $C_y(t)$ by a Monte Carlo time average for a large number of Monte Carlo time-steps N. This yields

$$C_y(t) \approx \frac{1}{N-t} \sum_{i=1}^{N-t} y_i y_{i+t} - \left(\frac{1}{N-t} \sum_{i=1}^{N-t} y_i \right) \left(\frac{1}{N-t} \sum_{i=1}^{N-t} y_{i+t} \right) \ , \tag{2.80}$$

and the variance is estimated by $\sigma_y^2 = C_y(0)$. To achieve configurations that are representative for the chain one has to choose $N \gg \tau_{\mathrm{int},y}$ and the standard error on correlated measurements is finally given by

$$\sigma_{\overline{y}} = \sqrt{\frac{2\tau_{\mathrm{int},y}}{N}} \sigma_y \, , \qquad \text{with} \quad \tau_{\mathrm{int},y} = \frac{1}{2} + \sum_{t=1}^{N} R_y(t) \, . \tag{2.81}$$

[9] In actual simulations, e.g., using the Metropolis algorithm, one does not store every accepted configuration. Instead, the accept-reject step is performed V times (one sweep) before appending the configuration to the Markov chain, to reduce autocorrelations.

I.e., the number of effectively independent data points is reduced by a factor of $1/(2\tau_{\mathrm{int},y})$. As a final remark we want to mention that $R_y(t)$ decreases exponentially for $t \to \infty$, which defines the exponential autocorrelation time τ_{exp}. In practice τ_{exp} provides a measure of the convergence rate of the Markov process towards its equilibrium as t grows. τ_{exp} is often approximated by the integrated autocorrelation time (2.78).

From the above considerations, we find that the autocorrelation time depends on the updating algorithm as well as on the simulation parameters. For the LQCD simulations shown in this thesis, one expects that the integrated autocorrelation time is proportional to the correlation length ξ_y of an observable y

$$\tau_{\mathrm{int},y} \sim \xi_y^z \sim a^{-z}\,, \tag{2.82}$$

where $z \geq 0$ is the dynamical critical exponent, depending on the updating algorithm. The simulation of finite lattices with linear size L further yields that $\xi \leq L$ and thus, near a critical point (where the correlation length ξ of the system diverges), the numerical cost increases like a power of the lattice extension L^z. This behavior is called critical slowing down.

2.3.5 Scale setting

In Section 2.3.1 we introduced the lattice spacing a to write down a discretized version of the QCD action in (2.39). If one starts generating gauge ensembles, using the methods presented in Section 2.3.4 and the LQCD action, the lattice spacing a is only set implicitly via the inverse coupling $\beta = 6/g_0^2$ using the bare coupling g_0. Thus, we simulate at finite lattice spacing a but the value of a in physical units is a priori unknown and depends mainly on the lattice coupling. To compare results at various couplings, and to connect to the physical world, we need to fix the scale.

A common way to set the scale is using the static quark potential $V(r)$ and compute the corresponding values for $r = 0$ and the Sommer parameter $r = r_0$ [114]. By simply counting the number of lattice points n between these two fixed points the lattice spacing a is determined by r_0/n. For a more detailed explanation see, e.g., [93].

However, for the Coordinated Lattice Simulations (CLS) gauge ensembles used in this work, the scale is set using another method, based on the determination of t_0 defined by the Wilson flow [115]. In contrast to the use of static quark potentials the determination of t_0 is independent of the renormalization, shows only mild quark mass and cut-off effects, and achieves comparatively high accuracy. The

flow equation of lattice gauge fields is given by

$$\partial_t V_t(n,\mu) = -g_0^2 \left(\partial_{n,\mu} S_G[V_t]\right) V_t(n,\mu) \ , \quad \text{with} \ \ V_t(n,\mu)\Big|_{t=0} = U_\mu(n) \ , \tag{2.83}$$

using the Wilson gauge action (2.38). With the help of numerical integration methods one can determine the gauge fields for an arbitrary but finite flow time t and compute observables as, e.g., the average action density

$$E(t) = \frac{1}{4|\Lambda|} \sum_{n\in\Lambda} F^{V_t}_{\alpha\beta}(n) F^{V_t}_{\alpha\beta}(n) \, , \tag{2.84}$$

using the four plaquette Wilson loops as the definition of the field strength tensor $F^{V_t}_{\alpha\beta}(n)$. As pointed out by Lüscher [115] perturbation theory prescribes the scaling behavior of $\langle E \rangle$ as a physical quantity of dimension 4. This can be checked using the reference scale t_0 defined as

$$t^2 \langle E \rangle \Big|_{t=t_0} = 0.3 \ . \tag{2.85}$$

If the expectation value $\langle E \rangle$ is a physical quantity the dimensionless ratio t_0/r_0^2 has to be independent of the lattice spacing up to corrections proportional to some power of a. Finally the values t_0 can be used as a reference scale analogous to the Sommer parameter. In actual lattice simulations the lattice spacing a is determined via various, discrete measurements of t/a^2 and equating (2.85).

2.3.6 CLS lattice action

In the following we will describe the framework that is used for the simulations in this thesis. The gauge configurations have been generated by the CLS effort, which is a trans-European project established in 2007 to combine human and computer resources in the field of lattice gauge theories. One of the main goals within the collaboration is to perform LQCD simulations for a wide range of lattice spacings, volumes, and pion masses, using a single lattice formulation [116]. A detailed overview of the CLS program for $N_f = 2 + 1$ flavor simulations is given in [117]. In this section, we recap the deliberations in [117] with special emphasis on the key elements used for the analysis in this work.

Based on the previous considerations in this section, it is obvious that the gauge fields used in our simulations must meet certain requirements. First of all, one needs configurations with quark masses close to the physical values combined with fine lattices, to minimize discretization effects, and large volumes to minimize finite volume effects. To also achieve reliable statistical accuracy one further has to use Markov chains with an adequate length, cf. (2.81). Due to the continuous progress

in computer development, the statistical accuracy of LQCD is still increasing over time and systematic effects become more visible and have to be taken into account. However, the generation of ensembles is the most demanding part of the computation, therefore the main goal is to balance the sources of systematic and statistical uncertainties to achieve precise final results. As a first step CLS gauge configurations for very fine lattices are generated using open boundary conditions in time to avoid freezing of the topological charge [118, 119]. This setup has the advantage that one can prevent exaggeratedly bad scaling behaviors due to critical slowing down (2.82) and by keeping the trajectory length constant in all runs we expect Langevin scaling $\tau_{\text{int}} \sim a^{-2}$ [117].

Next we write down the action analogous to (2.39). For the gauge fields the Lüscher-Weisz action [101] is used

$$S_G[U] = \frac{\beta}{6}\left(\frac{5}{3}\sum_p \text{tr}[\mathbb{I} - U(p)] - \frac{1}{12}\sum_r \text{tr}[\mathbb{I} - U(r)]\right) , \tag{2.86}$$

where $\beta = 6/g_0^2$ is the inverse gauge coupling. The sums run over the plaquette and rectangle terms of the elementary loops on the lattice, cf. Tab. 1 in [101], and are multiplied by their respective coefficients[10]. The fermion action is defined analogous to (2.40), including a sum over $N_f = 2+1$ flavors and using the Wilson-Dirac operator [46]

$$D_W(m_{0,f}) = \frac{1}{2}\sum_\mu \left[\gamma_\mu\left(\nabla_\mu^* + \nabla_\mu\right) - a\nabla_\mu^*\nabla_\mu\right] + a\, c_{\text{SW}} \sum_{\mu,\nu} \frac{i}{4}\sigma_{\mu\nu}\hat{F}_{\mu\nu} + m_{0,f} , \tag{2.87}$$

where the Sheikholeslami-Wohlert term [102] is included for $\mathcal{O}(a)$ improvement of the action[11] [120] and $m_{0,f}$ is the bare quark mass for flavor f. An explicit form of the discretized field strength tensor $\hat{F}_{\mu\nu}$ can be found in [121] and non-perturbatively determined values for c_{SW} are given in [120].

In the case of the $N_f = 2+1$ simulations by CLS the physical quark masses are fixed by the pion and kaon masses using

$$\begin{aligned} \phi_2 &= 8t_0 m_\pi^2, & \phi_4 &= 8t_0\left(m_k^2 + \frac{1}{2}m_\pi^2\right), \\ \phi_2 &\sim m_u + m_d, & \phi_4 &\sim m_u + m_d + m_s, \end{aligned} \tag{2.88}$$

[10] In general one could also sum over parallelograms and bent rectangles, however, the corresponding coefficients are set to 0 by definition.

[11] To avoid confusion we follow the notation in [117] and use the operators ∇ and ∇^* for the covariant forward and backward derivatives instead of the explicit notation in Section 2.3.1.

where the scale is set through t_0 and the relations to the quark masses follow from leading order chiral perturbation theory [122, 123]. However, the parameters of the simulations have to obey certain restrictions to, e.g., achieve $\mathcal{O}(a)$ improvement. In Section 2.3.5 we have introduced bare parameters in general as functions of a. This is especially important for the strong coupling g_0. To improve g_0 it was shown in [121, 124] that the strong coupling has to be improved using a mass-dependent term. Keeping the modified version of g_0 fixed allows us to define trajectories in the $\phi_2 - \phi_4$ plane. At the current stage, the CLS ensembles are generated along three different trajectories in the renormalized quark mass plane

- $\mathrm{tr}[M] = \text{const.}$: The trace of the quark mass matrix is kept constant near its physical value.
- $m_s = m_{s,\mathrm{phy}}$: The strange quark mass is kept constant close to its physical value [125].
- $m_l = m_s$: The symmetric line.

All ensembles available along the three trajectories are depicted in Fig. 2.3.2. Fig. 2.3.3 shows the three different trajectories in the $m_\pi^2 - m_k^2$ plane. The three solid lines depict the behavior of m_k^2 as a function of m_π^2 for the three trajectories using the standard Gell-Mann–Oakes–Renner relations. For the symmetric line this yields the simple relation $m_k^2 = m_\pi^2$ while we get

$$\begin{aligned} m_k^2 &\approx \frac{2m_{k,\mathrm{phy}}^2 + m_{\pi,\mathrm{phy}}^2 - m_\pi^2}{2}, \qquad && \text{for } \mathrm{tr}[M] = \text{const.}, \\ m_k^2 &\approx \frac{2m_{k,\mathrm{phy}}^2 - m_{\pi,\mathrm{phy}}^2 + m_\pi^2}{2}, \qquad && \text{for } m_s = m_{s,\mathrm{phy}}, \end{aligned} \tag{2.89}$$

where $m_{k/\pi,\mathrm{phy}}$ are the physical pion and kaon masses [51]. The data points are plotted using the ensemble parameters m_k and m_π respectively. In contrast to a similar plot in the $\phi_2 - \phi_4$ plane Fig. 2.3.3 has the advantage that it makes the extrapolation strategy, using CLS ensembles, intelligible in terms of physical masses. While the $\mathrm{tr}[M] = \text{const.}$ and the $m_s = m_{s,\mathrm{phy}}$ trajectories intersect at the point of nearly physical pion and kaon masses (quark mass extrapolation) the $m_l = m_s$ trajectory extrapolates to the chiral limit.

In the remainder of this section we briefly discuss some subtleties regarding the action used in the actual simulations and the determination of t_0. Using the Wilson-Dirac operator (2.87) it is possible to produce barriers of infinite action, created by zero eigenvalues of D_W, during the simulations. To overcome this issue it was proposed in [126] to modify the action with a twisted-mass term that generally increases the stability of simulations and avoids such configurations.

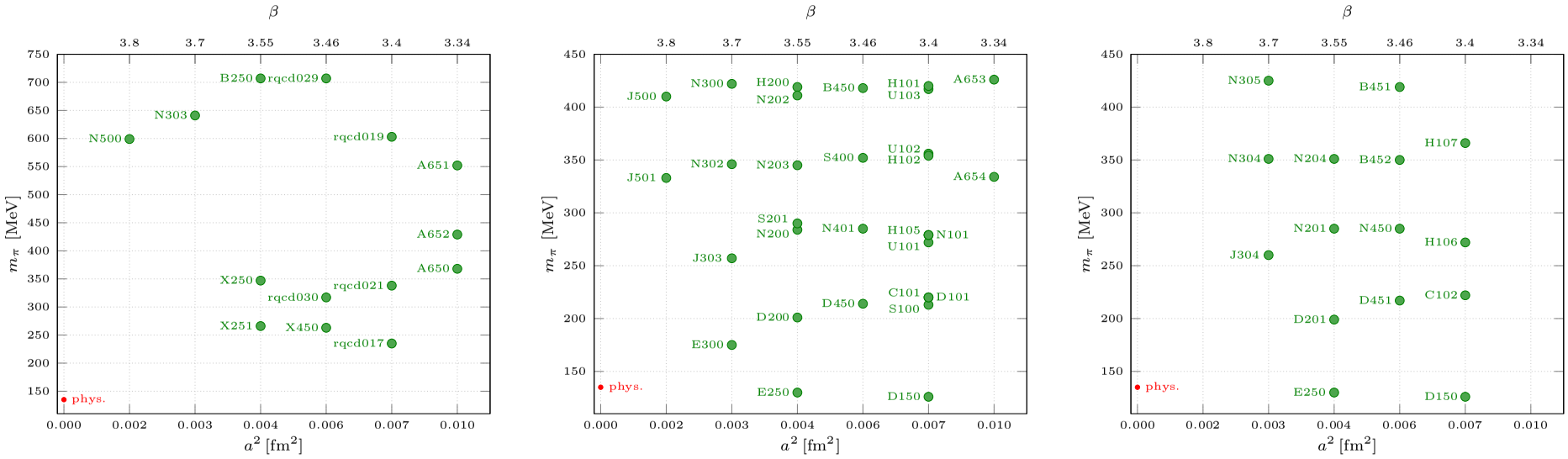

(a) $m_l = m_s$ **(b)** $\mathrm{tr}[M] = \mathrm{const.}$ **(c)** $m_s = m_{s,\mathrm{phy}}$

Figure 2.3.2: Landscape of all available CLS and rqcd gauge configurations used by our group. From left to right we depict the three different trajectories respectively. In general we achieve pion masses from 720 MeV down to 120 MeV and lattice-spacings between 0.04 fm and 0.1 fm. The red point in the bottom left corner of every plot shows the physical point for $a = 0$ and $m_\pi \approx 139$ MeV. All data points are taken from [127].

This extra term is subsequently compensated by a reweighting factor W^ℓ at the analysis stage. For the generation of the CLS gauge ensembles we use the exact relation [126]

$$\det\left[D_\ell^\dagger D_\ell\right] = W^\ell \det\left[\frac{\left(D_\ell^\dagger D_\ell + \mu^2\right)^2}{D_\ell^\dagger D_\ell + 2\mu^2}\right], \tag{2.90}$$

to rewrite the determinant[12] of the light quark pair in the action. Here μ serves as an infrared regularization and shifts the spectrum of the Dirac operator along the positive real axis. The corresponding reweighting factor is given by

$$W^\ell = \det\left[\frac{D_\ell^\dagger D_\ell}{\left(D_\ell^\dagger D_\ell + \mu^2\right)^2}\left(D_\ell^\dagger D_\ell + 2\mu^2\right)\right]. \tag{2.91}$$

In the actual simulations only the determinant in (2.90) is computed and contains the major contribution to the fermion force.

Contrary to the two mass degenerate light quarks the strange quark mass is simulated using the rational hybrid Monte Carlo algorithm [130, 131]. Including strange quarks we get

$$\det D_s = \pm\left|\det D_s\right|. \tag{2.92}$$

Following [117] the positive square root $\sqrt{D_s^\dagger D_s}$ can be approximated by

$$\det\left[\sqrt{D_s^\dagger D_s}\right] \approx \det R_s\,, \qquad \text{with} \qquad R_s = A^{-1}\prod_{i=1}^{N_p}\frac{D_s^\dagger D_s + \overline{\mu}_i^2}{D_s^\dagger D_s + \overline{\nu}_i^2}\,, \tag{2.93}$$

where the matrix A and the parameters $\overline{\mu}$ and $\overline{\nu}$ are computed using Zolotarev's approximation and N_p denotes the number of poles. The approximation error of the rational approximation in (2.93) can be taken into account by reweighting with

$$W^s = \det\left[D_s R_s^{-1}\right]. \tag{2.94}$$

Note that the rooting needed to simulate the strange quarks gives rise to a second multiplicative contribution to the reweighting factor $W = W^\ell W^s$, see also [132]. Primary quantities A can finally be measured using expectation values estimated

[12]Note that in the actual simulations the determinant is split up further into several factors to allow for frequency splitting in the Monte-Carlo time integration using Hasenbusch's mass factorization [128, 129].

by the modified action via

$$\langle A \rangle = \frac{\sum_i W^i A^i}{\sum_i W^i}. \tag{2.95}$$

To simulate the complete action a hybrid Monte Carlo algorithm [113] with a hierarchical integration scheme [133] is used. The simulation setup is described in [119] and is implemented in the OpenQCD code [134] for ensemble production.

The lattice scale for the setup chosen in the CLS simulations in use is set via the Wilson flow introduced in Section 2.3.5, see also [117, 127, 135]. Note that, for lattices with open boundary conditions in time, the value $E(t)$ in (2.84) is an average over the central points only. In the analysis of this work we define the value t_0^* [136] by

$$\phi_4\Big|_{t_0=t_0^*} = 8t_0 \left(m_k^2 + \frac{1}{2}m_\pi^2\right)\Bigg|_{t_0=t_0^*} = 12 t_0 m_\pi^2\Big|_{t_0=t_0^*} = 1.110\,, \tag{2.96}$$

along the symmetric trajectory $m_l = m_s$. Following the discussions in [136] and [127] we use

$$\sqrt{8t_0^*} = 0.413\,\mathrm{fm}\,, \tag{2.97}$$

in our analysis[13]. To compute, e.g., the lattice spacing a, the ratio t_0/a^2 is determined on a specific ensemble and $a = 0.170569\,\mathrm{fm}/(8t_0^* a^{-2})$.

However, CLS is only one among many other simulation programs. For the sake of completeness, we finally want to give an (incomplete) list of several other simulation programs that use different actions, fermions, algorithms, etc. to create gauge ensembles, which can also be used for LQCD computations. Simulations using Wilson fermions are also performed by PACS-CS [137], QCDSF [138], and the Hadron Spectrum collaboration [139]. Twisted mass fermions are used by ETM [140] and domain wall fermions are used by MILC [141], JLQCD [142], and RBC-UKQCD [143].

2.3.7 Bootstrap error estimation

In Section 2.3.4 we introduced the concept of Monte Carlo simulations to compute Euclidean correlation functions on the lattice and we have shown how to compute the corresponding expectation values and errors in (2.81). However, in practical simulations, we are interested in two kinds of quantities and distinguish between

[13] [127] was not published at the time of writing this thesis. The numerical values were provided by G.S. Bali (private communication).

- primary quantities, measured separately on each configuration for which the expectation value can be estimated by a sample average,

- secondary quantities, all quantities which are not primary quantities, e.g., fit parameters.

Especially the latter play an important role in the analysis elaborated on in this thesis. Using a brute force method it would be possible to perform measurements of the correlation functions on all configurations available and average all the results to perform the fit. To get a naive error estimate from these computations one would have to create many such sets of data and finally apply the methods shown in Section 2.3.4, which is very expensive in terms of computer time. Hence, resampling methods like jackknife or bootstrap, see, e.g., [144], are used to estimate observables and the corresponding errors. We will use the latter in this work.

Let's assume we want to compute a secondary quantity $Q(S)$, computed from a sample S of N independent configurations given by

$$S = \left\{ \mu_t \,|\, t = 1, \ldots, N \right\} . \tag{2.98}$$

A bootstrap-sample (or pseudo-sample) $S_{(i)}$ with $i = 1, \ldots, M$, is given by randomly choosing N configurations out of S with replacement, i.e., allowing for duplicates. This resampling comes along with no additional cost in terms of the Monte Carlo simulation, since we just recycle the available results. Next we compute the M pseudo measurements $Q_{(i)} = Q\left(S_{(i)}\right)$ to obtain the bootstrap estimate of the standard error via

$$\sigma_Q = \sqrt{M^{-1} \sum_{i=1}^{M} \left(Q_{(i)} - \overline{Q}_B \right)^2} , \qquad \text{with } \overline{Q}_B = \frac{1}{M} \sum_{i=1}^{M} Q_{(i)} . \tag{2.99}$$

The bootstrap estimate of the standard error on $Q(S)$ is the standard deviation of the pseudo measurements $Q_{(i)}$, given by

$$Q = Q(S) \pm \sigma_Q \ . \tag{2.100}$$

In terms of bootstrap measurements, N is called the sample size and determines the size of the standard error, while M is the number of bootstrap samples. We stress that the error decreases with increasing the sample size N and not M, however, for $M \to \infty$ the error σ_Q will converge to its expectation value for a sample of size N. To achieve valid error estimations it is further important to remove autocorrelations. In our implementation the minimization of correlations is ensured by the binning method, where we divide the N measurements into n_B

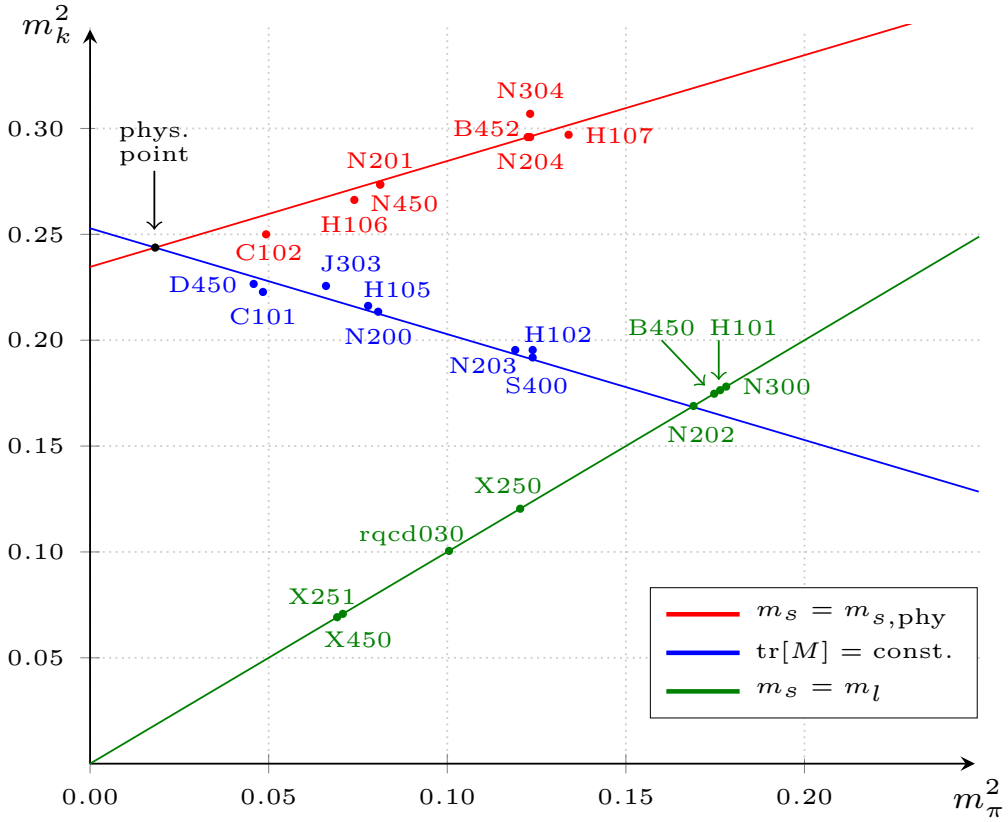

Figure 2.3.3: Visulaization of the subset of CLS gauge configurations analyzed in this thesis. We plot the three different trajectories as solid lines, using (2.89), and the corresponding data points in the m_π^2 – m_k^2 plane. This plot directly shows the extrapolation strategy to reach the physical point. However, as one can see the data points are partly located slightly above or below their corresponding trajectory, which is attributed to small (but natural) inaccuracies in the parameter tuning of the ensembles. This issue can be overcome by applying appropriate shifts when plotting the data-points in extrapolations, etc. .

blocks of block size (bin size) $N_{(i)}$, finally used to measure an observable. If the blocks are large enough the measurements on successive blocks can be considered as independent if $N_{(i)} \gg \tau_{\mathrm{int}}$. Typically we generate 500 bootstrap samples with a bin size of 40 molecular dynamics units.

3

Structure functions and deep inelastic scattering

A common way to investigate the internal structure of hadrons are DIS experiments, realized by the scattering of leptons off a hadronic target. Prominent examples are the DIS experiments by HERA [87, 88] and at JLab Hall A [89] (cf. the conditionally approved proposal [145]). In a nutshell, the term DIS describes scattering processes with a highly virtual photon transfer from the lepton to the target hadron, resulting in an (unknown) final state of many hadrons with large invariant mass. The corresponding processes are characterized by three sub-groups: If all final states are known (measured) the process is called exclusive DIS, if the final states are only partially known it is called semi-inclusive (or semi-exclusive) DIS, and if the final state remains unknown the process is called inclusive DIS. Note that the final lepton momentum is measured in all cases. For this thesis, we will restrict ourselves to the case of inclusive DIS using the basic diagram shown in Fig. 2.2.1.

There are various valuable introductions to DIS. However, the introduction given here relies mainly on [61, 146, 147] and the lecture notes of the QCD courses attended at the University of Regensburg. Parts of this chapter were also already published in [148]. Whenever necessary, additional references are provided.

3.1 Inclusive deep inelastic scattering

In typical DIS experiments one measures the scattering of an incoming lepton with energy E off a fixed hadronic target. The corresponding detectors measure the energy and direction of the scattered lepton while the final hadronic state (denoted by X) remains unknown for the moment, cf. Fig. 2.2.1a. Interactions between the lepton and the hadron take place by the interchange of a virtual photon, which is absorbed by the hadron to produce the final state X. In the DIS region the target hadron is blown apart by the virtual photon and fragments into many particles.

To produce predictions which can be compared to experiment the main goal of this section is to write down the cross-section of a DIS process in terms of the leptonic tensor $L_{\mu\nu}$, containing the information about the initial and final lepton, and the hadronic tensor $W^{\mu\nu}$. Starting point of the computation is the general expression for the DIS cross-section depicted in Fig. 2.2.1

$$i\mathcal{M} = (-ie)^2 \, \frac{-ig_{\mu\nu}}{q^2} \, \langle k', s_l'| \, J_l^\mu(0) \, |k, s_l\rangle \, \langle X| \, J_h^\nu(0) \, |p, \lambda\rangle \ , \tag{3.1}$$

where λ is the target and s_l the lepton polarization along a quantization axis and $J_{l/h}$ describe the leptonic and hadronic currents respectively. The differential cross-section is then obtained by squaring (3.1) and multiplying with the corresponding phase space factors

$$\mathrm{d}\sigma = \frac{e^4}{(q^2)^2} \frac{\mathrm{d}^3 k'}{(2\pi)^3 \, 2E'} \, \frac{4\pi L_{\mu\nu} W^{\mu\nu}(p,q)_{\lambda\lambda}}{4k \cdot p} \ , \tag{3.2}$$

with

$$L_{\mu\nu} = \sum_{s'} \langle k, s_l| \, J_{l,\mu}(0) \, |k', s_l'\rangle \, \langle k', s_l'| \, J_{l,\nu}(0) \, |k, s_l\rangle \ , \tag{3.3}$$

$$W^{\mu\nu}(p,q)_{\lambda,\lambda'} = \frac{1}{4\pi} \int \mathrm{d}^4 x e^{iq\cdot x} \, \langle p, \lambda'| \, [J^\mu(x), J^\nu(0)] \, |p, \lambda\rangle \ . \tag{3.4}$$

Note that the commutator in the definition of (3.4) is purely conventional because the subtracted term vanishes for a ground-state hadron. It is inserted to achieve a nicer analytical structure when continued away from the physical region [146], which we will exploit in subsequent calculations. All information about the DIS process is contained in (3.3) and (3.4). While the leptonic tensor will be computed explicitly in the next section the hadronic tensor is a priori unknown, as it depends on the internal quark-gluon structure of the target hadron.

3.2 Structure functions

In the last section, and also in Section 2.2, we have shown that the cross-section of a DIS experiment can be factorized into a leptonic and a hadronic tensor. The main goal of this section is to describe these objects and to finally relate the hadronic tensor to structure functions analogous to (2.19). After the more technical decomposition of $W_{\mu\nu}$ we interpret the structure functions in the naive parton model and also using helicity amplitudes.

3.2.1 The leptonic tensor

Leptons are point-like fermions and the leptonic tensor (3.3) can be computed explicitly. Rewriting (3.3) yields

$$L_{\mu\nu} = \sum_{s_l'} \overline{u}(k, s_l)\gamma_\mu u(k', s_l')\, \overline{u}(k', s_l')\gamma_\nu u(k, s_l) \ , \tag{3.5}$$

where we sum over the unknown final spin s_l'. Imposing that the polarization of a spin-1/2 particle is given by[1] $2s_l^\mu = \overline{u}(k, s_l)\gamma^\mu\gamma_5 u(k, s_l)$ and using the identies

$$\sum_{s_l'} u(k', s_l')\, \overline{u}(k', s_l') = \left(\not{k}' + m_l\right) \ , \tag{3.6a}$$

$$u(k, s_l)\, \overline{u}(k, s_l) = (\not{k} + m_l)\, \frac{1 + \gamma_5\, \not{s}_l m_l^{-1}}{2} \ , \tag{3.6b}$$

one can rewrite the initial definition by

$$\begin{aligned} L_{\mu\nu} &= \mathrm{tr}\left[(\not{k}' + m_l)\gamma_\mu(\not{k} + m_l)\frac{1 + \gamma_5\not{s}_l/m_l}{2}\gamma_\nu\right] \\ &= 2\left(k_\mu k_\nu' + k_\nu k_\mu' - g_{\mu\nu}k\cdot k' - i\,\epsilon_{\mu\nu\alpha\beta}q^\alpha s_l^\beta\right) + \mathcal{O}\left(m_l\right) \ . \end{aligned} \tag{3.7}$$

Note that the spin-dependent part of $L_{\mu\nu}$ is antisymmetric in $\mu\nu$ while the spin-independent part is symmetric. I.e., the symmetric part of the hadronic tensor can be probed with an unpolarized lepton beam, while probing the antisymmetric part requires a polarized beam. As a final remark we want to state that the current is conserved via $\partial_\mu J^\mu = 0$ and thus $q^\mu L_{\mu\nu} = q^\nu L_{\mu\nu} = 0$. Both, the symmetry considerations and the current conservation will become important in the remainder of this section.

[1] Here we use the normalization given in [146], omitting the fermion mass.

3.2.2 The hadronic tensor

The cross-section of deep inelastic scattering can be written as a product of a leptonic and a hadronic part as shown in (3.2). In this factorization the hadronic tensor characterizes the full hadron structure relevant for DIS experiments as a function of the polarizations λ and $\lambda^{'}$ (i.e., the spin along the polarization axis) and the spatial target momentum $\boldsymbol{p}$. For the sake of this thesis we will extend the familiar spin-1/2 definition of the hadronic tensor given in, e.g., [146], to the spin-1 case presented in [147].

We start the discussion with a brief reminder on the density matrix formalism. If one thinks about the states in, e.g., unpolarized DIS experiments one notices that the description by so-called pure states is not sufficient to characterize the system adequately. E.g., we have no information about the helicity of the initial hadronic target. To overcome this issue we make probabilistic statements instead by introducing the density matrix

$$\rho = \sum_i p_i \left|\psi_i\right\rangle \left\langle\psi_i\right| \ , \tag{3.8}$$

where p_i is the probability to find a pure state $|\psi_i\rangle$ of the ensemble, with $\sum_i p_i = 1$. In general, the density matrix of these mixed states is hermitian, positive, and normalized as $\mathrm{tr}[\rho] = 1$. The expectation value of an observable A is given by

$$\langle A\rangle_\rho = \mathrm{tr}[\rho A] = \sum_i p_i \left\langle\psi_i\right| A \left|\psi_i\right\rangle \ . \tag{3.9}$$

In contrast to the density matrix of a pure state the relation $\rho^2 = \rho$ does not hold in the mixed case, however, a further computation of $\mathrm{tr}[\rho^2]$ yields a measure for the mixedness of a density matrix. For pure states it is equal to 1 while it is ≤ 1 for mixed states.

Considering the polarization states of a spin J target the most general form of the density matrix can be written down as [146]

$$\rho = \sum_{\lambda,\lambda'=-J}^{J} \left|\lambda\right\rangle p_{\lambda\lambda'} \left\langle\lambda'\right| \ . \tag{3.10}$$

Since the polarization states transform as the spin-J representation under the rotation group the density matrix can be decomposed into $2J + 1$ irreducible

tensors. Following [149, 150] one obtains

$$\begin{aligned}
\rho_0 &= 1 && \text{(spin-0)}, \\
\rho_{\frac{1}{2}} &= \frac{1}{2}\left(1 + \boldsymbol{\sigma}\cdot\boldsymbol{a}\right) && \text{(spin-1/2)}, \\
\rho_1 &= \frac{1}{3}\left(1 + \boldsymbol{P}\cdot\boldsymbol{J} + W_{ij}T_{ij}\right) && \text{(spin-1)}.
\end{aligned} \tag{3.11}$$

While the spin-0 case is trivial in the spin-1/2 case the real vector $\boldsymbol{a}$ is a measure for the mixedness and, thus, one finds three parameters for the polarization. In the spin-1 density matrix we find 8 parameters. The product $\boldsymbol{P}\cdot\boldsymbol{J}$ belongs to the antisymmetric part while T_{ij} is the symmetric part defined as

$$T_{ij} = \frac{1}{2}\left(J_iJ_j + J_jJ_i\right) - \frac{2}{3}\delta_{ij}\,, \qquad \text{with } i,j \in [1,2,3]\,, \quad \text{and} \quad i \leq j\,, \tag{3.12}$$

where the J_i's are the angular momentum operators for spin-1. Note that the symmetric case does not include the identity $\sim \delta_{ij}$. In this way, we introduced the additional quadrupole moment J_iJ_j to identify the ensemble. The hadronic tensor for a spin-J particle is finally defined as

$$W_{\mu\nu}(p,q,\rho) = \rho_{\lambda'\lambda}\, W_{\mu\nu}(p,q)_{\lambda\lambda'} = \mathrm{tr}[\,\rho W_{\mu\nu}(p,q)]\,, \tag{3.13}$$

treating $W(p,q)$ as a matrix in spin space. The (general) argument ρ corresponds to the density matrices (3.11). For spin-1/2 it contains the spin information of the initial and final state spinors, for spin-1 additional contributions arise. Following the discussions in [146, 147] one imposes parity $\mathcal{P}$ and time reversal $\mathcal{T}$ invariance as well as photon crossing symmetry and current conservation $q^\mu W_{\mu\nu} = q^\nu W_{\mu\nu} = 0$ which allow to decompose the hadronic tensor into a generic tensor structure including functions of the Lorentz invariants of the process. While the $\mathcal{P}$ and $\mathcal{T}$ invariance conditions are straightforward to show crossing symmetry is achieved by exchanging μ and ν and replacing $q \to -q$. In the case of a spin-1 target the decomposition of the hadronic tensor can be written down as

$$\begin{aligned}
W^{\mu\nu} =& -F_1\, g^{\mu\nu} + \frac{F_2}{p\cdot q}p^\mu\, p^\nu + \frac{ig_1}{p\cdot q}\epsilon^{\mu\nu\lambda\sigma}\, q_\lambda s_\sigma + \frac{ig_2}{(p\cdot q)^2}\epsilon^{\mu\nu\lambda\sigma}q_\lambda\left(p\cdot q s_\sigma - s\cdot q p_\sigma\right) \\
&- b_1 r^{\mu\nu} + \frac{1}{6}b_2\left(s^{\mu\nu} + t^{\mu\nu} + u^{\mu\nu}\right) + \frac{1}{2}b_3\left(s^{\mu\nu} - u^{\mu\nu}\right) + \frac{1}{2}b_4\left(s^{\mu\nu} - t^{\mu\nu}\right).
\end{aligned} \tag{3.14}$$

At this point, we already omitted all terms proportional to q^ν or q^ν in the definition of the hadronic tensor due to the current conservation of the leptonic tensor described at the end of Section 3.2.1. Note that this removes the explicit current

conservation, and, thus, (3.14) is only valid as long as it is contracted with a tensor $L_{\mu\nu}$ that fulfills $q^\mu L_{\mu\nu} = q^\nu L_{\mu\nu} = 0$. However, with the decomposition of $W^{\mu\nu}$ in (3.14) we introduced a multitude of new variables and functions.

In the remainder of this section, we provide definitions to all yet unknown objects needed in subsequent calculations and discussions. The kinematic factors r, s, t, and u depend on the momentum transfer q, the target momentum p, and the target polarization ϵ. They are defined as

$$\begin{aligned}
r^{\mu\nu} &= \frac{1}{(p\cdot q)^2}\left[q\cdot\epsilon^*\, q\cdot\epsilon - \frac{1}{3}(p\cdot q)^2\kappa\right] g^{\mu\nu}\ , \\
s^{\mu\nu} &= \frac{2}{(p\cdot q)^3}\left[q\cdot\epsilon^*\, q\cdot\epsilon - \frac{1}{3}(p\cdot q)^2\kappa\right] p^\mu p^\nu\ , \\
t^{\mu\nu} &= \frac{1}{(p\cdot q)^2}\left[(q\cdot\epsilon^*)p^{\{\mu}\epsilon^{\nu\}} + (q\cdot\epsilon)p^{\{\mu}(\epsilon^*)^{\nu\}} - \frac{2}{3}(p\cdot q)p^\mu p^\nu\right]\ , \\
u^{\mu\nu} &= \frac{2}{p\cdot q}\left[(\epsilon^*)^{\{\mu}\epsilon^{\nu\}} + \frac{1}{3}M^2 g^{\mu\nu} - \frac{1}{3}p^\mu p^\nu\right]\ ,
\end{aligned} \tag{3.15}$$

using the shorthand symmetrization notation given in Appendix A.7 and the definition of the polarization vectors ϵ given in Appendix A.8. Note that the quantities (3.15) are constructed such that they vanish upon averaging over the target spin. Furthermore the target hadron mass is denoted by M and $\kappa \equiv 1 + (Mq)^2/(p\cdot q)^2$. The vector s^μ is the equivalent to the spin four-vector of the spin-1/2 case and is defined by

$$s^\mu = -i\epsilon^{\mu\nu\rho\sigma} e^*_\nu e_\rho p_\sigma\,. \tag{3.16}$$

What remains is the discussion of the eight structure functions. As already mentioned above the structure functions can only depend on the Lorentz invariants of the process, in particular, $p\cdot q$ and $-q^2$, further we use that $p^2 = M^2 = \text{const.}$. It is, however, convenient to rewrite this dependence in the standard notation using

$$Q \equiv \sqrt{-q^2} > 0, \qquad \text{and} \quad x \equiv \frac{Q^2}{2p\cdot q}, \tag{3.17}$$

to finally obtain functions of the form, e.g., $F_1(x, Q^2)$. The variable x is also known as the Bjorken variable [52] and is crucial for the understanding of DIS. We have seen in Section 2.2 that QCD predicts that the structure functions are independent of Q^2 in leading order calculations, i.e., the mass scale M becomes irrelevant if the target constituents are treated as almost free, point-like particles for very high energies.

Which of the structure functions can contribute depends on the target spin: In the case of spin-0 only F_1 and F_2 do. For spin-1/2 targets one has F_1, F_2, g_1,

and g_2, where the measurement of g_1 and g_2 requires a longitudinally polarized beam. In the case of spin-1 targets the full set of eight structure functions can contribute. Notably, as argued in ref. [147], the additional structure functions b_{1-4} can be measured using an unpolarized electron and polarized hadron beam.

3.2.3 Operator product expansion and momentum sum rules

One possible interpretation of the structure function can be obtained by deriving sum rules for each structure function using the operator product expansion (OPE). This approach has the advantage that it does not depend on the hadronic model and therefore provides a direct test of QCD. The starting point of our calculation is the optical theorem, which relates the hadronic tensor to the imaginary part of the forward virtual Compton scattering amplitude, cf. Fig. 3.2.1, via

$$W^{\mu\nu} = \frac{1}{2\pi} T^{\mu\nu} \ , \tag{3.18}$$

where the Compton scattering amplitude T is defined analogously to the hadronic tensor

$$T^{\mu\nu}(p,q)_{\lambda,\lambda'} = \frac{i}{4\pi} \int \mathrm{d}^4x e^{iq\cdot x} \left\langle p,\lambda' \right| T\left[J^\mu(x) J^\nu(0)\right] \left| p,\lambda \right\rangle \ , \tag{3.19}$$

replacing the commutator with the time-ordered product. However, the disappearance of the commutator introduces a little subtlety concerning the photon crossing symmetry used in the decomposition of $W^{\mu\nu}$, because the interchange of J^μ and J^ν in the commutator produces an additional minus sign while the time-ordered product does not. This implies that a decomposition of (3.19) into structure functions $\widetilde{F}_1(\omega), \ldots$, analogous to (3.14), yields functions depending exclusively on even or odd powers of $\omega = 1/x$. In the physical region $1 \leq \omega \leq \infty$ the Compton scattering structure functions are related to the structure functions of the hadronic tensor by

$$\begin{aligned}
\mathrm{Im}\, \widetilde{F}_1(\omega + i\epsilon) &= 2\pi F_1(\omega), \\
\mathrm{Im}\, \widetilde{F}_2(\omega + i\epsilon) &= 2\pi F_2(\omega), \\
\mathrm{Im}\, \widetilde{g}_1(\omega + i\epsilon) &= 2\pi g_1(\omega), \\
&\cdots \\
\mathrm{Im}\, \widetilde{b}_4(\omega + i\epsilon) &= 2\pi b_4(\omega) \, .
\end{aligned} \tag{3.20}$$

What remains is the computation of $\widetilde{F}_1(\omega), \ldots$, using (l)QCD methods to make predictions about the hadronic structure.

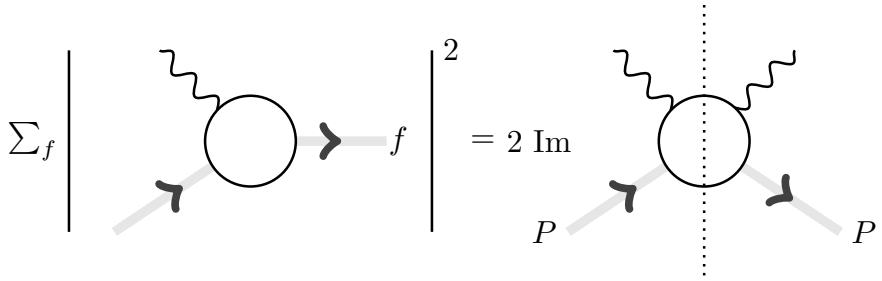

Figure 3.2.1: The hadronic tensor is related to forward virtual Compton scattering via the optical theorem. Twice the imaginary part of the forward scattering amplitude is the total cross-section.

A well-known approach for the computation of $T^{\mu\nu}$ is the OPE[2]. Let us start with a product of two operators in the limit $z \to 0$

$$\lim_{z\to 0} \mathcal{O}_a(z)\, \mathcal{O}_b(0) = \sum_k c_{abk}(z)\, \mathcal{O}_k(0)\,, \tag{3.21}$$

with structure constants $c_{abk}(z)$, which allows us to rewrite the product of operators as a sum over local operators, assuming that the momentum components of the external states under consideration are small compared to the inverse separation $1/z$. Using this concept we can expand the product of the electromagnetic currents in (3.19) into a series of local operators multiplied by coefficient functions, depending solely on the momentum transfer q. However, this is only valid for target matrix elements provided that the virtuality of the transferred momentum $\sqrt{-q^2}$ is much larger than the typical hadronic mass scale Λ_{QCD}.

For any general symmetric and traceless operator $\mathcal{O}_{d,n}^{\mu_1\cdots\mu_n}$ of mass dimension d and spin n one can show that the terms in the expansion have the structure

$$c_{\mu_1\ldots\mu_n} \mathcal{O}_{d,n}^{\mu_1\cdots\mu_n} \to \omega^n \left(\frac{Q}{M}\right)^{2-t}\,, \tag{3.22}$$

where M is the target hadron mass and $t = d-n$ is the twist. I.e., the contribution of a specific local operator matrix element to the DIS process is determined by the operator's twist. Associating the twist quantum number to the matrix element of any bilocal operator is fairly straightforward by dimensional analysis. We simply count the powers of mass introduced in the Lorentz-tensor decomposition of the matrix element and compensate it at the end of the calculation by corresponding powers of Q in the denominator, which completely determines t. The most dominant operators are those with $t = 2$ where we get no suppression at all, i.e., contributions of $\mathcal{O}(1)$. In QCD calculations we may restrict ourselves to operators

[2]The OPE is a standard tool introduced in most QCD textbooks. We will follow [146, 151] for the general introduction and [147] for the special case of spin-1 targets.

Quantum No.	q	$G_{\mu\nu}$	D^μ
d	3/2	2	1
s	1/2	1	1
t	1	1	0

Table 3.2.1: Dimension, spin and twist of QCD operator constituents.

built from quark fields q, the gluon field strength G, and the covariant derivative D, with quantum numbers listed in Tab. 3.2.1. Any gauge-invariant object is built by at least two quark fields or two gluon field strength tensors and an arbitrary number of derivatives, i.e., $t \geq 2$, provided that the operators are symmetrized and traceless. With these restrictions and in the limit of vanishing quark masses of the lightest quarks $q \in \{u, d, s\}$, a possible basis can be written down as six towers of twist-two operators [81]

$$\mathcal{O}^{\mu_1\dots\mu_n} = \frac{1}{2^{n-1}}\, \mathcal{S}\, \bar{q}\, \gamma^{\mu_1} i\overleftrightarrow{D}^{\mu_2} \dots i\overleftrightarrow{D}^{\mu_n}\, q\,, \tag{3.23a}$$

$$\mathcal{O}_5^{\mu_1\dots\mu_n} = \frac{1}{2^{n-1}}\, \mathcal{S}\, \bar{q}\, \gamma^{\mu_1}\, \gamma_5 i\overleftrightarrow{D}^{\mu_2} \dots i\overleftrightarrow{D}^{\mu_n}\, q\,, \tag{3.23b}$$

$$\mathcal{O}_\delta^{\mu_1\dots\mu_n\alpha} = \frac{1}{2^{n-1}}\, \mathcal{S}\, \bar{q}\, \sigma^{\mu_1\alpha}\, i\overleftrightarrow{D}^{\mu_2} \dots i\overleftrightarrow{D}^{\mu_n}\, q\,, \tag{3.23c}$$

$$\mathcal{O}_g^{\mu_1\dots\mu_n} = \frac{1}{2^{n-2}}\, \mathcal{S}\, G^{\mu_1\alpha} i\overleftrightarrow{D}^{\mu_2} \dots i\overleftrightarrow{D}^{\mu_{n-1}} G_\alpha^{\mu_n}\,, \tag{3.23d}$$

$$\widetilde{\mathcal{O}}_g^{\mu_1\dots\mu_n} = \frac{1}{2^{n-2}}\, \mathcal{S}\, G^{\mu_1\alpha} i\overleftrightarrow{D}^{\mu_2} \dots i\overleftrightarrow{D}^{\mu_{n-1}} \widetilde{G}_\alpha^{\mu_n}\,, \tag{3.23e}$$

$$\mathcal{O}_{\delta g}^{\mu_1\dots\mu_n\alpha\beta} = \frac{1}{2^{n-2}}\, \mathcal{S}\, G^{\mu_1\alpha} i\overleftrightarrow{D}^{\mu_2} \dots i\overleftrightarrow{D}^{\mu_{n-1}} G^{\mu_n\beta}. \tag{3.23f}$$

The covariant, symmetrized derivatives are defined as $\overleftrightarrow{D}^\mu = \overrightarrow{D}^\mu - \overleftarrow{D}^\mu$ and $\mathcal{S}$ projects out the completely symmetrized and traceless components of the r.h.s. tensor. While the gluon operators (3.23d) - (3.23f) and the quark operator (3.23c) are interesting in their own right, e.g., for the computation of transversity PDFs [152, 153], we will restrict ourselves to (3.23a) and (3.23b), which correspond to the structure functions shown in (3.14).

In the next step, we compute the leading order coefficient functions of the operators by evaluating on-shell quark matrix elements[3]. Following [146] the matrix element of the lowest order contribution to the OPE of the time-ordered product

[3]In principle one has to compute on-shell matrix elements of gluonic operators also. However, the gluon field comes along with a factor $(\alpha_s)^1$ and can be neglected in leading order $(\alpha_s)^0$ computations.

in (3.19) is given by the Feynman diagrams in Fig. 3.2.2. An explicit calculation [146] yields

$$\mathcal{M}^{\mu\nu} = -\frac{2}{q^2}\sum_f e_f^2 \sum_{n=0}^{\infty} \omega^n \left[(p+q)^\mu p^\nu + (p+q)^\nu q^\nu - g^{\mu\nu} p\cdot q + ih\epsilon^{\mu\nu\alpha\lambda} q_\alpha q_\lambda\right], \tag{3.24}$$

where the sum over f runs over all quark flavors with electrical charge e_f and h denotes the quark helicity. Using $\mathcal{M}^{\mu\nu}$ as the l.h.s. of (3.21) the next step is to compute on-shell matrix elements of the operators (3.23a) and (3.23b) that correspond to the r.h.s. of (3.21). The matrix elements in a free quark state read

$$\langle p,s|\, \mathcal{O}^{\mu_1\cdots\mu_n}\, |p,s\rangle = p^{\mu_1}\cdots p^{\mu_n}\ , \tag{3.25a}$$

$$\langle p,s|\, \mathcal{O}_5^{\mu_1\cdots\mu_n}\, |p,s\rangle = p^{\mu_1}\cdots p^{\mu_n}\, h. \tag{3.25b}$$

As stated above the coefficient functions depend only on q while the matrix elements depend on p and s. Taking this to our advantage we split all the terms in (3.24) into a q and a p dependent part respectively to read off the leading order coefficient functions. For the spin-dependent part this yields

$$\mathcal{M}^{[\mu\nu]} = \sum_{n=1,3,5,\ldots}^{\infty} \frac{2^n q^{\mu_2}\ldots q^{\mu_n}}{(-q^2)^n}\, i\epsilon^{\mu\nu\alpha\mu_1}\, q_\alpha \sum_f e_f^2 \left\langle \mathcal{O}_{5,f}^{\mu_1\cdots\mu_n}\right\rangle, \tag{3.26}$$

and the spin independent part is given by

$$\begin{aligned}\mathcal{M}^{\{\mu\nu\}} = &\sum_{n=2,4,\ldots}^{\infty}\left(-g_{\mu\nu}+\frac{q_\mu q_\nu}{q^2}\right)\frac{2^n q_{\mu_1}\cdots q_{\mu_n}}{(-q^2)^n}\ \sum_f e_f^2\left\langle \mathcal{O}_f^{\mu_1\cdots\mu_n}\right\rangle \\ &+\sum_{n=2,4,\ldots}^{\infty}\left(g_{\mu\mu_1}-\frac{q_\mu q_{\mu_1}}{q^2}\right)\left(g_{\nu\mu_2}-\frac{q_\nu q_{\mu_2}}{q^2}\right)\frac{2^n q_{\mu_3}\cdots q_{\mu_n}}{(-q^2)^{n-1}}\ \sum_f e_f^2\left\langle \mathcal{O}_f^{\mu_1\cdots\mu_n}\right\rangle.\end{aligned} \tag{3.27}$$

We know that electroproduction is a charge conjugation even process, which is validated by (3.26) and (3.27). While in the spin-dependent part of the scattering amplitude only odd spin axial vectors (charge conjugation odd) occur the spin independent part is exclusively built from even spin axial vectors (charge conjugation even). Writing down the most general decomposition of the time-ordered product in (3.19) yields

$$\begin{aligned}&\int \mathrm{d}^4x\, e^{iq\cdot x}\, T\,[J^\mu(x)J^\nu(0)] = \\ &\quad = \sum_{n=2,4,\ldots}^{\infty}\left(-g_{\mu\nu}+\frac{q_\mu q_\nu}{q^2}\right)\frac{2^n q_{\mu_1}\cdots q_{\mu_n}}{(-q^2)^n}\ \sum_j 2\, C_{j,n}^{(1)}\ \mathcal{O}_j^{\mu_1\ldots\mu_n}\ +\Big|\ \text{next page}\ \Big|\end{aligned}$$

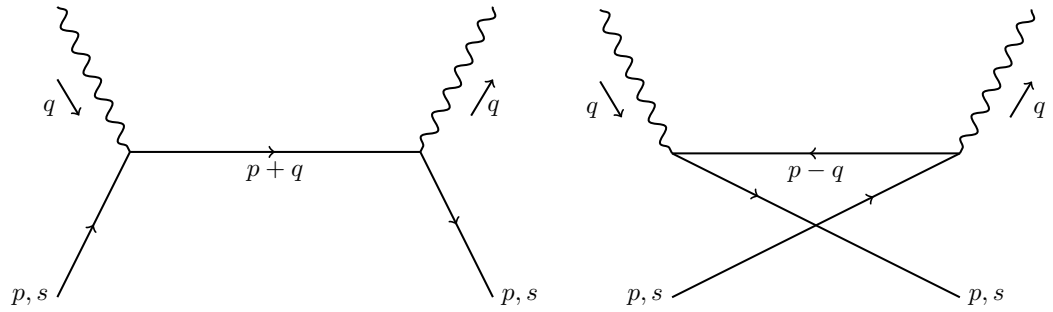

Figure 3.2.2: Leading order contributions to the time-ordered product of the two electromagnetic currents in (3.19).

$$
\begin{aligned}
&+ \sum_{n=2,4,\ldots}^{\infty} \left(g_{\mu\mu_1} - \frac{q_\mu q_{\mu_1}}{q^2}\right)\left(g_{\nu\mu_2} - \frac{q_\nu q_{\mu_2}}{q^2}\right) \frac{2^n q_{\mu_3}\cdots q_{\mu_n}}{(-q^2)^{n-1}} \sum_j 2\, C_{j,n}^{(2)}\, \mathcal{O}_j^{\mu_1\ldots\mu_n} \\
&+ \sum_{n=1,3,\ldots}^{\infty} i\epsilon_{\mu\nu\lambda\mu_1} q^\lambda \frac{2^n q_{\mu_2}\cdots q_{\mu_n}}{(-q^2)^n} \sum_j 2\, C_{j,n}^{(3)}\, \mathcal{O}_{j,5}^{\mu_1\ldots\mu_n} \\
&+ \ldots ,
\end{aligned} \tag{3.28}
$$

and allows us to identify the leading order Wilson coefficients $C_{j,n}^{(k)}$ as $C_{j,n}^{(1)} = C_{j,n}^{(2)} = C_{j,n}^{(3)} = e_f^2$ for a single quark of flavor f. Note that the coefficients of gluon contributions are zero in leading order, so all gluonic contributions are hidden in the ellipses at the end of (3.28).

However, for the computation of $T^{\mu\nu}$, cf. (3.19), we have to compute the a priori unknown hadronic matrix elements of the operators (3.23a) and (3.23b). A Lorentz decomposition of the forward matrix elements using the operators for spin-0 targets yields

$$
\langle \boldsymbol{p}| \mathcal{O}^{\mu_1\ldots\mu_n} |\boldsymbol{p}\rangle = 2\,\mathcal{S}\left[v_n^q p^{\mu_1}\cdots p^{\mu_n}\right], \tag{3.29}
$$

and defines the reduced matrix element v_n. Operators containing γ_5 do not contribute because of symmetry relations. For a spin-1 particle [147, 154] we find three independent structures

$$
\begin{aligned}
&\langle \boldsymbol{p},\lambda| \mathcal{O}^{\mu_1\ldots\mu_n} |\boldsymbol{p},\lambda\rangle = \qquad\qquad (3.30a)\\
&\quad 2\,\mathcal{S}\left[a_n^q p^{\mu_1}\cdots p^{\mu_n} + d_n^q \left(m^2 \epsilon^{*\mu_1}(\boldsymbol{p},\lambda)\,\epsilon^{\mu_2}(\boldsymbol{p},\lambda) - \frac{1}{3} p^{\mu_1} p^{\mu_2}\right) p^{\mu_3}\cdots p^{\mu_n}\right], \\
&\langle \boldsymbol{p},\lambda| \mathcal{O}_5^{\mu_1\ldots\mu_n} |\boldsymbol{p},\lambda\rangle = 2i\,\mathcal{S}\left[r_n^q \epsilon^{\rho\sigma\tau\mu_1} \epsilon_\rho^*(\boldsymbol{p},\lambda)\epsilon_\sigma(\boldsymbol{p},\lambda) p_\tau\, p^{\mu_2}\cdots p^{\mu_n}\right], \qquad (3.30b)
\end{aligned}
$$

where we use the convention that $\varepsilon^{0123} = -1$, cf. Appendix A.1, and the polarization vectors ϵ defined in Appendix A.8. By substituting (3.30a) and (3.30b)

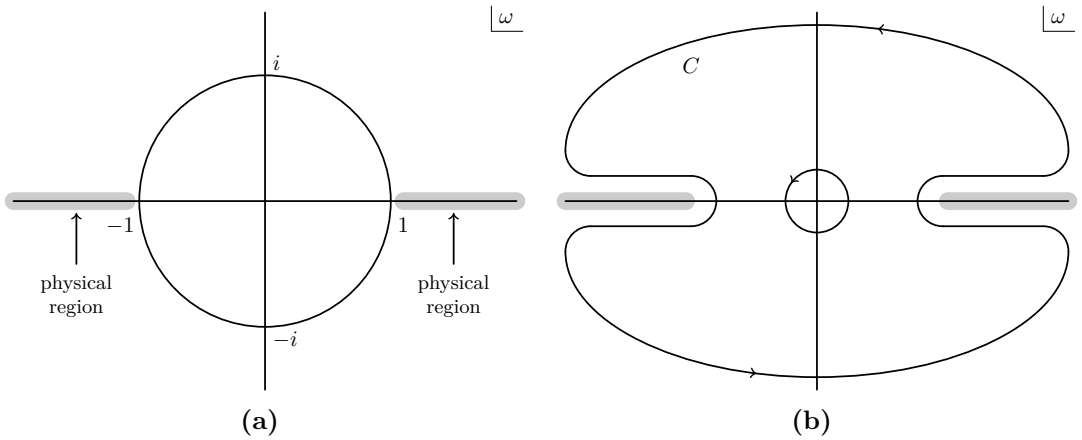

Figure 3.2.3: **(a)** Analytic structure of the tensor (3.19) in the complex ω-plane. **(b)** Contour integral for the derivation of momentum sum rules for the structure functions. The inner circle depicts the naive contour $|\omega| < 1$ while C represents the deformed contour used in the actual integration.

into (3.28) one can finally use the decomposition into structure functions $\widetilde{F}_1, \ldots$ given in (3.20) to establish relations to the reduced matrix elements via

$$\begin{aligned}
\widetilde{F}_1(\omega) &= \sum_{n=2,4,\ldots}^{\infty} 2\, C_n^{(1)}\, a_n\, \omega^n, \\
\widetilde{F}_2(\omega) &= \sum_{n=2,4,\ldots}^{\infty} 4\, C_n^{(2)}\, a_n\, \omega^{n-1}, \\
\widetilde{b}_1(\omega) &= \sum_{n=2,4,\ldots}^{\infty} 2\, C_n^{(1)}\, d_n\, \omega^n, \\
\widetilde{b}_2(\omega) &= \sum_{n=2,4,\ldots}^{\infty} 4\, C_n^{(2)}\, d_n\, \omega^{n-1}, \\
\widetilde{g}_1(\omega) &= \sum_{n=1,3,\ldots}^{\infty} 2\, C_n^{(3)}\, r_n\, \omega^n.
\end{aligned} \tag{3.31}$$

The structure functions g_2, b_3, and b_4 do not contribute at leading twist. The n-th term in their expansions corresponds to a spin-n contribution but is still twist $t = 2$. Broadly speaking (3.31) parameterizes the structure functions via a power series around $\omega = 0$ with convergence radius $|\omega| = 1$, as shown in Fig. 3.2.3a. The gray bands on the real axis depict the physical regions $1 \leq \omega \leq \infty$ for particles and $-\infty \leq \omega \leq -1$ for antiparticles. So the structure functions are computed near $\omega = 0$. An ad hoc explanation for this behavior follows directly from the deep inelastic limit (x fixed, $Q^2 \to \infty$) using light-cone coordinates, cf. Appendix A.8, to obtain

$$x = \frac{1}{\omega} = \frac{q^+}{p^+}\ , \tag{3.32}$$

where we used $Q^2 = 2q^+q^-$ for fixed q^+. I.e., DIS probes the structure of the hadron along the light-cone and is not a priori a short distance process. Nevertheless, taking the limit $\omega \to 0$ additionally forces $q^+ \to \infty$ and thus the expansion around $\omega = 0$ can be computed in QCD. To finally relate the structure functions estimated in the unphysical region to values of $|\omega| \geq 1$ we extract the coefficient functions in (3.31) by the contour integral shown in Fig. 3.2.3b. The contour of the naive integral, depicted by the inner circle in Fig. 3.2.3b, can be deformed to the outer contour C and the coefficient function is given by, e.g.,

$$2C_n^{(1)} a_n = \frac{1}{2\pi i} \oint_C \frac{\mathrm{d}\omega}{\omega^{n+1}} \widetilde{F}_1(\omega)\,, \tag{3.33}$$

assuming that C vanishes for $|\omega| \to \infty$ and only the discontinuities along the cuts contribute to the integral. Following (3.20) and exploiting the explicit symmetries of the structure functions, e.g, $\widetilde{F}_1(-\omega) = \widetilde{F}_1(\omega)$, the structure functions can be expressed by their Mellin moments

$$2M_n(F_1) = 2\int_0^1 \mathrm{d}x\, x^{n-1} F_1(x) = C_n^{(1)}\, a_n\,, \qquad\qquad n \text{ even}, \tag{3.34}$$

where we used that the n-th moment of a function is defined as

$$M_n(f) = \int_0^1 \mathrm{d}x\, x^{n-1}\, f(x) = \langle x^{n-1} \rangle_f\ . \tag{3.35}$$

A generic structure function F is always obtained as the sum over the contributions from quarks and antiquarks for the individual quark flavors weighted by the square of their electric charge e_q,

$$F = \sum_q e_q^2 \Big(F^q + F^{\bar{q}} \Big)\,. \tag{3.36}$$

Comparing this to (3.34) one notices that the series used above yields information about either the even or the odd moments of a given structure function, but not both. For spin-0 targets one finds

$$2M_n(F_1^{q+\bar{q}}) = C_n^{(1)} v_n^q\,, \qquad M_{n-1}(F_2^{q+\bar{q}}) = C_n^{(2)} v_n^q\,, \qquad n \text{ even}\,, \tag{3.37}$$

while one finds

$$\begin{aligned} 2M_n(F_1^{q+\bar{q}}) &= C_n^{(1)} a_n^q\,, & M_{n-1}(F_2^{q+\bar{q}}) &= C_n^{(2)} a_n^q\,, & n &\text{ even}\,, \\ 2M_n(b_1^{q+\bar{q}}) &= C_n^{(1)} d_n^q\,, & M_{n-1}(b_2^{q+\bar{q}}) &= C_n^{(2)} d_n^q\,, & n &\text{ even}\,, \\ 2M_n(g_1^{q+\bar{q}}) &= C_n^{(3)} r_n^q\,, & & & n &\text{ odd}\,, \end{aligned} \tag{3.38}$$

for spin-1 targets [147]. The antiparticle contributions are obtained by expanding (3.35) from $0 \leq x \leq 1$ to $-1 \leq x \leq 1$, where the negative x values correspond to the antiparticle with momentum fraction $-x$. At this point, we have obtained a set of momentum sum rules (3.37) and (3.38) for the structure functions of spin-0 and spin-1 particles respectively. Analogous results can be achieved in the general spin-n case by adapting the formalism presented above. After these technical deliberations, we finally want to emphasize that the computation of the reduced matrix elements defined in (3.30a) and (3.30b), for the special case of $n = 2$, is the main objective of this thesis. Nevertheless, before we start the actual computation of the reduced matrix elements we want to introduce two more possibilities to interpret the hadronic structure functions, starting with the parton model interpretation in the next section.

3.2.4 Parton model interpretation

In Section 2.2 we introduced the parton model and stated that DIS processes can be factorized into a hard scattering kernel, which is calculated perturbatively, and in PDFs containing the non-perturbative information. We now want to use this interpretation to relate the structure functions introduced in Section 3.2.3 to PDFs. The full set of quark PDFs can be found in, e.g., [82, 83], and reads

$$f_{q,h}^{\lambda} = \int_{-\infty}^{\infty} \frac{dz^-}{4\pi} e^{-ixp^+z^-} \langle \boldsymbol{p}, \lambda | \, \overline{q}(z)\gamma^+ q(0) \, | \boldsymbol{p}, \lambda \rangle \ , \tag{3.39a}$$

$$\Delta f_{q,h}^{\lambda} = \int_{-\infty}^{\infty} \frac{dz^-}{4\pi} e^{-ixp^+z^-} \langle \boldsymbol{p}, \lambda | \, \overline{q}(z)\gamma^+\gamma_5 q(0) \, | \boldsymbol{p}, \lambda \rangle \ , \tag{3.39b}$$

$$\delta f_{q,h}^{\lambda} = \int_{-\infty}^{\infty} \frac{dz^-}{4\pi} e^{-ixp^+z^-} \langle \boldsymbol{p}, \lambda | \, \overline{q}(z)\sigma^{+i} q(0) \, | \boldsymbol{p}, \lambda \rangle \ , \tag{3.39c}$$

defining the unpolarized-, helicity-, and transversity-PDFs, respectively. In all cases we use light-cone coordinates described in Appendix A.8. Note that in analogy to the quark PDFs one can define three additional gluon PDFs, see, e.g., [81]. The structure functions defined in (3.14) are related to the PDFs (3.39a) and (3.39b). Therefore we will restrict ourselves to the consideration of the unpolarized and helicity PDFs. To assure gauge invariance the fields in the non-local operators have to be connected by Wilson lines (cf. Section 2.2) which we do not write out explicitly here.

The PDF in (3.39a) corresponds to the sum $f_q = f_{q,\uparrow} + f_{q,\downarrow}$, while the PDF in (3.39b) corresponds to the difference $\Delta f_q = f_{q,\uparrow} - f_{q,\downarrow}$ of the densities for quarks with opposite helicity. For spin-1 hadrons reflection symmetry implies that distri-

butions for different polarizations, $\lambda = +, 0, -$, are related [147, 154]

$$f_q^+ = f_q^- \,, \qquad \Delta f_q^+ = -\Delta f_q^- \,, \qquad \Delta f_q^0 = 0 \,, \tag{3.40}$$

such that only three independent quark PDFs remain. The quark PDFs defined above support $-1 < x < 1$, where the values at negative x have to be interpreted as momentum fractions of anti-quarks

$$f_q^\lambda(x) = -f_{\bar{q}}^\lambda(-x) \,, \qquad \Delta f_q^\lambda(x) = \Delta f_{\bar{q}}^\lambda(-x) \,, \qquad \text{for} \;\; x < 0 \,. \tag{3.41}$$

In Section 3.2.3 we introduced the OPE to relate the product of operators to six towers of operators defined in (3.23a) - (3.23f). It is shown in, e.g., [82], that the unpolarized PDF and the helicity PDF can be related to (3.23a) and (3.23b), respectively, via

$$\begin{aligned} \int_{-1}^{1} dx\, x^{n-1} f_q(x) &= \langle x^{n-1} \rangle_{f_q} + (-1)^n \langle x^{n-1} \rangle_{f_{\bar{q}}} \\ &= \frac{1}{2p_+^n} n_{\mu_1}^- \cdots n_{\mu_n}^- \, \langle \boldsymbol{p} | \, \mathcal{O}_q^{\mu_1 \cdots \mu_n} \, | \boldsymbol{p} \rangle \;, \end{aligned} \tag{3.42a}$$

$$\begin{aligned} \int_{-1}^{1} dx\, x^{n-1} \Delta f_q(x) &= \langle x^{n-1} \rangle_{\Delta f_q} - (-1)^n \langle x^{n-1} \rangle_{\Delta f_{\bar{q}}} \\ &= \frac{1}{2p_+^n} n_{\mu_1}^- \cdots n_{\mu_n}^- \, \langle \boldsymbol{p} | \, \mathcal{O}_{q,5}^{\mu_1 \cdots \mu_n} \, | \boldsymbol{p} \rangle \;, \end{aligned} \tag{3.42b}$$

where the moments of the PDFs are defined in (3.35). Note that we made the flavor index q of the operators explicit in (3.42a) and (3.42b). At leading order perturbation theory and to leading twist accuracy the structure functions are directly related to the PDFs, see, e.g., refs. [147, 154], using the generic definition (3.36). For spin-0 targets one obtains

$$F_1^q(x) = \frac{1}{2} f_q(x) + \mathcal{O}(\alpha_s) \,, \tag{3.43a}$$

$$F_2^q(x) = x f_q(x) + \mathcal{O}(\alpha_s) \,, \tag{3.43b}$$

satisfying the Callan-Gross relation (2.19). The gluon PDF does not appear at leading order, since the gluons do not carry electric charge, and thus can only couple through a quark loop, cf. the discussion in Section 3.2.3. For spin-1 targets the hadronic tensor depends on the hadron spin. By averaging over the target spins one finds

$$F_1^q(x) = \frac{1}{6} \Big(f_q^+(x) + f_q^0(x) + f_q^-(x) \Big) + \mathcal{O}(\alpha_s) \,, \tag{3.44a}$$

$$F_2^q(x) = \frac{x}{3} \Big(f_q^+(x) + f_q^0(x) + f_q^-(x) \Big) + \mathcal{O}(\alpha_s) \,. \tag{3.44b}$$

Considering the difference between targets with polarization $\lambda = \pm$ and $\lambda = 0$ one finds

$$g_1^q(x) = \frac{1}{2}\Delta f_q^+(x) + \mathcal{O}(\alpha_s)\,, \tag{3.45a}$$

$$b_1^q(x) = \frac{1}{2}\Big(f_q^0(x) - f_q^+(x)\Big) + \mathcal{O}(\alpha_s)\,, \tag{3.45b}$$

$$b_2^q(x) = x\Big(f_q^0(x) - f_q^+(x)\Big) + \mathcal{O}(\alpha_s)\,, \tag{3.45c}$$

which means that b_1 and b_2 are sensitive to a possible dependence of the quark densities on the hadron polarization. We stress again that the structure functions g_2, b_3, and b_4 do not contribute at leading twist.

The relation to the reduced matrix elements defined in (3.37) and (3.38) is given by substituting (3.29) into the PDF definition (3.42a) for a spin-0 target

$$\begin{aligned} v_n^q &= \langle x^{n-1}\rangle_{f_q + f_{\bar q}}\,, \qquad && n \text{ even}\,, \\ v_n^q &= \langle x^{n-1}\rangle_{f_q - f_{\bar q}}\,, \qquad && n \text{ odd}\,, \end{aligned} \tag{3.46}$$

and by substituting (3.30a) into (3.42a) for a spin-1 target

$$\begin{aligned} a_n^q &= \frac{1}{3}\sum_{\lambda=\pm,0} \langle x^{n-1}\rangle_{f_q^\lambda + f_{\bar q}^\lambda}\,, && n \text{ even}\,, \\ a_n^q &= \frac{1}{3}\sum_{\lambda=\pm,0} \langle x^{n-1}\rangle_{f_q^\lambda - f_{\bar q}^\lambda}\,, && n \text{ odd}\,, \\ d_n^q &= \langle x^{n-1}\rangle_{f_q^0 + f_{\bar q}^0} - \langle x^{n-1}\rangle_{f_q^+ + f_{\bar q}^+}\,, && n \text{ even}\,, \\ d_n^q &= \langle x^{n-1}\rangle_{f_q^0 - f_{\bar q}^0} - \langle x^{n-1}\rangle_{f_q^+ - f_{\bar q}^+}\,, && n \text{ odd}\,. \end{aligned} \tag{3.47}$$

In the spin-1 case a similar relation holds for the reduced matrix element r_n given by the axial vector operator (3.30b), however, in this thesis we restrict ourselves to the computation of a_n, d_n, and v_n. Interpreting $f_q(x)$ as the probability to find a quark with momentum fraction x in the target hadron, a simple probabilistic interpretation of the structure functions can be read off from (3.46) and (3.47). The reduced matrix element a_n^q yields the polarization average, while d_n^q corresponds to the difference between hadrons with polarization $\lambda = \pm$ and $\lambda = 0$. In the following we will be particularly interested in the second moments, since the corresponding operator (cf. (3.23a) with $n = 2$) is equivalent to the quark part of the energy-momentum tensor [155], and describes the distribution of the momentum within the hadron. For instance, in the spin-1 case a non-zero value of d_2^q indicates that the portion of the momentum carried by quarks of flavor q depends on the polarization direction of the hadron.

Furthermore, it is shown in [147] that the parton model description of the leading

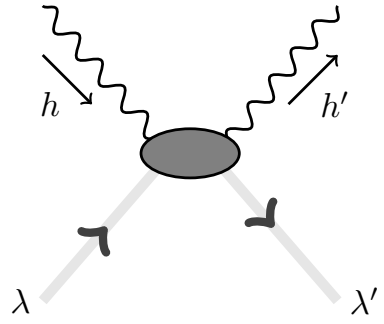

Figure 3.2.4: General helicity structure of the Compton scattering contributing to PDFs. The incoming hadron (photon) has helicity λ (h), the outgoing hadron (photon) λ' (h').

twist structure function computations can easily be generalized to spin-J targets. One finds $2(2J+1)$ PDFs $f^{\lambda}_{q,\uparrow/\downarrow}$ with $-J \leq \lambda \leq J$, obeying symmetry considerations, analogous to (3.40). This yields $2J+1$ independent distributions for integer values of J and, if $2J$ is odd, there are $J+1/2$ contributions to the polarization average and $J+1/2$ contributions to the polarization difference, respectively. For $2J$ even one finds $J+1$ contributions to the polarization average and J contributions to the polarization difference. We assume in both cases that $\lambda > 0$.

3.2.5 Helicity amplitudes

The structure functions and PDFs introduced in the last two sections can also be classified and interpreted using the more phenomenological approach of so-called helicity amplitudes. In Section 3.2.3 and Section 3.2.4 we related the distribution functions to discontinuities in the Compton scattering amplitude. This process is basically described by the amplitude shown in Fig. 3.2.4 [146, 147, 156].[4] We now label the process by the helicities of the incoming hadron (photon) λ (h) and the outgoing hadron (photon) λ' (h') and define the helicity amplitude

$$\mathcal{A}_{h\lambda,h'\lambda'} = \varepsilon^{*\mu}_{h'} W^{\lambda\lambda'}_{\mu\nu} \varepsilon^{\nu}_{h}\,, \tag{3.48}$$

omitting the explicit momentum dependence given in the definition of the hadronic tensor (3.4). The photon polarization vectors are defined as

$$\varepsilon_{\pm} = \mp\frac{1}{\sqrt{2}}(0,1,\pm i,0) \quad \text{(spacelike)}, \qquad \varepsilon_0 = \frac{1}{Q}(q^3,0,0,q^0) \quad \text{(timelike)}, \tag{3.49}$$

[4]The process can also be described by a u-channel discontinuity as shown in [82, 151]. However, we found the ansatz shown in the original literature particularly advantageous since it is associated with a direct counting rule for the number of structure functions in an arbitrary spin-J target.

with three possible polarizations $h = \pm, 0$ respectively. We now use angular momentum conservation plus parity and time reversal invariance to find

$$\lambda + h = \lambda' + h' \,, \quad \mathcal{A}_{-\lambda-\mu,-\lambda'-\mu'} = \mathcal{A}_{\lambda\mu,\lambda'\mu'} \,, \quad \text{and} \quad \mathcal{A}_{\lambda\mu,\lambda'\mu'} = \mathcal{A}_{\lambda'\mu',\lambda\mu} \,, \tag{3.50}$$

which yields $6J+2$ $(6J+1)$ amplitudes for integer (half-integer) valued J's given by

$$\begin{array}{llll} \mathcal{A}_{\pm\lambda,\pm\lambda} & (\lambda > 0), & \mathcal{A}_{+0,+0} \quad (\lambda = 0), & \text{diagonal transvers,} \\ \mathcal{A}_{0\lambda,0\lambda} & (\lambda \geq 0), & & \text{diagonal longitudinal,} \\ \mathcal{A}_{+\lambda,0(\lambda+1)} & (\lambda \geq 0), & \mathcal{A}_{-\lambda,-(\lambda-1)}(\lambda > 0), & \text{helicity flip,} \\ \mathcal{A}_{+(\lambda-1),-(\lambda+1)}(\lambda > 0), & & & \text{double helicity flip,} \end{array} \tag{3.51}$$

cf. the discussion at the end of Section 3.2.4. From this general behavior one can extract a simple but very useful counting rule: The considerations above provide a fixed number of independent helicity amplitudes which are directly related to the same number of structure functions.

For the special case of a spin-1 target the relation between $\mathcal{A}$ and the structure functions is obtained by substituting (3.14) into (3.48). Due to (3.51) we have some freedom for the choice of the $6+2$ helicity amplitudes and use

$$\begin{aligned} \mathcal{A}_{++,++} &= F_1 + \frac{1}{3}\kappa b_1 + \frac{M^2}{6(p\cdot q)}\frac{b_2}{3-b_3} - g_1 + (\kappa - 1)\, g_2 \,, \\ \mathcal{A}_{+0,+0} &= F_1 + \frac{2}{3}\kappa b_1 - \frac{M^2}{3(p\cdot q)}\frac{b_2}{3-b_3} \,, \\ \mathcal{A}_{+-,+-} &= F_1 - \frac{1}{3}\kappa b_1 + \frac{M^2}{6(p\cdot q)}\frac{b_2}{3-b_3} + g_1 - (\kappa-1) g_2 \,, \\ \mathcal{A}_{0+,0+} &= -F_1 + \kappa\left(\frac{F_2}{2x} + \frac{1}{3}b_1\right) - \frac{1}{18x}\left(\kappa^2 + \kappa + 1\right) b_2 \,, \\ \mathcal{A}_{00,00} &= -F_1 + \kappa\left(\frac{F_2}{2x} - \frac{1}{3}b_1\right) - \frac{1}{9x}\left(\kappa^2 + \kappa + 1\right) b_2 \,, \\ &\quad - \frac{1}{3x}\left(1 - \kappa^2\right) b_3 - \frac{\kappa}{3x}(1-\kappa) b_4 \,, \end{aligned} \tag{3.52}$$

for the diagonal amplitudes and

$$\begin{aligned} \mathcal{A}_{+0,0+} &= \sqrt{\kappa - 1}\,(g_1 + g_2) + \frac{M}{4Q}\left(\frac{2b_2}{3-b_3} + \kappa\frac{b_2}{3-b_4}\right) \,, \\ \mathcal{A}_{+-,00} &= \sqrt{\kappa - 1}\,(g_1 + g_2) - \frac{M}{4Q}\left(\frac{2b_2}{3-b_3} + \kappa\frac{b_2}{3-b_4}\right) \,, \\ \mathcal{A}_{+-,-+} &= \frac{M^2}{(p\cdot q)}\frac{b_2}{3-b_3} + \frac{1}{6x}\left(1-\kappa^2\right) b_3 + \frac{\kappa}{6x}(1-\kappa) b_4 \,, \end{aligned} \tag{3.53}$$

for the (double) helicity flip amplitudes. Both cases follow the notation in [147]. While the diagonal amplitudes approach finite values in the scaling limit the helicity flip amplitudes fall off like $1/Q$ and the double helicity flip amplitude falls off like $1/Q^2$. If one further uses the Callan-Gross relation (2.19) (and the analogous relation $b_2 = 2xb_1$) the diagonal amplitudes $\mathcal{A}_{0+,0+}$ and $\mathcal{A}_{00,00}$ vanish too. The structure functions are obtained by solving the system of equations (3.52) and (3.53) which requires to use the definition (3.14). However, in [157] another approach is shown, where the structure functions are redefined such that they all scale properly in the Bjorken limit and yield rather simple solutions to represent the structure functions in terms of helicity amplitudes.

Representing the structure functions by helicity amplitudes allows us to also compute the differential cross-section (3.2) in terms of helicity amplitudes. Nevertheless, there is a minor disadvantage one has to keep in mind: in general, the hadron helicities used in the computation of (3.51) are defined with respect to the direction $\boldsymbol{q}$ while it is better to define the helicity of cross-sections with respect to a fixed direction in the laboratory frame. The transformation is given by the Wigner rotation matrix and the final cross-sections are given in [156]. Fortunately, the Bjorken limit yields a trivial transformation and the helicity eigenstates with respect to the beam direction are also eigenstates with respect to the photon direction.

With these remarks we finish our introduction to structure functions. In summary, we presented three approaches to represent and interpret DIS structure functions and the corresponding kinematics. Each method comes along with numerous advantages but also with some peculiarities. In the next chapter we compute the reduced matrix elements v_2 for the pion and a_2, d_2 for the rho meson and introduce all necessary technical details needed for the analysis of the LQCD gauge ensembles used in this work.

4

Second moments of meson PDFs

After the general introduction of LQCD in Chapter 2 and DIS structure functions in Chapter 3 our prime goal is to compute Mellin moments of spin-dependent and independent PDFs of the pion and the rho meson. To this end, we will first introduce general techniques to analyze the CLS gauge ensembles used in this work and treat the occurrence of 2π states in the ρ meson spectrum before we finally show the results of the second PDF moments v_2 (pion) and a_2, d_2 (rho) including also disconnected contributions. We determine both, singlet and non-singlet flavor combinations. The numerical analysis includes 26 ensembles, with pion masses ranging from 420 MeV down to 214 MeV and with 5 different lattice spacings in the range of 0.1 fm to 0.05 fm. This enables us to take the continuum limit, as well as to resolve the quark mass dependencies reliably. Note that the results and most of the deliberations given in this chapter have been published in [148].[1]

The pion and the rho are not random examples of mesons but are both interesting in their own right. The pion is the pseudo-Goldstone boson of dynamical chiral symmetry breaking (DCSB) and is, as such, much lighter as any constituent quark model would suggest, and acts as the main carrier of the nuclear force. It is exciting to study whether its quark structure could differ substantially from that

[1] M. Löffler is the main author of this publication, however, the paper arose from a collaboration with mainly P. Wein and A. Schäfer. Some parts are taken over without further comments. Whenever necessary the co-workers are mentioned explicitly.

of other mesons. If so, the flavor singlet sea quark contribution is a natural place for such a difference to show up. For the pion there exists quite some experimental data, primarily from two classes of experiments[2], namely Drell-Yan reactions with (secondary) pion beams, e.g., $\pi + N \to \mu^+ + \mu^- + X$, which are sensitive to the pion PDF at large $x \gtrsim 0.15$, and semi-inclusive (tagged) DIS, e.g., $e + N \to e' + N + X$, which is sensitive to small x and exploits the fact that the electron can scatter off the nucleon pion cloud via the Sullivan process [158]. Experiments of the first type were performed by NA10 [159], E326 [160], E615 [161], and, more recently, by COMPASS [162]. This will be continued by AMBER at CERN [59, 60]. Experiments of the second type were performed at HERA [87, 88] (see also [163–165]) and are currently pursued at JLab Hall A [89] (cf. the conditionally approved proposal [145]). They are also under consideration for the physics program at the EIC [57].

For the rho meson the situation is somewhat different. Due to its resonance structure there exists only very little relevant experimental data and we are only aware of one actual lattice study analyzing its quark structure [154] (also discussed in [166, 167]). The rho meson is the lightest strongly decaying particle with a branching fraction of $> 99.9\%$ into 2 pions [51]. It has spin-1 which implies the existence of novel polarization-dependent structure functions as shown in Chapter 3, however, gaining information about its structure is rather challenging in experiments and on the lattice due to its unstable nature. Nevertheless, studying the quark-gluon structure of resonances is interesting. For this intent the rho is one of the most attractive light mesons to explore. To the best of our knowledge, no existing or planned experiment will investigate the spin structure of the rho, and so lattice calculations may offer the best, if not only, chance to determine it. In ref. [154] it was speculated whether one could analyze the spin structure of the ρ in the meson cloud of a nucleon in a (polarized) Sullivan process (see also ref. [163]), but the interpretation of such measurements would be very non-trivial because of the required analytic continuation from the t to the s channel [168]. However, the b_1 structure function of the deuteron was measured by HERMES [169], using DIS on tensor-polarized deuteron gas with negligible vector polarization. It turned out to be surprisingly large for such a loosely bound system. Also, while the data for a limited x range cannot really test the Close–Kumano sum rule for the first moment of $b_1(x)$ [170], one can conclude that an unexpected behavior outside of the measured x range is needed to fulfill this sum rule. Overall the results differ from the expectation that the deuteron is in an S wave with only

[2]The list of experiments and the corresponding descriptions resulted from private communication with A. Schäfer, who is also a member of the HERMES collaboration, and P. Wein.

a small D wave admixture, cf. e.g., ref. [171]. Also, there are efforts to measure the deuteron b_1 via the proton-deuteron Drell-Yan process (conditionally approved proposal at JLab Hall C [172] and feasibility studies for Fermilab [171, 173]), as well as discussions of measurements via DIS at the EIC [58].

By now the structure of hadrons is studied for more than three decades using LQCD. While in the early days mostly quenched fermion representations were used, cf. [154, 166, 167, 174–177], more recent simulations [178–183] take the fermion determinant, and thus the quark sea, into account using, e.g., (clover-improved) dynamical Wilson fermions. However, what all these studies have in common is that they neglect disconnected contributions. On the one hand, these contributions are fairly easy to compute, but on the other hand, they usually come with a large statistical error. During our analysis, we found that the noise for the light and strange quark disconnected loops is highly correlated. We can use this to our advantage by looking at the non-singlet ($\overline{u}u + \overline{d}d - 2\overline{s}s$) and singlet ($\overline{u}u + \overline{d}d + \overline{s}s$) flavor combinations instead of the light and strange loops themselves. Obviously, the large statistical errors persist for the flavor singlet combination but the difference in the flavor non-singlet combination reduces the error by more than one order of magnitude, which allows us to obtain quite precise results in this case even though we take the disconnected contributions fully into account.

In Chapter 3 we gave an in-depth introduction to the computation of the moments of structure functions. The second moments are computed using operators of the form (3.23a) for $n = 2$, i.e., with one covariant derivative. We want to stress that the procedure shown in this section is completely analogous for higher moments but not directly applicable, since one would face the problem of mixing with lower-dimensional operators. Sparked by the presentation in ref. [184], position space methods have recently fueled a lot of excitement, since they, in principle, allow for a resolution of the complete PDF. There are recent studies on the pion PDF exploring possible methods, such as the current-current method [185, 186], large momentum effective theory [187, 188] (using quasi PDFs), or Ioffe time distributions [189] (using pseudo PDFs). For the rho meson, we found only one prior lattice study in the literature, which was based on a quenched simulation at large pion masses of $\sim 600\,\mathrm{MeV}$. The usage of such large pion (quark) masses is maybe due to the additional difficulty raised by the instability of the rho meson in the continuum limit. At a first glance we will not find a continuum of two pion final states on the lattice because of the discretization of space-time and the corresponding finite volume used in actual simulations. I.e., the rho meson cannot decay dynamically into two pions. Nevertheless, the discretized set of two-pion (or, at higher energies, even multi-pion) finite volume states is present and should mix with the contribution from the rho in the correlation function. We discuss

this issue in detail in Section 4.3.

In the next sections we will introduce the numerical setup along with the two- and three-point correlation functions needed to build ratios and extract the reduced matrix elements of our choice from the lattice. Furthermore, we will briefly discuss operator renormalization and the delicate issue of two pion states that may arise in our computations before we finally come to the statistical setup and fitting routines used to produce our results.

4.1 Numerical setup

To calculate the second moment of the structure functions introduced in Chapter 3 we have analyzed a subset of the lattice gauge ensembles generated within the CLS effort, introduced in Section 2.3.6. A complete list of the gauge ensembles used in this work is shown in Tab. 4.2.1. We use five different lattice spacings from 0.0497 fm up to 0.0984 fm and m_π covers a range from $\sim 420\,\mathrm{MeV}$ down to $\sim 220\,\mathrm{MeV}$ with volumes Lm_π between 3.8 and 6.4, see Tab. 4.2.1.

The two- and three-point functions introduced in Section 4.2 are computed on the lattice using the gauge configurations in Tab. 4.2.1. While we get the two-point functions by inversions of the lattice Dirac operator using common numerical solvers (in particular, we use a modified version of the Wuppertal adaptive algebraic multigrid code DD-αAMG [190, 191] on single instruction multiple data (SIMD) architectures [192–195] and the IDFLS solver [196, 197] on other architectures) the computation of the three-point functions is more involved. The three-point function connected and disconnected parts of all ensembles are computed using stochastic estimators as described in Section 4.2. To improve the overlap of the interpolating currents at the source and the sink timeslice we use Wuppertal smeared [198] quarks by iteratively applying the smearing kernel

$$\Phi(x,y) = \frac{1}{1+6\delta}\left(\delta(x,y) + \delta \sum_{j=\pm 1}^{\pm 3} U_j(x)\,\delta(x+a\hat{\jmath},y)\right), \tag{4.1}$$

where $U_j(x)$ is an APE-smoothed gauge link [199] at position x pointing in spatial direction $\hat{\jmath}$, to the source and sink interpolators. The number of iterations (4.1) is applied to the source and the sink of the propagator is denoted by sm_ℓ for the light quarks, cf. Tab. 4.2.1. In combination with the parameter $\delta = 0.25$ the number of smearing iterations are tuned such that the corresponding smearing radii are $r_{\mathrm{sm}} \approx 0.7\,\mathrm{fm}$, see, e.g., [200–202] for a more detailed derivation.

All the computations are performed using the Chroma software package [203] and additional libraries implemented by our group.

4.2 Correlation functions

To calculate the DIS structure functions on the lattice one has to compute two- and three-point correlation functions in the forward limit:

$$C^{(\mu\nu)}_{2,\boldsymbol{p},t} = a^3 \sum_{\boldsymbol{x}} e^{-i\boldsymbol{p}\cdot\boldsymbol{x}} \langle O^{(\mu)}_M(\boldsymbol{x},t) \overline{O}^{(\nu)}_M(\boldsymbol{0},0)\rangle \,, \tag{4.2}$$

$$C^{(\mu\nu)}_{3,\boldsymbol{p},t,\tau} = a^6 \sum_{\boldsymbol{x},\boldsymbol{y}} e^{-i\boldsymbol{p}\cdot\boldsymbol{x}} \langle O^{(\mu)}_M(\boldsymbol{x},t) \mathcal{O}(\boldsymbol{y},\tau) \overline{O}^{(\nu)}_M(\boldsymbol{0},0)\rangle \,. \tag{4.3}$$

We will consider pions ($M = \pi$) and rho mesons ($M = \rho$), where the Lorentz indices are only necessary in the latter case. The interpolating current $\overline{O}^{(\mu)}_M$ creates a meson state with matching quantum numbers at the source timeslice t_{src} while $O^{(\nu)}_M$ annihilates the meson at the sink time slice t_{snk}. They read

$$O_\pi = \overline{q}_f \gamma_5 q_g \,, \qquad\qquad O^i_\rho = \overline{q}_f \gamma^i q_g \,, \tag{4.4}$$

with appropriately chosen quark flavors f and g and $i = 1, 2, 3$. The quark fields in the interpolating currents are spatially smeared (see Section 4.1) to enhance the ground-state overlap. In addition to the two interpolating currents the three-point function contains an insertion current $\mathcal{O}$ at timeslice τ with $0 < \tau < t$. The extraction of the ground-state matrix element of $\mathcal{O}$ is the key task in the subsequent calculations. In this work we set $t = t_{\text{snk}} - t_{\text{src}}$, $\tau = t_{\text{ins}} - t_{\text{src}}$ and $t_{\text{src}} = 0$ due to translational invariance.

4.2.1 Two-point correlation functions

Let's start the explicit introduction of correlation functions with an example, given by the field strength renormalization of an interacting scalar field theory [61]. A two-point correlation function, abbreviated as two-point function from now on, is the amplitude of a particle propagating from $y \to x$ given by $\langle 0| T\phi(x)\phi(y) |0\rangle$, where T denotes the time-ordered product. According to [204, 205] the two-point function can be written as

$$\langle 0| T\phi(x)\phi(y) |0\rangle = \frac{1}{2\pi} \int_0^\infty \mathrm{d}M^2 \, \rho(M^2) D_F(x-y, M^2) \,, \tag{4.5}$$

where D_F denotes the Feynman propagator and the spectral density function is defined by

$$\rho(M^2) = \sum_\lambda 2\pi\delta\left(M^2 - m^2_\lambda\right) \left| \langle 0| \phi(0) |\lambda_0\rangle \right|^2 . \tag{4.6}$$

Ens.	β	$N_s \times N_t$	bc	a[fm]	m_π[MeV]	Lm_π	t/a	sm_ℓ	n_{cnfgs}	traj.
A653	3.34	24×48	p	0.0984	426	5.1	[7, 9, 11, 13]	150	2525	sym
A650	3.34	24×48	p	0.0984	368	4.4	[7, 9, 11, 13]	160	2216	sym
H101	3.4	32×96	o	0.0859	420	5.9	[8, 10, 12, 14]	220	2016	trm/sym
H102r001	3.4	32×96	o	0.0859	352	4.9	[8, 10, 12, 14] (2)	250	1992	trm
H102r002	3.4	32×96	o	0.0859	356	5.0	[8, 10, 12, 14] (2)	250	2016	trm
H105	3.4	32×96	o	0.0859	279	3.9	[8, 10, 12, 14]	300	2052	trm
H106	3.4	32×96	o	0.0859	272	3.8	[8, 10, 12, 14]	250	1543	ms
H107	3.4	32×96	o	0.0859	366	5.1	[8, 10, 12, 14]	250	1564	ms
C101	3.4	48×96	o	0.0859	220	4.6	[8, 10, 12, 14]	350	1997	trm
C102	3.4	48×96	o	0.0859	222	4.6	[8, 10, 12, 14]	350	1465	ms

Continued on next page

Table 4.2.1: CLS gauge ensembles analyzed in this work labeled by their identifier and sorted by the inverse coupling β and m_π. We also label lattice volume in spatial and temporal direction, the boundary condition in time, open (o) or periodic (p), the lattice spacing, the pion mass, and the volume in terms of Lm_π. The list of source-sink distances analyzed for the connected three-point function of the ensemble is labeled by t and if more than one measurement for a set of source-sink separations was performed we denote the corresponding number of measurements in parenthesis. In physical units these distances roughly correspond to $[0.7, 0.9, 1.0, 1.2]$ fm. We also provide the number of smearing iterations sm_ℓ for the light quarks. The number of configurations analyzed for the ensemble is denoted as n_{cnfgs} and traj. specifies the trajectory in the quark mass plane of the ensemble, cf. Section 2.3.6.

Ens.	β	$N_s \times N_t$	bc	a[fm]	m_π[MeV]	Lm_π	t/a	sm_ℓ	n_{cnfgs}	traj.
B450	3.46	32×64	p	0.0760	418	5.2	[9, 11, 14, 16]	270	1612	trm/sym
B452	3.46	32×64	p	0.0760	350	4.3	[9, 11, 14, 16]	310	1944	ms
D450	3.46	64×128	p	0.0760	214	5.3	[9, 11, 14, 16]	480	617	trm
N450	3.46	48×128	p	0.0760	285	5.3	[9, 11, 14, 16]	375	1131	ms
S400	3.46	32×128	o	0.0760	352	4.3	[9, 11, 14, 16]	310	2001	ms
X450	3.46	48×64	p	0.0760	263	4.9	[9, 11, 14, 16]	400	400	sym
rqcd030	3.46	32×64	p	0.0760	317	3.9	[9, 11, 14, 16]	355	1222	sym
N201	3.55	48×128	o	0.0643	285	4.5	[11, 14, 16, 19]	540	1522	ms
N202	3.55	48×128	o	0.0643	411	6.4	[11, 14, 16, 19]	390	899	trm/sym
N203	3.55	48×128	o	0.0643	345	5.4	[11, 14, 16, 19] (2)	445	3086	trm
N204	3.55	48×128	o	0.0643	351	5.5	[11, 14, 16, 19]	445	1500	ms
N200	3.55	48×128	o	0.0643	284	4.4	[11, 14, 16, 19] (2)	540	3424	trm
X250	3.55	48×64	p	0.0643	348	5.4	[11, 14, 16, 19]	445	345	sym
X251	3.55	48×64	p	0.0643	267	4.2	[11, 14, 16, 19]	540	434	sym
J303	3.7	64×192	o	0.0497	257	4.2	[14, 17, 21, 24]	950	1068	trm
N300	3.7	48×128	o	0.0497	422	5.1	[14, 17, 21, 24]	640	1539	trm/sym
N304	3.7	48×128	o	0.0497	351	4.3	[14, 17, 21, 24]	750	1726	ms

Note that the sum runs only over the zero momentum eigenstates λ_0 of the corresponding interacting Hamiltonian. The squared matrix element refers to the field strength renormalization factor $Z = \left| \langle 0| \phi(0) |\lambda_0\rangle \right|^2$ and a one-particle state contributes a single delta function, where m corresponds to the observable, physical mass. Furthermore, Z can be interpreted as the probability for $\phi(0)$ to create a given state from the vacuum. Of course, this is only one oversimplified way to relate bare and renormalized parameters but it is not chosen without a reason. If one takes the Fourier transformation of (4.5) one finds an isolated simple pole in the complex p^2 plane for stable particles ($p^2 = m^2$), further multi-particle bound states along the real p^2 axis, and a branch cut at $p^2 = 4m^2$, as shown in Fig. 4.2.1. However, within this thesis, we analyze the rho meson, which rapidly decays into 2 pions [51]. This resonance character gives rise to the occurrence of (multi) particle states in the branch cutoff region of the spectrum (4.6). We want to stress that these additional multi-particle states could occur with ground-state energies below the rho meson mass and are in principle indistinguishable from the rho itself. A further discussion of this delicate issue can be found in Section 4.3. In the remainder of this section we will introduce the necessary formalism used to analyze two-point functions on the lattice.

From the above considerations, we can generalize the overlap of the ground-state with the interpolating currents (4.4) at the source and the sink in case of the pion and the rho as

$$\langle 0| O_\pi |\boldsymbol{p}\rangle = \sqrt{Z^\pi_{\boldsymbol{p}}}\,, \qquad\qquad \langle 0| O^\mu_\rho |\boldsymbol{p},\lambda\rangle = \sqrt{Z^\rho_{\boldsymbol{p}}}\epsilon^\mu(\boldsymbol{p},\lambda)\,, \tag{4.7}$$

where $|\boldsymbol{p}\rangle$ abbreviates a state by its momentum quantum number and λ denotes the polarization. Note that the overlap factor $Z_{\boldsymbol{p}}$ is now a smearing-dependent quantity, i.e., it depends on the actual setup used in the simulations. To simplify the following computations we have chosen the same smearing setup for the source and sink interpolators. For the rho we further use the polarization vectors shown in Appendix A.8. Inserting a complete set of states into (4.2) allows us to expand the two-point correlation function in terms of hadronic matrix elements. At large Euclidian times the correlation function can be approximated by the ground-state contribution

$$C_{2,\boldsymbol{p},t} = Z^\pi_{\boldsymbol{p}} \frac{e^{-E^\pi_{\boldsymbol{p}} t}}{2E^\pi_{\boldsymbol{p}}} \left[1 + \mathcal{O}\left(e^{-\Delta E^\pi_{\boldsymbol{p}} t}\right)\right] \qquad \text{(pion)}, \tag{4.8}$$

$$C^{\mu\nu}_{2,\boldsymbol{p},t} = -Z^\rho_{\boldsymbol{p}} \frac{e^{-E^\rho_{\boldsymbol{p}} t}}{2E^\rho_{\boldsymbol{p}}} \left(g^{\mu\nu} - \frac{p^\mu p^\nu}{m^2_\rho}\right) \left[1 + \mathcal{O}\left(e^{-\Delta E^\rho_{\boldsymbol{p}} t}\right)\right] \qquad \text{(rho)}\,, \tag{4.9}$$

where $E = \sqrt{\boldsymbol{p}^2 + m^2}$ is the ground-state energy imposing the continuum disper-

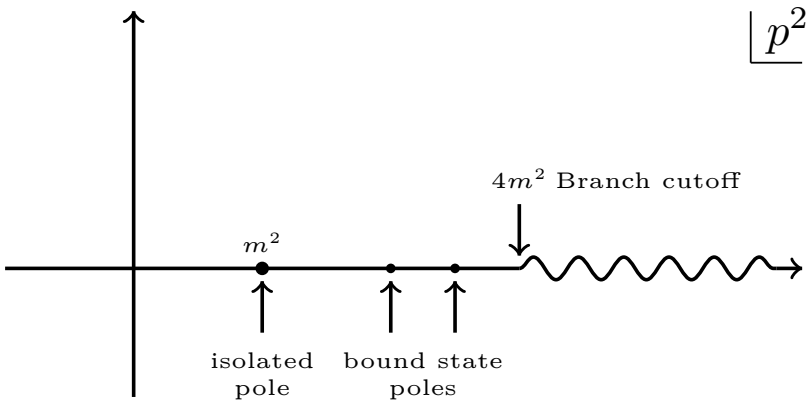

Figure 4.2.1: Analytic structure of the two-point correlator in the complex p^2 plane [61]. Poles occur for one particle states at m^2 and for an arbitrary number of bound multi-particle states. The branch cut at $4m^2$ corresponds to free multi-particle states.

sion relation and ΔE corresponds to the energy difference between the ground-state and the first excited state. We assume that $E^\rho_{\boldsymbol{p}}$ is the contribution from the rho meson, which is the leading one-particle state at large Euclidean times. Depending on the simulation parameters also two pion contributions, see above, with energies $< E^\rho_{\boldsymbol{p}}$ can occur. Note that, in the computation of (4.9) a complete set of states was inserted, which includes a sum over all possible polarizations, cf. (A.40).

Before we proceed with the introduction of three-point functions in the next section we want to have a closer look at the excited state contaminations in (4.8) and (4.9). In Section 4.4 we will fit various two-point function correlators to extract the rho mass m_ρ for the ensembles given in Tab. 4.2.1. For all ensembles with open boundary conditions we decided to include a generic excited state contribution of the form

$$C^{\mu\nu}_{2,\boldsymbol{p},t} = -Z^\rho_{\boldsymbol{p}} \frac{e^{-E^\rho_{\boldsymbol{p}} t}}{2E^\rho_{\boldsymbol{p}}} \left(g^{\mu\nu} - \frac{p^\mu p^\nu}{m_\rho^2} \right) \left(1 + A\, e^{-\Delta E^\rho_{\boldsymbol{p}} t} \right) , \tag{4.10}$$

where A is the excited state amplitude, depending on the interpolating currents at the source and the sink, their smearing, and the momentum $\boldsymbol{p}$. The construction of an analogous ansatz for the pion is straightforward by omitting the first term in parenthesis and replacing the energies and amplitudes with their pion counterparts.

4.2.2 Three-point correlation functions

The spectral decomposition of three-point functions is similar to the two-point function case in the last section. One just includes two complete sets of states

into (4.3) to obtain

$$C_{3,\boldsymbol{p},t,\tau} = Z^{\pi}_{\boldsymbol{p}} \frac{e^{-E^{\pi}_{\boldsymbol{p}} t}}{(2E^{\pi}_{\boldsymbol{p}})^2} \langle \boldsymbol{p} | \, \mathcal{O} \, | \boldsymbol{p} \rangle + \dots \qquad \text{(pion)}, \tag{4.11}$$

$$C^{\mu\nu}_{3,\boldsymbol{p},t,\tau} = Z^{\rho}_{\boldsymbol{p}} \frac{e^{-E^{\rho}_{\boldsymbol{p}} t}}{(2E^{\rho}_{\boldsymbol{p}})^2} \sum_{\lambda',\lambda} \epsilon^{\mu}(\boldsymbol{p},\lambda')\epsilon^{\nu *}(\boldsymbol{p},\lambda) \, \langle \boldsymbol{p},\lambda' | \, \mathcal{O} \, | \boldsymbol{p},\lambda \rangle + \dots \qquad \text{(rho)}, \tag{4.12}$$

for large Euclidean times. In practice, it turns out that especially for the three-point functions the signal-to-noise ratio decreases exponentially with the source-sink separation in time. At small time distances between the operators, however, there are still noticeable excited state effects. We take these into account by allowing for a generic excited state contribution in the spectral decomposition of the correlation functions. Analogous to (4.10) our ansatz for the vector three-points functions is given by

$$\begin{aligned} C^{\mu\nu}_{3,\boldsymbol{p},t,\tau} = Z^{\rho}_{\boldsymbol{p}} \frac{e^{-E^{\rho}_{\boldsymbol{p}} t}}{(2E^{\rho}_{\boldsymbol{p}})^2} \sum_{\lambda',\lambda} \epsilon^{\mu}(\boldsymbol{p},\lambda')\epsilon^{\nu *}(\boldsymbol{p},\lambda) \, \langle \boldsymbol{p},\lambda' | \, \mathcal{O} \, | \boldsymbol{p},\lambda \rangle \\ \times \left(1 + B_{10} e^{-\Delta E_{\boldsymbol{p}}(t-\tau)} + B_{01} e^{-\Delta E_{\boldsymbol{p}} \tau} + B_{11} e^{-\Delta E_{\boldsymbol{p}} t}\right), \end{aligned} \tag{4.13}$$

where the energy difference $E_{\boldsymbol{p}}$ to the first excited state may differ from the energy difference given for the two-point function. Note that, B_{10}, B_{01}, and B_{11} depend on the operator insertion $\mathcal{O}$, the interpolating currents, their smearing, and momentum. For the pion case we perform the analysis analogously by neglecting the spin-dependent part of (4.13).

At this point, we also want to underline that, especially for ensembles with small pion mass and large volume, the occurrence of two (or even multiple) pion states in the energy spectrum of the three-point function cannot be fully excluded. Analogous to the discussion in Section 4.2.1 these multi-particle states could also occur with energies smaller than the expected ground-state energy of the rho itself. We tried to explicitly resolve these multi-particle states in the two-point correlator of the ensemble D200 using an ansatz analogous to (4.10), including additional energy terms, where we fixed the estimated mass of the n-pion states ($n = 2, 3$) by the ensemble parameters. However, non of our tests gave any evidence for the occurrence of two pion states. Possible explanations will be discussed in Section 4.3.

After explaining the general idea of three-point function computations we proceed with the technical intricacies in the actual computations. Using the Wick contractions introduced in Section 2.3.2 it is clear that three-point function computations can be grouped into two subgroups referring to connected and disconnected quark-line contributions, as depicted in Fig. 4.2.2. While both types of

diagrams correspond to the same physical process each contribution encounters physics-independent subtleties on the software side. One of the key tasks of this thesis was the finalization of a software package to compute connected three-point functions using stochastic estimators. Hence a more in-depth introduction to these computations is given in Section 4.2.3. Quark-line disconnected contributions will be discussed in Section 4.2.5.

4.2.3 Connected three-point functions using stochastic estimators

Parts of this introduction were already published in [56, 148, 206]. We will collect the main results in this section which are partly identical to the cited publica-

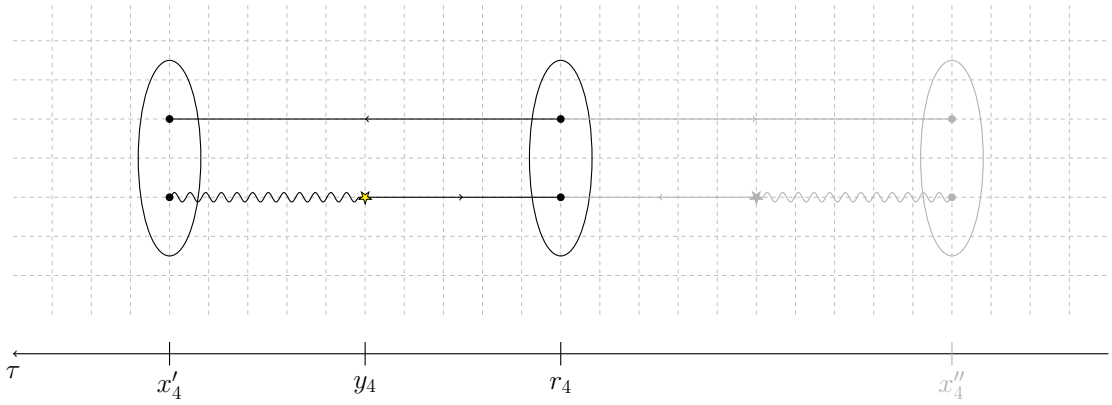

(a) Connected three-point function.

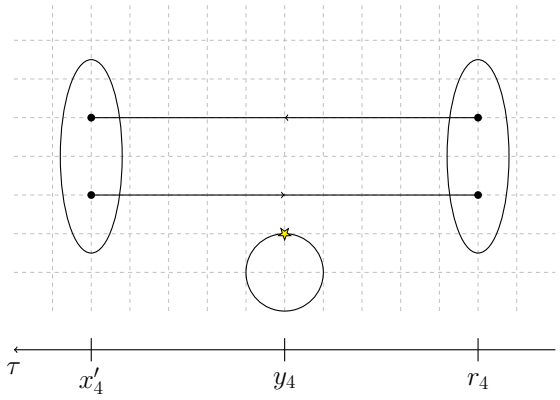

(b) Disconnected three-point function.

Figure 4.2.2: (a) Sketch of a generic meson three-point function in forward and backward (grayed out) direction. The source timeslice is r_4, the backward/forward sink timeslice x_4'/x_4'' and the current is located at timeslice y_4. While the solid lines represent point-to-all propagators the wiggly line illustrates the stochastic timeslice-to-all propagator connecting the sink and the operator insertion. A similar figure was published in [56, 148, 206]. **(b)** Sketch of a generic meson disconnected three-point function. The source timeslice is r_4, the sink timeslice x_4' and the current (loop) is located at timeslice y_4. While the solid lines represent point-to-all propagators the solid circle represents a quark loop. A similar figure was published in [148].

tions. In addition, it should be mentioned that parts of the work was done in collaboration with R. H. Rödl who implemented an analogous version for baryon three-point function computations presented in [207].

The standard setup for connected three-point function computations in the forward and backward direction is shown in Fig. 4.2.2a, where the ellipses at r_4 and x_4' depict the initial and final meson interpolators, respectively, while the star at y_4 represents the operator insertion for Euclidean times τ. Furthermore, we denote the particle flow by arrows in the middle of the individual quark-lines. Computations of mesonic three-point functions, in general, involve the computation of two so-called all-to-all propagators, connecting all points of the lattice (the wiggly line and the propagator connecting y_4 and r_4) plus one point-to-all propagator connecting the source and the sink (top line). Exploiting γ_5-hermiticity of the propagator, we can change the direction of the quark-line connecting y_4 and r_4, i.e., we reduce the problem to the computation of only one all-to-all propagator. Nevertheless, a direct computation is not feasible, because it would need an inversion of lattice Dirac operators containing $12V \times 12V$ elements, where V denotes the lattice volume. For common CLS gauge ensembles, e.g., H102 $V = 32^3 \times 96 \approx \mathcal{O}(10^7)$.

A traditional approach to overcome this issue is the sequential source method [208]. In this method the propagators connecting the source position with all other points of the lattice are computed using the point-to-all method. To compute the propagator connecting the sink timeslice x_4' with all insertion timeslices y_4 we define the sequential propagator as

$$\Sigma(y,0) = \sum_{\boldsymbol{x}'} G(y,x')\ \Gamma_{\text{snk}}\ G(x',0)\ e^{-i\boldsymbol{p}'\cdot\boldsymbol{x}'}\,, \tag{4.14}$$

where G denotes the standard quark propagator and Γ_{snk} corresponds to the sink interpolator. It is computed by an additional inversion of the Dirac matrix for each choice of the final momentum $\boldsymbol{p}'$

$$\sum_{y} D(z,y)\ \Sigma(y,0) = \Gamma_{\text{snk}}\ G(z,0)\ e^{-i\boldsymbol{p}'\cdot\boldsymbol{z}}. \tag{4.15}$$

Hence a new sequential propagator has to be computed for every change of the sink properties (x_4', final momentum, field interpolator, smearing) and every choice of the Γ-structure within the sequential propagator. As a consequence computations of various sink quantities become rather expensive and hence one often uses only a small number of final momenta for the computations. To avoid these restrictions other methods were introduced. A particular example are stochastic estimators

to approximate the all-to-all propagator

$$G(y,x') \equiv D^{-1}(y,x') = \frac{1}{N}\sum_{i=1}^{N} s_i(y)\ \eta_i^*(x') + \mathcal{O}\left(\frac{1}{\sqrt{N}}\right), \tag{4.16}$$

using the noise vectors η defined in Appendix A.9. Here s denotes the solution vector defined by

$$D(x,y)\, s_i(y) = \eta_i(x). \tag{4.17}$$

To improve the estimation it is necessary to choose N large enough so that the gauge noise dominates over the stochastic noise term $\mathcal{O}(1/\sqrt{N})$.

Following the conventions in [56, 206] we use the propagator estimation (4.16) to factorize (4.3) into two completely independent parts. In the first step we rewrite (4.3) in terms of quark field creation and annihilation operators and use Wick's theorem to obtain

$$\begin{aligned}
&\delta_{a'b'}\,\delta_{\widetilde{a}\widetilde{b}}\,\delta_{ba}\,\Gamma_{\text{snk}}^{\alpha'\beta'}\,\Gamma_{\text{ins}}^{\widetilde{\alpha}\widetilde{\beta}}\,\Gamma_{\text{src}}^{\beta\alpha}\,\Big\langle \overline{q}_{f_1}(x')_{a'}^{\alpha'}\ \overline{q_{f_2}(x')_{b'}^{\beta'}\ \overline{q}_{f_3}(y)_{\widetilde{a}}^{\widetilde{\alpha}}}\ \overline{q_{f_4}(y)_{\widetilde{b}}^{\widetilde{\beta}}\ \overline{q}_{f_6}(r)_{b}^{\beta}}\ q_{f_5}(r)_{a}^{\alpha}}\Big\rangle_c \\
&\qquad = \delta_{a'b'}\,\delta_{\widetilde{a}\widetilde{b}}\,\delta_{ba}\,\Gamma_{\text{snk}}^{\alpha'\beta'}\,\Gamma_{\text{ins}}^{\widetilde{\alpha}\widetilde{\beta}}\,\Gamma_{\text{src}}^{\beta\alpha}\ G_{f_1}(r,x')_{aa'}^{\alpha\alpha'}\ G_{f_2}(x',y)_{b'\widetilde{a}}^{\beta'\widetilde{\alpha}}\ G_{f_4}(y,r)_{\widetilde{b}b}^{\widetilde{\beta}\beta}\,,
\end{aligned} \tag{4.18}$$

where $\langle \dots \rangle_c$ denotes the configuration average. The abbreviations Γ_{src}, Γ_{snk}, and Γ_{ins} correspond to the spin structure of the individual interpolating currents while Γ_{ins} can contain additional local derivatives. Of course one has to take into account a second contraction, which corresponds to an inverted propagation direction in Fig. 4.2.2a, as shown in [206]. However, for the sake of readability, we will omit the second contraction in the following.

The introduction of the stochastic propagator allows us to replace the propagator connecting the sink and the insertion timeslice and thus factorize[3] the correlation function

$$C_{3,\boldsymbol{p}'}(x_4', y_4, r_4) \approx \frac{a^6}{N}\sum_{i=1}^{N} \Gamma_{\text{snk}}^{\alpha'\beta'}\ \Gamma_{\text{ins}}^{\widetilde{\alpha}\widetilde{\beta}}\ \Gamma_{\text{src}}^{\beta\alpha}\ S_{i,\,f_1}(\boldsymbol{p}, x_4')_{a}^{\beta'\,\alpha'\,\alpha}\ I_{i,\,f_2,\,f_4}(\boldsymbol{q}, y_4)_{a}^{\widetilde{\alpha}\,\widetilde{\beta}\,\beta}\,, \tag{4.19}$$

where we define the spectator $S_{i,\,f_1}(\boldsymbol{p}, x_4')_{a}^{\beta'\,\alpha'\,\alpha}$ and the insertion $I_{i,\,f_2,\,f_4}(\boldsymbol{q}, y_4)_{a}^{\widetilde{\alpha}\,\widetilde{\beta}\,\beta}$

[3]The idea of factorizing three-point correlation functions is not new. Early considerations can be found in, e.g., [209], and further investigations of the RQCD group were published in, e.g., [210, 211].

parts as

$$S_{i,\,f_1}(\boldsymbol{p}', x_4')_a^{\beta'\,\alpha'\,\alpha} = \sum_{\boldsymbol{x}'} \; e^{-i\boldsymbol{p}'\cdot\boldsymbol{x}'} \; \delta_{a'b'} \; [\eta_i(x') \; \gamma_5]_{b'}^{\beta'} \left[\gamma_5 \; G_{f_1}^{\dagger}(x', r) \; \gamma_5\right]_{a'a}^{\alpha'\alpha}, \tag{4.20}$$

$$I_{i,\,f_2,\,f_3}(\boldsymbol{q}, y_4)_a^{\widetilde{\alpha}\,\widetilde{\beta}\,\beta} = \sum_{\boldsymbol{y}} \; e^{i\boldsymbol{q}\cdot\boldsymbol{y}} \; \delta_{ab} \; \delta_{\widetilde{a}\widetilde{b}} \; \left[\gamma_5 \; s_{i,\,f_2}^{*}(y)\right]_{\widetilde{a}}^{\widetilde{\alpha}} \; G_{f_4}(y, r)_{\widetilde{b}b}^{\widetilde{\beta}\beta}, \tag{4.21}$$

for $\mathbf{r} = 0$. A closer look at the factorization (4.19) and the corresponding propagator particle flow directions reveals that the insertion part (4.21) can be reused in the estimation of baryonic three-point functions and vice versa. This is accompanied by additional multiplications of γ_5 matrices and a reshaping in the spectator part of the meson. However, the advantages of a re-usable insertion part more than compensate all drawbacks. In the next section we will introduce the software stack used to analyze the three-point functions, which was one of the main technical tasks during this thesis.

4.2.4 Connected three-point functions software stack

Most important in the considerations presented in Section 4.2.3 is the amount of disk space needed to store the individual objects (4.20) and (4.21), were all spin indices, one color index, the stochastic index i, the flavor indices f_i, and the momentum indices are kept open. For a single configuration this yields[4]

$$\begin{aligned} N_{\text{spectator}} &= N_s^3 \cdot N_c \cdot N_i \cdot N_{\text{mom}} \cdot N_{\text{fwd/bwd}} \cdot N_{\text{flavor}} \cdot N_{\text{src}} \,, \\ N_{\text{insertion}} &= N_s^3 \cdot N_c \cdot N_i \cdot N_{\text{mom}} \cdot N_{\text{fwd/bwd}} \cdot N_{\text{flavor}} \cdot N_{\text{ins}} \cdot N_{\text{sol. flavor}} \cdot N_{\text{der}} \,, \end{aligned} \tag{4.22}$$

complex numbers. A typical numerical setup for the CLS ensemble J303 is shown in Tab. 4.2.2. N_i denotes the number of stochastic estimates, N_{src} the number of source timeslices, N_{mom} the number of momentum combinations, $N_{\text{fwd/bwd}}$ the forward/backward part of the three-point function (used to increase statistics via averaging), and N_{flavor} the number of flavor combinations for the meson. The usual abbreviations N_s and N_c denote the number of spin and color components respectively. Our example calculation (4.22) for J303 yields $N_{\text{spectator}} \approx 8.3 \cdot 10^6$ complex numbers for the spectator part, cf. Tab. 4.2.2a, which correspond to $\sim 127\,\text{MB}$ of disk space. The insertion part requires the computation on every operator insertion timeslice and typically includes all directions of the first derivative. Using the parameters shown in Tab. 4.2.2b this yields $N_{\text{insertion}} \approx 2.86 \cdot 10^9$ additional complex numbers corresponding to $\sim 42\,\text{GB}$ of disk space. Incorporating the baryon

[4]Here we corrected a misprint in [206].

Parameter	Value
N_s	4
N_c	3
N_i	100
N_{mom}	27
$N_{\text{fwd/bwd}}$	2
N_{flavor}	2
N_{src}	4
$N_{\text{spectator}}$	$\sim 8.3 \cdot 10^6$

(a) Spectator part

Parameter	Value
N_s, N_c, N_i	4, 3, 100
N_{mom}	54
$N_{\text{fwd/bwd}}$	2
N_{flavor}	3
N_{src}	4
N_{ins}	23
N_{der}	1 + 4
$N_{\text{insertion}}$	$\sim 2.86 \cdot 10^9$

(b) Insertion part

Table 4.2.2: Analysis parameters for the stochastic three-point function simulation of the CLS ensemble J303.

spectator part[5], which is included in most of our runs, we eventually end up at a total file size of $\sim 43\,\text{GB}$ per configuration, which is dominated by the insertion part contribution.

This example calculation highlights the importance of a reusable insertion. An ensemble like J303 contains 1073 configurations and thus produces $\sim 46\,\text{TB}$ of data. Summing up all current runs on the various CLS gauge ensembles, we already produced $\sim 1.8\,\text{PB}$ of data [212] and the number would roughly be twice as big if we had to produce the insertion part data for both cases. Considering the storage systems available at present it is, however, already a non-trivial task to manage the reduced amount of data[6].

The memory and disk space requirements we had to solve were a further key challenge at the time we published [56, 206]. In previous simulations we used the chroma/QDP++ software stack [203], which was not optimized for the Intel Xeon Phi (KNC/KNL) processors used by various computing centers and also in the QPACE-2 and QPACE-3 supercomputers of our group. To overcome this issue at the beginning of 2015 S. Heybrock started to implement a library called LibHadronAnalysis (LHA) which was incorporated into the chroma/QDP++ software stack

[5] An in-depth explanation of the baryon case is given in [207].

[6] The management of data among the various computing-centers and our university storage system, was done in collaboration with S. Weishäupl and R. H. Rödl in terms of software and infrastructure development.

and came along with a lot of optimizations solely for the Intel Xeon Phi architecture. The new memory layout implemented to exploit the 512 bit wide AVX vector registers of the KNL SIMD architecture is one of the most essential building blocks of the code. Omitting some technical details, the main idea of the new layout is given by rearranging parts of the for-loops in the original implementation as shown in[7] Alg. 1 and Alg. 2.

```
for 3 spin indices do
    for color indices a,b do
        for all sites in the local
         lattice do
        |
        end
    end
end
```

Algorithm 1: Chroma

```
for all sites in the local lattice do
    for 1 spin index do
        for color indices a,b do
            for 2 spin indices
             SIMD vect. do
            |
            end
        end
    end
end
```

Algorithm 2: LibHadronAnalysis

In a nutshell, this implies that the innermost loop over all lattice sites in Alg. 1 is moved to the very outside in Alg. 2 while we split the loops over the spin indices such that we can compute multiple spin operations with only one instruction in the innermost loop in Alg. 2. Corresponding timings for the reference as well as the LHA implementation can be found in [56, 207].

Based on these basic tools there were already implementations to, e.g., compute meson and baryon distribution amplitudes. However, it was up to us to implement the three-point function computations using stochastic estimators [213] as shown in (4.19), which is by now the most complex part of the library. In the actual computation we implemented the spectator parts (meson and baryon) and the insertion part as separate blocks to further parallelize the code. The computation of the spectator part consists of the contractions of propagators at the timeslices where the source and the sink are located. Naively only the MPI ranks on the timeslices r_4 and x_4', x_4'' would work, cf. Fig. 4.2.2a. In our implementation we prepare a set of propagators sourced from different temporal source positions and redistribute these propagators among the different MPI ranks in such a way that each rank has at least one propagator. The computation of the spectator part for each source position is then performed simultaneously and the Fourier transformation in (4.20) fixes the momentum $\boldsymbol{p}'$ at the sink.

[7] Algorithms are taken from [210].

The insertion part corresponds to the contraction of the stochastic propagator, i.e., the solution of the lattice Dirac equation sourced by random noise vectors, with the point-to-all propagator. This has to be repeated for each operator timeslice y_4 between the sinks x_4' and x_4'' and the source r_4. Again, to keep a good workload balance we redistribute the data from the timeslices where the insertion is present among all MPI ranks in such a way that each rank has approximately the same number of insertion positions to work with. Finally, we perform all the computations in parallel. Note that a separate Fourier transformation in (4.21) allows us to select the desired momentum $\boldsymbol{q}$ flowing through the insertion. The results of our computations are stored in the HDF5-file format. A brief introduction of the specific file structure is given in Appendix A.10.

However, there is a subtlety in the actual implementation concerning the Fourier transformations in the spectator and insertion parts producing wrongly labeled results, which we have to correct. For the Fourier transformation we use standard chroma methods which take an offset argument set by the first spatial source position of the measurement, i.e., if one computes four source positions the offset corresponds to the source position which occurs first in the input file. Therefore we have to multiply all subsequent Fourier transformations by a global phase factor and rewrite the spectator and insertion part as

$$\widetilde{S}_{i,\,f_1}(\boldsymbol{p}', x_4')_a^{\beta'\,\alpha'\,\alpha} = e^{-i\boldsymbol{p}'\cdot\Delta\boldsymbol{r}}\; S_{i,\,f_1}(\boldsymbol{p}', x_4')_a^{\beta'\,\alpha'\,\alpha}, \tag{4.23}$$

$$\widetilde{I}_{i,\,f_2,\,f_3}(\boldsymbol{q}, y_4)_a^{\widetilde{\alpha}\,\widetilde{\beta}\,\beta} = e^{-i\boldsymbol{q}\cdot\Delta\boldsymbol{r}}\; I_{i,\,f_2,\,f_3}(\boldsymbol{q}, y_4)_a^{\widetilde{\alpha}\,\widetilde{\beta}\,\beta}, \tag{4.24}$$

where $\Delta\boldsymbol{r} = \boldsymbol{r}_k - \boldsymbol{r}_0$ defines the offset between the k-th and the first source position of the measurement[8] with $0 < k < N_{\mathrm{src}}$. The analysis software created for the purpose of this project already contains the correction factors for the spectator parts of the baryon and meson.

Once we have created the spectator and insertion data we have to further process the data. The general idea of our software stack[9] for this task is shown in Fig. 4.2.3. In the following we will briefly discuss the individual constituents starting with the chromaXML package [214].

A common choice of feeding chroma with input data, e.g., source positions, smearing parameters, etc., is the use of extensible markup language (XML) files

[8]For all readers with technical intents: The source positions of every measurement can be found in the meta-data of the HDF5 output-file where also the data is stored. Additionally one should keep in mind that for the implementation of the phase correction it is essential to convert the lattice momenta to physical units, i.e., $\boldsymbol{p} = \frac{2\pi}{N_s}\boldsymbol{k}$ where N_s is the spatial lattice extend.

[9]For more detailed information we refer to [207], where also example code and timings are provided.

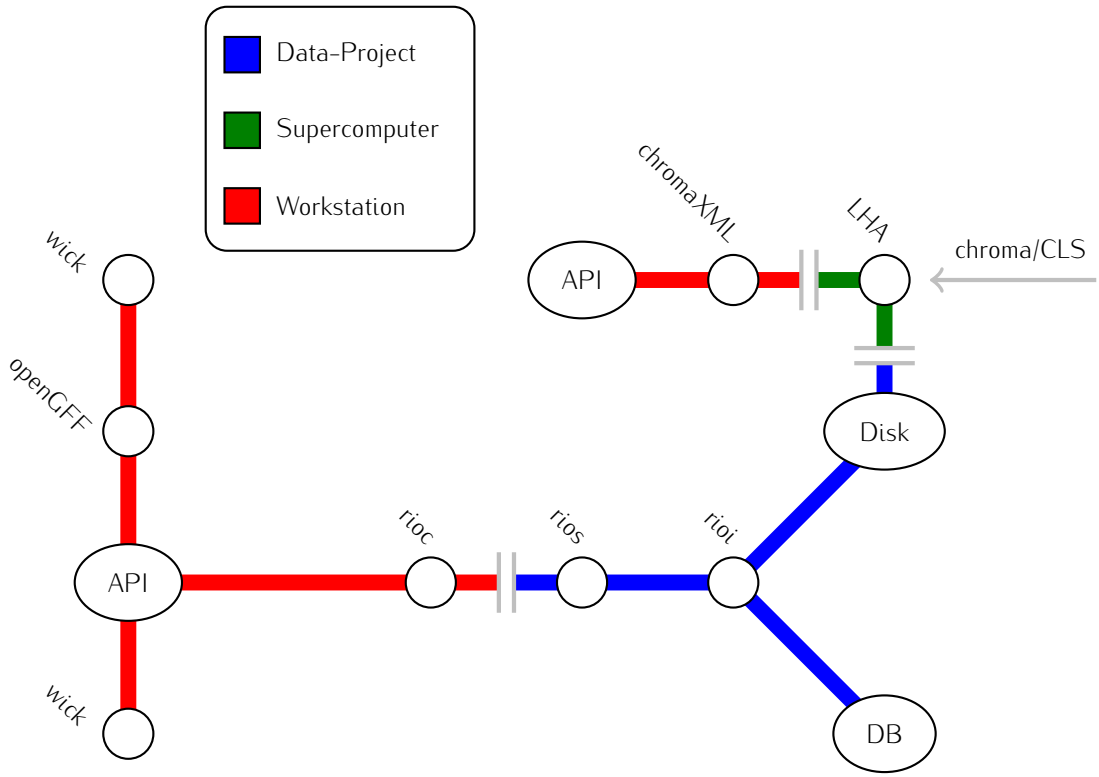

Figure 4.2.3: Overview of the software stack used to extract physical results from the stochastic three-point function estimates. The red lines depict the user's personal workstation or any server computer used for daily work. In our case, the application programming interface (API) is just a shorthand notation for the operating system providing basic properties like python and other standard tools and the circles denote the individual software packages implemented to extract the data. The blue part corresponds to infrastructure mostly located in data or computing centers where we run a server and interface structure to get data from disk and store it in a database. The green part in the top right corner finally describes a supercomputer where we run our code combined with the chroma software package to analyze CLS gauge configurations.

where the input arguments are stored in so-called tags. These files can easily contain several thousand lines of arguments and thus become very confusing at first sight. To simplify the workflow we developed a lightweight python module that allows us to collect all the input parameters in one place to subsequently be able to use the capabilities of a programming language to create the XML files in a comprehensible way.

Let's assume that the spectator and insertion data is already created and stored on disk. To obtain physical quantities one first has to choose a specific Wick contraction, cf. (4.18), and explicit spin structures Γ for the interpolating currents. Of course one also has to provide additional meta-data, e.g., the number of stochastic indices to use, the source-sink distance, etc. . These tasks are governed by the wick [215] and the openGFF [216] packages, which assemble human-readable requests to software objects and assure that the request does not contain logical

errors. However, in order to cope with the very large amount of data, we decided not to process the request directly on the user's workstation and thus set up a server-client structure that allows us to leave the main data in a central storage system and only load the data of interest. The main constituents of this structure are the rioc (Regensburg IO client) package [217] which sends the user request to the rios (Regensburg IO server) package [218] via any network connection. Once the request has arrived on the server-side we hand it over to the rioi (Regensburg IO interface) package [219] and start a case differentiation. If the data has never been requested before the interface loads the corresponding numbers for the spectator and insertion part from disk and first creates an object of the form

$$\mathcal{C}^{\beta'\,\alpha'\,\alpha\,\widetilde{\alpha}\,\widetilde{\beta}\,\beta}_{3,\boldsymbol{p}',\boldsymbol{q}}(x_4', y_4, r_4) = \widetilde{S}_i(\boldsymbol{p}', x_4', r_4)^{\beta'\,\alpha'\,\alpha}_{a}\ \widetilde{I}_i(\boldsymbol{q}, y_4, r_4)^{\widetilde{\alpha}\,\widetilde{\beta}\,\beta}_{a}\,, \tag{4.25}$$

where we already handled the sum over the color and stochastic indices. In the next step we compute the remaining spin contractions

$$C_{3,\boldsymbol{p}',\boldsymbol{q}}(x_4', y_4, r_4) \approx \frac{a^6}{N}\ \Gamma^{\alpha'\beta'}_{\text{snk}}\ \Gamma^{\widetilde{\alpha}\widetilde{\beta}}_{\text{ins}}\ \Gamma^{\beta\alpha}_{\text{src}}\ \mathcal{C}^{\beta'\,\alpha'\,\alpha\,\widetilde{\alpha}\,\widetilde{\beta}\,\beta}_{3,\boldsymbol{p}',\boldsymbol{q}}(x_4', y_4, r_4)\,, \tag{4.26}$$

to achieve a single three-point function object for given source, sink, and operator timeslices as well as requested sink momentum $\boldsymbol{p}'$ and momentum transfer $\boldsymbol{q}$. This task is quite expensive in terms of computer time so we decided to store already stripped results in a distributed database (DB) provided by the NoSQL Apache Cassandra environment [220]. If the data is requested a second time we skip the steps shown above and instantly get the data from the DB which drastically speeds up computations. More precisely, this workflow is designed to complete tasks that otherwise would take at least several hours in just a few seconds, corresponding timings are shown in [207].

For the sake of completeness, we want to mention that there are of course alternative approaches in terms of analysis software. A new, promising example is, e.g., the Grid Python Toolkit (GPT) [221] that is being (co-)developed by our group at the time of this work. However, to our knowledge the three-point function computation using stochastic estimates and the factorization (4.19) was not implemented by other groups so far.

At this point we want to sum up the work of our group by providing two numbers: Till the submission of this thesis we generated 1.8 PB of connected three-point function data using LHA and overall we wrote more than 50.000 lines of code to accomplish these simulations. A detailed introduction, including example code and documentation, of the individual software layers presented in Fig. 4.2.3 can be found in chapter 5 of [207]. Further projects using the software stack and data

presented in this section are, e.g, [201, 222, 223], and other upcoming projects, e.g., the computation of vector form factors for the nucleon, are still in progress.

Besides the contributions of connected three-point functions, we also need disconnected contributions. In the next section we will briefly motivate the underlying diagrams and introduce the computation procedure before we come to the actual results.

4.2.5 Disconnected three-point functions using stochastic estimators

In addition to the connected contributions of the three-point function, which we treated in Section 4.2.3, we also compute the disconnected contributions illustrated in Fig. 4.2.2b. The corresponding Wick contraction reads

$$\begin{aligned}\delta_{a'b'}\,\delta_{\widetilde{a}\widetilde{b}}\,\delta_{ba}\,\Gamma_{\text{snk}}^{\alpha'\beta'}\,\Gamma_{\text{ins}}^{\widetilde{\alpha}\widetilde{\beta}}\,\Gamma_{\text{src}}^{\beta\alpha}\,\Big\langle \overline{q}_{f_1}(x')_{a'}^{\alpha'}\;\overline{q_{f_2}(x')_{b'}^{\beta'}\;\overline{q}_{f_3}(y)_{\widetilde{a}}^{\widetilde{\alpha}}}\;q_{f_4}(y)_{\widetilde{b}}^{\widetilde{\beta}}}\;\overline{q}_{f_6}(r)_{b}^{\beta}\;\overline{q_{f_5}(r)_{a}^{\alpha}}\Big\rangle_c \\ = \delta_{a'b'}\,\delta_{\widetilde{a}\widetilde{b}}\,\delta_{ba}\,\Gamma_{\text{snk}}^{\alpha'\beta'}\,\Gamma_{\text{ins}}^{\widetilde{\alpha}\widetilde{\beta}}\,\Gamma_{\text{src}}^{\beta\alpha}\;G_{f_1}(r,x')_{aa'}^{\alpha\alpha'}\;G_{f_2}(x',r)_{b'b}^{\beta'\beta}\;L_{f_3}(y,y)_{\widetilde{b}\widetilde{a}}^{\widetilde{\beta}\widetilde{\alpha}}\,,\end{aligned} \tag{4.27}$$

where we denote the quark propagator connecting the space-time points y to themselves by L_{f_3}. Using the two-point function definition given in Section 4.2.1 we can rewrite the disconnected contribution by the product of a two-point function with the disconnected loop $\mathcal{L}_{\boldsymbol{q}}^{\Gamma_{\text{ins}}}(y_4)$ [224], which reads

$$C_{3,\boldsymbol{p}',\boldsymbol{q}}(x_4',y_4,r_4)\,a^{-6} = \Big\langle C_2(x_4',r_4)\mathcal{L}_{\boldsymbol{q}}^{\Gamma_{\text{ins}}}(y_4)\Big\rangle_{\text{c}} - \Big\langle C_2(x_4',r_4)\Big\rangle_{\text{c}}\Big\langle \mathcal{L}_{\boldsymbol{q}}^{\Gamma_{\text{ins}}}(y_4)\Big\rangle_{\text{c}}\,, \tag{4.28}$$

where $\langle\dots\rangle_{\text{c}}$ makes the configuration average explicit. The loop is given by

$$\mathcal{L}_{\boldsymbol{q}}^{\Gamma_{\text{ins}}}(y_4) = \sum_{\boldsymbol{y}}\; e^{i\boldsymbol{q}\cdot\boldsymbol{y}}\,\text{tr}[L_{f_3}(y,y)\Gamma_{\text{ins}}]\,, \tag{4.29}$$

where $\boldsymbol{q}$ denotes the momentum transfer in the non-forward case. Note that the dependence on the final momentum $\boldsymbol{p}'$ is contained in the definition of the two-point function.

Analogous to Section 4.2.3 the computation of (4.29) involves a very large matrix that is prohibitively expensive to compute exactly and therefore is estimated by stochastic methods. Detailed information about the estimation used in our simulations can be found in [225] and an application is shown, e.g., in [202]. In the following, we will compile the information presented in the cited literature which is also relevant for our analysis code [226]. Similar to (4.16) we estimate

the propagator using complex $\mathbb{Z}_2$ noise vectors, cf. Appendix A.9, to reduce the $\mathcal{O}(12V \times 12V)$ problem to a $\mathcal{O}(N \times 12V)$ problem in terms of computer time and memory. The number of noise vectors is tuned such that the statistical error arising from the Monte Carlo simulation is larger than the additional uncertainty introduced by the stochastic estimation. Furthermore, we use three different techniques to reduce the stochastic noise at given computational cost (i.e., without increasing the number of stochastic estimates):

1. time partitioned sources (also known as diluted sources),

2. the hopping parameter expansion (HPE),

3. the truncated solver method (TSM).

Since time dilution [227–229] plays a minor part in the data used in this thesis we will not go into further details. The HPE was already introduced in Section 2.3.3 and can be used to eliminate some of the noise contributions by exploiting the locality of the action [230, 231]. In particular, we expand the trace given in (4.29) in terms of the hopping parameter κ, cf. (2.55), as

$$\mathrm{tr}[L\Gamma_{\mathrm{ins}}] = \sum_{i=0}^{n-1} \kappa^i \ \mathrm{tr}\Big[H^i\Gamma_{\mathrm{ins}}\Big] + \kappa^n \ \mathrm{tr}[H^n\Gamma_{\mathrm{ins}}] \ , \tag{4.30}$$

where we have split the terms on the right-hand side into two parts. The first part contains n contributions with $\mathrm{tr}[H^i\Gamma_{\mathrm{ins}}] = 0$ while the remainder corresponds to the first non-vanishing term of the expansion. In general n depends on Γ_{ins}, however, for all insertion currents analyzed in this work we find $n = 3$. A more in-depth analysis of (4.16) gives rise to stochastic noise with larger amplitudes from terms close to the diagonal arising from the first sum in (4.30). Instead of increasing the number of stochastic estimates to handle these contributions we follow, e.g., [202], and apply the Dirac operator n times to the solution to achieve an improved estimate of the trace.

In the last step we use the TSM [232], where we exploit that the numerical solvers converge to correct results, within an accuracy of the size of the stochastic error, already for a small number of iterations [233]. We can utilize this behavior in practical simulations and relax the requirement on the residual when solving for stochastic sources. However, this introduces a systematic bias, at least at the level of configuration averages used in the analysis of complete ensembles. To overcome this issue we reassemble the propagator estimation by two uncorrelated estimates

given by

$$L(y,y) \approx \frac{1}{N_1}\sum_{i=1}^{N_1} s_{i,(n_t)}(y)\ \eta_i^*(y) + \frac{1}{N_2}\sum_{i=N_1+1}^{N_1+N_2}\Big[s_i(y) - s_{i,(n_t)}(y)\Big]\eta_i^*(y)\,, \qquad (4.31)$$

where (n_t) labels the number of solver iterations. Note that omitting (n_t), i.e., using only solves within numerical accuracy, restores (4.16). Although (4.31) is an approximation the decomposition on the right-hand side is exact and the algorithms used to solve both parts are well defined. Now we use the fact that the terms for $i \leq N_1$ and $N_1 < i \leq N_2$ are uncorrelated and thus we are able to reconstruct an unbiased estimate. Ideally one simulates a large number $N_1 \gg N_2$ of cheap estimates for a small number of solver iterations and finally corrects the results by a small number N_2 of expensive solves to machine precision. A detailed discussion of the parameter tuning can be found in [225]. In principle, the TSM is comparable to the HPE if one would estimate the first term in (4.30) with many sources and the second, more expensive, term by a smaller number of sources. However, on the one hand, modern iterative solvers converge much fast than the HPE and on the other hand, the TSM does not depend on the locality of the action.

The methods presented above can easily be combined as shown in [225] and even more technical details can be found by directly studying the code [226]. In actual simulations we use the already implemented methods with a small subtlety. Instead of truncating the number of solver iterations n_t in (4.31) we compute the corresponding residuals for ~ 10 randomly chosen configurations of the ensemble of interest using $n_t = 7$. From this range of residue we finally choose the maximum value which is used as cut-off instead of n_t in the simulation of the complete ensemble. This strategy is more robust for less well conditioned Dirac matrices compared to a simple n_t cut-off. The final analysis data is then stored in HDF5 files analogous to Appendix A.10 and further processed using python packages implemented by our group [234, 235][10] to extract physical results.

4.2.6 Ratios of correlation functions

Instead of performing a fit to three-point functions, one can equivalently fit to ratios of two- and three-point functions. As discussed in [201], this can be advantageous due to the cancellation of unwanted correlations between two- and three-point functions. Furthermore, the ratio can be chosen such that contributions from the ground-state directly correspond to the matrix element we are

[10]The main author of these packages is T. Wurm. Additional features were implemented by D. Jenkins and M. Löffler.

interested in. For pseudoscalar correlation functions we define

$$R_{\boldsymbol{p}} = \frac{C_{3,\boldsymbol{p},t,\tau}}{C_{2,\boldsymbol{p},t}} \xrightarrow{t\gg\tau\gg 0} \frac{\langle \boldsymbol{p}|\, \mathcal{O}\, |\boldsymbol{p}\rangle}{2E^{\pi}_{\boldsymbol{p}}}\,, \tag{4.32}$$

which holds for any operator insertion $\mathcal{O}$ in the three-point function.

For the vector meson case we will consider the diagonal case with the same Lorentz indices at the sink and at the source, i.e., $\mu = \nu = i$ in (4.2) and (4.3). Defining

$$J^{\boldsymbol{p}}_{\lambda'\lambda} \equiv \frac{\langle \boldsymbol{p},\lambda'|\, \mathcal{O}\, |\boldsymbol{p},\lambda\rangle}{2E^{\rho}_{\boldsymbol{p}}}\,, \tag{4.33}$$

one obtains

$$R^{i}_{\boldsymbol{p}} = \frac{C^{ii}_{3,\boldsymbol{p},t,\tau}}{C^{ii}_{2,\boldsymbol{p},t}} \xrightarrow{t\gg\tau\gg 0} \frac{m_\rho^2}{(E^{\rho}_{\boldsymbol{p}})^2} \sum_{\lambda,\lambda'} \epsilon^{i}(\boldsymbol{p},\lambda')\epsilon^{i*}(\boldsymbol{p},\lambda) J^{\boldsymbol{p}}_{\lambda'\lambda}\,, \tag{4.34}$$

where i is fixed (no summation). On the right-hand side a sum over multiple matrix elements occurs, which can be evaluated explicitly for the chosen three-momentum. Let us now consider the case of on-axis momenta $\hat{\boldsymbol{p}} = \pm\boldsymbol{e}_i$. Evaluating the sums one finds

$$\begin{aligned}
&\underline{\hat{\boldsymbol{p}} = \pm\boldsymbol{e}_1:}\\
&\qquad R^1_{\boldsymbol{p}} = J^{\boldsymbol{p}}_{00}\,,\\
&\qquad R^2_{\boldsymbol{p}} = \frac{1}{2}\Big(J^{\boldsymbol{p}}_{++} + J^{\boldsymbol{p}}_{--}\Big) - \frac{1}{2}\Big(J^{\boldsymbol{p}}_{+-} + J^{\boldsymbol{p}}_{-+}\Big)\,,\\
&\qquad R^3_{\boldsymbol{p}} = \frac{1}{2}\Big(J^{\boldsymbol{p}}_{++} + J^{\boldsymbol{p}}_{--}\Big) + \frac{1}{2}\Big(J^{\boldsymbol{p}}_{+-} + J^{\boldsymbol{p}}_{-+}\Big)\,,
\end{aligned} \tag{4.35}$$

etc., which can be written in a more compact form for the polarization conserving cases:

$$\begin{aligned}
&\underline{\hat{\boldsymbol{p}} = \pm\boldsymbol{e}_i:}\\
&\qquad J^{\boldsymbol{p}}_{00} = R^i_{\boldsymbol{p}}\,, \qquad\qquad J^{\boldsymbol{p}}_{++} + J^{\boldsymbol{p}}_{--} = \sum_{j\neq i} R^j_{\boldsymbol{p}} + R^j_{\boldsymbol{p}}\,.
\end{aligned} \tag{4.36}$$

However, as a final remark, we want to add that for the case of on-axis momenta the decomposition into irreducible representations is particularly simple, as we will see in Section 4.3.

4.3 Resonance character of the rho meson

Considering an infinite volume a continuum of states would contribute to the spectral decomposition above the particle creation threshold[11]. For the computations presented in this work this especially affects the decomposition (4.9), where a continuum of two pion states would contribute above the $2m_\pi$ threshold. For the special case of non-interacting particles the center of mass energies of two pions with momenta $-\boldsymbol{k}$ and $\boldsymbol{k}$ are given by

$$E_{\mathrm{cm}}^2 = 4\left(m_\pi^2 + \boldsymbol{k}^2\right) , \tag{4.37}$$

measured in the center of mass frame. However, in a finite volume, as used in our computations, momenta are quantized such that a discrete set of states contributes.

At non-zero total three-momentum $\boldsymbol{p}$ the energies of the two-pion states are given by

$$E = \sqrt{m_\pi^2 + \boldsymbol{p}_1^2} + \sqrt{m_\pi^2 + \boldsymbol{p}_2^2} , \tag{4.38}$$

$$\Rightarrow E_{\mathrm{cm}} = \sqrt{\left(\sqrt{m_\pi^2 + \boldsymbol{p}_1^2} + \sqrt{m_\pi^2 + \boldsymbol{p}_2^2}\right)^2 - \boldsymbol{p}^2} , \tag{4.39}$$

where $\boldsymbol{p}_1 + \boldsymbol{p}_2 = \boldsymbol{p}$, and $\boldsymbol{p}_1$ and $\boldsymbol{p}_2$ are again quantized in a finite volume. This means, that for each value of $\boldsymbol{p}$ a different set of states with different center of mass energies will contribute. Hence, despite the fact that the dispersion relation holds for each individual state, any ansatz that enforces the dispersion relation and assumes that the states contribute for all values of total momentum $\boldsymbol{p}$, cannot describe the contribution of the two-pion states properly.

The rest frame and the laboratory frame are related by a Lorentz boost

$$\Lambda = \begin{pmatrix} \gamma & \gamma\boldsymbol{\beta}^T \\ \gamma\boldsymbol{\beta} & \Lambda_3 \end{pmatrix} , \qquad \text{with} \qquad \Lambda_3^{ij} = \delta^{ij} + (\gamma - 1)\frac{\beta^i\beta^j}{\beta^2} , \tag{4.40}$$

where the velocity is given by $\boldsymbol{\beta} = \boldsymbol{p}/E = \boldsymbol{p}/\sqrt{E_{\mathrm{cm}}^2 + \boldsymbol{p}^2}$ and $\gamma = 1/\sqrt{1-\beta^2}$. To relate the difference between the pion three-momenta in the laboratory frame, $\boldsymbol{p}_1$ and $\boldsymbol{p}_2$, to the three-momenta in the center of mass frame one only needs the

[11] The insights presented in this section were elaborated in close collaboration with P. Wein. Especially all the figures shown in this section were initially created by P. Wein and refined by M. Löffler. All input parameters were provided by M. Löffler.

$\boldsymbol{d}^2$	LG($\boldsymbol{p}$)	Γ
0	O_h	T1u
1	C_{4v}	A1 $\oplus$ E
2	C_{2v}	A1 $\oplus$ B1 $\oplus$ B2
3	C_{3v}	A1 $\oplus$ E
4	C_{4v}	A1 $\oplus$ E

(a) Little groups and decomposition.

$\boldsymbol{d}^2$	Γ	$\phi_\Gamma^{\boldsymbol{d}}$
0	T1u	$w_{0,0} - w_{2,0} - \sqrt{6}w_{2,2}$
1	A1	$w_{0,0} + 2w_{2,0}$
1	E	$w_{0,0} - w_{2,0}$
...	...	...

(b) Scattering phase shifts.

Table 4.3.1: (a) Little groups and decomposition of angular momentum 1 in irreducible representations for all momentum sectors $\boldsymbol{d}^2 \leq 4$, where $\boldsymbol{p} = \frac{2\pi}{L}\boldsymbol{d}$. The groups are isomorphic for each representative of a sector. Table taken from [238]. **(b)** Scattering phase shifts (assuming that only the P-wave contributes) for momentum sectors $\boldsymbol{d}^2$ and irreducible representations Γ. See [236, 238] for more details. Table taken from [148].

spatial part of a Lorentz boost matrix, because

$$\frac{1}{2}(p_1 - p_2)\bigg|_{\text{cm}} = \begin{pmatrix} 0 \\ \boldsymbol{k} \end{pmatrix} \quad \Rightarrow \quad \frac{1}{2}(\boldsymbol{p}_1 - \boldsymbol{p}_2) = \Lambda_3 \boldsymbol{k} \quad \Rightarrow \quad \boldsymbol{k} = \Lambda_3^{-1}\frac{1}{2}(\boldsymbol{p}_1 - \boldsymbol{p}_2)\,. \tag{4.41}$$

Using $\boldsymbol{p} = \frac{2\pi}{L}\boldsymbol{d}$ and $\boldsymbol{p}_i = \frac{2\pi}{L}\boldsymbol{d}_i$, where on a torus $\boldsymbol{d}$, $\boldsymbol{d}_1$, $\boldsymbol{d}_2 \in \mathbb{Z}^3$, one obtains the quantization condition for k at a given value for $\boldsymbol{p}$ after replacing $\boldsymbol{p}_2 = \boldsymbol{p} - \boldsymbol{p}_1$. It reads

$$\frac{L\boldsymbol{k}}{2\pi} \in \Gamma_{\boldsymbol{d}}\,, \qquad \text{with} \qquad \Gamma_{\boldsymbol{d}} = \left\{ \boldsymbol{z} \,\middle|\, \boldsymbol{z} = \Lambda_3^{-1}\big(\boldsymbol{n} - \boldsymbol{d}/2\big)\,, \boldsymbol{n} \in \mathbb{Z}^3 \right\}. \tag{4.42}$$

Considering particles of integer spin in the center of mass frame, i.e., at zero momentum, the full symmetry group in terms of LQCD is the octahedral group $O_h = O \otimes I$ defined as the direct product of the cubic group O (consisting of 24 rotations) and the group of space inversions I. For particles of half-integer spin the corresponding double covers of O and O_h have to be taken into account. However, as shown in, e.g., [236–238], the symmetry in a moving frame is reduced to the so-called little groups, cf. Tab. 4.3.1a, together with a decomposition into irreducible representations for the P-wave ($l = 1$).

The latter is relevant because not all combinations of pion momenta $\boldsymbol{p}_1$ and $\boldsymbol{p}_2$ that are possible for a given value of $\boldsymbol{p}$ do contribute to all irreducible representations, which leads to "missing" energy levels in some cases. A list of momentum combinations leading to the lowest possible two pion energy levels (for the case $l = 1$) in each representation has been given in [238], and is reproduced in Tab. 4.3.2. Plugging these momentum combinations into (4.38) and (4.39) one obtains the corresponding energy levels and center of mass energies shown in Fig. 4.3.1, where we use the parameters of the CLS ensemble D200 ($N_s \times N_t = 64 \times 128, m_\pi = 201\,\text{MeV}, m_\rho = 746\,\text{MeV}$).

How to connect infinite volume phase shifts with the finite volume energy spectrum is shown in [239, 240] while further, recent discussions can be found in [236–238]. However, since we are only interested in the rho resonance in the vector channel it is sufficient to only consider P-wave ($l = 1$) contributions. It was shown in, e.g., [241, 242], that nonzero phase shifts in higher odd partial waves are usually not required to describe the two pion spectrum. In this situation it is possible to directly relate the P-wave phase shift δ_1 to the quantized two pion energy levels in finite volumes by the condition

$$\cot \delta_1 \stackrel{!}{=} \cot \phi_\Gamma^{\boldsymbol{d}} \,. \tag{4.43}$$

The scattering phase shifts $\phi_\Gamma^{\boldsymbol{d}}$, for the momentum sectors $\boldsymbol{d}^2 \leq 1$ we are interested in, can be taken from Tab. 4.3.1b. For explicit computations we use the definitions

$$w_{lm} = \frac{Z_{lm}^{\boldsymbol{d}}(1, q^2)}{\pi^{3/2}\sqrt{2l+1}\,\gamma\, q^{l+1}}\,, \qquad q = \frac{Lk}{2\pi}\,, \qquad k = \sqrt{\frac{E_{\mathrm{cm}}^2}{4} - m_\pi^2}\,, \tag{4.44}$$

where $Z_{lm}^{\boldsymbol{d}}(1, q^2)$ is a generalized form of the zeta function. One possible representation of $Z_{lm}^{\boldsymbol{d}}(1, q^2)$, which we use for numerical evaluations, is given in [236] and reads

$$\begin{aligned} Z_{lm}^{\boldsymbol{d}}(1, q^2) = &\sum_{\boldsymbol{z} \in \Gamma_{\boldsymbol{d}}} \frac{\mathcal{Y}_{lm}(\boldsymbol{z})}{\boldsymbol{z}^2 - q^2}\, e^{-(\boldsymbol{z}^2 - q^2)} + \gamma\, \frac{\pi}{2}\, \delta_{l0}\, \delta_{m0} \sum_{n=0}^{\infty} \frac{q^{2n}}{(n - 1/2)\, n!} \\ &+ \gamma \pi^{3/2} \int_0^1 dt\, \frac{e^{tq^2}}{t^{3/2}} \left(\frac{i}{2t}\right)^l \sum_{\substack{\boldsymbol{n} \in \mathbb{Z}^3 \\ \boldsymbol{n} \neq 0}} e^{-i\pi \boldsymbol{d} \cdot \boldsymbol{n}}\, \mathcal{Y}_{lm}(2\pi \Lambda_3 \boldsymbol{n})\, e^{-(\pi \Lambda_3 \boldsymbol{n})^2 / t}\,, \end{aligned} \tag{4.45}$$

with

$$\mathcal{Y}_{lm}(\boldsymbol{r}) = r^l Y_{lm}(\theta, \phi)\,, \tag{4.46}$$

where $Y_{lm}(\theta, \phi)$ are spherical harmonics.

To finally obtain the energy levels in the interacting case we use (4.43) and equate the phase shifts $\phi_\Gamma^{\boldsymbol{d}}$ with a phenomenological parametrization. Following [243] we first define the rho mass and width for any given parametrization by

$$\begin{aligned} &\cot \delta_1 \Big|_{s = m_\rho^2} = 0, \\ &m_\rho \Gamma_\rho = \left(\frac{d\delta_1}{ds}\right)^{-1}_{s = m_\rho^2} = -\left(\frac{d \cot \delta_1}{ds}\right)^{-1}_{s = m_\rho^2} = \frac{-k_\rho^3}{m_\rho} \left(\frac{d \frac{k^3}{\sqrt{s}} \cot \delta_1}{ds}\right)^{-1}_{s = m_\rho^2}, \end{aligned} \tag{4.47}$$

$\boldsymbol{d}$	Γ	$\boldsymbol{d}_1 \otimes \boldsymbol{d}_2$
$(0,0,0)$	T1u	$(0,0,1) \otimes (0,0,-1)$, $(1,0,1) \otimes (-1,0,-1)$
$(0,0,1)$	A1	$(0,0,1) \otimes (0,0,0)$, $(0,0,2) \otimes (0,0,-1)$, $(1,0,1) \otimes (-1,0,0)$, $(1,1,1) \otimes (-1,-1,0)$
$(0,0,1)$	E	$(0,1,1) \otimes (0,-1,0)$, $(1,1,1) \otimes (-1,-1,0)$
$(1,1,0)$	A1	$(1,1,0) \otimes (0,0,0)$, $(1,1,1) \otimes (0,0,-1)$, $(1,-1,0) \otimes (0,2,0)$
$(1,1,0)$	B1	$(1,1,1) \otimes (0,0,-1)$, $(1,0,1) \otimes (0,1,-1)$
$(1,1,0)$	B2	$(1,0,0) \otimes (0,1,0)$, $(1,0,1) \otimes (0,1,-1)$, $(2,0,0) \otimes (-1,1,0)$
$(1,1,1)$	A1	$(1,1,1) \otimes (0,0,0)$, $(1,0,1) \otimes (0,1,0)$, $(2,0,0) \otimes (-1,1,1)$
$(1,1,1)$	E	$(1,0,1) \otimes (0,1,0)$, $(1,-1,1) \otimes (0,2,0)$
$(0,0,2)$	A1	$(0,0,2) \otimes (0,0,0)$
$(0,0,2)$	E	$(0,1,1) \otimes (0,-1,1)$

Table 4.3.2: Combinations $\boldsymbol{d}_1 \otimes \boldsymbol{d}_2$ (where the momenta are given by $\boldsymbol{p}_i = \frac{2\pi}{L}\boldsymbol{d}_i$) that yield the lowest pion energy levels in each representation. Only one representative total momentum $\boldsymbol{p} = \frac{2\pi}{L}\boldsymbol{d}$ is given for each momentum sector. The momentum combinations depend on the irreducible representation Γ because not all combinations couple to all irreducible representations. Furthermore, the shift of the energy levels due to interactions can be different for each representation. This Table is taken from ref. [238].

using the Mandelstam variable $s = E_{\rm cm}^2$. Subsequently we use two different parametrizations, namely

- the Breit-Wigner (BW) ansatz,
- the Gounarius-Sakurai (GS) parametrization [243],

to extract the phase shifts $\delta_1^{\rm BW}$ and $\delta_1^{\rm GS}$. Using a relativistic BW ansatz this reads

$$\frac{k^3}{\sqrt{s}}\cot\delta_1^{\rm BW} = \frac{6\pi\left(m_\rho^2 - s\right)}{g_{\rho\pi\pi}^2} = \frac{k_\rho^3\left(m_\rho^2 - s\right)}{\Gamma_\rho m_\rho^2}, \qquad \text{with} \quad \Gamma_\rho = \frac{g_{\rho\pi\pi}^2 k_\rho^3}{6\pi m_\rho^2}, \tag{4.48}$$

where $k = \sqrt{s/4 - m_\pi^2}$, as defined in (4.44), and

$$k_\rho = k\Big|_{s=m_\rho^2} = \sqrt{m_\rho^2/4 - m_\pi^2}\,. \tag{4.49}$$

The alternative GS parametrization yields

$$\frac{k^3}{\sqrt{s}}\cot\delta_1^{\rm GS} = k^2 h(s) + a + bk^2\,, \quad \text{with} \quad h(s) = \frac{2}{\pi}\frac{k}{\sqrt{s}}\ln\left(\frac{\sqrt{s}+2k}{2m_\pi}\right). \tag{4.50}$$

To further simplify (4.50) we compute the contributions a and b via

$$\begin{aligned} 0 &= k_\rho^2\Big(h(m_\rho^2) + b\Big) + a \qquad &\Rightarrow \quad & a = -k_\rho^2(b + h(m_\rho^2)), \\ \frac{-k_\rho^3}{m_\rho^2\Gamma_\rho} &= \frac{h(m_\rho^2)+b}{4} + k_\rho^2 h'(m_\rho^2) \qquad &\Rightarrow \quad & b = -h(m_\rho^2) - \frac{4k_\rho^3}{m_\rho^2\Gamma_\rho} - 4k_\rho^2 h'(m_\rho^2), \\ & & & a = k_\rho^2\left(\frac{4k_\rho^3}{m_\rho^2\Gamma_\rho} + 4k_\rho^2 h'(m_\rho^2)\right), \end{aligned} \tag{4.51}$$

to finally obtain

$$\begin{aligned} &\frac{k^3}{\sqrt{s}}\cot\delta_1^{\rm GS} = k^2(h(s) - h(m_\rho^2)) + (k_\rho^2 - k^2)c\,, \\ &\text{with} \quad c = \frac{4k_\rho^3}{m_\rho^2\Gamma_\rho} + 4k_\rho^2 h'(m_\rho^2) = \frac{4k_\rho^3}{m_\rho^2\Gamma_\rho} + \frac{4k_\rho^2}{\pi m_\rho^2}\left(1 + \frac{m_\pi^2}{m_\rho k_\rho}\ln\left(\frac{m_\rho + 2k_\rho}{2m_\pi}\right)\right). \end{aligned} \tag{4.52}$$

Note that we can measure the value of F_π on each of our lattices. Therefore, we can apply the Kawarabayashi-Suzuki-Riazuddin-Fayyazuddin relation [244, 245], $m_\rho^2 = 2g_{\rho\pi\pi}^2 F_\pi^2$, (which, as argued in ref. [246], is a consequence of chiral symmetry and the requirement of renormalizability for the EFT) such that both the BW and the GS parametrizations are determined solely by the rho mass (given that the pion decay constant F_π is well-known and the width of the rho is linked to the rho-pi-pi coupling constant $g_{\rho\pi\pi}$ via (4.48)).

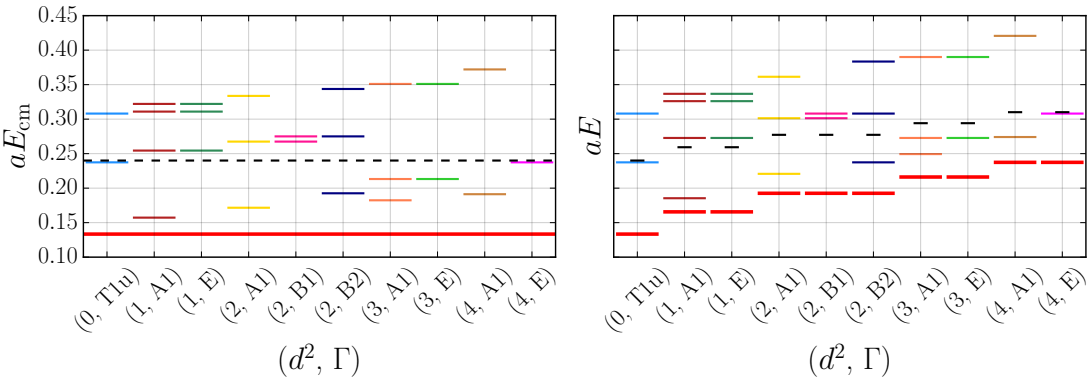

Figure 4.3.1: Center of mass energies E_{cm} and energies E of the two pion states that contribute at different total momenta $\boldsymbol{p} = \frac{2\pi}{L}\boldsymbol{d}$ and irreducible representations Γ. Here we have used the volume and the pion mass for D200. The red line corresponds to the two-pion threshold in the continuum. The black dashed lines correspond to the rho mass we have extracted on this ensemble.

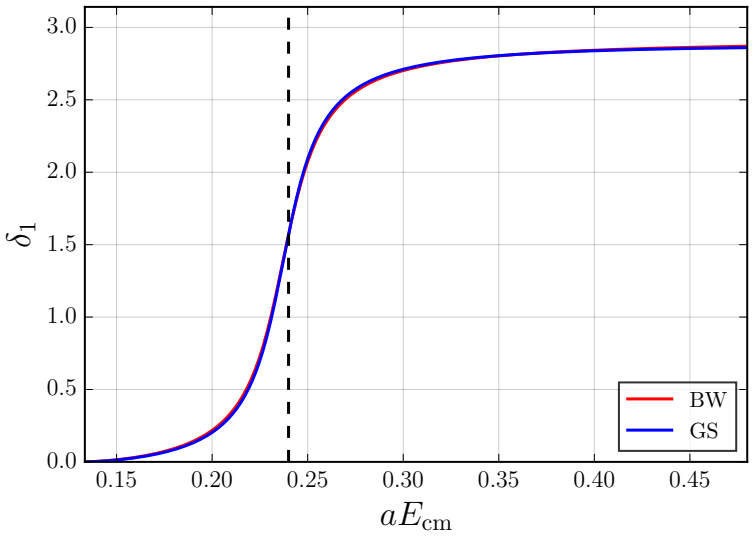

Figure 4.3.2: Comparison of the BW (red) and GS (blue) phase shift parametrizations. We again use the D200 input parameters including the naively measured rho mass. The rho-pi-pi coupling constant is set to the phenomenological value $g_{\rho\pi\pi} = 5.96$. Figure taken from [148].

A comparison of the BW and GS phase shifts for the P-wave are shown in Fig. 4.3.2 where we again use the parameters of the CLS gauge ensemble D200 as input. As one can see the two different parametrizations agree very well and lie almost on top of each other. The same holds for the presentation shown in Fig. 4.3.3 where we show $\cot\delta_1$ as a function of the center of mass energy. In addition we illustrate the quantization condition (4.43). The corresponding energy levels are situated at the intersections between the BW and GS parametrizations and the curves for $\cot\phi^{\boldsymbol{d}}_{\Gamma}$. The positions of the poles correspond to E_{cm} of the non-interacting system.

It was shown in [243], that the phase shifts are linked to the pion form factor via

$$F_\pi(s) = \frac{f(0)}{f(s)}, \qquad \text{with} \quad f(s) = \frac{k^3}{\sqrt{s}} \left(\cot \delta_1 - i\right). \tag{4.53}$$

Obviously this relation holds only in case of the GS parametrization, since $f(s)$ diverges for $s = 0$ in the BW ansatz. Thus only the GS parametrization is used in the following calculations. Using (4.52) one finds

$$F_\pi(s) = \frac{m_\pi^2 h(m_\rho^2) + \frac{c}{4} m_\rho^2 - \frac{1}{\pi} m_\pi^2}{\frac{k^3}{\sqrt{s}}\left(\cot \delta_1^{\mathrm{GS}} - i\right)}. \tag{4.54}$$

From the form factor we can derive the overlap factor of the two-pion states with a local (unsmeared) vector current using the formula derived in [247][12]

$$|F_\pi(s)|^2 = \frac{\gamma}{g(\gamma)^2}\left(q\frac{\partial \phi_\Gamma^{\boldsymbol{d}}}{\partial q} + k\frac{\partial \delta_1(k)}{\partial k}\right)\frac{3\pi s}{k^5}\ |\langle 0|\hat{\boldsymbol{b}}\cdot\boldsymbol{j}(0)|\pi\pi, n\rangle_V|^2\,,$$

$$\text{with } g(\gamma) = \begin{cases} \gamma & \text{for } \boldsymbol{b} \parallel \boldsymbol{p}\,, \\ 1 & \text{for } \boldsymbol{b} \perp \boldsymbol{p}\,, \end{cases} \tag{4.55}$$

$$\Rightarrow \quad |F_\pi(s)|^2 = \left(q\frac{\partial \phi_\Gamma^{\boldsymbol{d}}}{\partial q} + k\frac{\partial \delta_1(k)}{\partial k}\right)\frac{6\pi\sqrt{s}}{k^5} Z_{\boldsymbol{p}}^{\pi\pi}\,.$$

Inverting (4.55) finally yields the overlap factors[13]

$$\begin{aligned} Z_{\boldsymbol{p}}^{\pi\pi}(s) &= \left(q\frac{\partial \phi_\Gamma^{\boldsymbol{d}}}{\partial q} + k\frac{\partial \delta_1(k)}{\partial k}\right)^{-1}\frac{k^5}{6\pi\sqrt{s}}|F_\pi(s)|^2 \\ &\overset{s>4m_\pi^2}{=} \frac{\sqrt{s}}{6\pi k}\left(q\frac{\partial \phi_\Gamma^{\boldsymbol{d}}}{\partial q} + k\frac{\partial \delta_1(k)}{\partial k}\right)^{-1}\left|\frac{m_\pi^2 h(m_\rho^2) + \frac{c}{4} m_\rho^2 - \frac{1}{\pi} m_\pi^2}{\cot \delta_1^{\mathrm{GS}} - i}\right|^2, \end{aligned} \tag{4.56}$$

from a given form factor, which, in turn, can be determined from the phase shift.

The form factors and corresponding overlap factors with two-pion states of

[12] A generalization for moving frames of the original derivation is given in [248].

[13] The vacuum polarization (two-point function) is defined in (4.2) and can be adapted to the calculations shown here by $C^{ij}_{\boldsymbol{p},t} = \sum_H e^{-E_{H,\boldsymbol{p}}t}\frac{Z^H_{\boldsymbol{p}}}{2E_{H,\boldsymbol{p}}}\left(\delta^{ij} + \frac{p^i p^j}{E^2_{\mathrm{cm},H}}\right)$, where H denotes the hadron and $E_{H,\boldsymbol{p}} = \sqrt{E^2_{\mathrm{cm},H} + \boldsymbol{p}^2}$. The overlap factors can be different in time direction $\mu = \nu = 0$, so we only treat spatial components in our computations. Compared to [247] equation (12) we thus need an extra factor $(2E)^{-1} = (2\gamma E_{\mathrm{cm}})^{-1} = (s\gamma\sqrt{s})^{-1}$ in our computations and the kinematic factor $g(\gamma)^2$ drops out. Furthermore, our current differs by a factor of 2 compared to [247].

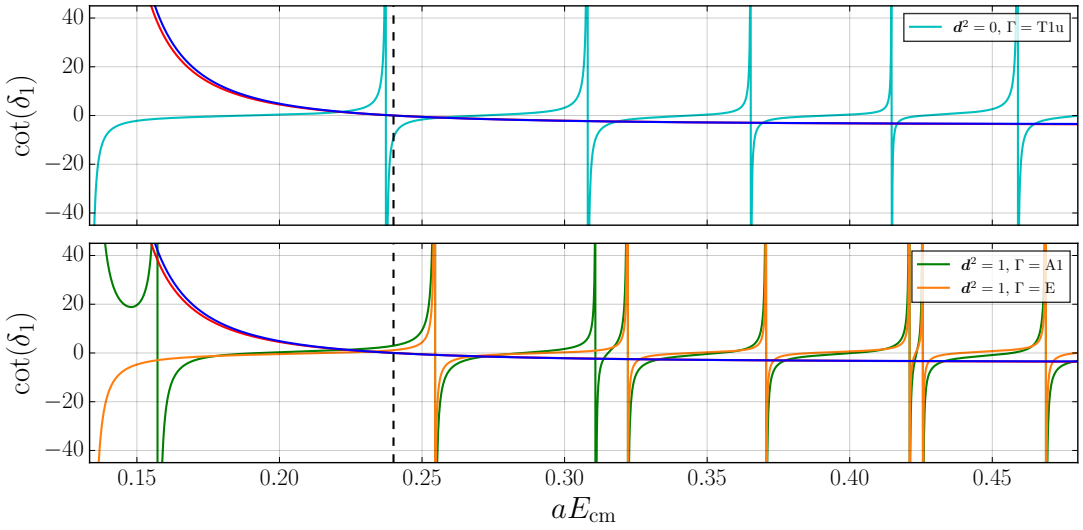

Figure 4.3.3: Illustration of (4.43). The BW (red) and GS (blue) parametrizations, cf. Fig. 4.3.2, are shown in addition to the scattering phase shifts $\phi_\Gamma^{\boldsymbol{d}}$ for different total momenta $\boldsymbol{p} = \frac{2\pi}{L}\boldsymbol{d}$ and irreducible representations Γ, calculated using the relations shown in Tab. 4.3.1b. We again use the input parameters of the CLS gauge ensembles D200. The poles occur at the positions of the noninteracting E_{cm}, while the energy levels are situated at the intersection of the curves. Figure taken from [148].

a local, i.e., unsmeared, vector current at the source and the sink are shown in Fig. 4.3.4 as a function of the center of mass energy. In the right column one immediately sees that two-pion states with $E_{\mathrm{cm}} \gg m_\rho$ (or $E_{\mathrm{cm}} \ll m_\rho$) are strongly suppressed. Comparing the top right panel of Fig. 4.3.4 to the lower right panel indicates that values computed in our example are suppressed by roughly a factor 100 compared to our estimate for the overlap of the rho meson itself, depicted by the horizontal red line in the top right panel. Thus, these states will not yield large contributions to the correlation functions at the intermediate time distances available in our simulations whilst being energetically favored. Eventually, this may explain why we do not see these states in our numerical analysis. However, the more problematic case occurs for $E_{\mathrm{cm}} \approx m_\rho$. The top right panel of Fig. 4.3.4 clearly indicates that the overlap of these states is strongly enhanced, and can be of the same size or even larger than the overlap of the rho meson. Our numerical analysis does not allow for a distinction between these two-particle contributions and the contribution of the rho meson itself in the spectral decomposition, which is particularly concerning. It is important to take this shortcoming into account when interpreting the results.

Nevertheless, in the analysis shown above, we only considered local currents and the situation might be less critical for the smeared currents that we use in our simulations. A posteriori, the trustworthiness of the numerical results presented in Section 4.8 could be enhanced significantly, if subsequent studies (e.g., by using

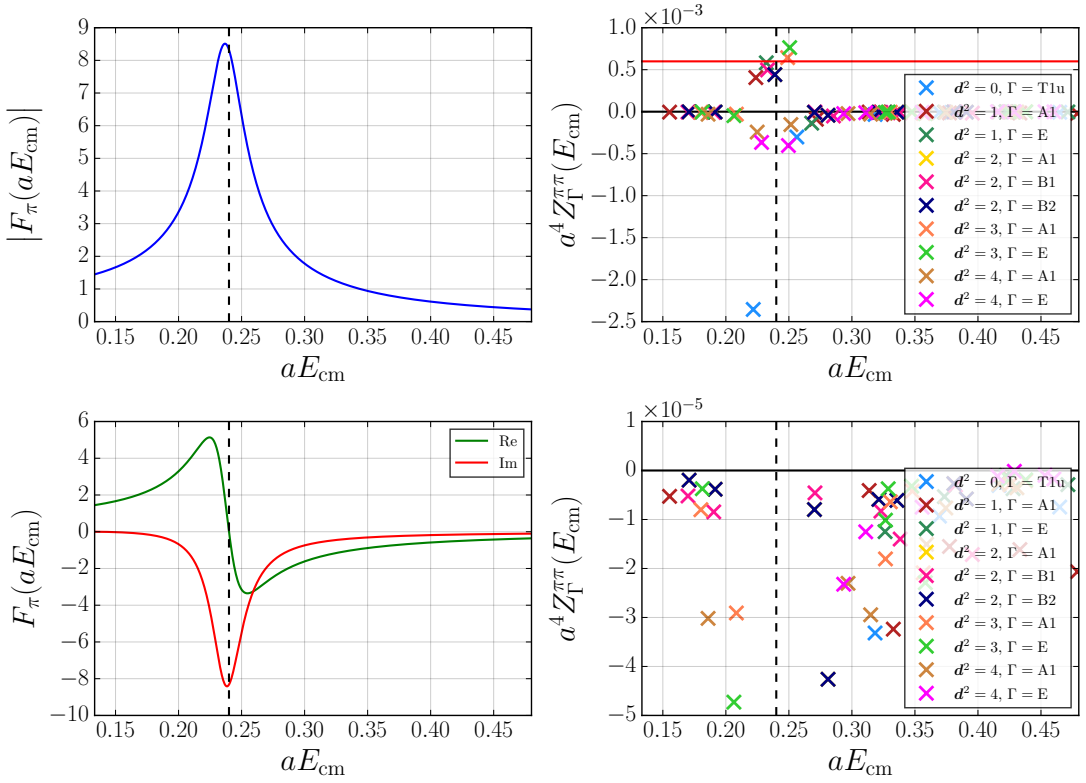

Figure 4.3.4: Left column: The pion form factor obtained using (4.55) and the corresponding overlap factors $Z_\Gamma^{\pi\pi}$ for the local currents from (4.56). Right column: The red line on the upper panel is plotted for comparison and corresponds to the estimated $Z^\rho = 2f_\rho^2 m_\rho^2$ for the local currents using the phenomenological value $f_\rho = 222\,\mathrm{MeV}$ as input. The lower panel corresponds to same values as shown at the top right but zoomed in on the y-axis. All input parameters are again taken from the CLS gauge ensemble D200 and the top row of the figure was already published in [148].

the generalized eigenvalue method with two-pion interpolating currents, cf. [237, 249–252]) can show that the overlap of smeared vector interpolating currents with the two-pion states is much smaller than for the local currents.

4.4 Pion and rho mass

To compute the reduced matrix elements introduced in Section 3.2 one has to determine the mass (energy) of the meson in the rest (boosted) frame, as an additional input parameter. While the values for m_π are taken from [127] the values for m_ρ are obtained by a direct fit to the spectral decomposition of the correlation function (4.9). Besides the mass (energy) itself two additional amplitudes (Z and A) and also the energy gap to the first excited state ΔE enter the fit as free parameters. However, using the ratio method introduced in Section 4.2.6 the additional amplitudes and also ΔE will not enter the results presented in this work.

The fits are performed using a constant fit window of $\sim$2 fm for all ensembles

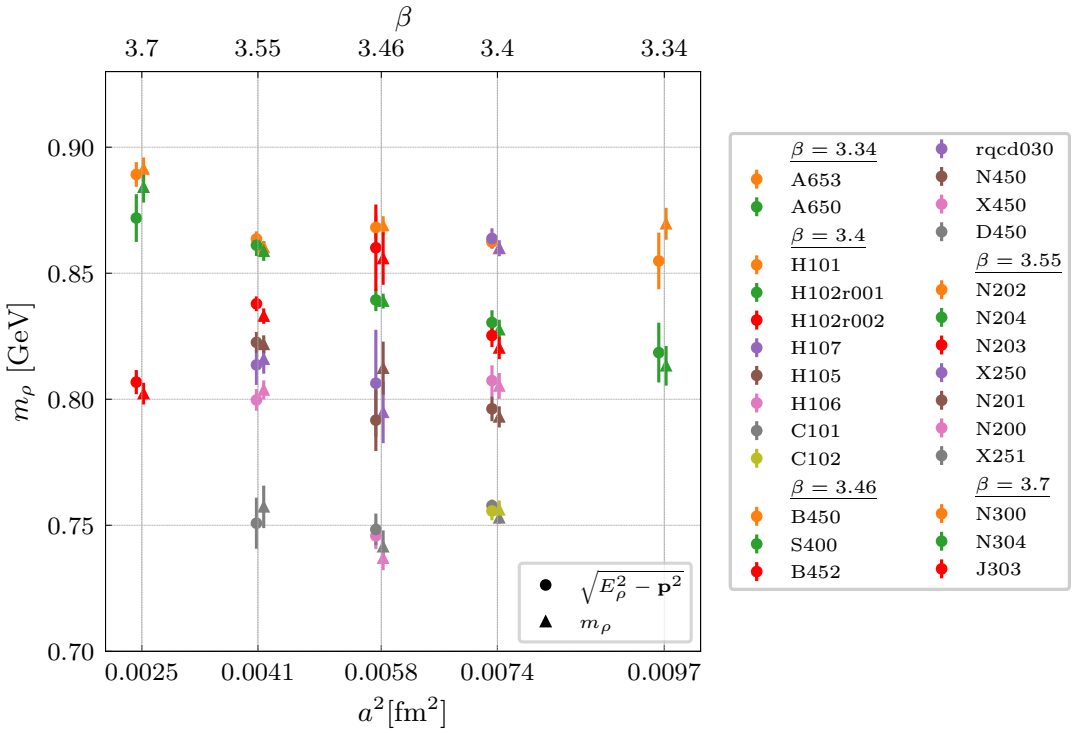

Figure 4.4.1: Rho masses for all ensembles analyzed from a double exponential fit (open boundaries) or a single exponential fit (periodic boundaries) to the two-point function correlator. The triangles depict the results in the rest frame ($\boldsymbol{p}^2 = 0$) while the circles correspond to fits in the boosted frame ($\boldsymbol{p}^2 = \frac{4\pi^2}{L^2}1$) projected to the rest frame using the continuum dispersion relation. Numerical values are shown in Tab. 4.4.1.

with open boundary conditions and we start 1 or 2 timeslices ($\sim 0.1\,\mathrm{fm}$) away from the source for the coarser or finer lattices. Due to the structure of (4.10) the values obtained by the fit for the ground-state and excited state energy can be interchanged. To overcome this technical issue we have introduced a cutoff for the double exponential fit at $t_{\mathrm{cut}} \approx 0.65\,\mathrm{fm}$ and fit only the single exponential $Z^\rho_{\boldsymbol{p}}(2E^\rho_{\boldsymbol{p}})^{-1}e^{-E^\rho_{\boldsymbol{p}}t}$ for larger times. In case of periodic boundary conditions we choose a symmetric ansatz of the form

$$C_{2,\boldsymbol{p},t} = Z^\rho_{\boldsymbol{p}}(2E^\rho_{\boldsymbol{p}})^{-1}(e^{-E^\rho_{\boldsymbol{p}}t} + e^{-E^\rho_{\boldsymbol{p}}(T-t)}) \,, \tag{4.57}$$

with $t_{\mathrm{cut}} \leq t \leq T - t_{\mathrm{cut}}$, where we only fit the amplitude and the ground-state energy. The final results of these fits are shown in Tab. 4.4.1 and Fig. 4.4.1, in the latter we depict the rest frame results by triangles and the boosted frame results by circles. Note that the continuum dispersion relation $E^\rho_{\boldsymbol{p}} = \sqrt{m_\rho^2 + \boldsymbol{p}^2}$ is used to project the energies onto their corresponding mass values and to check that the dispersion relation is well satisfied for the momenta in use.

Ens.	$\sqrt{E_\rho^2 - \boldsymbol{p}^2}$	m_ρ	Ens.	$\sqrt{E_\rho^2 - \boldsymbol{p}^2}$	m_ρ
A653	0.855 (11)	0.870 (11)	N450	0.792 (12)	0.812 (12)
A650	0.819 (12)	0.813 (12)	X450	0.746 (5)	0.737 (5)
H101	0.862 (2)	0.860 (2)	D450	0.748 (6)	0.741 (6)
H102r001	0.830 (5)	0.828 (5)	N202	0.864 (3)	0.860 (3)
H102r002	0.825 (5)	0.820 (5)	N204	0.861 (4)	0.859 (4)
H107	0.864 (4)	0.860 (4)	N203	0.838 (3)	0.833 (3)
H105	0.796 (5)	0.793 (5)	X250	0.814 (8)	0.816 (8)
H106	0.807 (6)	0.805 (6)	N201	0.823 (4)	0.822 (4)
C101	0.758 (2)	0.753 (2)	N200	0.800 (4)	0.804 (4)
C102	0.756 (4)	0.756 (4)	X251	0.751 (1)	0.757 (1)
B450	0.868 (5)	0.869 (5)	N300	0.889 (5)	0.891 (5)
S400	0.839 (4)	0.839 (4)	N304	0.872 (9)	0.884 (9)
B452	0.860 (17)	0.856 (17)	J303	0.807 (5)	0.802 (5)
rqcd030	0.806 (21)	0.795 (21)			

Table 4.4.1: Rho masses for all ensembles analyzed from a double exponential fit (open boundaries) or a single exponential fit (periodic boundaries) to the two-point function correlator. The first column denotes the ensemble identifier while the second and the third column show the results obtained from the boosted frame ($\boldsymbol{p}^2 = \frac{4\pi^2}{L^2}$) and the rest frame ($\boldsymbol{p}^2 = 0$) respectively, including the statistical error. A graphical illustration can be found in Fig. 4.4.1.

4.5 Extraction of ground-state matrix elements

In Section 4.2.5 we already remarked that three-point correlation functions can contain quark-line disconnected contributions. A common approach to circumvent this problem is the usage of isovector current insertions, e.g., used in [201], where the up and down quark disconnected loops cancel each other in the limit of exact isospin symmetry. However, in terms of the two mesons studied in this thesis, this is not a viable solution, since also the connected parts would vanish for isovector currents and all results would be identical to zero. So on the one hand, we are forced to take disconnected contributions into account, but on the other hand, these contributions lead to large statistical errors which, in principle, drastically deteriorate the quality of our results. Fortunately, we found that large statistical errors do not occur in general, see below.

Often one finds, that the signal of disconnected contributions yields results that are zero within the error and thus one might be tempted to simply drop the corresponding contributions. However, if one includes all contributions in the final results one finds that the inclusion of quark-line disconnected contributions can shift the mean and, even more importantly, can increase the error for the final results substantially. I.e., they have to be included, if one wants to provide reliable error estimates for phenomenological applications. Nevertheless, we perform a

second analysis in these cases, where we solely use the connected part, which allows us to compare to other lattice results for connected contributions.

In Section 4.2.3 and Section 4.2.5 we have introduced our implementations for the computation of connected and disconnected three-point function contributions, respectively. Both methods rely on the usage of stochastic estimators. While the connected part is computed using a setup with fixed sink timeslice, to obtain the results for all possible insertion timeslices, the disconnected part is computed using a setup with fixed loop timeslices. Using these different methods it is no longer advantageous to add the connected and disconnected contributions already at the correlation function level, i.e., we separate the statistical analysis of both contributions and add them only at the very end of our analysis. Otherwise we would have to throw away a large part of our data since we could only use disconnected contributions, where we also have corresponding connected insertion timeslices τ and final timeslices t. This would be prohibitively wasteful. Therefore, we will perform the extraction of the ground-state matrix elements separately for the connected and the disconnected contribution.

Next, we extract the ground-state contributions from the ratios defined in Section 4.2.6. To directly relate the reduced matrix elements v_2, cf. (3.29), a_2, and d_2, cf. (3.30a), with the corresponding ground-state contribution of the ratios we use appropriate kinematic prefactors and, in case of the rho, adequate linear combinations of data points. For on-axis momenta $\hat{\boldsymbol{p}} = \pm \boldsymbol{e}_i$ we obtain

$$v_2 = \frac{1}{p^i} R_{\boldsymbol{p}}\Big(\mathcal{O}^i_{\mathrm{v2a}}\Big)\,, \tag{4.58a}$$

$$a_2 = \frac{1}{3p^i} \sum_j R^j_{\boldsymbol{p}}\Big(\mathcal{O}^i_{\mathrm{v2a}}\Big)\,, \tag{4.58b}$$

$$d_2 = \frac{3}{4p^i}\Big[2R^i_{\boldsymbol{p}}\Big(\mathcal{O}^i_{\mathrm{v2a}}\Big) - \sum_{j\neq i} R^j_{\boldsymbol{p}}\Big(\mathcal{O}^i_{\mathrm{v2a}}\Big)\Big]\,, \tag{4.58c}$$

with operator $\mathcal{O}^i_{\mathrm{v2a}}$ as inserted current, and for $\mathcal{O}_{\mathrm{v2b}}$ we find

$$v_2 = \frac{3E}{4E^2 - m^2} R_{\boldsymbol{p}}\Big(\mathcal{O}_{\mathrm{v2b}}\Big)\,, \tag{4.59a}$$

$$a_2 = \frac{E}{4E^2 - m^2} \sum_j R^j_{\boldsymbol{p}}\Big(\mathcal{O}_{\mathrm{v2b}}\Big)\,, \tag{4.59b}$$

$$d_2 = \frac{3E}{8(E^2 - m^2)}\Big[2R^i_{\boldsymbol{p}}\Big(\mathcal{O}_{\mathrm{v2b}}\Big) - \sum_{j\neq i} R^j_{\boldsymbol{p}}\Big(\mathcal{O}_{\mathrm{v2b}}\Big)\Big]\,. \tag{4.59c}$$

Here we suppress the superscripts π, ρ, and the subscript $\boldsymbol{p}$ for the mass and energy. To avoid mixing as far as possible we have chosen operator combinations $\mathcal{O}^i_{\mathrm{v2a}} = \mathcal{O}^{0i}$ and $\mathcal{O}_{\mathrm{v2b}} = \frac{4}{3}\mathcal{O}^{00}$, using (3.23a), that posses a definite C-parity and

transform according to irreducible representations of H(4), cf. [154, 253]. For the case of $n = 2$, i.e., only first derivatives and thus two operator indices, the projection onto leading twist via the symmetrizing and trace-subtracting operator $\mathcal{S}$ is defined by

$$\mathcal{S}\mathcal{O}^{\mu\nu} = \mathcal{S}^{\mu\nu}_{\rho\sigma}\mathcal{O}^{\rho\sigma} = \frac{1}{2}\Big(g^\mu_\rho g^\nu_\sigma + g^\mu_\sigma g^\nu_\rho - \frac{2}{d} g^{\mu\nu} g_{\rho\sigma}\Big)\mathcal{O}^{\rho\sigma}\,. \tag{4.60}$$

Making this definition explicit in (3.29) yields

$$\langle \boldsymbol{p}|\, \mathcal{O}^i_{\text{v2a}}\, |\boldsymbol{p}\rangle = 2v_2^q\, E p^i\,, \tag{4.61a}$$

$$\langle \boldsymbol{p}|\, \mathcal{O}_{\text{v2b}}\, |\boldsymbol{p}\rangle = 2v_2^q\, \frac{4E^2 - m^2}{3}\,. \tag{4.61b}$$

for the pion and inserting (4.60) into (3.30a) yields

$$\langle \boldsymbol{p},\lambda|\, \mathcal{O}^i_{\text{v2a}}\, |\boldsymbol{p},\lambda\rangle = 2Ep^i \begin{cases} a_2^q + \frac{2}{3} d_2^q & \text{for } \lambda = 0\,, \\ a_2^q - \frac{1}{3} d_2^q & \text{for } \lambda = \pm\,, \end{cases} \tag{4.62a}$$

$$\langle \boldsymbol{p},\lambda|\mathcal{O}_{\text{v2b}}|\boldsymbol{p},\lambda\rangle = 2\Big(a_2^q - \frac{d_2^q}{3}\Big)\frac{4E^2 - m^2}{3} + 2\frac{d_2^q}{3} \begin{cases} 4E^2 - 3m^2 & \text{for } \lambda = 0\,, \\ m^2 & \text{for } \lambda = \pm\,, \end{cases} \tag{4.62b}$$

for the rho. In the actual computations we use the explicit operators

$$\mathcal{O}^i_{\text{v2a}} = O^{\{0i\}}, \qquad \text{with } i = 1,2,3, \tag{4.63}$$

$$\mathcal{O}_{\text{v2b}} = O^{00} + \frac{1}{3}\Big(O^{11} + O^{22} + O^{33}\Big), \tag{4.64}$$

with

$$O_{\mu\nu} = \frac{i}{2}\,\overline{q}\,\gamma^\mu \overleftrightarrow{D}^\nu\, q. \tag{4.65}$$

The conversion between Minkowski and Euclidean convention is finally given by

$$\mathcal{O}^{(E),i}_{\text{v2a}} = -i\,\mathcal{O}^i_{\text{v2a}}\,, \qquad \text{and} \qquad \mathcal{O}^{(E)}_{\text{v2b}} = -\mathcal{O}_{\text{v2b}}\,, \tag{4.66}$$

see [154] for details.

One immediately finds that the computation of $\mathcal{O}^i_{\text{v2a}}$ requires non-zero momentum contributions in direction i while the computation of $\mathcal{O}_{\text{v2b}}$ also gets along with vanishing three-momentum, except for the computation of d_2, which always requires finite momenta. The reason for this is that d_2 corresponds to the differ-

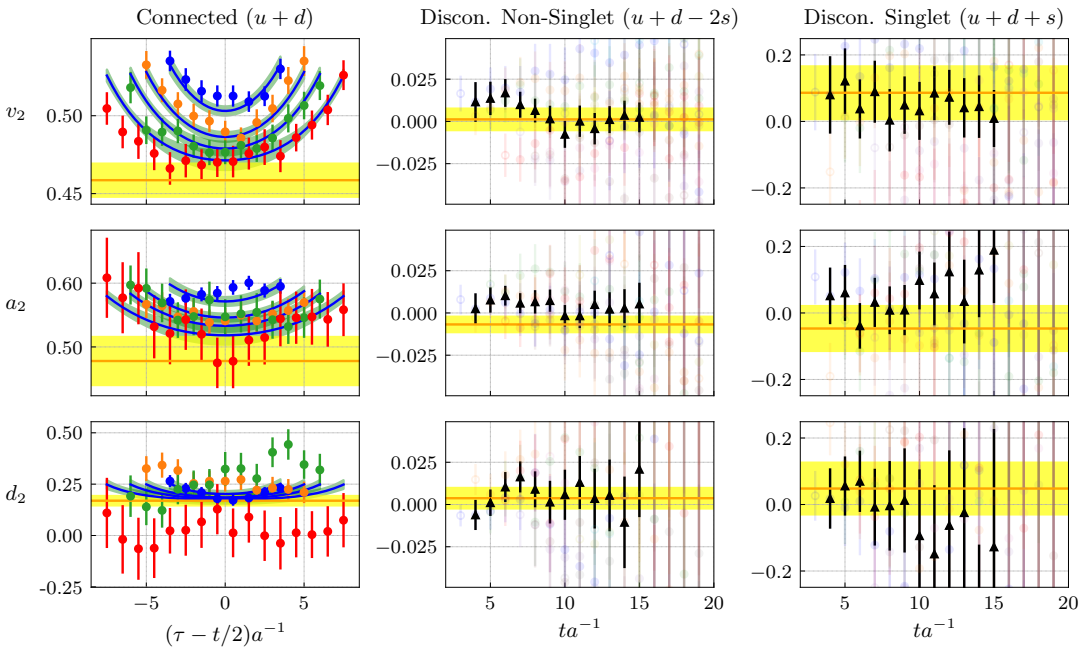

Figure 4.5.1: Extraction of renormalized values for v_2, a_2, and d_2 from the ratios obtained in (4.58a) – (4.58c) using the operator combination $\mathcal{O}_{\text{v2a}}$. For illustrative purposes we only show the data points and individual fits (solid blue lines in the first column) for all momentum combinations with $\boldsymbol{k}^2 = 1$, however, the ground-state results (orange lines) are obtained by a simultaneous fit to the operator combinations $\mathcal{O}_{\text{v2a}}$ and $\mathcal{O}_{\text{v2b}}$ using all possible momenta for the corresponding matrix element with $\boldsymbol{k}^2 \leq 1$ for the connected, disconnected non-singlet, and disconnected singlet contributions respectively. The analysis shown in this plot has been performed on the ensemble N204. The solid blue lines in the first column correspond to a simultaneous fit to the four source-sink separations of the ensemble, cf. Tab. 4.2.1, for the insertion current $(\overline{u}u + \overline{d}d)$ needed to construct the flavor (non-)singlet operator contributions. In case of v_2 and a_2, the fits allow for an excited state on top of the ground-state. The orange line depicts the extracted ground-state contribution and directly correspond to the values of the reduced matrix elements. In the second and third column we show the disconnected contributions for the non-singlet $(\overline{u}u + \overline{d}d - 2\overline{s}s)$ and singlet $(\overline{u}u + \overline{d}d + \overline{s}s)$ operators as function of the final timeslice t. In addition to the original data points (grayed out) we also show an average over all insertion times for every final timeslice t (black triangle markers). Figure taken from [148].

ence of the PDF moment between longitudinally and transversally polarized rho mesons, which is no useful concept for mesons in their rest frame.

In Fig. 4.5.1 and Fig. 4.5.2, we show examples of the ratio fits for the ensemble N204. For the statistical analysis we generate 500 bootstrap samples per ensemble using a bin size of 40 molecular dynamics units to eliminate autocorrelations, cf. the discussion in Section 2.3.7. To visualize the fits and corresponding data points we only present plots for $\boldsymbol{k}^2 = 1$, with lattice momentum $\boldsymbol{k} = \frac{L}{2\pi}\boldsymbol{p}$, using the operator combinations (4.58a) – (4.59c). However, the results for the reduced matrix elements v_2, a_2, and d_2 in the left column are obtained by combined fits to

Fit Parameter	$\mathcal{O}_{\text{v2a}}(\boldsymbol{k}^2=1)$	$\mathcal{O}_{\text{v2b}}(\boldsymbol{k}^2=1)$	$\mathcal{O}_{\text{v2b}}(\boldsymbol{k}^2=0)$
B_0	✓	✓	✓
$B_1\,(\mathcal{O}_{\text{v2a}}, \boldsymbol{k}^2=1)$	✓	✗	✗
$B_1\,(\mathcal{O}_{\text{v2b}}, \boldsymbol{k}^2=1)$	✗	✓	✗
$B_1\,(\mathcal{O}_{\text{v2b}}, \boldsymbol{k}^2=0)$	✗	✗	✓
$\Delta E_{\boldsymbol{k}^2=1}$	✓	✓	✗
$\Delta E_{\boldsymbol{k}^2=0}$	✗	✗	✓

Table 4.5.1: Summary of the occurrence of the individual fit parameters in the ansatz (4.67) for the extraction of v_2 (pion) and a_2 (rho). A green check mark indicates that the fit parameter is present in the corresponding operator combination, whereas the red crosses indicate that the fit parameter is not present.

all ratios using an ansatz similar to (4.13) with the definitions (4.32) and (4.34). In the case of pseudoscalar mesons this reads

$$R(\mathcal{O}, \boldsymbol{p}^2, t, \tau) = B_0 + B_1(\mathcal{O}, \boldsymbol{p}^2)\; e^{-\Delta E_{\boldsymbol{p}^2}\;(t-\tau)} + B_1(\mathcal{O}, \boldsymbol{p}^2)\; e^{-\Delta E_{\boldsymbol{p}^2}\;\tau}, \tag{4.67}$$

where the ratio R explicitly depends on $\boldsymbol{p}^2$, the operator $\mathcal{O} \in \{\mathcal{O}_{\text{v2a}}, \mathcal{O}_{\text{v2b}}\}$, the sink timeslice t, and the insertion timeslice τ. For the operator combination $\mathcal{O}^i_{\text{v2a}}$, with $i = 1, 2, 3$, we average the three spatial directions and fit to the data using the parameters B_0, $B_1\,(\mathcal{O}_{\text{v2a}}, \boldsymbol{k}^2 = 1)$, and the excited state energy is given by $\Delta E_{\boldsymbol{k}^2=1}$, independent of the operator combination. Note that we require nonzero momentum in direction i for $\mathcal{O}_{\text{v2a}}$. Additionally the operator combination $\mathcal{O}_{\text{v2b}}$ gives rise to the further excited state amplitudes $B_1\,(\mathcal{O}_{\text{v2b}}, \boldsymbol{k}^2)$ and the excited state energy $\Delta E_{\boldsymbol{k}^2=0}$. All in all, this yields a simultaneous fit to three operator combinations for each source-sink separation, to resolve the individual parameters. The actual fit is performed simultaneously to all source-sink separations, cf. Tab. 4.2.1. A summary of the individual contributions is given in Tab. 4.5.1. One can easily deduce that the ground-state contribution B_0 is obtained from all data sets while the excited state amplitudes and energies depend on the operator combination and $\boldsymbol{k}^2$ respectively. A similar approach holds for the extraction of a_2 and d_2. However, for d_2 the statistical error is much larger such that the inclusion of a generic excited state in the fit is not promising. Therefore we fix the excited state energies $\Delta E_{\boldsymbol{k}^2=1}$ by an additional, simultaneous fit to the two-point function (4.10) in case of the reduced matrix element d_2.

In summary, this means that the fits do not only take into account the data points shown in Fig. 4.5.1 and Fig. 4.5.2 but are actually based on a larger data

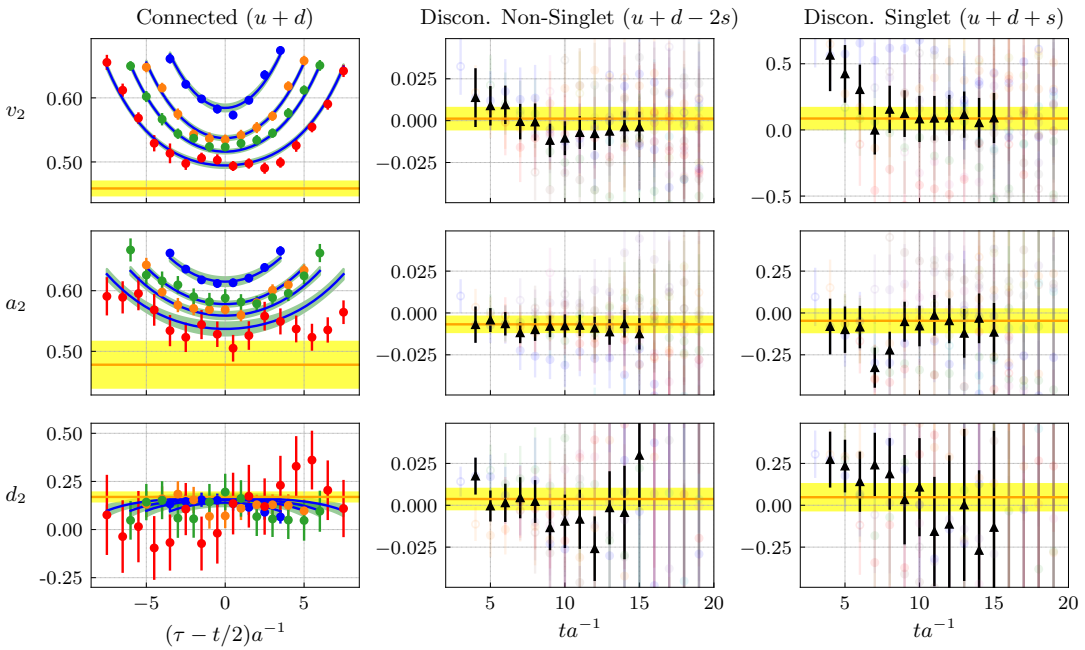

Figure 4.5.2: Extraction of renormalized values for v_2, a_2, and d_2 from the ratios obtained in (4.59a) – (4.59c) using the operator combination $\mathcal{O}_{\text{v2b}}$. The data is visualized in the same way as in Fig. 4.5.1, i.e., we only plot the data points and individual fits for $\boldsymbol{p}^2 = 1$. Also here we want to stress, that the ground-state results (orange line) are obtained by a simultaneous fit to the operator combinations $\mathcal{O}_{\text{v2a}}$ and $\mathcal{O}_{\text{v2b}}$ using all possible momenta for the corresponding matrix element with $\boldsymbol{p}^2 \leq 1$ for the connected, disconnected non-singlet, and disconnected singlet contributions respectively. Figure taken from [148].

set stemming from various operator and momentum configurations. However, the prefactors in (4.58a) – (4.59c) are solely determined by the results shown in Section 4.4 and the corresponding momentum contributions. As discussed above, we perform the extraction of the ground-state matrix elements separately for the connected (left column) and the disconnected (middle and right column) contributions. In the analysis of the disconnected contribution we found a high correlation between the noise on the light and the strange quark loop. This can be used to our advantage if we build non-singlet $(\overline{u}u + \overline{d}d - 2\overline{s}s)$ and singlet $(\overline{u}u + \overline{d}d + \overline{s}s)$ flavor combinations, instead of using the light and strange loops themselves. As depicted impressively in the middle and the right column of Fig. 4.5.1 and Fig. 4.5.2 (note the difference in scale), the statistical error is smaller by more than one order of magnitude for the non-singlet operator. For the disconnected contributions we do not see an indication for a significant excited state contribution and thus use a constant fit to extract the ground-state signal, using the combined fits shown above.

In contrast to the connected contributions the disconnected three-point functions are computed for a large number of final timeslices t and operator timeslices τ

equally distributed over the central part of the lattice. The grayed out point in the middle and the right column of Fig. 4.5.1 and Fig. 4.5.2 show the disconnected three-point correlator as a function of the final timeslice t where all datapoints per t (aligned on top of each other) correspond to the possible insertion timeslices between the source and the sink. The statistical scattering of these data points alone can lead to the misconception that the statistical error of the extracted ground-state (yellow band) is underestimated. In order to convince the reader that this is not the case we also show the black points, where we first sum up all data points per t and finally divide the result by the corresponding number of data points. Using the results for v_2, a_2, and d_2 shown in this section and building appropriate flavor combinations finally allows us to establish three sets of data points that can be used to extrapolate the reduced matrix elements to the physical and the continuum limit as shown Section 4.7.

4.6 Renormalization

In the last section we used the operator combinations

$$\mathcal{O}^i_{\mathrm{v2a}} = \mathcal{O}^{0i}, \qquad \text{and} \qquad \mathcal{O}_{\mathrm{v2b}} = \frac{4}{3}\,\mathcal{O}^{00}, \tag{4.68}$$

without any further justification. However, the main reason for the usage of these operator combinations directly follows from the renormalization procedure used to obtain physically meaningful results from the bare operators introduced in (3.23a) – (3.23f). The consideration of isosinglet $\mathcal{O}_{\mathrm{singlet}}$ and non-singlet $\mathcal{O}_{\mathrm{non-singlet}}$ operator combinations shown in Section 4.5 in principle requires different renormalization approaches. Regarding the non-singlet components we get the simple, schematic, relation

$$\mathcal{O}^{\mathrm{R}}_{\mathrm{non-singlet}} = Z^{qq}\,\mathcal{O}_{\mathrm{non-singlet}}\ , \tag{4.69}$$

where Z^{qq} is the quark non-singlet renormalization constant. In the case of isosinglet operators one faces the additional difficulty that the quark operators will mix under renormalization with gluonic contributions due to

$$\begin{pmatrix} \mathcal{O}^{\mathrm{R}}_{\mathrm{singlet}} \\ \mathcal{O}^{\mathrm{R}}_{g} \end{pmatrix} = \begin{pmatrix} Z^{qq}_{\mathrm{s}} & Z^{qg} \\ Z^{gq} & Z^{gg} \end{pmatrix} \begin{pmatrix} \mathcal{O}_{\mathrm{singlet}} \\ \mathcal{O}_{g} \end{pmatrix}, \tag{4.70}$$

β	3.34	3.4	3.46	3.55	3.7
Z^{qq}_{v2a}	1.0731	1.1010	1.1251	1.1578	1.2053
Z^{qq}_{v2b}	1.0672	1.0938	1.1170	1.1485	1.1949

Table 4.6.1: Renormalization factors Z^{qq} for the operator combinations $\mathcal{O}_{\mathrm{v2a}}$ and $\mathcal{O}_{\mathrm{v2b}}$ used in this work. All values taken from Tab. XIII in [256].

where Z^{qq}_{s} is the isosinglet renormalization constant and all superscripts g denote gluonic contributions. For the quark operator this means

$$\mathcal{O}^{\mathrm{R}}_{\mathrm{singlet}} = Z^{qq}_{\mathrm{s}}\mathcal{O}_{\mathrm{singlet}} + Z^{qg}\mathcal{O}_g\,. \tag{4.71}$$

It was shown in [254, 255] that the admixture in the opposite direction, i.e., mixing of quark operators into gluon operators, is only a few percent effect. Assuming that the same is true for the admixture of gluonic operators into quark operators we will classify these contributions as negligible in the statistical accuracy of our work. Still, this caveat has to be kept in mind and needs to be addressed in future work. Furthermore, we will approximate $Z^{qq}_{\mathrm{s}} \approx Z^{qq}$ using the non-perturbatively computed isovector renormalization factor Z^{qq}. Within a perturbative renormalization procedure this is only exact in next to leading order.

In LQCD the continuous Euclidean symmetry group O(4) is reduced to its finite hypercubic subgroup H(4) where symmetry imposes much weaker constraints on the mixing of operators under renormalization. This mixing, especially with lower-dimensional operators, is suppressed as far as possible by the usage of operators chosen from suitable multiplets that possess a definite C-parity and transform according to irreducible representations of H(4) as shown in, e.g., [154, 253]. To be specific we use the operator definitions (4.68), cf. also Section 4.5.

An in-depth description of the renormalization procedure used in our work is given in [256], including subtleties due to the use of open boundary conditions in the CLS gauge ensembles and details about the perturbative subtraction of lattice artifacts. To this end, we adopt the two-step procedure shown there: First, we calculate the renormalization factors non-perturbatively in the RI′/SMOM scheme. These are then converted to the $\overline{\mathrm{MS}}$ scheme using perturbative QCD. Our results are finally given in the $\overline{\mathrm{MS}}$ scheme at a scale of 2 GeV and to be more specific: We use the values for Z_{v2a} and Z_{v2b} based on RI′/SMOM as intermediate scheme presented in [256], with the perturbative subtraction of lattice artifacts without using the so-called fixed scale method. The actual numbers used in our computations are listed in Tab. 4.6.1.

4.7 Quark mass dependence and continuum extrapolation

In Fig. 2.3.3 we have shown how the CLS gauge ensembles are distributed in the m_π^2 – m_k^2 plane along three different trajectories which allows us, in combination with the 5 different values of β, to extrapolate our results to physical masses and the continuum limit $a = 0$. To this end, we perform the extrapolation employing a parametrization of the form

$$f(a, m_\pi^2, m_k^2) = c_0 + c_1 a + c_2 m_\pi^2 + c_3 m_k^2 \ , \tag{4.72}$$

where the pion mass m_π, the kaon mass m_k and the lattice spacing a are used as input parameters, defined by the individual ensembles, and (4.72) is inserted into a least square fit to obtain the parameters c_i. Note that we have to use a linear term in the lattice spacing as leading contribution although our lattice action is order a improved because we lack the order a improvement for the inserted currents.

In Fig. 4.8.1, Fig. 4.8.2, and Fig. 4.8.3 the yellow bands show the extrapolations for the flavor singlet and flavor non-singlet operator combinations as functions of m_π^2, a, and for data points where we average all values per β. In all cases we plot the three different trajectories $\mathrm{tr}[M] = \text{const.}$, $m_s = \text{const.}$, and $m_l = m_s$ from the left to the right. The data points in Fig. 4.8.1 are corrected for lattice spacing effects while the data points in Fig. 4.8.2 and Fig. 4.8.3 are corrected for pion mass effects. The data sets are finally shifted to the corresponding trajectories. This description of the data allows us to draw conclusions about various physical aspects. Using the representation shown in Fig. 4.8.1 for, e.g., the $\mathrm{tr}[M] = \text{const.}$ line keeps the average quark mass fixed using the fitted model shown above. This allows us to see the effect of flavor symmetry breaking. As pointed out in Section 4.5, and explicitly shown in Fig. 4.5.1 and Fig. 4.5.2, it is hard to draw any convincing conclusions from the flavor singlet operator combinations, due to large statistical errors. However, these results will allow us to give at least an upper bound for the reduced matrix elements v_2, a_2, and d_2. In contrast to the flavor singlet combinations the situation for the flavor non-singlet case is much better and we can draw serious conclusions from the various extrapolations. Fig. 4.8.1 and Fig. 4.8.2 show the extrapolations for the quark mass and lattice spacing dependence, respectively. Another representation of the lattice spacing dependency is shown in Fig. 4.8.3 where we average for all ensembles with the same value of β using the weighted average

$$\overline{A}_i = \sum_i^{N_\beta} w_i \, A_i \ , \qquad \text{with} \qquad w_i = \frac{1/\sigma_i^2}{\sum_i^{N_\beta} 1/\sigma_i^2} \ , \tag{4.73}$$

where N_β is the number of data points A_i (ground-state matrix elements) per β with corresponding errors σ_i. To visualize solely the discretization effects all the data points used in the average were corrected for mass effects, again using the fitted model, i.e., they were translated to physical masses along the fitted curve. However, we want to stress that the averaging procedure for the data points was only used for illustrative purposes. The yellow bands still correspond to the actual fit performed using the original data points, cf. Fig. 4.8.2.

The final results for the reduced matrix elements are given in Tab. 4.8.1. In addition to the statistical error we provide estimates for the systematic uncertainties due to the quark mass extrapolation and the continuum extrapolation. For the error estimation we have performed additional fits with cuts in the mass range $\overline{m} = \sqrt{(2m_K^2 + m_\pi^2)/3} < 450\,\text{MeV}$ and $a < 0.09\,\text{fm}$, respectively. We then take the difference between the results from these fits and our main result as an estimate of the corresponding systematic uncertainties.

4.8 Discussion

What remains is the reconstruction of structure functions as a sum over reduced matrix elements using (3.36) in combination with (3.37) and (3.38). At leading twist accuracy we write down ratios of the second moments of the structure functions F_1, F_2, and b_1 with their corresponding Wilson coefficient $C_n^{(k)} = 1 + \mathcal{O}(\alpha_s)$ as a sum over the related reduced matrix element

$$\frac{2M_2(F_1)_\pi}{C_2^{(1)}} = \frac{M_1(F_2)_\pi}{C_2^{(2)}} = \sum_q e_q^2 v_2^q = \frac{2}{9}\left(v_2^{\text{fs}} + \frac{1}{4} v_2^{\text{fns}}\right), \tag{4.74a}$$

$$\frac{2M_2(F_1)_\rho}{C_2^{(1)}} = \frac{M_1(F_2)_\rho}{C_2^{(2)}} = \sum_q e_q^2 a_2^q = \frac{2}{9}\left(a_2^{\text{fs}} + \frac{1}{4} a_2^{\text{fns}}\right), \tag{4.74b}$$

$$\frac{2M_2(b_1)_\rho}{C_2^{(1)}} = \frac{M_1(b_2)_\rho}{C_2^{(2)}} = \sum_q e_q^2 d_2^q = \frac{2}{9}\left(d_2^{\text{fs}} + \frac{1}{4} d_2^{\text{fns}}\right), \tag{4.74c}$$

where we assume exact isospin symmetry and $\text{fs} \equiv u + d + s$ is the flavor singlet while $\text{fns} \equiv u + d - 2s$ is the flavor non-singlet combination. If we only consider the connected part, the strange quark contribution drops out entirely. The result can be written in terms of the light quark connected contribution as

$$\frac{2M_2(F_1)_\pi^{\text{conn.}}}{C_2^{(1)}} = \frac{M_1(F_2)_\pi^{\text{conn.}}}{C_2^{(2)}} = \frac{5}{9} v_2^{\ell,\text{conn.}}, \tag{4.75a}$$

$$\frac{2M_2(F_1)_\rho^{\text{conn.}}}{C_2^{(1)}} = \frac{M_1(F_2)_\rho^{\text{conn.}}}{C_2^{(2)}} = \frac{5}{9} a_2^{\ell,\text{conn.}}, \tag{4.75b}$$

$$\frac{2M_2(b_1)_\rho^{\text{conn.}}}{C_2^{(1)}} = \frac{M_1(b_2)_\rho^{\text{conn.}}}{C_2^{(2)}} = \frac{5}{9} d_2^{\ell,\text{conn.}}. \tag{4.75c}$$

Matrix element	Final result	χ^2/d.o.f.
$v_2^{(u+d+s)}$	$0.220\ (95)_s(98)_m(155)_a$	1.71
$a_2^{(u+d+s)}$	$0.285\ (90)_s(76)_m(271)_a$	1.78
$d_2^{(u+d+s)}$	$0.226\ (112)_s(6)_m(54)_a$	0.72
$v_2^{(u+d-2s)}$	$0.344\ (20)_s(3)_m(19)_a$	1.72
$a_2^{(u+d-2s)}$	$0.384\ (29)_s(11)_m(42)_a$	1.33
$d_2^{(u+d-2s)}$	$0.163\ (38)_s(5)_m(7)_a$	0.58
$v_2^{(u+d),\text{conn.}}$	$0.357\ (16)_s(2)_m(15)_a$	1.74
$a_2^{(u+d),\text{conn.}}$	$0.393\ (29)_s(10)_m(35)_a$	1.47
$d_2^{(u+d),\text{conn.}}$	$0.180\ (38)_s(5)_m(7)_a$	0.59

Table 4.8.1: Results obtained from the extrapolations in Figs. 4.8.1 and 4.8.2 and the corresponding connected-only contributions for the flavor combination $(u+d)$, all at $\mu = 2\,\text{GeV}$. The final statistical error is subscribed by $()_s$, the estimates of the systematic uncertainties due to the quark mass by $()_m$, and due to the continuum extrapolation by $()_a$. The values of χ^2 per degrees of freedom are obtained from the corresponding extrapolation.

Structure function	Final result	χ^2/d.o.f.
$CM_2(F_1)_\pi$	$0.132\ (33)_s(32)_m(57)_a$	1.75
$CM_2(F_1)_\rho$	$0.156\ (33)_s(23)_m(102)_a$	1.84
$CM_2(b_1)_\rho$	$0.108\ (41)_s(1)_m(13)_a$	0.72
$CM_2(F_1)_\pi^{\text{conn.}}$	$0.099\ (5)_s(0)_m(4)_a$	1.74
$CM_2(F_1)_\rho^{\text{conn.}}$	$0.109\ (8)_s(2)_m(9)_a$	1.47
$CM_2(b_1)_\rho^{\text{conn.}}$	$0.050\ (10)_s(1)_m(2)_a$	0.59

Table 4.8.2: Estimated results for the second moments of the structure functions F_1 and b_1 exploiting (4.74a) – (4.75c) and performing the extrapolations as discussed in Section 4.7. We use the abbreviation $C \equiv 2/C_2^{(1)}$. Table taken from [148].

Our final results for the linear combinations (4.74a) – (4.75c) are given in Tab. 4.8.2.

While the first three lines in Tab. 4.8.2 correspond to the results obtained by (4.74a) – (4.74c), and thus have relatively large errors due to the isosinglet contribution, the last three lines correspond the 'connected-only' contribution (4.75a) – (4.75c), which drastically reduces the errors. The latter is meant to be used for comparison with other studies, e.g., [154], where only connected contributions were considered. The reader should be aware of the fact that we use the flavor non-

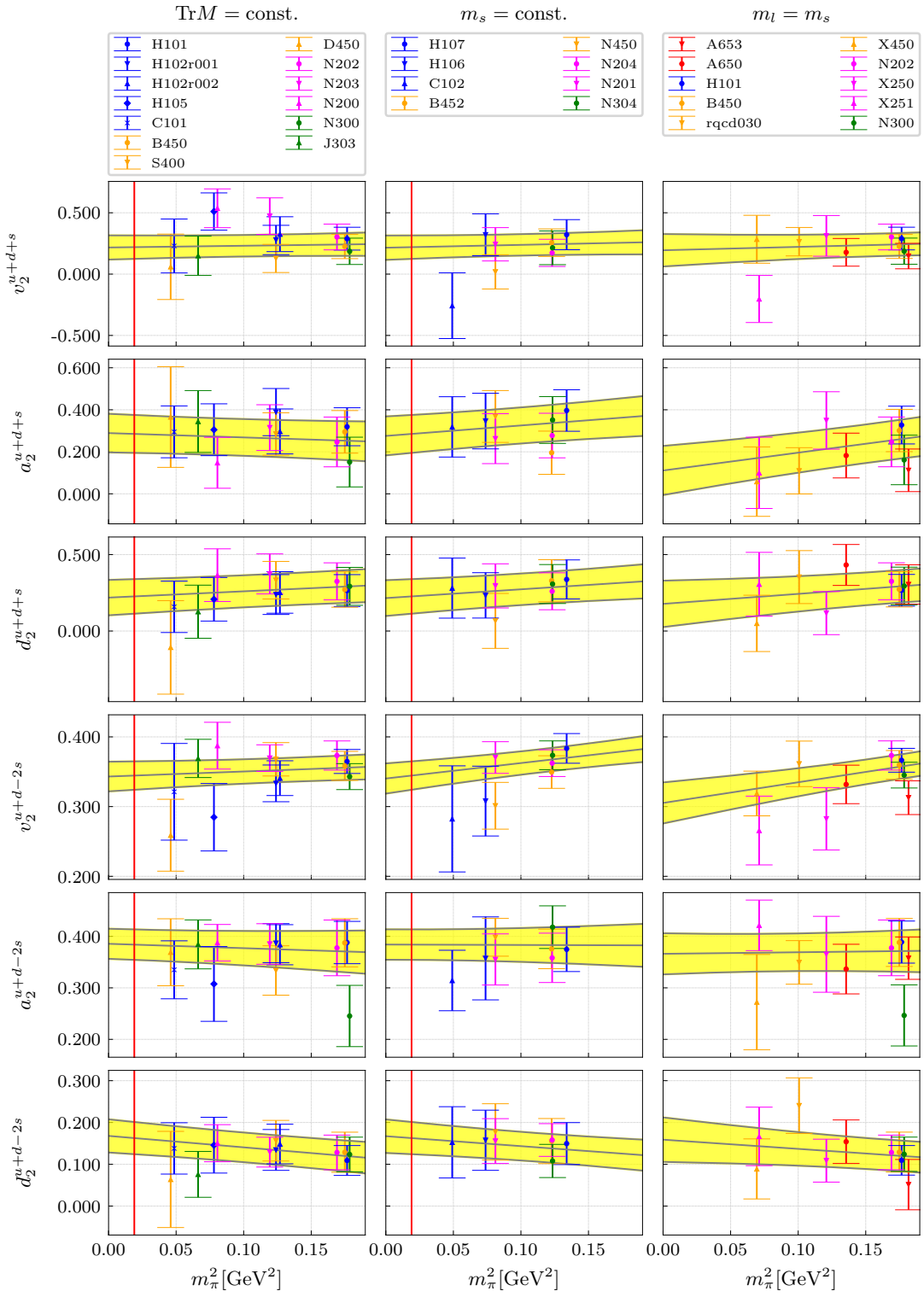

Figure 4.8.1: Extrapolation for the flavor singlet ($\overline{u}u+\overline{d}d+\overline{s}s$) and flavor non-singlet operator combinations ($\overline{u}u+\overline{d}d-2\overline{s}s$) as a function of pion mass m_π using the fits shown in, e.g., Fig. 4.5.1. From left to right we show the m_π^2 dependence of the reduced matrix elements v_2 (pion), a_2, and d_2 (both rho) for the three different trajectories we use in our analysis. The vertical red line denotes the physical point. Note that the symmetric trajectory $m_l = m_s$ with exact SU(3) flavor symmetry does not approach the physical point but the chiral limit in the quark mass plane. Figure taken from [148].

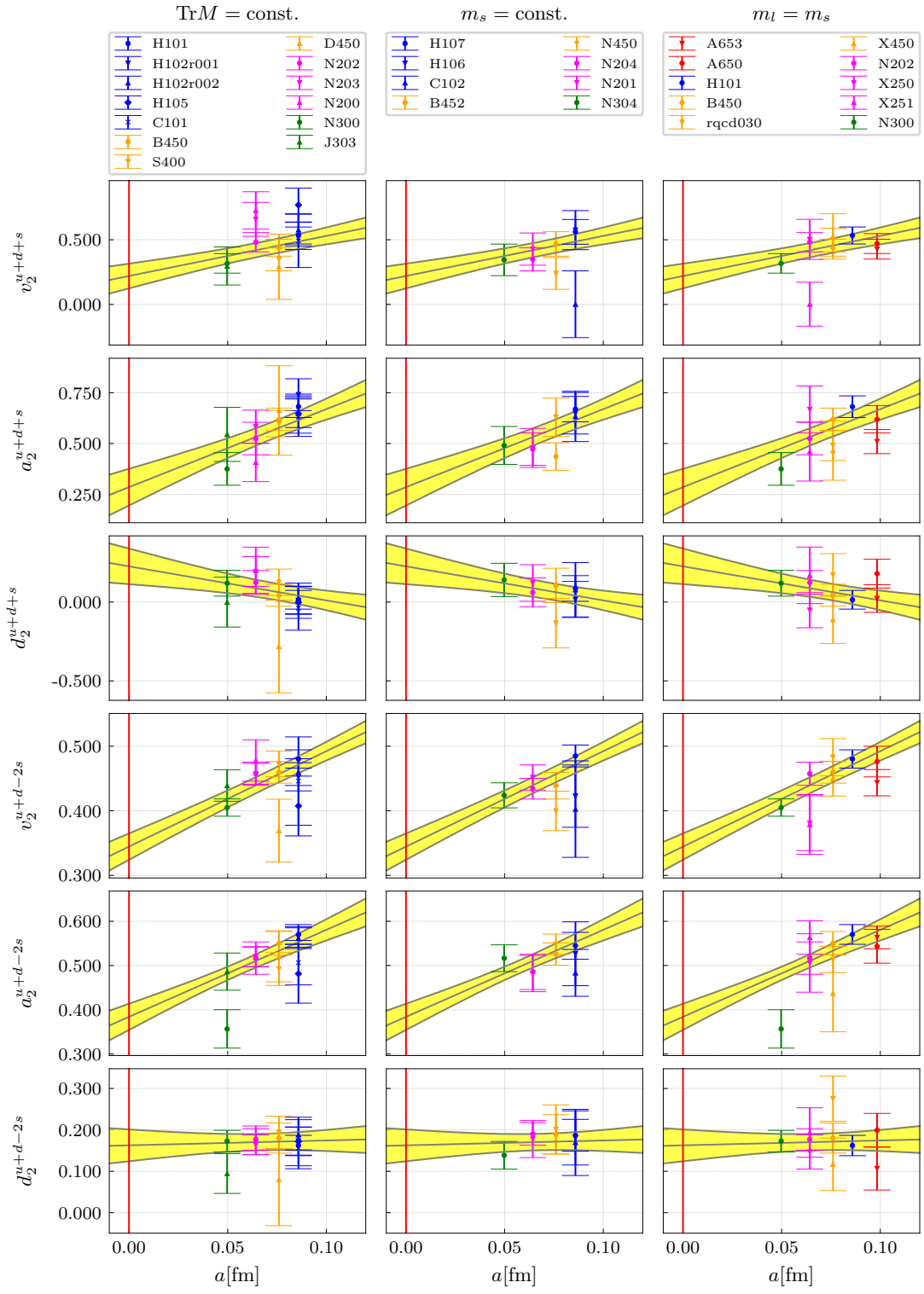

Figure 4.8.2: Extrapolation for the flavor singlet ($\overline{u}u+\overline{d}d+\overline{s}s$) and flavor non-singlet operator combinations ($\overline{u}u+\overline{d}d-2\overline{s}s$) as a function of the lattice spacing a using the fits shown in, e.g., Fig. 4.5.1. From left to right we show the a dependence of the reduced matrix elements v_2 (pion), a_2, and d_2 (both rho) for the three different trajectories we use in our analysis. The vertical red line denotes the continuum limit for $a = 0$. Figure taken from [148].

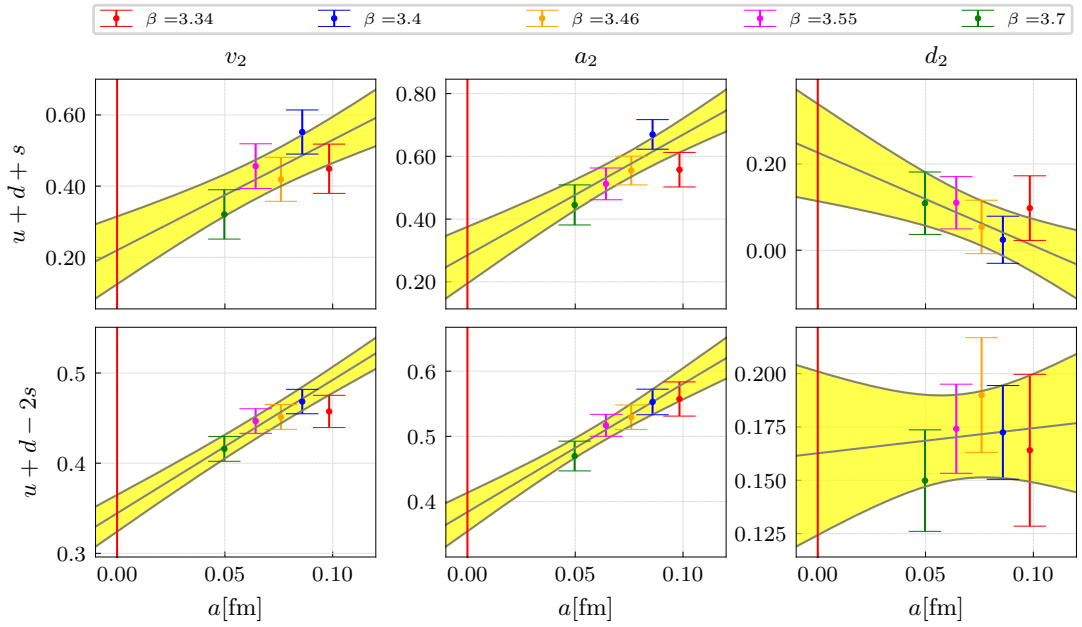

Figure 4.8.3: Lattice spacing dependence of the extrapolations for the flavor singlet ($\overline{u}u + \overline{d}d + \overline{s}s$) and flavor non-singlet ($\overline{u}u + \overline{d}d - 2\overline{s}s$) operator combinations using the fits shown in, e.g., Fig. 4.5.1 and Fig. 4.5.2. The reduced matrix elements v_2 (pion), a_2, and d_2 (both rho) have been obtained by a translation to physical quark masses and averaging measurements with the same values of β using the weighted average given in (4.73). From coarsest to finest lattice spacing, this corresponds to averaging the data of 2, 8, 7, 7, and 3 independent ensembles, cf. Tab. 4.2.1. The non-averaged plots for the individual trajectories can be found in Fig. 4.8.2. Figure taken from [148].

singlet renormalization constants in both cases, which is only an approximation as stated in Section 4.6.

In contrast to the only partially meaningful final results given for the full structure functions in Tab. 4.8.2, remember the various approximations and the large statistical errors, we obtain very precise results for the flavor non-singlet contributions shown in Tab. 4.8.1, and this even though we consider all possible contributions. As shown in Section 4.6 the non-singlet operator combinations do not mix with gluonic operators under renormalization and necessary renormalization factors have been computed non-perturbatively in [256]. A comparison of the connected only results from Tab. 4.8.2, of course divided by the corresponding prefactors given in (4.75a) – (4.75c), to the flavor non-singlet results given in Tab. 4.8.1 shows very good agreement for the unpolarized structure functions F_1^π and F_1^ρ as well as for the structure function b_1 and the corresponding reduced matrix elements and, of course, reflects the connected-only values in Tab. 4.8.1. Following the discussion in Section 4.5 this comes as no surprise since the quark-line disconnected contributions are small compared to their connected counterparts in the extraction of the ground-state matrix elements. In leading order the structure

function $F_1^q(x)$ corresponds to one half of the probability to find a quark of flavor q with momentum fraction x. Starting from (3.46) we find that the reduced matrix elements for the pion are related to the moments of the PDFs via

$$v_2^{u+d+s} = \langle x \rangle_{u+\overline{u}} + \langle x \rangle_{d+\overline{d}} + \langle x \rangle_{s+\overline{s}} \qquad \text{(flavor singlet)}, \tag{4.76a}$$

$$v_2^{u+d-2s} = \langle x \rangle_{u+\overline{u}} + \langle x \rangle_{d+\overline{d}} - 2\langle x \rangle_{s+\overline{s}} \qquad \text{(flavor non-singlet)}, \tag{4.76b}$$

where we use the shorthand notation $q \equiv f_q$. Treating the special case of, e.g., a π^+ meson with u and $\overline{d}$ valence quarks, i.e., $\langle x \rangle_u = \langle x \rangle_{u_{\text{val}}} + \langle x \rangle_{u_{\text{sea}}}$ and $\langle x \rangle_{\overline{d}} = \langle x \rangle_{\overline{d}_{\text{val}}} + \langle x \rangle_{\overline{d}_{\text{sea}}}$, the relations (4.76a) and (4.76b) can be further split up in moments of valence and sea quark PDFs

$$\begin{aligned} v_2^{u+d+s} = \langle x \rangle_{u_{\text{val}}} + \langle x \rangle_{u_{\text{sea}}} + \langle x \rangle_{\overline{u}_{\text{sea}}} \\ + \langle x \rangle_{\overline{d}_{\text{val}}} + \langle x \rangle_{d_{\text{sea}}} + \langle x \rangle_{\overline{d}_{\text{sea}}} \\ + \langle x \rangle_{s_{\text{sea}}} + \langle x \rangle_{\overline{s}_{\text{sea}}} \,, \end{aligned} \tag{4.77a}$$

$$\begin{aligned} v_2^{u+d-2s} = \langle x \rangle_{u_{\text{val}}} + \langle x \rangle_{u_{\text{sea}}} + \langle x \rangle_{\overline{u}_{\text{sea}}} \\ + \langle x \rangle_{\overline{d}_{\text{val}}} + \langle x \rangle_{d_{\text{sea}}} + \langle x \rangle_{\overline{d}_{\text{sea}}} \\ - 2\langle x \rangle_{s_{\text{sea}}} - 2\langle x \rangle_{\overline{s}_{\text{sea}}} \,, \end{aligned} \tag{4.77b}$$

depending on the operator insertion. Following [165] we assume charge symmetry for the π^+ valence PDF, i.e.,

$$\langle x \rangle_{\text{val}}^{\pi^+} \equiv \langle x \rangle_{u_{\text{val}}} = \langle x \rangle_{\overline{d}_{\text{val}}} \,, \tag{4.78}$$

and exact SU(3) flavor symmetry for the quark sea

$$\langle x \rangle_{\text{sea}}^{\pi^+} \equiv \langle x \rangle_{u_{\text{sea}}} = \langle x \rangle_{d_{\text{sea}}} = \langle x \rangle_{s_{\text{sea}}} = \langle x \rangle_{\overline{u}_{\text{sea}}} = \langle x \rangle_{\overline{d}_{\text{sea}}} = \langle x \rangle_{\overline{s}_{\text{sea}}} \,. \tag{4.79}$$

Using this assumption we rewrite (4.77a) and (4.77b) as

$$v_2^{u+d+s} = 2\langle x \rangle_{\text{val}}^{\pi^+} + 6\langle x \rangle_{\text{sea}}^{\pi^+} \,, \qquad v_2^{u+d-2s} = 2\langle x \rangle_{\text{val}}^{\pi^+} \,, \tag{4.80}$$

and find that the flavor singlet operator combination describes the full quark PDF and the flavor non-singlet combination corresponds to the valence quark PDF respectively. Similar relations can be constructed for the reduced matrix elements a_2 and d_2 of the rho meson. Thus, the results in Tab. 4.8.2 imply that in the pion the valence quarks carry about 35% of the total momentum, while in the rho they carry about 40% of the total momentum under the assumption of exact SU(3)

flavor symmetry in the quark sea. It is remarkable that these values justify the assumption $F_1(x)^\pi \sim F_1(x)^\rho$, which is often used in phenomenological estimates. The structure functions $b_1(x)$ and $b_2(x)$ are sensitive to a possible dependence of the quark densities on the hadron polarization, i.e., they measure the difference in quark distributions of a spin projected $\lambda = 0$ and $\lambda = +/-$ rho meson. If the quarks were in a relative S-wave state one would expect $b_1 = b_2 = 0$. However, our results show a large contribution (compared to the scale of a_2) to the approximated valence quark contribution d_2 with a relative error of only $\sim$10%. This confirms the conclusion in [154] that the quarks carry substantial orbital angular momentum and also reflects the results of the various phenomenological studies cited at the very beginning of Chapter 4.

5
Summary

In this thesis we presented the first computation of the PDF moments v_2, a_2, and d_2 of the pion and the rho meson including disconnected quark-line contributions. Our final results are expressed in terms of flavor singlet $(u + d + s)$ and non-singlet $(u + d - 2s)$ operator combinations. The latter has a drastically smaller statistical error and allows for serious conclusions of the momentum fractions carried by the quarks in the pion and the rho meson. Our numerical analysis includes 26 gauge ensembles, mainly generated by the CLS effort, with pion masses ranging from 420 MeV down to 214 MeV and with five different lattice spacings in the range of 0.1 fm to 0.05 fm. Without the work of the CLS collaboration, generating ensembles and other configuration related data, this work would have been inconceivable.

We have presented the, to our knowledge, very first computation of the second moments for the structure functions F_1^π, F_1^ρ, and b_1, including quark-line disconnected contributions. As shown in Section 4.7 our final results are tainted with very large statistical errors due to the flavor singlet disconnected contributions, however, we are able to provide accurate results for the flavor non-singlet combinations $u+d-2s$. While finishing this thesis another preprint, also treating quark-line disconnected contributions, for the pion PDF moments, using $N_f = 2+1+1$ LQCD, was published [257] and gave rise to questions. A comparison of our results to the results presented in [257], and to phenomenological values presented in [258, 259], was shown in [257] and is captured in Tab. 5.0.1. In [257] it is stated, that a com-

Matrix element	This work	[257]	[258]	[259]
$v_2^{(u+d+s)}$	$0.220(95)_s(98)_m(155)_a$	$0.68(05)_s$	$0.58(9)_s$	$0.75(18)_s$
$v_2^{(u+d-2s)}$	$0.344(20)_s(3)_m(19)_a$	$0.48(01)_s$	–	–

Table 5.0.1: Comparison of pion PDF results presented in this thesis to the values given in [257]. Both values are given in the $\overline{\text{MS}}$ scheme at 2 GeV.

parison of the flavor singlet contribution is not meaningful, since, in contrast to our work, in [257–259] also gluonic contributions are considered. Of course this is true, however, we want to stress that especially the values shown in [257] are computed using only one ensemble with $m_\pi \approx m_{\pi,\text{phys.}}$ and $a = 0.08029(41)$ fm. We have shown in Fig. 4.8.3 that our results for v_2 show a strong dependence on the lattice spacing a, which is ignored in [257] and thus the corresponding comparison is pointless. In contrast to the flavor singlet combinations the flavor non-singlet operators are not affected by gluonic mixing, however, since also in this case no continuum extrapolation was performed in [257] the corresponding value given in Tab. 5.0.1 is at least questionable. To further illustrate this one could compare the value $v_2^{(u+d-2s)} = 0.48(01)_s$ of [257] to our value $v_2^{(u+d-2s)} = 0.468(16)_s$ at $a = 0.0859$ fm, corresponding to the blue data-point in the bottom left panel of Fig. 4.8.3. Despite the fact that a different action is used in [257] the values show good agreement and one could assume that both results agree. However, this does not reflect the extrapolated results at all and thus the comparison imposed in [257] is disputable. In summary this means that the lattice results and/or the results presented in [165, 259] have to be further investigated to clarify the continuum limit. Our results yield a first, crucial contribution to this process.

Furthermore, we can compare with the pion valence quark contributions shown in [165]. Adapting the approximations about the sea quark contributions in [165], i.e., $v_{2,\text{sea}}^{u+d-2s} = 0$, to our results we can interpret the value $v_2^{u+d-2s} = 0.344(28)$ as the valence quark contribution of the pion, measured on the lattice, cf. Section 4.8. However, our value of $\sim 35\%$ differs from the results presented in [165] by $\sim 10\%$. The reason for this discrepancy is a priori not clear. On the one hand, there are various assumptions used in [165], which are at least open to debate. On the other hand, we found a strong dependence on the lattice spacing, which may cause the lower value.

As an additional subtlety we had a closer look at possible two-pion contributions which might occur in our analysis of the rho meson. We did not find any evidence for a significant contribution of these multi-particle states. Nevertheless, using our analysis techniques we cannot fully exclude them either, which is particularly

true for two-pion states close to the resonance energy as shown in Fig. 4.3.4. The precision of our numerical results could be enhanced a posteriori, if future studies (e.g., by using the generalized eigenvalue method with two-pion interpolating currents, cf. [237, 249–252]) can show that the overlap of smeared vector interpolating currents with the two-pion states is much smaller than for the local currents.

Although we present comprehensive results including disconnected contributions for the first time we have reduced the statistical error considerably. This can be seen comparing the error of the connected-only contribution with earlier studies. However, to determine the phenomenologically important moments of the structure functions (at leading twist), one needs the flavor singlet combination, where the statistical error is still large. Future studies will have to aim at a further reduction of these statistical errors. Once this is achieved, also a non-perturbative calculation of the singlet renormalization factors and the inclusion of mixing with gluonic operators is possible.

Our main results show a significant dependence on the lattice spacing, which justifies the CLS strategy, and can be summarized as

$$
\begin{aligned}
v_2^{(u+d+s)} &= 0.220(207)\,, & v_2^{(u+d-2s)} &= 0.344(28)\,,\\
a_2^{(u+d+s)} &= 0.285(295)\,, & a_2^{(u+d-2s)} &= 0.384(52)\,,\\
d_2^{(u+d+s)} &= 0.226(124)\,, & d_2^{(u+d-2s)} &= 0.163(39)\,,
\end{aligned}
$$

for the second moment v_2 of the pion structure function F_1, the second moment a_2 of the rho structure function F_1, and the second moment d_2 of the rho structure function b_1 respectively. All results are presented in the $\overline{\text{MS}}$ scheme at $\mu = 2\,\text{GeV}$. Our results imply that the valence quarks of the pion and the rho meson carry the same amount of total momentum within the error. Furthermore, we were able to show that the quarks in the rho meson carry a substantial amount of orbital angular momentum via the finite value of d_2.

We finally want to remind of the upcoming AMBER experiment at the CERN super proton synchrotron [59, 60], which will produce further relevant data. We presented our results [148] at the Perceiving the Emergence of Hadron Mass through AMBER@CERN - VI online workshop and thus could impact on upcoming experiments. We are very curious what the results of these experiments will be.

In summary we presented a LQCD study of the second Mellin moments of PDFs for the pion and the rho meson including extrapolations to the continuum and physical quarks masses. There are two novel aspects in this thesis. First of all, we systematically included disconnected quark contributions into our results and used these values within our extrapolations. Secondly we also computed the Mellin

moments a_2 and d_2 of the rho meson PDF. While typical LQCD computations tend to focus on the nucleon and the pion, only little is known about the structure of other hadrons.

A

Appendix

A.1 Antisymmetric Tensor

The completely antisymmetric tensor (Levi-Civita symbol) is defined as

$$\varepsilon_{i_1,i_2,i_3,\ldots,i_n} = \begin{cases} +1 & \text{if } (i_1,i_2,i_3,\ldots,i_n) \text{ is an even permutation of } (1,2,3,\ldots,n), \\ -1 & \text{if } (i_1,i_2,i_3,\ldots,i_n) \text{ is an odd permutation of } (1,2,3,\ldots,n), \\ 0 & \text{if at least two indices } i_j \text{ are equal.} \end{cases} \tag{A.1}$$

A.2 Gell-Mann matrices

For SU(3), i.e., unitary matrices U with $\det U = 1$, the defining representation can be written as

$$U_{3\times 3} = e^{i\sum_{j=1}^{8}\theta_j t_j}\,, \qquad \text{with} \qquad [t_j,t_k] = i f_{jkl}\, t_l\,, \tag{A.2}$$

where f_{jkl} are the structure constants defined in Tab. A.2.1. Note that in general there are N^2-1 generators t_j of the Lie group. The standard choice for the 8

j	k	l	f_{jkl}
1	2	3	1
1	4	7	1/2
1	5	6	-1/2
2	4	6	1/2
2	5	7	1/2
3	4	5	1/2
3	6	7	-1/2
4	5	8	$\sqrt{3}/2$
6	7	8	$\sqrt{3}/2$

Table A.2.1: Totally antisymmetric structure constants for SU(3) for semi-simple compact Lie algebras. All other coefficients vanish.

independent matrices in the SU(3) case are the Gell-Mann matrices

$$\begin{aligned}
\lambda_1 &= \begin{pmatrix} 0 & 1 & 0 \\ 1 & 0 & 0 \\ 0 & 0 & 0 \end{pmatrix}, & \lambda_2 &= \begin{pmatrix} 0 & -i & 0 \\ i & 0 & 0 \\ 0 & 0 & 0 \end{pmatrix}, \\
\lambda_4 &= \begin{pmatrix} 0 & 0 & 1 \\ 0 & 0 & 0 \\ 1 & 0 & 0 \end{pmatrix}, & \lambda_5 &= \begin{pmatrix} 0 & 0 & -i \\ 0 & 0 & 0 \\ i & 0 & 0 \end{pmatrix}, \\
\lambda_6 &= \begin{pmatrix} 0 & 0 & 0 \\ 0 & 0 & 1 \\ 0 & 1 & 0 \end{pmatrix}, & \lambda_7 &= \begin{pmatrix} 0 & 0 & 0 \\ 0 & 0 & -i \\ 0 & i & 0 \end{pmatrix}, \\
\lambda_3 &= \begin{pmatrix} 1 & 0 & 0 \\ 0 & -1 & 0 \\ 0 & 0 & 0 \end{pmatrix}, & \lambda_8 &= \frac{1}{\sqrt{3}} \begin{pmatrix} 1 & 0 & 0 \\ 0 & 1 & 0 \\ 0 & 0 & -2 \end{pmatrix},
\end{aligned} \tag{A.3}$$

where the normalization is chosen such that $\mathrm{tr}[\lambda_i^2] = 2$. The Gell-Mann matrices form the representation with the smallest matrices acting on vectors with the smallest number of elements, for SU(3) this means 3. Therefore this specific matrix representation is called the fundamental representation. The relation to (A.2) is given by

$$t_j = \frac{\lambda_j}{2}, \qquad \text{with} \quad [\lambda_j, \lambda_k] = 2i f_{jkl}\, \lambda_l. \tag{A.4}$$

A.3 Dirac matrices (Minkowski)

The four contravariant Dirac matrices (also known as gamma matrices) are defined as

$$\gamma^0 = \begin{pmatrix} 0 & 0 & 1 & 0 \\ 0 & 0 & 0 & 1 \\ 1 & 0 & 0 & 0 \\ 0 & 1 & 0 & 0 \end{pmatrix}, \qquad \gamma^1 = \begin{pmatrix} 0 & 0 & 0 & -1 \\ 0 & 0 & -1 & 0 \\ 0 & 1 & 0 & 0 \\ 1 & 0 & 0 & 0 \end{pmatrix},$$
$$\gamma^2 = \begin{pmatrix} 0 & 0 & 0 & i \\ 0 & 0 & -i & 0 \\ 0 & -i & 0 & 0 \\ i & 0 & 0 & 0 \end{pmatrix}, \qquad \gamma^3 = \begin{pmatrix} 0 & 0 & -1 & 0 \\ 0 & 0 & 0 & 1 \\ 1 & 0 & 0 & 0 \\ 0 & -1 & 0 & 0 \end{pmatrix}, \tag{A.5}$$

in the Weyl (chiral) representation. They obey the anticommutation relation

$$\{\gamma^\mu, \gamma^\nu\} = 2\eta^{\mu\nu}\mathbb{I}\,, \tag{A.6}$$

using the Minkowski metric $\eta_{\mu\nu} = \mathrm{diag}(1, -1, -1, -1)$. Further, the gamma matrices are chosen such that

$$(\gamma^\mu)^\dagger = \gamma^0\gamma^\mu\gamma^0\,, \tag{A.7}$$

and the fifth gamma matrix is defined by

$$\gamma^5 \equiv \gamma_5 = i\gamma^0\gamma^1\gamma^2\gamma^3\,, \tag{A.8}$$

with the properties

$$(\gamma_5)^2 = \mathbb{I}\,, \qquad \gamma_5^\dagger = \gamma_5\,, \qquad \{\gamma_5, \gamma^\mu\} = 0\,. \tag{A.9}$$

Using the common Pauli matrices σ^i it is convenient to rewrite

$$\gamma^0 = \begin{pmatrix} 0 & \mathbb{I} \\ \mathbb{I} & 0 \end{pmatrix}, \qquad \gamma^i = \begin{pmatrix} 0 & \sigma^i \\ -\sigma^i & 0 \end{pmatrix}, \qquad \gamma^5 = \begin{pmatrix} -\mathbb{I} & 0 \\ 0 & \mathbb{I} \end{pmatrix}. \tag{A.10}$$

A.4 Dirac matrices (Euclidean)

Denoting the Minkowski gamma matrices shown in Appendix A.3 by γ^M we define their Euclidean equivalents γ_μ as

$$\gamma_i = -i\gamma_i^M, \qquad \gamma_4 = \gamma_0^M\,. \tag{A.11}$$

Analogous to (A.6) the Euclidean gamma matrices obey the anticommutation relation

$$\{\gamma_\mu, \gamma_\nu\} = 2\,\delta_{\mu\nu}\mathbb{I} \tag{A.12}$$

and we define γ_5 as

$$\gamma_5 = \gamma_1\gamma_2\gamma_3\gamma_4\,, \tag{A.13}$$

with the properties

$$(\gamma_5)^2 = \mathbb{I}\,, \qquad \gamma_5^\dagger = \gamma_5\,, \qquad \{\gamma_5, \gamma_\mu\} = 0\,. \tag{A.14}$$

In the Weyl (chiral) representation an explicit form is given by

$$\begin{aligned}
\gamma_1 &= \begin{pmatrix} 0 & 0 & 0 & -i \\ 0 & 0 & -i & 0 \\ 0 & i & 0 & 0 \\ i & 0 & 0 & 0 \end{pmatrix}, & \gamma_3 &= \begin{pmatrix} 0 & 0 & -i & 0 \\ 0 & 0 & 0 & i \\ i & 0 & 0 & 0 \\ 0 & -i & 0 & 0 \end{pmatrix}, \\
\gamma_2 &= \begin{pmatrix} 0 & 0 & 0 & -1 \\ 0 & 0 & 1 & 0 \\ 0 & 1 & 0 & 0 \\ -1 & 0 & 0 & 0 \end{pmatrix}, & \gamma_4 &= \begin{pmatrix} 0 & 0 & 1 & 0 \\ 0 & 0 & 0 & 1 \\ 1 & 0 & 0 & 0 \\ 0 & 1 & 0 & 0 \end{pmatrix},
\end{aligned} \tag{A.15}$$

and using the Pauli matrices σ_i yields

$$\gamma_4 = \begin{pmatrix} 0 & \mathbb{I} \\ \mathbb{I} & 0 \end{pmatrix}, \qquad \gamma_i = \begin{pmatrix} 0 & -i\sigma_i \\ i\sigma_i & 0 \end{pmatrix}, \qquad \gamma_5 = \begin{pmatrix} \mathbb{I} & 0 \\ 0 & -\mathbb{I} \end{pmatrix}. \tag{A.16}$$

We close this section with two general remarks about the replacements needed for four-vectors and covariant derivatives when going from Minkowski to Euclidean space

$$\begin{aligned}
x^0_{\mathrm{M}} &\to -i x^4_{\mathrm{E}}\,, & D^0_{\mathrm{M}} &\to i D^4_{\mathrm{E}}\,, \\
x^i_{\mathrm{M}} &\to x^i_{\mathrm{E}}\,, & D^0_{\mathrm{M}} &\to -D^i_{\mathrm{E}}\,.
\end{aligned} \tag{A.17}$$

A.5 Grassmann numbers

In this section we provide an excerpt about Grassmann numbers and properties of Grassmann variables following [93]. A more detailed textbook introduction can be found in, e.g., [260]. In general Grassmann numbers are anticommuting numbers

satisfying

$$\Theta\eta = -\eta\Theta\,, \tag{A.18}$$

so that the square for any Grassmann number is zero, i.e., the Taylor expansion of any function $f(\Theta) = A + B\Theta$, with commuting numbers A and B vanishes after the linear term. From this one can define the indefinite integral

$$\int \mathrm{d}\Theta\, \mathrm{f}(\Theta) = \int \mathrm{d}\Theta(\mathrm{A} + \mathrm{B}\Theta) = \mathrm{A}\int \mathrm{d}\Theta + \mathrm{B}\int \mathrm{d}\Theta\,\Theta\,, \tag{A.19}$$

where we require invariance under a shift $\Theta \to \Theta+\eta$ and thus immediately see that $\int \mathrm{d}\Theta = 0$. However, the second integral is arbitrary and we define $\int \mathrm{d}\Theta\,\Theta = 1$. For multiple integrals there is a sign ambiguity, and we define

$$\int \mathrm{d}\Theta \int \mathrm{d}\eta\,\eta\Theta = +1\,, \tag{A.20}$$

i.e., the innermost integral is performed first. Note that, however, the interchange of any two variables in the integrand as well as the interchange of $\mathrm{d}\Theta$ and $\mathrm{d}\eta$ would yield additional minus signs. Complex conjugation is defined by reversing the order of two complex Grassmann numbers

$$(\Theta\eta)^* = \eta^*\Theta^* = -\Theta^*\eta^*\,, \tag{A.21}$$

and for their integration we get

$$\int \mathrm{d}\Theta^*\mathrm{d}\Theta\,\Theta\Theta^* = 1\,. \tag{A.22}$$

Gaussian integrals over Grassmann numbers with a single complex variable are given by

$$\int \mathrm{d}\Theta^*\mathrm{d}\Theta\,\mathrm{e}^{-\Theta^*\mathrm{b}\Theta} = \mathrm{b}\,, \tag{A.23}$$

whereas in higher dimensions an integral is nonzero only if we have only one factor of Θ_i^* and Θ_i in the integrand. Further any integral is invariant under unitary transformations $\Theta_i' = U_{ij}\Theta_i$. Starting from $\prod_i \Theta_i' = \det U \prod_i \Theta_i$ one finds

$$\left(\prod_i \Theta_i'\right)\left(\prod_i \Theta_i'^*\right) = \det U\,(\det U)^*\left(\prod_i \Theta_i\right)\left(\prod_i \Theta_i^*\right)\,, \tag{A.24}$$

and similar for the measures. To compute Gaussian integrals containing a Hermitian matrix B we diagonalize B and get

$$\left(\prod_i \int \mathrm{d}\Theta_{\mathrm{i}}^* \mathrm{d}\Theta_{\mathrm{i}}\right) e^{-\Theta_i^* B_{ij} \Theta_j} = \det B\,, \tag{A.25}$$

$$\left(\prod_i \int \mathrm{d}\Theta_{\mathrm{i}}^* \mathrm{d}\Theta_{\mathrm{i}}\right) \Theta_k \Theta_l\, e^{-\Theta_i^* B_{ij} \Theta_j} = \det B \left(B^{-1}\right)_{kl}. \tag{A.26}$$

Finally, we state the following rules and conventions for derivatives

$$\frac{\partial}{\partial\Theta_i} 1 = 0, \quad \frac{\partial}{\partial\Theta_i}\Theta_i = 1, \quad \frac{\partial}{\partial\Theta_i}\frac{\partial}{\partial\Theta_j} = -\frac{\partial}{\partial\Theta_j}\frac{\partial}{\partial\Theta_i}, \quad \frac{\partial}{\partial\Theta_i}\Theta_j = -\Theta_j\frac{\partial}{\partial\Theta_i}. \tag{A.27}$$

A.6 Fourier transformation on the lattice

In this section we discuss the Fourier transformation $\widetilde{f}(p)$ of functions $f(n)$ on the lattice following [93].

For the function $f(n)$ we impose toroidal boundary conditions for each direction μ, i.e.,

$$f(n + \hat{\mu} N_\mu) = e^{i2\pi\Theta_\mu} f(n)\,, \tag{A.28}$$

Further $\hat{\mu}$ denotes the unit vector pointing in μ-direction and $\Theta_\mu = 0$ (periodic boundary conditions) and $\Theta_\mu = 1/2$ (open boundary conditions). The momentum space $\widetilde{\Lambda}$ corresponding to the lattice Λ introduced in Section 2.3 is defined as

$$\widetilde{\Lambda} = \left\{ p = (p_1, p_2, p_3, p_4) \middle| p_\mu = \frac{2\pi}{a N_\mu}\left(k_\mu + \Theta_\mu\right), k_\mu = -\frac{N_\mu}{2} + 1, \ldots, \frac{N_\mu}{2} \right\}. \tag{A.29}$$

If one now uses the algebraic property

$$\frac{1}{N}\sum_{N/2+1}^{N/2} e^{i\frac{2\pi}{N}lj} = \frac{1}{N}\sum_{j=0}^{N-1} e^{i\frac{2\pi}{N}lj} = \delta_{l0}\,, \tag{A.30}$$

we get the identities

$$\frac{1}{|\Lambda|}\sum_{p\in\widetilde{\Lambda}} e^{ip\cdot(n-n')a} = \delta(n-n') = \delta_{n_1,n_1'}\delta_{n_2,n_2'}\delta_{n_3,n_3'}\delta_{n_4,n_4'}\,, \tag{A.31}$$

$$\frac{1}{|\Lambda|}\sum_{n\in\Lambda} e^{i(p-p')\cdot na} = \delta(p-p') = \delta_{k_1,k_1'}\delta_{k_2,k_2'}\delta_{k_3,k_3'}\delta_{k_4,k_4'}\,, \tag{A.32}$$

by combining four times the one-dimensional sum in (A.30). Using these identities

the Fourier transformation and its inverse are defined by

$$\widetilde{f}(p) = \frac{1}{\sqrt{|\Lambda|}} \sum_{n\in\Lambda} e^{-ip\cdot na} f(n)\,, \tag{A.33}$$

$$f(n) = \frac{1}{\sqrt{|\Lambda|}} \sum_{p\in\widetilde{\Lambda}} e^{ip\cdot na} \widetilde{f}(p)\,. \tag{A.34}$$

A.7 Operator (anti-) symmetrization

In the computation we often use a shorthand notation to (anti-) symmetrize operators. Curly brackets around the indices denote the symmetrization of an operator

$$\hat{O}_{\{\mu_1\mu_2\ldots\mu_n\}} = \frac{1}{n!} \sum_{\pi\in S_n} \hat{O}_{\pi(\mu_1)\pi(\mu_2)\ldots\pi(\mu_n)}\,. \tag{A.35}$$

In general one finds $n!$ permutations and π is used to sum over all possible permutations.

Square brackets around the indices denote the anti-symmetrization of an operator

$$\hat{O}_{[\mu_1\mu_2\ldots\mu_n]} = \frac{1}{n!} \sum_{\pi\in S_n} \mathrm{sgn}(\pi)\hat{O}_{\pi(\mu_1)\pi(\mu_2)\ldots\pi(\mu_n)}\,. \tag{A.36}$$

In addition to the $n!$ permutations in S_n the contribution is multiplied by the signature of the permutation defined by

$$\mathrm{sgn}(\pi) = \begin{cases} +1 & \text{(even permutations)}, \\ -1 & \text{(odd permutations)}. \end{cases} \tag{A.37}$$

A.8 Light-cone coordinates and polarization vectors

This section is following [148]. We define light-cone coordinates in such a way that the perpendicular (or transverse) part of the momentum always vanishes, i.e., $p_T = 0$ and p_+ is its large component. To achieve this let v be any four-vector and $\hat{\boldsymbol{p}}$ the direction of the three-momentum. Then,

$$v^\mu = v^+ n_+^\mu + v^- n_-^\mu + v_T^\mu\,, \qquad \text{with} \quad n_\pm^\mu = \frac{1}{\sqrt{2}} \begin{pmatrix} 1 \\ \pm\hat{\boldsymbol{p}} \end{pmatrix}^\mu, \tag{A.38}$$

where $v^\pm = n_\mp \cdot v$ and

$$v_T^\mu = \begin{pmatrix} 0 \\ \boldsymbol{v_T} \end{pmatrix}^\mu , \qquad \text{with} \quad \boldsymbol{v}_T = \boldsymbol{v} - (\hat{\boldsymbol{p}} \cdot \boldsymbol{v})\hat{\boldsymbol{p}} , \tag{A.39}$$

such that $\boldsymbol{v}_T \perp \hat{\boldsymbol{p}}$. For the momentum we then have $p^\pm = E \pm |\boldsymbol{p}|$ and $p_T = 0$.

For the polarization vectors we use a dimensionless definition. They obey the general transversality condition

$$\sum_\lambda \epsilon_\mu(\boldsymbol{p},\lambda)\epsilon_\nu^*(\boldsymbol{p},\lambda) = -\left(g_{\mu\nu} - \frac{p_\mu p_\nu}{m^2}\right) , \tag{A.40}$$

where m is the hadron mass. For momenta in x direction the polarization vectors in the rest frame are given by $(0, \boldsymbol{e}_\lambda)$ with

$$\boldsymbol{e}_0^x = \boldsymbol{e}_0\Big|_{\hat{\boldsymbol{p}}=\hat{\boldsymbol{e}}_1} = \begin{pmatrix} 1 \\ 0 \\ 0 \end{pmatrix} , \qquad \boldsymbol{e}_\pm^x = \boldsymbol{e}_\pm\Big|_{\hat{\boldsymbol{p}}=\hat{\boldsymbol{e}}_1} = \frac{1}{\sqrt{2}} \begin{pmatrix} 0 \\ \mp 1 \\ -i \end{pmatrix} , \tag{A.41}$$

where $\boldsymbol{e}_0^x$ corresponds to the longitudinal polarization, while $\boldsymbol{e}_\pm^x$ to the circular polarizations. For momenta in an arbitrary direction, we have to rotate these vectors to

$$\boldsymbol{e}_0 = \hat{\boldsymbol{p}} , \qquad \boldsymbol{e}_\pm = \boldsymbol{e}_\pm^x - \frac{\hat{\boldsymbol{p}} \cdot \boldsymbol{e}_\pm^x}{1 + \hat{\boldsymbol{p}} \cdot \boldsymbol{e}_0^x}(\boldsymbol{e}_0^x + \hat{\boldsymbol{p}}) , \tag{A.42}$$

to obtain the longitudinal polarization vector $\boldsymbol{e}_0$ and the polarization vectors for the circular polarizations $\boldsymbol{e}_\pm$. Last but not least, we have to perform a boost to the laboratory frame. This only affects $\boldsymbol{e}_0$ ($\boldsymbol{e}_\pm$ are invariant because they are perpendicular to $\boldsymbol{p}$), and we obtain

$$\epsilon^\mu(\boldsymbol{p},0) = \begin{pmatrix} \frac{|\boldsymbol{p}|}{m} \\ \frac{E}{m}\hat{\boldsymbol{p}} \end{pmatrix}^\mu , \qquad \epsilon^\mu(\boldsymbol{p},\pm) = \begin{pmatrix} 0 \\ \boldsymbol{e}_\pm \end{pmatrix}^\mu . \tag{A.43}$$

In terms of the light-cone coordinates introduced above this yields

$$\epsilon^\pm(\boldsymbol{p},0) = \pm p^\pm/m , \qquad \epsilon_T^\mu(\boldsymbol{p},0) = 0 , \tag{A.44}$$

$$\epsilon^\pm(\boldsymbol{p},+) = 0 , \qquad \epsilon_T^\mu(\boldsymbol{p},+) = \epsilon^\mu(\boldsymbol{p},+) , \tag{A.45}$$

$$\epsilon^\pm(\boldsymbol{p},-) = 0 , \qquad \epsilon_T^\mu(\boldsymbol{p},-) = \epsilon^\mu(\boldsymbol{p},-) . \tag{A.46}$$

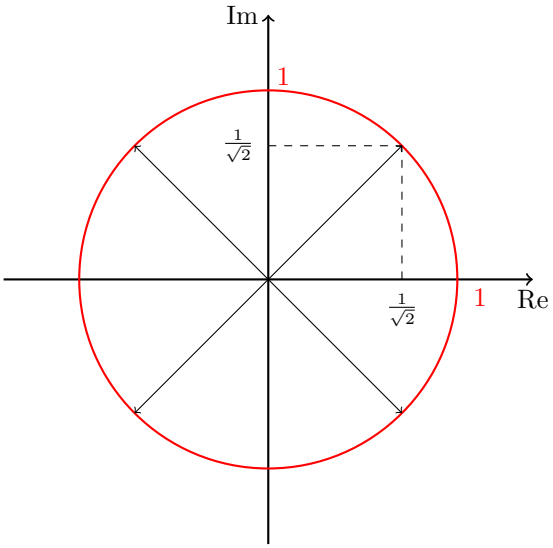

Figure A.9.1: Illustration of the $\mathbb{Z}_2$ noise vectors in the complex plane. Figure taken from [206].

A.9 Noise vectors

This section follows M. Löffler's masterthesis [206]. In Chapter 4 we use stochastic estimators to approximate all-to-all propagators in the computation of three-point correlation functions. From a general perspective one could use every set of noise vectors η that obeys

$$\frac{1}{N}\sum_{i=1}^{N}\left(\eta_i\right)(x)_a^{\alpha} = 0 + \mathcal{O}\left(\frac{1}{\sqrt{N}}\right), \tag{A.47}$$

$$\frac{1}{N}\sum_{i=1}^{N}\left(\eta_i\right)(x)_a^{\alpha}\left(\eta_i^*\right)(x')_{a'}^{\alpha'} = \delta_{xx'}\,\delta_{\alpha\alpha'}\,\delta_{aa'} + \mathcal{O}\left(\frac{1}{\sqrt{N}}\right). \tag{A.48}$$

However, following [210, 211] so-called $\mathbb{Z}_2$ noise vectors [209] η defined as

$$\left(\eta_i\right)_a^{\alpha}(x) \in \begin{cases} (\mathbb{Z}_2 \otimes \mathrm{i}\mathbb{Z}_2)/\sqrt{2} & \text{if } x_4 = \pm x_4', \\ 0 & \text{otherwise,} \end{cases} \tag{A.49}$$

are a particular good and numerical favorable choice. The additional factor $1/\sqrt{2}$ is introduced to obey (A.48). A graphical illustration is given in Fig. A.9.1. Altogether this yields the four possible tuples corresponding to values of the vectors in Equation A.49

$$\frac{\mathbb{Z}_2 \otimes \mathrm{i}\mathbb{Z}_2}{\sqrt{2}} = \left\{\frac{1}{\sqrt{2}}(1+i)\,;\,\frac{1}{\sqrt{2}}(1-i)\,;\,\frac{1}{\sqrt{2}}(-1+i)\,;\,\frac{1}{\sqrt{2}}(-1-i)\right\}. \tag{A.50}$$

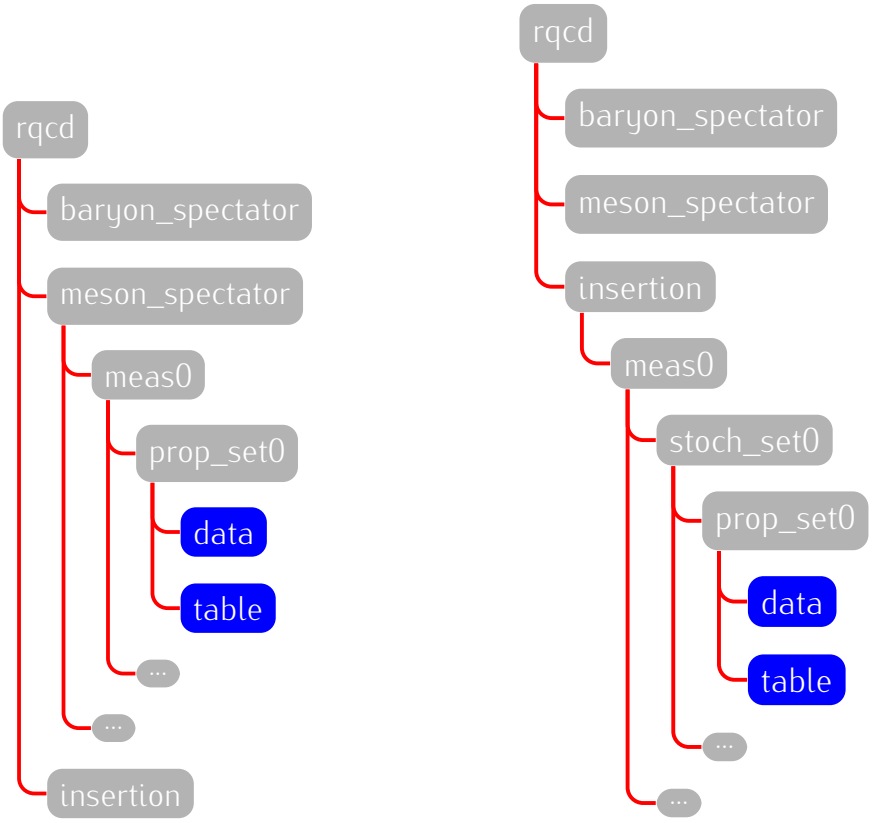

(a) Spectator part **(b)** Insertion part

Figure A.10.1: HDF5-file layout for LHA data. **(a)** depicts a simplified overview of the spectator data while **(b)** represents the insertion part.

A.10 LibHadronAnalysis output file layout

The output data of our production code introduced in Section 4.2.4 is stored in the HDF5-file format [261]. In this section we want to provide a simplified roadmap to find and thus extract data from our output files. The general file structure is depicted in Fig. A.10.1. HDF5-files can be illustrated in a simplified way as directory structures while in our case the base directory is always called *rqcd*. On the next level one finds the folders *baryon_spectator*, *meson_spectator*, and *insertion* denoting the measurements of the spectator and insertion parts respectively. Following the way down in Fig. A.10.1a and Fig. A.10.1b we find the *meas0* folder of the meson spectator and the insertion. In general there are n measurements, denoted by the dots at the end of the tree, depending on the number of flavor and smearing combinations used in the actual simulation. For the insertion part the next folder is called *stoch_set0* and reflects the stochastic index i of the insertion, so we get N_i such entries denoted by the dots at the end of the tree, cf. Tab. 4.2.2. Note that the stochastic index is set implicitly in the

prop_set of the spectator. The *prop_set0* entry finally reflects the source position of the individual propagators used in the individual measurements, i.e., we find N_{src} such folders. On the innermost level we get the data and the corresponding meta-information table to identify the individual rows of the data-set by their corresponding momenta, derivatives, operator timeslices, ... As a last remark, we want to state that real and imaginary parts of the numbers in the data-sets are stored alternately, i.e., $\text{Re}, \text{Im}, \text{Re}, \ldots$.

HDF5-files have many more (technical) features, which we cannot explain all within the scope of this thesis. However, with this introduction it should be possible for everyone to extract data from the files.

List of Figures

List of Tables

List of Acronyms

API application programming interface

BRST Becchi, Rouet, Stora, and Tyutin

BW Breit-Wigner

CLS Coordinated Lattice Simulations

DB database

DCSB dynamical chiral symmetry breaking

DGLAP Dokshitzer, Gribov, Lipatov, Altarelli, and Parisi

DIS deep inelastic scattering

GPT Grid Python Toolkit

GS Gounarius-Sakurai

HPE hopping parameter expansion

LHA LibHadronAnalysis

LQCD lattice QCD

$\overline{\text{MS}}$ modified minimal subtraction

OPE operator product expansion

PDF parton distribution function

QCD quantum chromodynamics

QED quantum electrodynamics

QFT quantum field theory

RG renormalization group

SIMD single instruction multiple data

SM standard model

TSM truncated solver method

UV ultra violet

XML extensible markup language

Bibliography

[1] J. J. Thomson, *XL. Cathode Rays*, The London, Edinburgh, and Dublin Philosophical Magazine and Journal of Science **44**, 293 (1897).

[2] J. J. Thomson, *LVII. On the charge of electricity carried by the ions produced by Röntgen rays*, The London, Edinburgh, and Dublin Philosophical Magazine and Journal of Science **46**, 528 (1898).

[3] J. J. Thomson, *LVIII. On the masses of the ions in gases at low pressures*, The London, Edinburgh, and Dublin Philosophical Magazine and Journal of Science **48**, 547 (1899).

[4] E. Rutherford, *LXXIX. The scattering of α and β particles by matter and the structure of the atom*, The London, Edinburgh, and Dublin Philosophical Magazine and Journal of Science **21**, 669 (1911).

[5] E. Rutherford and J. Chadwick, *The collected papers of Lord Rutherford of Nelson*, Vol. 1-3 (Allen & Unwin, 1962).

[6] M. Planck, *Zur Theorie des Gesetzes der Energieverteilung im Normalspektrum*, Verhandlungen der Deutschen Physikalische Gesellschaft **2**, 237 (1900).

[7] M. Planck, *Physikalische Abhandlungen und Vorträge* (Vieweg & Sohn, 1958).

[8] N. Bohr, *I. On the constitution of atoms and molecules*, The London, Edinburgh, and Dublin Philosophical Magazine and Journal of Science **26**, 1 (1913).

[9] M. Born and P. Jordan, *Zur Quantenmechanik*, Zeitschrift für Physik **34**, 858 (1925).

[10] W. Heisenberg, *Über quantentheoretische Umdeutung kinematischer und mechanischer Beziehungen*, Zeitschrift für Physik **33**, 879 (1925).

[11] W. Heisenberg, *Über den anschaulichen Inhalt der quantentheoretischen Kinematik und Mechanik*, Zeitschrift für Physik **43**, 172 (1927).

[12] M. Born, W. Heisenberg, and P. Jordan, *Zur Quantenmechanik II*, Zeitschrift für Physik **35**, 557 (1926).

[13] L. de Broglie, *Ondes et quanta. (French) [Waves and quanta]*, Comptes rendus de l'Académie des sciences, Paris **177**, 517 (1923).

[14] L. de Broglie, *Quanta de lumière, diffraction et interférences. (French) [Light quanta, diffraction, and interference]*, Comptes rendus de l'Académie des sciences, Paris **177**, 548 (1923).

[15] L. de Broglie, *Les quanta, la théorie cinétique des gas et le principe de Fermat. (French) [Quanta, the kinetic theory of gases, and the Fermat principle]*, Comptes rendus de l'Académie des sciences, Paris **177**, 630 (1923).

[16] L. de Broglie, *Recherches sur la théorie des quanta. (French) [Research on quantum theory]*, Ann. Physique, X. Sér **3**, 22 (1925), this is the author's doctoral dissertation.

[17] E. Schrödinger, *Quantisierung als Eigenwertproblem*, Annalen der Physik **384**, 361 (1926).

[18] E. Schrödinger, *Gesammelte Abhandlungen*, Vol. 1-4 (Österreichische Akademie der Wissenschaften, 1984).

[19] P. A. M. Dirac, *Quantum theory of emission and absorption of radiation*, Proc. Roy. Soc. Lond. A **114**, 243 (1927).

[20] S. Tomonaga, *On a Relativistically Invariant Formulation of the Quantum Theory of Wave Fields**, Progress of Theoretical Physics **1**, 27 (1946).

[21] R. P. Feynman, *A Relativistic Cut-Off for Classical Electrodynamics*, Phys. Rev. **74**, 939 (1948).

[22] J. Schwinger, *On Quantum-Electrodynamics and the Magnetic Moment of the Electron*, Phys. Rev. **73**, 416 (1948).

[23] F. J. Dyson, *The Radiation Theories of Tomonaga, Schwinger, and Feynman*, Phys. Rev. **75**, 486 (1949).

[24] L. Morel, Z. Yao, and P. Cladé, *Determination of the fine-structure constant with an accuracy of 81 parts per trillion*, Nature **588**, 61 (2020).

[25] T. Aoyama, M. Hayakawa, T. Kinoshita, and M. Nio, *Tenth-Order QED Contribution to the Electron g−2 and an Improved Value of the Fine Structure Constant*, Phys. Rev. Lett. **109**, 111807 (2012).

[26] T. Aoyama, T. Kinoshita, and M. Nio, *Theory of the Anomalous Magnetic Moment of the Electron*, Atoms **7**, 28 (2019).

[27] S. Laporta, *High-precision calculation of the 4-loop contribution to the electron g-2 in QED*, Physics Letters B **772**, 232 (2017).

[28] W. C. Röntgen, *Ueber eine neue art von strahlen*, Annalen der Physik **300**, 12 (1898).

[29] P. Curie and M. Sklodowska-Curie, *Sur une substance nouvelle radioactive contenue dans la pechblende. (French) [On a new radio-active substance contained in pitchblende]*, C R Acad Sci Paris **127**, 175 (1898).

[30] P. Curie, M. Curie, and Bémont, *Sur une nouvelle substance fortement radioactive contenue dans la pechblende. (French) [On a new, strongly radioactive substance contained in pitchblende]*, C R Acad Sci Paris **127**, 1215 (1898).

[31] E. Fermi, *An attempt of a theory of beta radiation. 1.*, Z. Phys. **88**, 161 (1934).

[32] S. L. Glashow, *Partial Symmetries of Weak Interactions*, Nucl. Phys. **22**, 579 (1961).

[33] A. Salam, *Weak and Electromagnetic Interactions*, Conf. Proc. C **680519**, 367 (1968).

[34] S. Weinberg, *A Model of Leptons*, Phys. Rev. Lett. **19**, 1264 (1967).

[35] G. Arnison *et al.* (UA1), *Experimental Observation of Isolated Large Transverse Energy Electrons with Associated Missing Energy at* $\sqrt{s} = 540$ *GeV*, Phys. Lett. B **122**, 103 (1983).

[36] M. Banner *et al.* (UA2), *Observation of Single Isolated Electrons of High Transverse Momentum in Events with Missing Transverse Energy at the CERN anti-p p Collider*, Phys. Lett. B **122**, 476 (1983).

[37] G. Arnison *et al.* (UA1), *Experimental Observation of Lepton Pairs of Invariant Mass Around 95-GeV/c**2 at the CERN SPS Collider*, Phys. Lett. B **126**, 398 (1983).

[38] P. Bagnaia *et al.* (UA2), *Evidence for $Z^0 \to e^+e^-$ at the CERN $\overline{p}p$ Collider*, Phys. Lett. B **129**, 130 (1983).

[39] D. Mohl, G. Petrucci, L. Thorndahl, and S. Van Der Meer, *Physics and Technique of Stochastic Cooling*, Phys. Rept. **58**, 73 (1980).

[40] H. Fritzsch, M. Gell-Mann, and H. Leutwyler, *Advantages of the Color Octet Gluon Picture*, Phys. Lett. B **47**, 365 (1973).

[41] M. Gell-Mann, *A Schematic Model of Baryons and Mesons*, Phys. Lett. **8**, 214 (1964).

[42] G. Zweig, *An SU(3) model for strong interaction symmetry and its breaking. Version 1* (1964).

[43] D. J. Gross and F. Wilczek, *Ultraviolet Behavior of Nonabelian Gauge Theories*, Phys. Rev. Lett. **30**, 1343 (1973).

[44] H. D. Politzer, *Reliable Perturbative Results for Strong Interactions?*, Phys. Rev. Lett. **30**, 1346 (1973).

[45] D. d'Enterria and P. Z. Skands, eds., *Proceedings, High-Precision α_s Measurements from LHC to FCC-ee: Geneva, Switzerland, October 2-13, 2015* (CERN, Geneva, 2015) arXiv:1512.05194 [hep-ph] .

[46] K. G. Wilson, *Confinement of Quarks*, Phys. Rev. D **10**, 2445 (1974).

[47] A. M. Jaffe, *The Millennium Grand Challenge in Mathematics*, Not. Amer. Math. Soc. **53**, 652 (2006).

[48] P. W. Higgs, *Broken symmetries, massless particles and gauge fields*, Phys. Lett. **12**, 132 (1964).

[49] P. W. Higgs, *Broken Symmetries and the Masses of Gauge Bosons*, Phys. Rev. Lett. **13**, 508 (1964).

[50] R. H. Parker, C. Yu, W. Zhong, B. Estey, and H. Müller, *Measurement of the fine-structure constant as a test of the Standard Model*, Science **360**, 191 (2018), arXiv:1812.04130 [physics.atom-ph] .

[51] P. Zyla *et al.* (PDG), *Review of Particle Physics*, Prog. Theor. Exp. Phys. **2020**, 083C01 (2020).

[52] J. D. Bjorken, *Asymptotic Sum Rules at Infinite Momentum*, Phys. Rev. **179**, 1547 (1969).

[53] J. Prentki and J. Steinberger, eds., *Proceedings, 14th International Conference on High-Energy Physics (ICHEP 68): Vienna, Austria, 28 Aug-5 Sep, 1968* (CERN, Geneva, 1968).

[54] R. P. Feynman, *Very high-energy collisions of hadrons*, Phys. Rev. Lett. **23**, 1415 (1969).

[55] J. D. Bjorken and E. A. Paschos, *Inelastic Electron Proton and gamma Proton Scattering, and the Structure of the Nucleon*, Phys. Rev. **185**, 1975 (1969).

[56] G. S. Bali, S. Collins, B. Glässle, S. Heybrock, P. Korcyl, M. Löffler, R. Rödl, and A. Schäfer, *Baryonic and mesonic 3-point functions with open spin indices*, EPJ Web Conf. **175**, 06014 (2018), arXiv:1711.02384 [hep-lat] .

[57] A. C. Aguilar *et al.*, *Pion and Kaon Structure at the Electron-Ion Collider*, Eur. Phys. J. A **55**, 190 (2019), arXiv:1907.08218 [nucl-ex] .

[58] D. Boer, *Overview of Spin Physics at EIC*, PoS **SPIN2018**, 167 (2019), arXiv:1903.01119 [hep-ph] .

[59] B. Adams *et al.*, *Letter of Intent: A New QCD facility at the M2 beam line of the CERN SPS (COMPASS++/AMBER)* (2018), arXiv:1808.00848 [hep-ex] .

[60] CERN, *Amber – a new qcd facility at the m2 beam line of the cern sps*, `https://nqf-m2.web.cern.ch/` (2021), [Online; accessed 29-July-2021].

[61] M. E. Peskin and D. V. Schroeder, *An Introduction to quantum field theory* (Addison-Wesley, Reading, USA, 1995).

[62] M. Gell-Mann, *The Eightfold Way: A Theory of strong interaction symmetry* (1961).

[63] S. Okubo, *Note on unitary symmetry in strong interactions*, Prog. Theor. Phys. **27**, 949 (1962).

[64] S. Okubo, *Note on Unitary Symmetry in Strong Interaction. II Excited States of Baryons*, Prog. Theor. Phys. **28**, 24 (1962).

[65] R. Aaij *et al.* (LHCb), *Observation of $J/\psi p$ Resonances Consistent with Pentaquark States in $\Lambda_b^0 \to J/\psi K^- p$ Decays*, Phys. Rev. Lett. **115**, 072001 (2015), arXiv:1507.03414 [hep-ex] .

[66] R. Aaij *et al.* (LHCb), *Observation of a narrow pentaquark state, $P_c(4312)^+$, and of two-peak structure of the $P_c(4450)^+$*, Phys. Rev. Lett. **122**, 222001 (2019), arXiv:1904.03947 [hep-ex] .

[67] R. Aaij *et al.* (LHCb), *Observation of structure in the J/ψ -pair mass spectrum*, Sci. Bull. **65**, 1983 (2020), arXiv:2006.16957 [hep-ex] .

[68] S. L. Olsen, T. Skwarnicki, and D. Zieminska, *Nonstandard heavy mesons and baryons: Experimental evidence*, Rev. Mod. Phys. **90**, 015003 (2018), arXiv:1708.04012 [hep-ph] .

[69] L. D. Faddeev and V. N. Popov, *Feynman Diagrams for the Yang-Mills Field*, Phys. Lett. B **25**, 29 (1967).

[70] C. Becchi, A. Rouet, and R. Stora, *Renormalization of gauge theories*, Annals of Physics **98**, 287 (1976).

[71] I. V. Tyutin, *Gauge Invariance in Field Theory and Statistical Physics in Operator Formalism* (1975), arXiv:0812.0580 [hep-th] .

[72] Wilczek, F., *How Feynman Diagrams Almost Saved Space*, `https://www.quantamagazine.org/why-feynman-diagrams-are-so-important-20160705/` (2016), [Online; accessed 25-August-2021].

[73] R. P. Feynman, *Space-time approach to nonrelativistic quantum mechanics*, Rev. Mod. Phys. **20**, 367 (1948).

[74] R. P. Feynman, *QED: The Strange Theory of Light and Matter* (Princeton University Press, 2014).

[75] J. C. Collins, *Renormalization: An Introduction to Renormalization, The Renormalization Group, and the Operator Product Expansion*, Cambridge Monographs on Mathematical Physics, Vol. 26 (Cambridge University Press, Cambridge, 1986).

[76] R. K. Ellis, in *1987 Theoretical Advanced Study Institute in Elementary Particle Physics (TASI 87)* (1988).

[77] G. 't Hooft and M. J. G. Veltman, *Regularization and Renormalization of Gauge Fields*, Nucl. Phys. B **44**, 189 (1972).

[78] W. A. Bardeen, A. J. Buras, D. W. Duke, and T. Muta, *Deep Inelastic Scattering Beyond the Leading Order in Asymptotically Free Gauge Theories*, Phys. Rev. D **18**, 3998 (1978).

[79] J. I. Friedman and H. W. Kendall, *Deep inelastic electron scattering*, Ann. Rev. Nucl. Part. Sci. **22**, 203 (1972).

[80] J. Callan, C.G. and D. Gross, *High-energy electroproduction and the constitution of the electric current*, Phys. Rev. Lett. **22**, 156 (1969).

[81] X.-D. Ji, *Off forward parton distributions*, J. Phys. G **24**, 1181 (1998), arXiv:hep-ph/9807358 .

[82] M. Diehl, *Generalized parton distributions*, Phys. Rept. **388**, 41 (2003), arXiv:hep-ph/0307382 .

[83] M. Constantinou, *The x-dependence of hadronic parton distributions: A review on the progress of lattice QCD*, Eur. Phys. J. A **57**, 77 (2021), arXiv:2010.02445 [hep-lat] .

[84] G. Altarelli and G. Parisi, *Asymptotic freedom in parton language*, Nucl. Phys. B **126**, 298 (1977).

[85] V. Gribov and L. Lipatov, *Deep inelastic ep scattering in perturbation theory*, Sov. J. Nucl. Phys. **15**, 438 (1972).

[86] Y. Dokshitzer, *Calculation of the structure functions for deep inelastic scattering and e^+e^- annihilation by perturbation theory in quantum chromodynamics*, Sov. Phys. JETP **46**, 641 (1977).

[87] S. Chekanov *et al.* (ZEUS), *Leading neutron production in e^+ p collisions at HERA*, Nucl. Phys. B **637**, 3 (2002), arXiv:hep-ex/0205076 .

[88] F. Aaron *et al.* (H1), *Measurement of leading neutron production in deep-inelastic scattering at HERA*, Eur. Phys. J. C **68**, 381 (2010), arXiv:1001.0532 [hep-ex] .

[89] R. Montgomery, J. Annand, D. Dutta, C. Keppel, P. King, B. Wojtsekhowski, and J. Zhang (TDIS, SBS), *Proposed Measurement of Tagged Deep Inelastic Scattering in Hall A of Jefferson lab*, AIP Conf. Proc. **1819**, 030004 (2017).

[90] J. C. Collins and D. E. Soper, *Back-To-Back Jets in QCD*, Nucl. Phys. B **193**, 381 (1981), [Erratum: Nucl.Phys.B 213, 545 (1983)].

[91] J. C. Collins, D. E. Soper, and G. F. Sterman, *Transverse Momentum Distribution in Drell-Yan Pair and W and Z Boson Production*, Nucl. Phys. B **250**, 199 (1985).

[92] J. Collins, *Foundations of perturbative QCD*, Vol. 32 (Cambridge University Press, 2013).

[93] C. Gattringer and C. B. Lang, *Quantum chromodynamics on the lattice*, Vol. 788 (Springer, Berlin, 2010).

[94] T. DeGrand and C. E. Detar, *Lattice methods for quantum chromodynamics* (World Scientific Publishing Company, 2006).

[95] I. Montvay and G. Munster, *Quantum fields on a lattice*, Cambridge Monographs on Mathematical Physics (Cambridge University Press, 1997).

[96] R. Hamming, *Numerical Methods for Scientists and Engineers*, International series in pure and applied mathematics (McGraw-Hill, 1962).

[97] R. Gupta, in *Les Houches Summer School in Theoretical Physics, Session 68: Probing the Standard Model of Particle Interactions* (1997) arXiv:hep-lat/9807028 .

[98] M. Bochicchio, L. Maiani, G. Martinelli, G. C. Rossi, and M. Testa, *Chiral Symmetry on the Lattice with Wilson Fermions*, Nucl. Phys. B **262**, 331 (1985).

[99] K. Symanzik, *Continuum Limit and Improved Action in Lattice Theories. 1. Principles and phi**4 Theory*, Nucl. Phys. B **226**, 187 (1983).

[100] K. Symanzik, *Continuum Limit and Improved Action in Lattice Theories. 2. O(N) Nonlinear Sigma Model in Perturbation Theory*, Nucl. Phys. B **226**, 205 (1983).

[101] M. Luscher and P. Weisz, *On-Shell Improved Lattice Gauge Theories*, Commun. Math. Phys. **97**, 59 (1985), [Erratum: Commun.Math.Phys. 98, 433 (1985)].

[102] B. Sheikholeslami and R. Wohlert, *Improved Continuum Limit Lattice Action for QCD with Wilson Fermions*, Nucl. Phys. B **259**, 572 (1985).

[103] R. P. Feynman and A. R. Hibbs, *Quantum mechanics and path integrals*, International series in pure and applied physics (McGraw-Hill, New York, NY, 1965).

[104] K. Osterwalder and E. Seiler, *Gauge Field Theories on the Lattice*, Annals Phys. **110**, 440 (1978).

[105] M. Luscher, *Construction of a Selfadjoint, Strictly Positive Transfer Matrix for Euclidean Lattice Gauge Theories*, Commun. Math. Phys. **54**, 283 (1977).

[106] H. R. Schwarz and N. Köckler, Numerische integration, in *Numerische Mathematik* (Vieweg+Teubner Verlag, Wiesbaden, 2011) pp. 307–341.

[107] C. Jacobi, *Ueber gauSS neue methode, die werthe der integrale näherungsweise zu finden.*, Journal für die reine und angewandte Mathematik **1826**, 301 (1826).

[108] M. Matsumoto and T. Nishimura, *Mersenne Twister: A 623-Dimensionally Equidistributed Uniform Pseudo-Random Number Generator*, ACM Trans. Model. Comput. Simul. **8**, 330 (1998).

[109] M. Luscher, *A Portable high quality random number generator for lattice field theory simulations*, Comput. Phys. Commun. **79**, 100 (1994), arXiv:hep-lat/9309020 .

[110] J. von Neumann, in *Monte Carlo Method*, National Bureau of Standards Applied Mathematics Series, Vol. 12, edited by A. S. Householder, G. E. Forsythe, and H. H. Germond (US Government Printing Office, Washington, DC, 1951) Chap. 13, pp. 36–38.

[111] N. Metropolis, A. W. Rosenbluth, M. N. Rosenbluth, A. H. Teller, and E. Teller, *Equation of state calculations by fast computing machines*, J. Chem. Phys. **21**, 1087 (1953).

[112] M. Creutz, *Monte Carlo Study of Quantized SU(2) Gauge Theory*, Phys. Rev. D **21**, 2308 (1980).

[113] S. Duane, A. D. Kennedy, B. J. Pendleton, and D. Roweth, *Hybrid Monte Carlo*, Phys. Lett. B **195**, 216 (1987).

[114] R. Sommer, *A New way to set the energy scale in lattice gauge theories and its applications to the static force and alpha-s in SU(2) Yang-Mills theory*, Nucl. Phys. B **411**, 839 (1994), arXiv:hep-lat/9310022 .

[115] M. Lüscher, *Properties and uses of the Wilson flow in lattice QCD*, JHEP **08**, 071 (2010), [Erratum: JHEP 03, 092 (2014)], arXiv:1006.4518 [hep-lat] .

[116] Carlos Pena, *CLS*, `https://wiki-zeuthen.desy.de/CLS/` (2014), [Online; accessed 10-August-2021].

[117] M. Bruno *et al.*, *Simulation of QCD with $N_f = 2 + 1$ flavors of non-perturbatively improved Wilson fermions*, JHEP **02**, 043 (2015), arXiv:1411.3982 [hep-lat] .

[118] M. Lüscher and S. Schaefer, *Lattice QCD without topology barriers*, JHEP **07**, 036 (2011), arXiv:1105.4749 [hep-lat] .

[119] M. Luscher and S. Schaefer, *Lattice QCD with open boundary conditions and twisted-mass reweighting*, Comput. Phys. Commun. **184**, 519 (2013), arXiv:1206.2809 [hep-lat] .

[120] J. Bulava and S. Schaefer, *Improvement of $N_f = 3$ lattice QCD with Wilson fermions and tree-level improved gauge action*, Nucl. Phys. B **874**, 188 (2013), arXiv:1304.7093 [hep-lat] .

[121] M. Luscher, S. Sint, R. Sommer, and P. Weisz, *Chiral symmetry and O(a) improvement in lattice QCD*, Nucl. Phys. B **478**, 365 (1996), arXiv:hep-lat/9605038 .

[122] M. Gell-Mann, R. J. Oakes, and B. Renner, *Behavior of current divergences under SU(3) x SU(3)*, Phys. Rev. **175**, 2195 (1968).

[123] O. Bar and M. Golterman, *Chiral perturbation theory for gradient flow observables*, Phys. Rev. D **89**, 034505 (2014), [Erratum: Phys.Rev.D 89, 099905 (2014)], arXiv:1312.4999 [hep-lat] .

[124] K. Jansen, C. Liu, M. Luscher, H. Simma, S. Sint, R. Sommer, P. Weisz, and U. Wolff, *Nonperturbative renormalization of lattice QCD at all scales*, Phys. Lett. B **372**, 275 (1996), arXiv:hep-lat/9512009 .

[125] G. Bali, E. Scholz, J. Simeth, and W. Söldner (RQCD), *Lattice simulations with $N_f = 2 + 1$ improved Wilson fermions at a fixed strange quark mass*, Phys. Rev. D **94**, 074501 (2016), arXiv:1606.09039 [hep-lat] .

[126] M. Luscher and F. Palombi, *Fluctuations and reweighting of the quark determinant on large lattices*, PoS **LATTICE2008**, 049 (2008), arXiv:0810.0946 [hep-lat] .

[127] G. S. Bali *et al.*, *Scale setting and the light hadron spectrum in $N_f = 2 + 1$ QCD with Wilson fermions* (t.b.p.), in preparation.

[128] M. Hasenbusch, *Speeding up the hybrid Monte Carlo algorithm for dynamical fermions*, Phys. Lett. B **519**, 177 (2001), arXiv:hep-lat/0107019 .

[129] M. Hasenbusch and K. Jansen, *Speeding up lattice QCD simulations with clover improved Wilson fermions*, Nucl. Phys. B **659**, 299 (2003), arXiv:hep-lat/0211042 .

[130] A. D. Kennedy, I. Horvath, and S. Sint, *A New exact method for dynamical fermion computations with nonlocal actions*, Nucl. Phys. B Proc. Suppl. **73**, 834 (1999), arXiv:hep-lat/9809092 .

[131] M. A. Clark and A. D. Kennedy, *Accelerating dynamical fermion computations using the rational hybrid Monte Carlo (RHMC) algorithm with multiple pseudofermion fields*, Phys. Rev. Lett. **98**, 051601 (2007), arXiv:hep-lat/0608015 .

[132] D. Mohler and S. Schaefer, *Remarks on strange-quark simulations with Wilson fermions*, Phys. Rev. D **102**, 074506 (2020), arXiv:2003.13359 [hep-lat] .

[133] J. C. Sexton and D. H. Weingarten, *Hamiltonian evolution for the hybrid Monte Carlo algorithm*, Nucl. Phys. B **380**, 665 (1992).

[134] M. Lüscher, *openqcd — simulation programs for lattice qcd*, `https://luscher.web.cern.ch/luscher/openQCD/`, [Online; accessed 17-September-2021].

[135] S. Borsanyi *et al.*, *High-precision scale setting in lattice QCD*, JHEP **09** (2012), 010, arXiv:1203.4469 [hep-lat] .

[136] M. Bruno, T. Korzec, and S. Schaefer, *Setting the scale for the CLS* $2 + 1$ *flavor ensembles*, Phys. Rev. D **95**, 074504 (2017), arXiv:1608.08900 [hep-lat] .

[137] S. Aoki *et al.* (PACS-CS), *Physical Point Simulation in 2+1 Flavor Lattice QCD*, Phys. Rev. D **81**, 074503 (2010), arXiv:0911.2561 [hep-lat] .

[138] W. Bietenholz *et al.*, *Tuning the strange quark mass in lattice simulations*, Phys. Lett. B **690**, 436 (2010), arXiv:1003.1114 [hep-lat] .

[139] H.-W. Lin *et al.* (Hadron Spectrum), *First results from 2+1 dynamical quark flavors on an anisotropic lattice: Light-hadron spectroscopy and setting the strange-quark mass*, Phys. Rev. D **79**, 034502 (2009), arXiv:0810.3588 [hep-lat] .

[140] R. Baron *et al.*, *Light hadrons from lattice QCD with light (u,d), strange and charm dynamical quarks*, JHEP **06**, 111 (2010), arXiv:1004.5284 [hep-lat] .

[141] A. Bazavov *et al.* (MILC), *Lattice QCD Ensembles with Four Flavors of Highly Improved Staggered Quarks*, Phys. Rev. D **87**, 054505 (2013), arXiv:1212.4768 [hep-lat] .

[142] S. Aoki *et al.* (JLQCD), *Two-flavor QCD simulation with exact chiral symmetry*, Phys. Rev. D **78**, 014508 (2008), arXiv:0803.3197 [hep-lat] .

[143] R. Arthur *et al.* (RBC, UKQCD), *Domain Wall QCD with Near-Physical Pions*, Phys. Rev. D **87**, 094514 (2013), arXiv:1208.4412 [hep-lat] .

[144] B. Efron, *Computers and the Theory of Statistics: Thinking the Unthinkable*, SIAM Review **21**, 460 (1979).

[145] C. Keppel *et al.*, *Measurement of Tagged Deep Inelastic Scattering (TDIS): Hall A and SBS Collaboration Proposal* (2015), PR12-15-006.

[146] A. Manohar, *An introduction to spin dependent deep inelastic scattering* (1992), arXiv:hep-ph/9204208 .

[147] P. Hoodbhoy, R. Jaffe, and A. Manohar, *Novel effects in deep inelastic scattering from spin-one hadrons*, Nucl. Phys. B **312**, 571 (1989).

[148] M. Löffler, P. Wein, T. Wurm, S. Weishäupl, D. Jenkins, R. Rödl, A. Schäfer, and L. Walter (RQCD Collaboration), *Mellin moments of spin dependent and independent PDFs of the pion and rho meson*, Phys. Rev. D **105**, 014505 (2022), arXiv:2108.07544 [hep-lat] .

[149] K. Blum, *Density matrix theory and applications; 3rd ed.*, Springer series on atomic, optical, and plasma physics (Springer, Berlin, 2012).

[150] D. Rubin, *Physics P6574 - Quantum Mechanics II - Spring 2015*, `https://www.classe.cornell.edu/~dlr/teaching/p6574/lectures/lecture1.pdf` (2015), [Online; accessed 17-September-2021].

[151] R. L. Jaffe, in *Ettore Majorana International School of Nucleon Structure: 1st Course: The Spin Structure of the Nucleon* (1996) pp. 42–129, arXiv:hep-ph/9602236 .

[152] P. Hoodbhoy and X.-D. Ji, *Helicity flip off forward parton distributions of the nucleon*, Phys. Rev. D **58**, 054006 (1998), arXiv:hep-ph/9801369 .

[153] M. Diehl, *Generalized parton distributions with helicity flip*, Eur. Phys. J. C **19**, 485 (2001), arXiv:hep-ph/0101335 .

[154] C. Best, M. Göckeler, R. Horsley, E.-M. Ilgenfritz, H. Perlt, P. Rakow, A. Schäfer, G. Schierholz, A. Schiller, and S. Schramm, *π and ρ structure functions from lattice QCD*, Phys. Rev. D **56**, 2743 (1997), arXiv:hep-lat/9703014 .

[155] X. Ji, *Gauge-Invariant Decomposition of Nucleon Spin*, Phys. Rev. Lett. **78**, 610 (1997), arXiv:hep-ph/9603249 .

[156] R. L. Jaffe and A. Manohar, *Deep Inelastic Scattering from Arbitrary Spin Targets*, Nucl. Phys. B **321**, 343 (1989).

[157] E. Sather and C. Schmidt, *Size and scaling of the double helicity flip hadronic structure function*, Phys. Rev. D **42**, 1424 (1990).

[158] J. D. Sullivan, *One-Pion Exchange and Deep-Inelastic Electron-Nucleon Scattering*, Phys. Rev. D **5**, 1732 (1972).

[159] B. Betev *et al.* (NA10), *Differential Cross-Section of High Mass Muon Pairs Produced by a* 194 GeV/c π^- *Beam on a Tungsten Target*, Z. Phys. C **28**, 9 (1985).

[160] H. B. Greenlee *et al.*, *The Production of Massive Muon Pairs in π^--Nucleus Collisions*, Phys. Rev. Lett. **55**, 1555 (1985).

[161] J. S. Conway *et al.*, *Experimental study of muon pairs produced by 252-GeV pions on tungsten*, Phys. Rev. D **39**, 92 (1989).

[162] M. Aghasyan *et al.* (COMPASS), *First Measurement of Transverse-Spin-Dependent Azimuthal Asymmetries in the Drell-Yan Process*, Phys. Rev. Lett. **119**, 112002 (2017), arXiv:1704.00488 [hep-ex] .

[163] H. Holtmann, G. Levman, N. N. Nikolaev, A. Szczurek, and J. Speth, *How to measure the pion structure function at HERA*, Phys. Lett. B **338**, 363 (1994).

[164] J. R. McKenney, N. Sato, W. Melnitchouk, and C.-R. Ji, *Pion structure function from leading neutron electroproduction and SU(2) flavor asymmetry*, Phys. Rev. D **93**, 054011 (2016), arXiv:1512.04459 [hep-ph] .

[165] P. C. Barry, N. Sato, W. Melnitchouk, and C.-R. Ji, *First Monte Carlo Global QCD Analysis of Pion Parton Distributions*, Phys. Rev. Lett. **121**, 152001 (2018), arXiv:1804.01965 [hep-ph] .

[166] C. Best, M. Göckeler, R. Horsley, H. Perlt, P. Rakow, A. Schäfer, G. Schierholz, A. Schiller, and S. Schramm, *The Deep-Inelastic Structure Functions of π and ρ Mesons*, Nucl. Phys. B (Proc. Suppl.) **63A-C**, 236 (1998), arXiv:hep-lat/9710037 .

[167] C. Best *et al.*, *Hadron structure functions from lattice QCD - 1997*, AIP Conf. Proc. **407**, 997 (1997), arXiv:hep-ph/9706502 .

[168] X.-D. Ji, private communication (2021), [July-2021].

[169] A. Airapetian *et al.* (HERMES), *Measurement of the Tensor Structure Function b(1) of the Deuteron*, Phys. Rev. Lett. **95**, 242001 (2005), arXiv:hep-ex/0506018 .

[170] F. E. Close and S. Kumano, *Sum rule for the spin-dependent structure function $b_1(x)$ for spin-one hadrons*, Phys. Rev. D **42**, 2377 (1990).

[171] S. Kumano and Q.-T. Song, *Estimate on Spin Asymmetry for Drell-Yan Process at Fermilab with Tensor-Polarized Deuteron*, JPS Conf. Proc. **13**, 020048 (2017), arXiv:1611.00474 [hep-ph] .

[172] K. Alleda *et al.*, *The Deuteron Tensor Structure Function b_1: A Proposal to Jefferson Lab PAC-40* (2013), PR12-13-011.

[173] Q.-T. Song, *Structure of Deuteron by Polarized Proton-Deuteron Drell-Yan Process*, JPS Conf. Proc. **26**, 031001 (2019).

[174] G. Martinelli and C. T. Sachrajda, *Pion structure functions from lattice QCD*, Phys. Lett. B **196**, 184 (1987).

[175] G. Martinelli and C. T. Sachrajda, *A lattice calculation of the pion's form-factor and structure function*, Nucl. Phys. B **306**, 865 (1988).

[176] M. Guagnelli, K. Jansen, F. Palombi, R. Petronzio, A. Shindler, and I. Wetzorke (ZeRo), *Non-perturbative pion matrix element of a twist-2 operator from the lattice*, Eur. Phys. J. C **40**, 69 (2005), arXiv:hep-lat/0405027 .

[177] S. Capitani, K. Jansen, M. Papinutto, A. Shindler, C. Urbach, and I. Wetzorke, *Parton distribution functions with twisted mass fermions*, Phys. Lett. B **639**, 520 (2006), arXiv:hep-lat/0511013 .

[178] D. Brömmel *et al.* (QCDSF/UKQCD), *Quark distributions in the pion*, PoS **LATTICE2007**, 140 (2008).

[179] G. S. Bali, S. Collins, B. Glässle, M. Göckeler, N. Javadi-Motaghi, J. Najjar, W. Söldner, and A. Sternbeck, *Pion structure from lattice QCD*, PoS **LATTICE2013**, 447 (2014), arXiv:1311.7639 [hep-lat] .

[180] A. Abdel-Rehim *et al.*, *Nucleon and pion structure with lattice QCD simulations at physical value of the pion mass*, Phys. Rev. D **92**, 114513 (2015), [Erratum: Phys. Rev. D **93**, 039904(E) (2016)], arXiv:1507.04936 [hep-lat] .

[181] M. Oehm, C. Alexandrou, M. Constantinou, K. Jansen, G. Koutsou, B. Kostrzewa, F. Steffens, C. Urbach, and S. Zafeiropoulos, *$\langle x \rangle$ and $\langle x^2 \rangle$ of the pion PDF from lattice QCD with $N_f = 2 + 1 + 1$ dynamical quark flavors*, Phys. Rev. D **99**, 014508 (2019), arXiv:1810.09743 [hep-lat] .

[182] C. Alexandrou, S. Bacchio, I. Clöet, M. Constantinou, K. Hadjiyiannakou, G. Koutsou, and C. Lauer, *The Mellin moments $\langle x \rangle$ and $\langle x^2 \rangle$ for the pion and kaon from lattice QCD* (2020), arXiv:2010.03495 [hep-lat] .

[183] C. Alexandrou, S. Bacchio, I. Cloët, M. Constantinou, K. Hadjiyiannakou, G. Koutsou, and C. Lauer (ETM), *The pion and kaon $\langle x^3 \rangle$ from lattice QCD and PDF reconstruction from Mellin moments* (2021), arXiv:2104.02247 [hep-lat] .

[184] X. Ji, *Parton Physics on a Euclidean Lattice*, Phys. Rev. Lett. **110**, 262002 (2013), arXiv:1305.1539 [hep-ph] .

[185] R. S. Sufian, J. Karpie, C. Egerer, K. Orginos, J.-W. Qiu, and D. G. Richards, *Pion valence quark distribution from matrix element calculated in lattice QCD*, Phys. Rev. D **99**, 074507 (2019), arXiv:1901.03921 [hep-lat] .

[186] R. S. Sufian, C. Egerer, J. Karpie, R. G. Edwards, B. Joó, Y.-Q. Ma, K. Orginos, J.-W. Qiu, and D. G. Richards, *Pion valence quark distribution from current-current correlation in lattice QCD*, Phys. Rev. D **102**, 054508 (2020), arXiv:2001.04960 [hep-lat] .

[187] J.-H. Zhang, J.-W. Chen, L. Jin, H.-W. Lin, A. Schäfer, and Y. Zhao, *First direct lattice-QCD calculation of the x-dependence of the pion parton distribution function*, Phys. Rev. D **100**, 034505 (2019), arXiv:1804.01483 [hep-lat] .

[188] T. Izubuchi, L. Jin, C. Kallidonis, N. Karthik, S. Mukherjee, P. Petreczky, C. Shugert, and S. Syritsyn, *Valence parton distribution function of pion from fine lattice*, Phys. Rev. D **100**, 034516 (2019), arXiv:1905.06349 [hep-lat] .

[189] B. Joó, J. Karpie, K. Orginos, A. V. Radyushkin, D. G. Richards, R. S. Sufian, and S. Zafeiropoulos, *Pion valence structure from Ioffe-time parton pseudodistribution functions*, Phys. Rev. D **100**, 114512 (2019), arXiv:1909.08517 [hep-lat] .

[190] R. Babich, J. Brannick, R. C. Brower, M. A. Clark, T. A. Manteuffel, S. F. McCormick, J. C. Osborn, and C. Rebbi, *Adaptive multigrid algorithm for the lattice Wilson-Dirac operator*, Phys. Rev. Lett. **105**, 201602 (2010), arXiv:1005.3043 [hep-lat] .

[191] A. Frommer, K. Kahl, S. Krieg, B. Leder, and M. Rottmann, *Adaptive aggregation based domain decomposition multigrid for the lattice Wilson Dirac operator*, SIAM J. Sci. Comput. **36**, A1581 (2014), arXiv:1303.1377 [hep-lat] .

[192] S. Heybrock, M. Rottmann, P. Georg, and T. Wettig, *Adaptive algebraic multigrid on SIMD architectures*, PoS **LATTICE2015**, 036 (2016), arXiv:1512.04506 [physics.comp-ph] .

[193] D. Richtmann, S. Heybrock, and T. Wettig, *Multiple right-hand-side setup for the DD-αAMG*, PoS **LATTICE2015**, 035 (2016), arXiv:1601.03184 [hep-lat] .

[194] P. Georg, D. Richtmann, and T. Wettig, *pMR: A high-performance communication library*, PoS **LATTICE2016**, 361 (2017), arXiv:1701.08521 [hep-lat] .

[195] P. Georg, D. Richtmann, and T. Wettig, *DD-αAMG on QPACE 3*, EPJ Web Conf. **175**, 02007 (2018), arXiv:1710.07041 [hep-lat] .

[196] M. Lüscher, *Local coherence and deflation of the low quark modes in lattice QCD*, JHEP **07**, 081 (2007), arXiv:0706.2298 [hep-lat] .

[197] M. Lüscher, *Deflation acceleration of lattice QCD simulations*, JHEP **12**, 011 (2007), arXiv:0710.5417 [hep-lat] .

[198] S. Güsken, *A study of smearing techniques for hadron correlation functions*, Nucl. Phys. B (Proc. Suppl.) **17**, 361 (1990).

[199] M. Falcioni, M. L. Paciello, G. Parisi, and B. Taglienti, *Again on SU(3) glueball mass*, Nucl. Phys. B **251**, 624 (1985).

[200] G. S. Bali, S. Collins, and C. Ehmann, *Charmonium spectroscopy and mixing with light quark and open charm states from n_F=2 lattice QCD*, Phys. Rev. D **84**, 094506 (2011), arXiv:1110.2381 [hep-lat] .

[201] G. S. Bali, L. Barca, S. Collins, M. Gruber, M. Löffler, A. Schäfer, W. Söldner, P. Wein, S. Weishäupl, and T. Wurm (RQCD), *Nucleon axial structure from lattice QCD*, JHEP **05**, 126 (2020), arXiv:1911.13150 [hep-lat] .

[202] G. S. Bali, V. Braun, S. Collins, A. Schäfer, and J. Simeth (RQCD), *Masses and decay constants of the η and η' mesons from lattice QCD*, JHEP **08**, 137 (2021), arXiv:2106.05398 [hep-lat] .

[203] R. G. Edwards and B. Joó (SciDAC, LHPC, UKQCD), *The Chroma Software System for Lattice QCD*, Nucl. Phys. B (Proc. Suppl.) **140**, 832 (2005), arXiv:hep-lat/0409003 .

[204] G. Kallen, *On the definition of the Renormalization Constants in Quantum Electrodynamics*, Helv. Phys. Acta **25**, 417 (1952).

[205] H. Lehmann, *On the Properties of propagation functions and renormalization contants of quantized fields*, Nuovo Cim. **11**, 342 (1954).

[206] M. Löffler, *Mesonic Three-Point Functions with open Spin Indices* (2017), this is the author's masterthesis.

[207] R. H. Rödl, *Nucleon generalized form factors from two-flavor lattice QCD and stochastic three-point functions with open indices*, Ph.D. thesis, Regensburg U. (2020).

[208] G. Martinelli and C. T. Sachrajda, *A Lattice Study of Nucleon Structure*, Nucl. Phys. B **316**, 355 (1989).

[209] S.-J. Dong and K.-F. Liu, *Stochastic estimation with Z(2) noise*, Phys. Lett. B **328**, 130 (1994), arXiv:hep-lat/9308015 .

[210] G. S. Bali, S. Collins, B. Gläßle, M. Göckeler, J. Najjar, R. Rödl, A. Schäfer, A. Sternbeck, and W. Söldner, *Nucleon structure from stochastic estimators*, PoS **LATTICE2013**, 271 (2014), arXiv:1311.1718 [hep-lat] .

[211] J. S. S. Najjar, *Nucleon structure from stochastic estimators*, Ph.D. thesis, Regensburg U. (2014).

[212] W. Simon, private communication (2021), [September-2021].

[213] RQCD collaboration, *LibHadronAnylsis*, `https://rqcd.ur.de:8443/mloeffler/lib-hadron-analysis` (2016), [Online; accessed 17-September-2021].

[214] RQCD collaboration, *chromaxml*, `https://rqcd.ur.de:8443/kern/chromaxml` (2016), [Online; accessed 17-September-2021].

[215] RQCD collaboration, *wick*, `https://rqcd.ur.de:8443/rudi_roedl/wick` (2016), [Online; accessed 17-September-2021].

[216] RQCD collaboration, *openGFF*, `https://rqcd.ur.de:8443/rudi_roedl/openGFF` (2016), [Online; accessed 17-September-2021].

[217] RQCD collaboration, *rioc*, `https://rqcd.ur.de:8443/rudi_roedl/rioc` (2018), [Online; accessed 17-September-2021].

[218] RQCD collaboration, *rios*, `https://rqcd.ur.de:8443/rudi_roedl/rios` (2018), [Online; accessed 17-September-2021].

[219] RQCD collaboration, *rioi*, `https://rqcd.ur.de:8443/rudi_roedl/rioi` (2018), [Online; accessed 17-September-2021].

[220] The Apache Software Foundation, *Cassandra*, `https://cassandra.apache.org/_/index.html` (2021), [Online; accessed 17-September-2021].

[221] C. Lehner *et al.*, *Grid Python Toolkit (GPT)*, `https://github.com/lehner/gpt` (2020), [Online; accessed 17-September-2021].

[222] G. S. Bali, S. Collins, P. Korcyl, R. Rödl, S. Weishäupl, and T. Wurm, *Hyperon couplings from $N_f = 2 + 1$ lattice QCD*, PoS **LATTICE2019**, 099 (2019), arXiv:1907.13454 [hep-lat] .

[223] P. L. J. Petrak, G. Bali, S. Collins, J. Heitger, D. Jenkins, S. Weishäupl, and T. Wurm, in *38th International Symposium on Lattice Field Theory* (2021) arXiv:2112.00586 [hep-lat] .

[224] G. S. Bali, S. Collins, D. Richtmann, A. Schäfer, W. Söldner, and A. Sternbeck (RQCD), *Direct determinations of the nucleon and pion σ terms at nearly physical quark masses*, Phys. Rev. D **93**, 094504 (2016), arXiv:1603.00827 [hep-lat] .

[225] G. S. Bali, S. Collins, and A. Schäfer, *Effective noise reduction techniques for disconnected loops in Lattice QCD*, Comput. Phys. Commun. **181**, 1570 (2010), arXiv:0910.3970 [hep-lat] .

[226] RQCD collaboration, *stoch_discon*, `https://rqcd.ur.de:8443/jakob_simeth/stoch_discon` (2016), [Online; accessed 21-September-2021].

[227] S. Bernardson, P. McCarty, and C. Thron, *Monte Carlo methods for estimating linear combinations of inverse matrix entries in lattice QCD*, Comput. Phys. Commun. **78**, 256 (1993).

[228] A. Ó Cais, K. J. Juge, M. J. Peardon, S. M. Ryan, and J.-I. Skullerud (TrinLat), *Improving algorithms to compute all elements of the lattice quark propagator*, Nucl. Phys. B Proc. Suppl. **140**, 844 (2005), arXiv:hep-lat/0409069 .

[229] J. Viehoff, N. Eicker, S. Gusken, H. Hoeber, P. Lacock, T. Lippert, K. Schilling, A. Spitz, and P. Uberholz (TXL), *Improving stochastic estimator techniques for disconnected diagrams*, Nucl. Phys. B Proc. Suppl. **63**, 269 (1998), arXiv:hep-lat/9710050 .

[230] C. Thron, S. J. Dong, K. F. Liu, and H. P. Ying, *Pade - Z(2) estimator of determinants*, Phys. Rev. D **57**, 1642 (1998), arXiv:hep-lat/9707001 .

[231] G. S. Bali, H. Neff, T. Duessel, T. Lippert, and K. Schilling (SESAM), *Observation of string breaking in QCD*, Phys. Rev. D **71**, 114513 (2005), arXiv:hep-lat/0505012 .

[232] S. Collins, G. Bali, and A. Schafer, *Disconnected contributions to hadronic structure: a new method for stochastic noise reduction*, PoS **LATTICE2007**, 141 (2007), arXiv:0709.3217 [hep-lat] .

[233] N. Eicker *et al.* (TXL), *Evaluating sea quark contributions to flavor singlet operators in lattice QCD*, Phys. Lett. B **389**, 720 (1996), arXiv:hep-lat/9608040 .

[234] RQCD collaboration, *PoleDancer*, `https://rqcd.ur.de:8443/twurm/PoleDancer` (2017), [Online; accessed 22-September-2021].

[235] RQCD collaboration, *PyFileReader*, `https://rqcd.ur.de:8443/twurm/PyFileReader` (2017), [Online; accessed 22-September-2021].

[236] M. Göckeler, R. Horsley, M. Lage, U.-G. Meißner, P. Rakow, A. Rusetsky, G. Schierholz, and J. Zanotti, *Scattering phases for meson and baryon resonances on general moving-frame lattices*, Phys. Rev. **D86**, 094513 (2012), arXiv:1206.4141 [hep-lat] .

[237] F. Erben, J. Green, D. Mohler, and H. Wittig, *Rho resonance, timelike pion form factor, and implications for lattice studies of the hadronic vacuum polarization*, Phys. Rev. **D101**, 054504 (2020), arXiv:1910.01083 [hep-lat] .

[238] M. Werner *et al.* (ETMC), *Hadron–Hadron interactions from $N_f = 2 + 1 + 1$ lattice QCD: the ρ-resonance*, Eur. Phys. J. **A56**, 61 (2020), arXiv:1907.01237 [hep-lat] .

[239] M. Lüscher, *Volume Dependence of the Energy Spectrum in Massive Quantum Field Theories. 2. Scattering States*, Commun. Math. Phys. **105**, 153 (1986).

[240] M. Lüscher, *Two-particle states on a torus and their relation to the scattering matrix*, Nucl. Phys. **B354**, 531 (1991).

[241] J. Dudek, R. Edwards, and C. Thomas (HSC), *Energy dependence of the ρ resonance in $\pi\pi$ elastic scattering from lattice QCD*, Phys. Rev. **D87**, 034505 (2013), [Erratum: Phys. Rev. **D90** (2014) 099902], arXiv:1212.0830 [hep-ph] .

[242] D. Wilson, R. Briceño, J. Dudek, R. Edwards, and C. Thomas, *Coupled $\pi\pi, K\overline{K}$ scattering in P-wave and the ρ resonance from lattice QCD*, Phys. Rev. D **92**, 094502 (2015), arXiv:1507.02599 [hep-ph] .

[243] G. Gounaris and J. Sakurai, *Finite-width corrections to the vector-meson-dominance prediction for $\rho \to e^+e^-$*, Phys. Rev. Lett. **21**, 244 (1968).

[244] K. Kawarabayashi and M. Suzuki, *Partially conserved axial-vector current and the decays of vector mesons*, Phys. Rev. Lett. **16**, 255 (1966).

[245] Riazuddin and Fayyazuddin, *Algebra of current components and decay widths of ρ and K^* mesons*, Phys. Rev. **147**, 1071 (1966).

[246] D. Djukanovic, M. Schindler, J. Gegelia, G. Japaridze, and S. Scherer, *Universality of the ρ meson coupling in effective field theory*, Phys. Rev. Lett. **93**, 122002 (2004), arXiv:hep-ph/0407239 .

[247] X. Feng, S. Aoki, S. Hashimoto, and T. Kaneko, *Timelike pion form factor in lattice QCD*, Phys. Rev. **D91**, 054504 (2015), arXiv:1412.6319 [hep-lat] .

[248] H. Meyer, *Lattice QCD and the Timelike Pion Form Factor*, Phys. Rev. Lett. **107**, 072002 (2011), arXiv:1105.1892 [hep-lat] .

[249] M. Lüscher and U. Wolff, *How to calculate the elastic scattering matrix in two-dimensional quantum field theories by numerical simulation*, Nucl. Phys. B **339**, 222 (1990).

[250] G. S. Bali, S. Collins, A. Cox, G. Donald, M. Göckeler, C. B. Lang, and A. Schäfer (RQCD), *ρ and K^* resonances on the lattice at nearly physical quark masses and $N_f = 2$*, Phys. Rev. D **93**, 054509 (2016), arXiv:1512.08678 [hep-lat] .

[251] M. Fischer, B. Kostrzewa, M. Mai, M. Petschlies, F. Pittler, M. Ueding, C. Urbach, and M. Werner (ETM), *The ρ-resonance with physical pion mass from $N_f = 2$ lattice QCD* (2020), arXiv:2006.13805 [hep-lat] .

[252] M. Fischer, B. Kostrzewa, J. Ostmeyer, K. Ottnad, M. Ueding, and C. Urbach, *On the generalised eigenvalue method and its relation to Prony and generalised pencil of function methods*, Eur. Phys. J. A **56**, 206 (2020), arXiv:2004.10472 [hep-lat] .

[253] M. Göckeler, R. Horsley, E.-M. Ilgenfritz, H. Perlt, P. E. L. Rakow, G. Schierholz, and A. Schiller, *Lattice operators for moments of the structure functions and their transformation under the hypercubic group*, Phys. Rev. D **54**, 5705 (1996), arXiv:hep-lat/9602029 .

[254] C. Alexandrou, M. Constantinou, K. Hadjiyiannakou, K. Jansen, H. Panagopoulos, and C. Wiese, *Gluon momentum fraction of the nucleon from lattice QCD*, Phys. Rev. D **96**, 054503 (2017), arXiv:1611.06901 [hep-lat] .

[255] P. E. Shanahan and W. Detmold, *Gluon gravitational form factors of the nucleon and the pion from lattice QCD*, Phys. Rev. D **99**, 014511 (2019), arXiv:1810.04626 [hep-lat] .

[256] G. S. Bali, S. Bürger, S. Collins, M. Göckeler, M. Gruber, S. Piemonte, A. Schäfer, A. Sternbeck, and P. Wein, *Nonperturbative Renormalization in Lattice QCD with three Flavors of Clover Fermions: Using Periodic and Open Boundary Conditions*, Phys. Rev. D **103**, 094511 (2021), arXiv:2012.06284 [hep-lat] .

[257] C. Alexandrou *et al.*, *Quark and gluon momentum fractions in the pion from $N_f = 2 + 1 + 1$ lattice QCD* (2021), arXiv:2109.10692 [hep-lat] .

[258] P. C. Barry, C.-R. Ji, N. Sato, and W. Melnitchouk (Jefferson Lab Angular Momentum (JAM)), *Global QCD analysis of pion parton distributions with threshold resummation* (2021), arXiv:2108.05822 [hep-ph] .

[259] I. Novikov *et al.*, *Parton Distribution Functions of the Charged Pion Within The xFitter Framework*, Phys. Rev. D **102**, 014040 (2020), arXiv:2002.02902 [hep-ph] .

[260] J. Zinn-Justin, *Quantum Field Theory and Critical Phenomena; 4th ed.*, International series of monographs on physics (Clarendon Press, Oxford, 2002).

[261] The HDF Group, *Hierarchical data format version 5*, `http://www.hdfgroup.org/HDF5` (2000-2010), [Online; accessed 16-September-2021].